University of Liège

Faculty of Applied Sciences

Crashworthiness of offshore wind turbine jackets based on the continuous element method

Dissertation submitted for the degree of
Doctor in Applied Sciences

by

Timothée Pire
FRIA Research-Fellow

September 2018

Abstract

Nowadays, the offshore wind industry is expanding fast and many wind farms will be built in the near future. For every new project, a complete collision risk analysis is required. Usually, the crashworthiness of an offshore structure is assessed with non linear finite element simulations that provide accurate results but are time-demanding. Such approach is relevant in the final design but is not suitable at pre-design stage for which hundreds or sometimes thousands of collision scenarios have to be investigated. The purpose of this PhD thesis is thus to develop simplified semi-analytical formulations to compute quickly the resistance of an offshore wind turbine jacket impacted by a ship.

Based on finite element simulations, the structural behaviour of a collided jacket is described and four deformation modes are identified, namely the local crushing of the impacted tubular members, the global deformation of the whole jacket, the punching of legs by compressed braces and the deformation at the base of the jacket legs.

For each of them, closed-form expressions describing the evolution of the resistant force with the ship penetration are developed and validated using the finite element software *LS-DYNA*. The resistance related to the deformation modes involving a cross-section modification is derived using an analytical approach based on the upper-bound theorem associated with a plastic limit analysis. Considering the global deformation of the overall jacket, a methodology similar to nonlinear finite elements is developed, in which each tubular member is modelled as one single 3D beam element.

The total resistant force of the collided jacket is computed with an algorithm based on the continuous elements method. The collision time is split into short time steps for which the resistant force is computed for the four deformation modes; the total resistant force at the considered time step is assumed to be the minimum one. As the deformation in one mode may have an effect on the other ones, their interactions are accounted for in the formulations previously described.

Resistant forces and dissipated energies calculated from this semi-analytical method are then compared to finite element simulations for a wide range of collision scenarios involving initial kinetic energies up to 75 MJ. Finite element and semi-analytical results are in good agreement, which validates the presented innovative developments and algorithm.

Résumé

Actuellement, l'industrie de l'éolien offshore grandit rapidement et plusieurs parcs d'éoliennes vont être construits dans un avenir proche. Pour chaque nouveau projet, une analyse de risque exhaustive est demandée. Habituellement, la résistance à l'impact d'une structure offshore est évaluée grâce à des simulations par éléments finis qui fournissent des résultats précis mais demandent un temps de calcul important. Une telle approche est pertinente dans la phase finale de dimensionnement mais n'est pas adaptée à une étape de pre-design pour laquelle des centaines voire des milliers des scenarios de collisions doivent être investigués. L'objectif de cette thèse de doctorat est donc de développer des formulations simplifiées semi-analytiques pour calculer rapidement la résistance d'une éolienne offshore impactée par un navire.

Sur base de simulations par éléments finis, la réponse structurelle d'un jacket impacté est décrite et quatre modes de déformation sont identifiés, à savoir l'écrasement local des cylindres impactés, la déformation globale de l'ensemble du jacket, le poinçonnement des legs par les braces comprimés et la déformation à la base des legs du jacket.

Pour chacun d'eux, des expressions univoques décrivant l'évolution de la force résistante par rapport à l'avancement du bateau sont développées et validées avec le logiciel de calcul par éléments finis *LS-DYNA*. La résistance liée aux modes de déformation qui impliquent une modification de la section transversale est obtenue en utilisant une approche analytique basée sur le théorème de la borne supérieure associé à une analyse limite plastique. Concernant la déformation globale du jacket, une méthode similaire à celle des codes éléments finis non linéaires est développée et chaque cylindre est modélisé en tant qu'un unique élément de poutre 3D.

La force résistante totale du jacket impacté est calculée à l'aide d'un algorithme basé sur la méthode des éléments continus. La durée de la collision est subdivisée en plusieurs courts pas de temps pour lesquels la force résistante est calculée pour chacun des quatre modes de déformation; la force résistante totale pour le pas de temps considéré est supposée être la force minimum. Puisque la déformation dans un mode peut avoir un effet sur les autres, leurs interactions sont prises en considération dans les formulations décrites précédemment et sont mises à jour à chaque pas de temps.

Les forces résistantes et énergies dissipées calculées avec cette méthode semi-analytique sont ensuite confrontées aux simulations par éléments finis pour une large gamme de scénarios de collision et avec des énergies cinétiques initiales allant jusque 75 MJ. Les résultats obtenus à l'aide du code semi-analytiques corrèlent bien avec ceux issus des calculs par élément finis, ce qui valide les développements innovants et l'algorithme présentés.

Remerciements

Alors qu'un doctorat peut de prime abord sembler être un travail individuel, de nombreuses personnes m'ont accompagné et soutenu dans ce projet et m'ont aidé à aboutir à ce résultat.

Je tiens tout d'abord à remercier mon promoteur, le Prof. Philippe Rigo, pour m'avoir proposé ce doctorat et pour m'avoir conseillé tout au long de celui-ci. De plus, grâce à ses nombreux contacts dans le domaine des structures hydrauliques, il m'a introduit auprès de scientifiques et industriels spécialisés dans mon domaine de recherche. Cela m'a ainsi permis d'apporter un point de vue neuf sur mon travail.

Mes remerciements vont également au Prof. Hervé Le Sourne de l'ICAM Nantes qui supervise le projet de recherche consacré aux impacts de navires au sein de son institution et de l'Université de Liège. Son expertise dans le domaine des méthodes numériques et analytiques qu'il a partagée sans réserve avec moi au cours de ses séjours réguliers à Liège ainsi que lors de mes visites à Nantes m'a été indispensable. Je le remercie également pour son implication et sa grande disponibilité.

Merci aux membres de mon comité de thèse, les Profs. Vincent Denoël et Laurent Duchêne, ainsi qu'aux membres du jury pour les conseils avisés qu'ils ont pu m'apporter.

Je remercie également tous mes collègues pour leur bonne humeur et tous les bons moments passés ensemble. Un merci plus spécifique pour ceux avec qui j'ai partagé le bureau, Loïc, Andreea et Sara, avec qui l'ambiance a souvent été studieuse mais heureusement régulièrement ponctuée de rires.

Ma famille m'a beaucoup soutenu et encouragé. Merci à mes parents, mes frères et soeurs, mes amis ; grâce à leurs questions et leur intérêt, j'ai appris à faire comprendre mon travail, à le rendre accessible à tous et ainsi à mieux l'exprimer.

Mon épouse, Tatiana, est également passée par le doctorat et sait ce que cela représente. Merci pour ses conseils, pour m'avoir poussé jusqu'au bout en toutes circonstances, mais aussi et sourtout pour son soutien et ses petites attentions quotidiennes.

Merci finalement à toutes les personnes qui, par leur bienveillance, m'ont donné la motivation et l'entrain jusqu'au terme de ce travail.

Je souhaite remercier le Fonds pour la Formation à la Recherche dans l'Industrie et l'Agriculture (FRIA-FNRS) pour la confiance donnée dans mon projet de doctorat et dans mes capacités à mener à bien ce travail ainsi que pour son soutien financier durant ces quatre années de recherches. Dans le cadre de cette bourse, le *Bureau Greisch* et *Electrabel* ont soutenu ce projet et m'ont aidé à cerner les besoins des entreprises.

Merci également à *STX France* et au *Bureau Veritas* pour leur participation dans la définition des objectifs du projet. Merci finalement à *MSC* (*PATRAN-NASTRAN*) et à *LSTC* (*LS-DYNA*) pour l'aide technique fournie durant ce doctorat.

Acronyms

CoV	Coefficient of Variation
DNV	Det Norske Veritas
EU	European Union
EWEA	European Wind Energy Association
FE	Finite Elements
FEA	Finite Element Analysis
GWEC	Global Wind Energy Council
ICAM	Institut Catholique d'Arts et Métiers
IPCC	Intergovernmental Panel on Climate Change (GIEC in French)
ISUM	Idealised Structural Unit Method
OSV	Offshore Supply Vessel
OWT	Offshore Wind Turbine
SI	International System of units
ULiège	University of Liège

Units

All the units used in the thesis are expressed in the SI.

Contents

Chapter 1

Introduction and state of the art

Abstract:

The purpose of this introduction is to describe the context of the offshore wind industry and the existing scientific work performed in relation to ship collisions in order to demonstrate the interest of this PhD.

It is agreed that earth global warming is related to pollution due to human activities, and a reduction of fossil fuel resources consumption appears to be mandatory to prevent major environmental damage. Renewable sources of energies need therefore to be more extensively developed. Amongst them the offshore wind industry is expanding quickly and the number of offshore wind turbines (OWT) installed worldwide is increasing yearly. Similarly, the number of ships rises also. Due to those two factors, the probability of a collision between a ship and an offshore wind turbine increases as well. As required by design standards, this loading case has to be investigated during the design process.

Several authors studied the resistance of offshore or naval structures impacted by a ship using experimental, empirical, numerical or analytical methods. Their main results are discussed and provide a useful state of the art for the present thesis. Regarding the crashworthiness of OWT jackets, numerical simulations were already performed to study the behaviour of such impacted structures. However, the large computation time required by the FE method makes it not suitable for a pre-design stage and complete collision risk assessment. The development of a simplified method, which is the aim of my PhD thesis, becomes therefore a major interest for a preliminary design phase.

The structure of the document finally is detailed in this Chapter.

1.1 Context of the research

For several years, the energetic context is being submitted to a complete mutation. In the past, fossil resources (fuel, coal, uranium, ...) were used as the only source of energy available for industry, transportation, personal use, ... Today, it appears that the use of those resources has to be limited.

First, the combustion of most fossil fuels produces several polluting gases, amongst them the well-known CO_2. Today, several scientific researches demonstrated that the global warming at earth scale is related to the increase of gases emission, which significantly started to increase at the beginning of the 20th century, with the development of industry and the emergence of additional countries in the worldwide economy. Princiotta [63] gives the record of carbon dioxide concentration and the global warming since 1750 and proposes a model to predict the values until 2100 (Figs. 1.1 and 1.2 respectively).

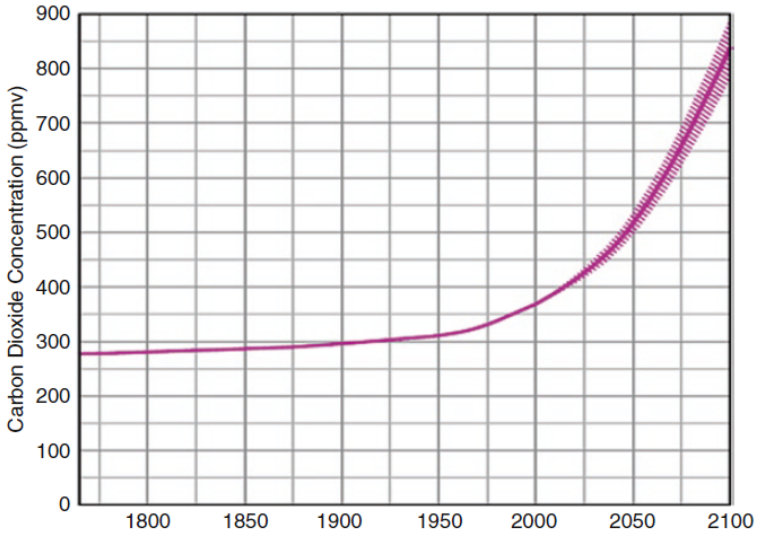

Figure 1.1: CO_2 concentration measurements and projections [63]

According to the 5th IPCC (GIEC in French) report published in 2013 [37], the global warming should be limited to $2°C$ with regard to the pre-industrial period to prevent irreversible climate changes and natural disasters such as cyclones, drought, loss of species, sea level elevation, ... This objective of $2°C$ temperature elevation was signed by 195 countries in 2015 during the COP21 taking place in Paris.

Uranium that is used in the nuclear power plants is also a fossil resource. Even if those plants do not emit any polluting gases, the treatment and storage of the nuclear wastes remains a challenging issue. The potential danger of such installation has also to be considered, as the accidents of Tchernobyl or Fukushima reminded.

In addition to the pollution issue, the fossil resources are depleting. Even if it is difficult to predict when the resources will be missing, it appears anyway that the cost required to get access to fossil fuels will increase with the complexity to extract them.

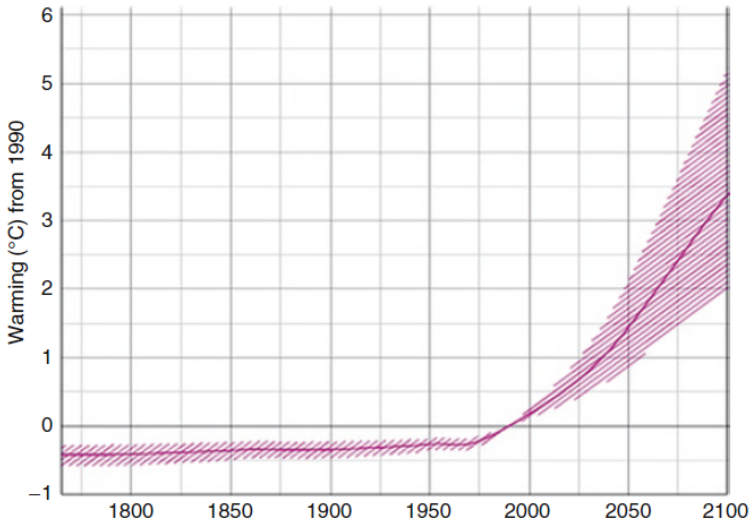

Figure 1.2: Temperature variation with regard to 1990 measurements and projections [63]

To overcome those issues, researches are performed to develop innovative sources of energy. In order to reduce as much as possible the amount of polluting substances emitted, renewable sources of energy are mainly investigated, such as wind (wind turbines), sun (solar or photovoltaic panels), water (hydroelectric power plants, technologies based on waves[1] or tidal, ...), biomass and geothermal energy. Any of those sources may be considered as better than another one. Their use depends on the local conditions where sources of energy are required, and it appears that all the technologies are complementary.

The present thesis focuses on wind energy, and specifically to offshore wind turbine jackets.

Wind energy was used for centuries for navigation purpose and for wind mills. The first record of a wind turbine developed to produce electricity is from 1887. It was created by Charles Brush and built in Cleveland, USA (Fig. 1.3) [23].

Later on, the technology was improved and the turbines power increased rapidly. The first generator with more than 1 MW was built in 1941.

The first offshore wind farm, named Vindeby, was built in Denmark in 1991. It consists in 11 turbines with a power of 450 kW each [65].

Until then, the wind power installed is increasing constantly. According to the *Global Wind Energy Council* (GWEC) [33], the wind power (onshore and offshore) installed yearly worldwide is increasing constantly since 2000 (except in 2013) until 2015, as can be seen in Fig. 1.4. The corresponding cumulative wind capacity is expanding fast, as represented in Fig. 1.5. Republic of China represents the largest wind power installed in the world in 2015, with 33.6% of the total worldwide capacity, followed by the USA (17.2%) and Germany (10.4%), as given in Fig. 1.6. As long as all the countries of EU are considered, they represent 32.7% with 141.6 GW installed [33].

[1]For example `https://www.pelamiswave.com/pelamis-technology/`

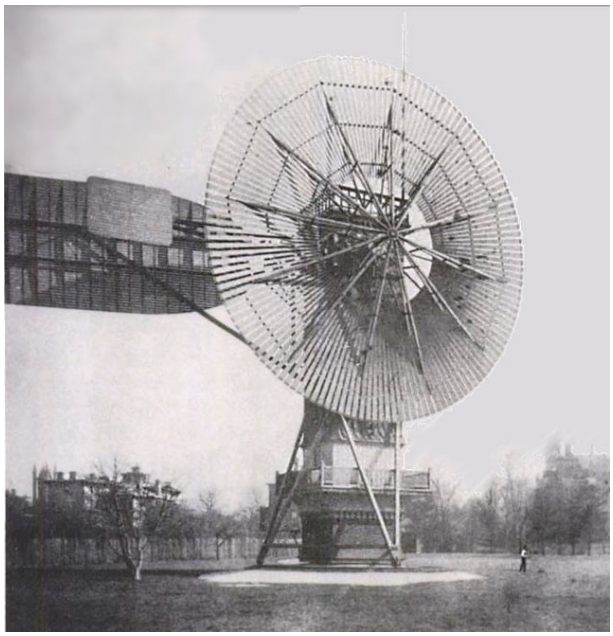

Figure 1.3: Turbine developed by Charles Brush in 1887 [23]

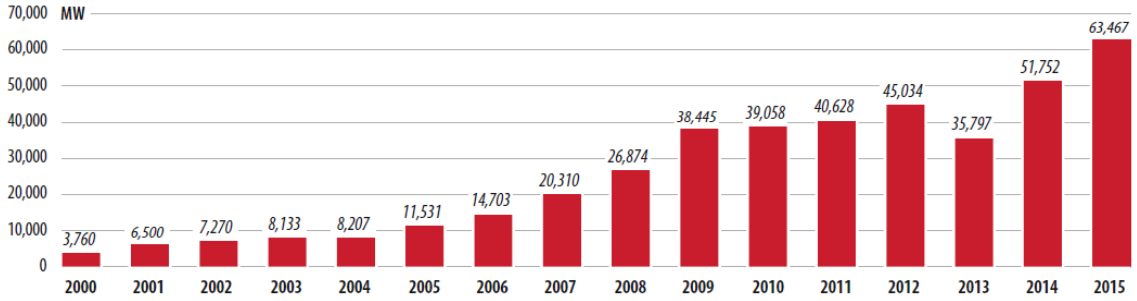

Figure 1.4: World annual wind capacity installed $[MW]$ [33]

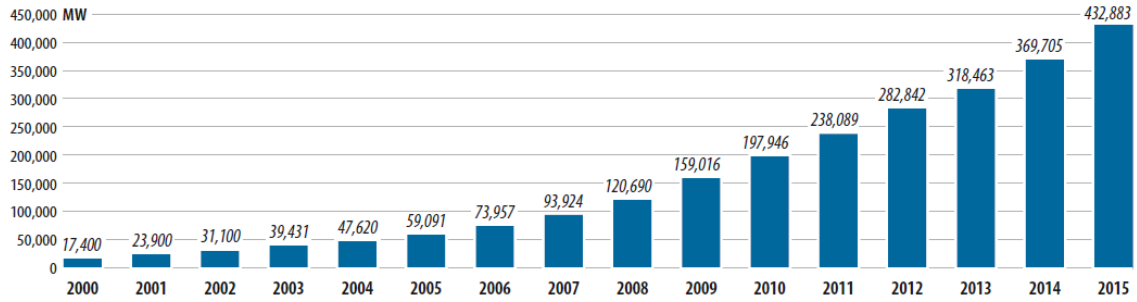

Figure 1.5: World cumulative wind capacity installed $[MW]$ [33]

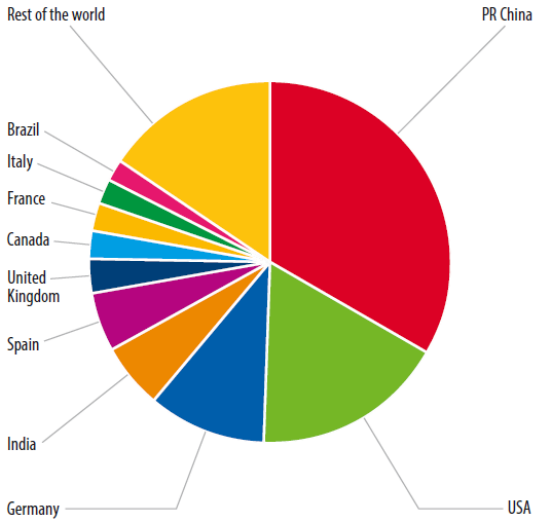

Country	MW	% Share
PR China	145,362	33.6
USA	74,471	17.2
Germany	44,947	10.4
India	25,088	5.8
Spain	23,025	5.3
United Kingdom	13,603	3.1
Canada	11,205	2.6
France	10,358	2.4
Italy	8,958	2.1
Brazil	8,715	2.0
Rest of the world	67,151	15.5
Total TOP 10	**365,731**	**84.5**
World Total	**432,883**	**100**

Figure 1.6: Worldwide repartition of cumulative wind capacity installed [33]

The *European Wind Energy Association* (EWEA) [32] collects wind data for the continent. Similarly to the worldwide trends, a large expansion of the cumulative wind capacity (onshore and offshore) may be noticed, as represented in Fig. 1.7. The total power installed was equal to 141.6 *GW* in 2015, which corresponds to 15.6% of the electricity production in EU (Fig. 1.8), less than gas and coal, but more than water and nuclear power [32]. The wind cumulative power for the most representative countries in EU is given in Table 1.1.

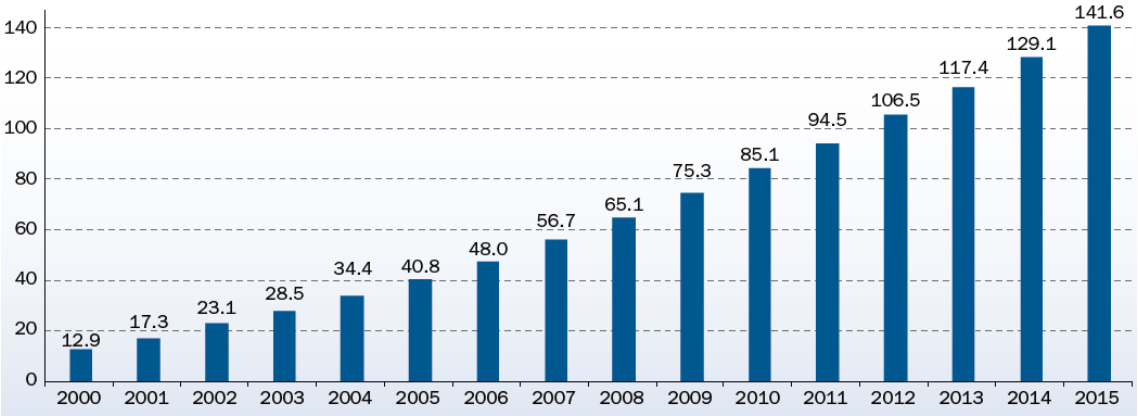

Figure 1.7: Europe cumulative wind capacity installed [*GW*] [32]

In EU, it appears that most of the wind power installed is onshore, but the part of offshore wind is increasing regularly, as can be seen in Fig. 1.9 [32], and is expected to continue growing.

With regard to onshore wind turbines, building offshore wind farms is more complex and more expensive. All the turbines have to be connected to a substation, and electricity is then driven to shore through a long cable, which causes a voltage drop and therefore a loss of power. Offshore maintenance is also a task more complex than onshore because it requires ships navigating within the wind farms, which makes it more expensive and increases the probability of collisions.

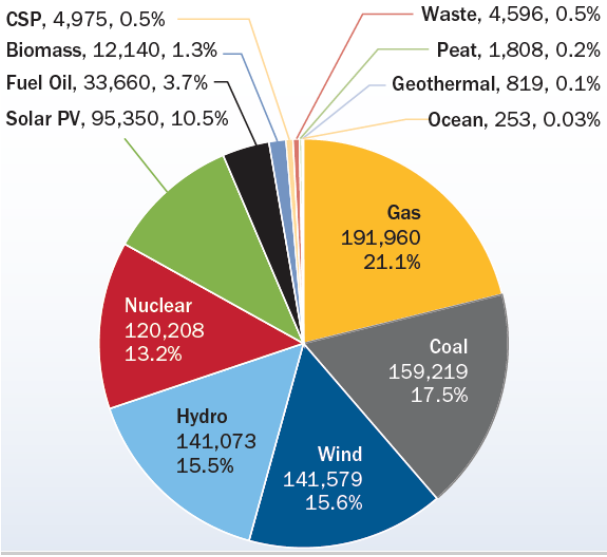

Figure 1.8: EU energy mix in 2015 [32]

Table 1.1: Cumulation wind power repartition in EU [32]

Pos.	Country	Cumulative wind power $[GW]$	EU percentage
1	Germany	44.9	31.7
2	Spain	23.0	16.2
3	UK	13.6	9.6
4	France	10.4	7.3
5	Italy	9.0	6.3
	...		
14	Belgium	2.2	1.6

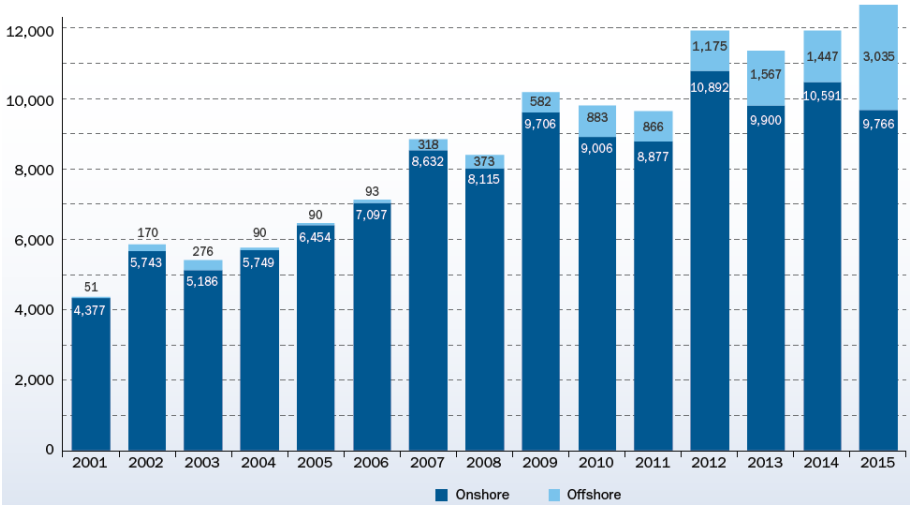

Figure 1.9: EU yearly installed wind power onshore and offshore $[MW]$ [32]

However, offshore wind farms may take advantage of higher and more constant wind speeds that are not disturbed by hills or buildings. In addition, they are built far from shore and have less incidence on human being (noise, landscape modification, ...). This allows also for larger wind turbines and therefore for larger unitary power.

Offshore wind remains therefore an attractive electricity power production system. The evolution of the offshore wind installed power in Europe is given in Fig. 1.10 [31].

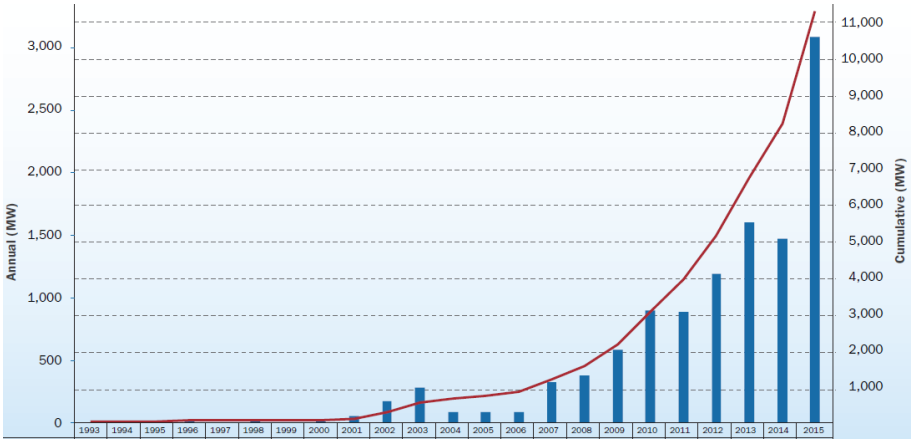

Figure 1.10: Yearly installed and cumulative offshore wind power installed in 2015 [31]

Most of the offshore power installed is in UK (45.9% of EU installed power in 2015), followed by Germany (29.9%), Denmark (11.5%) and Belgium (6.5%) [31]. The detail of total number of farms, wind turbines and offshore power installed in 2015 is given in Fig. 1.11.

Country	BE	DE	DK	ES	FI	IE	NL	NO	PT	SE	UK	Total
No. of farms	5	18	13	1	2	1	6	1	1	5	27	**80**
No. of turbines	182	792	513	1	9	7	184	1	1	86	1,454	**3,230**
Capacity installed (MW)	712	3,295	1,271	5	26	25	427	2	2	202	5,061	**11,027**

Figure 1.11: EU wind farms, wind turbines and offshore wind power installed in 2015 [31]

Several types of offshore wind turbine substructures exist, mainly chosen according to the water depth at the wind turbine location, as represented in Fig. 1.12 [6]. Up to 30 m, monopiles are mainly used. Until 60 m, jackets are the most common structures while floating wind turbines are preferred for deeper waters.

In 2016, monopiles represented more than 80% of the offshore wind turbines substructures installed, while the part of jackets was 6.6%. Only 1 floating turbine was installed, corresponding to less than 0.1% of substructures, and the rest consists in tripods, tripiles and gravity base foundations.

In this thesis, we focus only on OWT jackets, which is a supporting structure composed of 4 legs (main tubular members) connected by many inclined braces (smaller tubular members). The general shape of that structure is a truncated pyramid with 4 faces (Fig. 1.13).

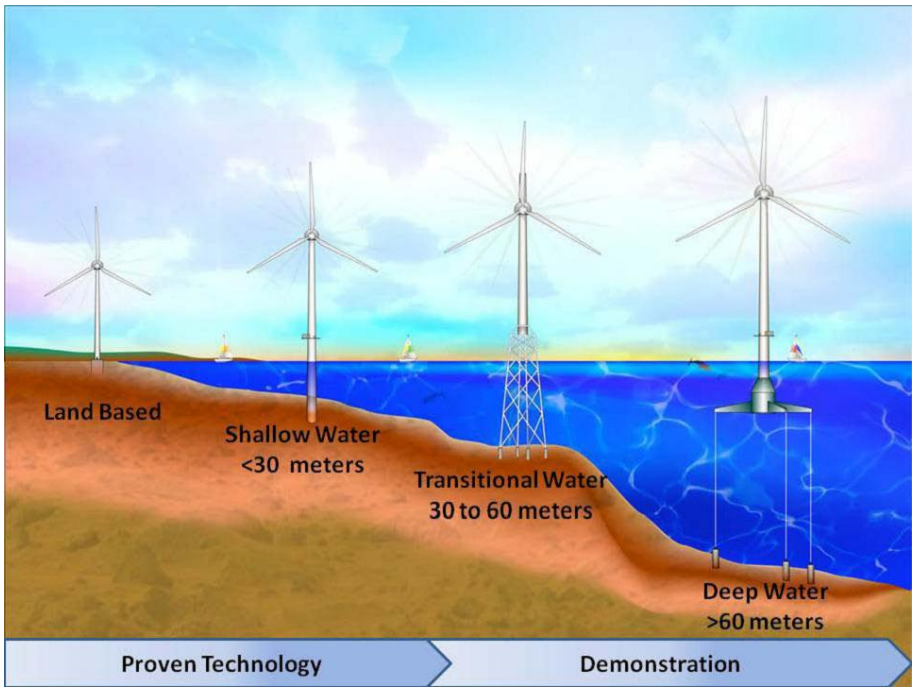

Figure 1.12: Offshore wind turbine foundation types [6]

Figure 1.13: Offshore wind turbine jacket [52]

The size and unitary power of the offshore wind turbines expands fast. Today, the length of a blade could reach more than 80 m, longer than the *Airbus A380* wingspan. The average turbine rated capacity in 2016 was 4.8 MW, while it was 4 MW in 2012, 3 MW in 2005 and 2 MW in 2000. Prototypes of turbines now even reach a power of 8 MW.

As can be seen from these data, the number of installed wind farms is growing, and it is still expected to develop in the next years.

In parallel, the number of navigating ships is also increasing worldwide. The vessels become in addition larger and heavier.

Combining the increase of offshore wind turbines and navigating ships rises the probability of a collision between them, even with the improvement of navigation systems (radar, GPS, ...). In the literature, only few accidents are reported. However, Kvitrud [43] listed the collisions involving ships and platforms in Norway. Since 1982, 115 collisions were reported, amongst them 26 in the period 2001-2010. No death or injuries were caused during those incidents, but the material damage was important in some cases. The main collision properties described in [43] are summarised in Table 1.2.

Table 1.2: Significant ship - platform collisions in Norway properties

Date	Mass $[tons]$	Velocity $[m/s]$	Energy $[MJ]$
March 7th, 2004	$\approx 5,000$	3.7	≈ 39
June 2nd, 2005	$\approx 4,700$	≈ 3	> 20
November 13th, 2006	$\approx 100,000$	1.2	≈ 60
July 18th, 2007	$\approx 3,100$	$1 - 3.5$	$1.5 - 20$
June 8th, 2009	$\approx 6,000$	≈ 4.8	≈ 70

Robson [66] collected all the incidents between ships and platforms in the UK Continental Shelf between January 1st, 1975 and October 31st, 2001. From the database, 557 collisions were recorded on that period, and amongst them 17 were considered as severe (without more details on the notion of severity).

In the Offshore Design Standards edited by *Det Norske Veritas* (DNV) [21] and the American Petroleum Institute (API) [5], it is required to perform a complete collision risk analysis for every new offshore project. This consists in assessing the structural behaviour of both the striking ship and the offshore structure for a large range of parameters related to the ship (type, geometry, internal reinforcement, material, ...), to the structure (geometry, material, ...) and the collision itself (impact point, ship trajectory, ship mass and initial velocity, ...). The notion of risk involves also the probability of a collision to occur, as will be discussed in Section 2.2.

The minimum collision energy that has to be investigated, according to DNV [21] is 14 MJ for sideways collisions and 11 MJ for bow or stern collisions, which corresponds to a ship with a $5,000$ tons displacement and an initial velocity of 2 m/s. The American Petroleum Institute (API) [5] requires to consider a vessel of $1,000$ tons colliding the structure at a velocity of

0.5 m/s, which is much lower than the DNV requirements. Those initial kinetic energies are below the collision energies reported by Kvitrud [43] (up to 70 MJ).

In practice, each collision scenario has to be investigated before validating the offshore structure design. Due to the large number of parameters, this represents hundreds or even thousands of scenario to analyse. Several design methods exist and are discussed in the next Section 1.2 and in Chapter 2.

1.2 Ship collisions state of the art

Ship collisions were investigated by many authors.

Zhang [96] listed four types of methods in the case of ship-ship collisions that are also valid for ship - offshore structures impacts, namely:

- Experimental methods;
- Empirical methods;
- Numerical methods;
- Simplified analytical methods.

1.2.1 Experimental methods

Experimental methods remain the most reliable ones, as they include all the physical phenomena involved in a real collision event.

Most of the experiments were conducted on small parts of the structure. One may note, as an example, the ship hull resistance to an impact in order to prevent oil spills that was investigated in many studies, amongst them in Amdahl [2], Pedersen et al. [58] or Qvist et al. [64]. More recently, other experiments were conducted to analyse the crushing resistance of some structural parts of a collided ship, such as the one performed by Liu et al. [47] for web girders, Karlsson et al. [41] or Zhang et al. [95] for plates with lateral deformation, Simonsen and Ocakli [68] for folded plates, amongst others.

Experiments were also conducted on tubular members, which compose an OWT jacket. For example, Cerik et al. [18] performed low-velocity mass impact on a tubular structures and discussed the effect of the geometrical parameters (diameter, thickness, length) on the local denting and global displacement of the structure. The deformed structure after the collision for one set of parameters is illustrated in Fig. 1.14. The results obtained with the experimental tests were used to validate numerical (*USFOS* and *ABAQUS*) and analytical tools, that were shown to be in good accordance for most cases.

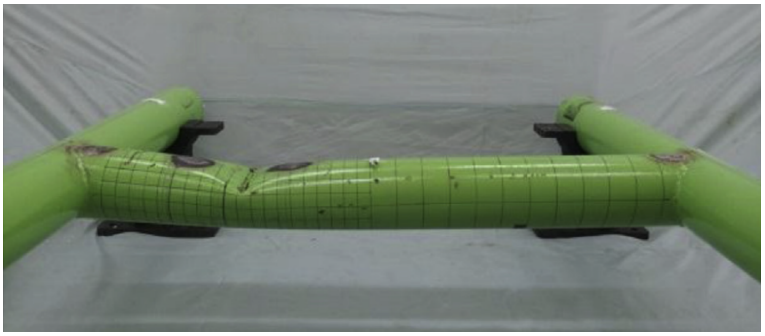

Figure 1.14: Deformation tubular structure after a low-velocity impact, as performed by Cerik et al. [18]

Other experimental studies were conducted by Watson et al. [83, 84], Ellinas and Walker [30], Jones et al. [40], Zeinoddini et al. [94] or Cho et al. [19], amongst others. For all those experiments, drop tests were performed on tubular members in order to analyse the influence of geometrical parameters. The results presented by those authors allow to identify the main parameters governing the tubular members behaviour, which are the tubular member diameter and thickness, the location of the impact and the energy dissipated during the impact.

Only few full-scale experimental tests of ship collisions were performed, due to the high complexity to built and install the experiment and to its cost. However, some results of full-scale ship collision are published by Wevers et al. [85], Tabri et al [75] (Fig. 1.15) or Ehlers [24]. The striking ship was equipped with a very rigid bulb and collided structures fixed on another vessel. Sensors were used to record forces and accelerations of both ships.

Figure 1.15: Full-scale ship collisions [75]

Scaled experiments were performed by Tabri et al. [76] by applying Froude scaling law on polyurethane foam ship models to analyse the external dynamics of the collision. However, the damage on both scaled ships could not be properly represented with those models.

Other scaled collisions were performed to optimise the stiffening systems of collided ships and analyse the influence of the striking ship shape. One may note for example the experiments conducted in Germany by Woisin [88] (Fig. 1.16) and in Japan whose results were presented by Akita et al. [1]. More recently, Calle et al. [17] also performed various experimental simulations

of scaled model including collisions against a rigid wall, grounding or ship-ship collisions. For all of them, validations were performed by comparison with finite element simulations.

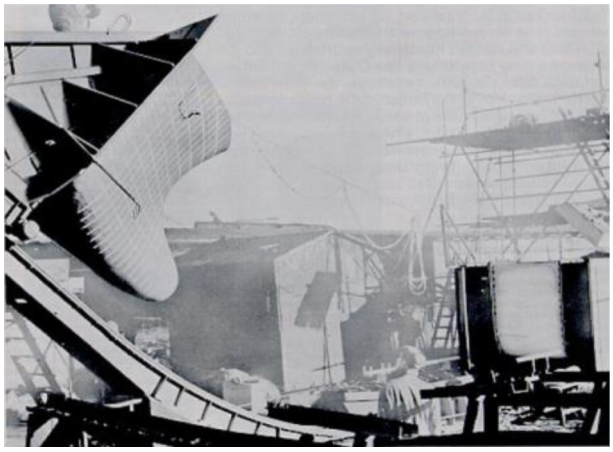

Figure 1.16: Scaled experiments of ship collisions performed by Woisin [88]

Regarding ship collisions on offshore wind turbine substructures, no article involving full-scale or scaled models were found in the literature.

1.2.2 Empirical methods

Empirical laws consists in expressions based on several experimental results used to describe physical phenomena. One of them was developed by Minorsky [50] to describe the dissipated energy and the volume destroyed for both the striking and struck ship after a collision. Other empirical formula were then established based on recorded accidents, such as Hagiwara et al. [34] or Suzuki et al. [74], but their application requires to investigate a ship with similar geometrical and mechanical properties than the ones considered to establish the formula.

Due to the lack of data available in the literature for ship - offshore structure, empirical laws do not exist to our knowledge in the investigated field.

1.2.3 Numerical methods

Nowadays, design offices mainly use finite element (FE) simulations to assess the resistance of an offshore structure impacted by a ship. Many researchers also used this method to investigate the structural behaviour of collided wind turbine jackets. Numerical assumptions that have to be performed were investigated by Biehl [11], Paik [53] or Pire et al. [60] amongst others.

As detailed in Section 1.1, design standards impose to consider initial kinetic energy of 14 MJ. Additional analyses were however performed to analyse the dynamic behaviour of a jacket impacted by ships with higher initial kinetic energies, such as performed by Amdahl and Johansen [4], Travanca and Hao [78, 80] or Moulas et al. [51] (Fig. 1.17). Those papers highlight the large deformation and plasticity that the jacket may suffer with energy impact of about 50

to 60 MJ. Vredeveldt and Schipperen [81] investigated the jacket geometrical and mechanical properties to improve the collision resistance and identified the best geometrical arrangements to resist ship impacts.

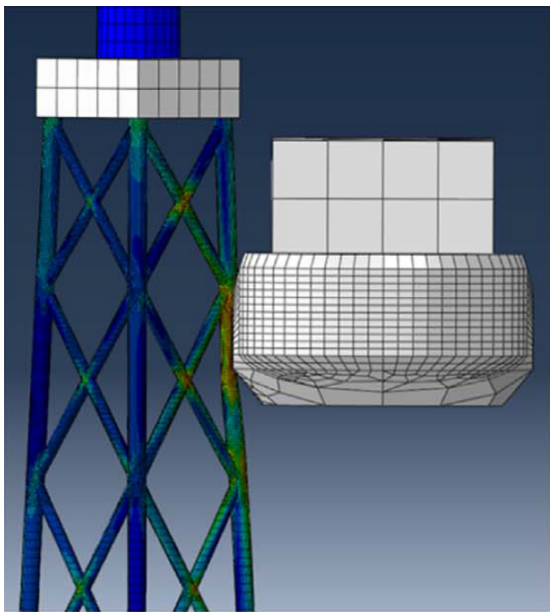

Figure 1.17: Ship - OWT jacket FE simulation, as performed by Moulas et al. [51]

Le Sourne et al. [44] investigated the effect of additional parameters, still using nonlinear FE simulations. It is shown that gravity loads have little influence on the behaviour of the jacket subjected to an impact and can therefore be neglected. They also conducted analyses with the soil stiffness as a parameter, considering it alternatively as rigid or as flexible. Comparisons between both behaviours show negligible differences. This will be discussed in more details in Section 3.3.

The stiffness of the striking ship is also important as the energy dissipation is related to the relative stiffness between both striking and struck structures. As shown in [44], several types of ships have completely different stiffnesses, an OSV bow being more flexible than an ice class bulk carrier side shell, for instance. Even if the striking ships will be considered as rigid in this thesis, the relative stiffness between the ship and the jacket will have to be investigated for further research.

Finite element simulations were also performed to assess the resistance of tubular members only submitted to lateral impacts. Soreide et al. [69, 71] computed the energy dissipation capacity of tubular members impacted laterally and discussed the residual resistant capacity of the dented cross-section. The reduction of carrying capacity of the dented section was also investigated by de Oliveira et al. [20]. Recent studies were conducted to analyse the effect of the indenter shape or the impact location along the tubular member, such as Travanca and Hao [79] (Fig. 1.18) or Cerik et al. [18].

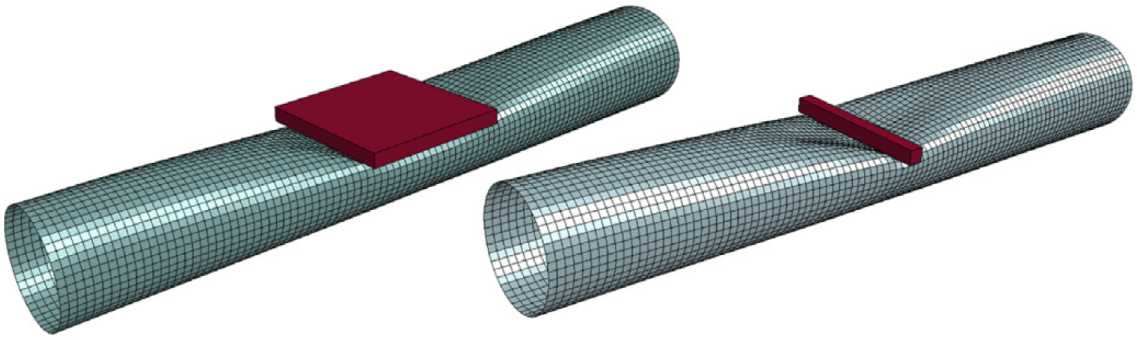

Figure 1.18: Deformation of the impacted tubular member for two indenter shape [79]

The effect of axial pre-loading on the tubular member resistance to lateral impact was also numerically investigated by Zeinoddini et al. [92, 93] or Khedmati et al. [42] and the models were validated with experimental results.

Even if FE algorithms are a useful tool to assess the resistance of a collided structure, two limitations remain, as mentioned here and detailed in Section A.

First of all, this method is time consuming because a fine mesh is required to get accurate results in the framework of collisions. In order to reduce the computation time, one may use FE formulations and consider each jacket tubular member as one single finite beam element. This idea was followed to create the software *USFOS* [70]. The software includes potential yielding at each tubular extremities and at midspan, large deformation formulations and joint resistance checks. However, the cross-section deformations are not included. Collisions simulations performed with *USFOS* were published by Tran [77] or Amdahl and Holmas [3], amongst others. This method is shown to provide accurate results with regard to FE simulations. Computation time may be also saved by combining numerical and semi-analytical method. As an example, Ehlers and Tabri [27] investigated the damage of a collided ship. Therefore, one single collision scenario is computed with FE simulation and the results are extended to other scenarios with semi-analytical expressions.

Then, modelling the rupture of a component is still arduous. Indeed, material rupture threshold are often defined using uniaxial traction tests. For collided structure, the stress state is most of time more complex than pure traction in the critical areas. Several material failure laws were developed for multiaxial stress states, but their application remain limited to some specific internal stresses distribution cases and most of them are not implemented in FE solvers yet. Failure laws are discussed with more details in Section A based on the work performed by Ehlers et al. [25, 26, 28], amongst others.

1.2.4 Simplified analytical methods

Another approach to compute quickly the resistance of an offshore jacket is to use simplified methods based on analytical formulations.

In the framework of collisions, this idea was first applied by Ito et al. [38], Yukio et al. [91] and Paik et al. [56] under the name of *Idealized Structural Unit Method* (ISUM). This method consists in dividing the structure into large sub-elements for which the plastic deformation is described by an analytical formulation, including folding, yielding, crushing or rupture. In addition, the interaction between all those sub-elements is ensured with a classical FE assembly method. It was demonstrated that this method provides accurate results within a computation time shorter than with FE simulations. Applications of this method were developed by Paik and Pedersen [54] to compute the damage of a collided ship, Paik and Thayamballi [57] for large steel plates transversally loaded or Pei et al. [59] for ships submitted to extreme wave loading, amongst others.

Other authors derived simplified analytical formulations for several impacted elements using the upper-bound theorem, as described by Jones [39]. One may note for example the work of Wierzbicki et al. [86], Wang et al. [82], Simonsen [67] or Zhang [96] (Fig. 1.19) for plates frontal crushing, Yu [90] for plates lateral loading or Amdahl [2] for plates crossings.

Figure 1.19: Initiation of plate folding [96]

As an extension to this work, Lützen [48] developed some analytical formulations to assess the deformation of a ship impacted by another ship. This involves formulations that describe the deformation of the bow, the decks and all the stiffening system of both striking and struck ships. The work of Lützen was then extended by Buldgen et al. [13] who adapted the so-called "super-element" method to ships oblique collisions and by Le Sourne et al. [45] who included the effects of hydrodynamic forces occurring during the ships rigid body movements. The scenarios of ship colliding lock gates was also studied by Buldgen et al. [15] for plane gates and by Buldgen et al. [16] for mitre gates. In the previous papers, the striking ship was considered to be rigid, which is conservative with regard to the collided structure.

Analytical formulations are similarly developed to assess the deformation of a ship colliding a rigid structure. The resistance and deformation of a ship bulb impacting an inclined rigid wall and rigid tubular member was studied by Buldgen et al. [12].

The deformation of tubular members, which compose the structure of an OWT jacket, was also investigated by several authors who developed analytical expressions able to describe their behaviour when submitted to localised lateral forces. The effect of local denting on the compressive load capacity of a tubular member is studied by Ellinas [29].

The model used for the local denting of such tubular members is later improved and described by Suh [73], Wierzbicki and Suh [87] or Hoo Fatt and Wierzbicki [35]. In those contributions, the authors introduce and describe a realistic deformation pattern of a tubular member submitted to a localised lateral load (Fig. 1.20). Using the principle of virtual velocities and plastic theorems, closed-form expressions are developed to assess the deformation of the cylindrical member for a given load. The effect of boundary conditions is also considered by applying rotation or axial displacement constraints at the tubular member extremities, and is demonstrated to have a large effect on the resistance to lateral loadings. The developed expressions are successfully validated by comparison with experimental results.

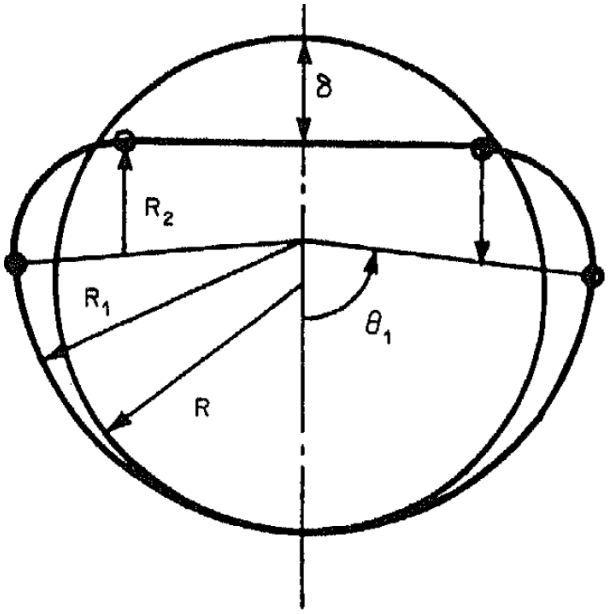

Figure 1.20: Dented cross-section, as modelled by Hoo Fatt and Wierzbicki [35]

While only local denting occurs for small indenter penetration, a global deformation is activated for larger ones, involving a plastic mechanism and a global deformation of the whole impacted tubular member. This phenomenon is described by analytical formulations developed by Paik et al. [55], taking into account several parameters such as the tubular member length, its diameter and thickness and the denting location.

1.3 Aim of the research

The state of the art detailed above confirms that the behaviour of impacted tubular members has been already investigated with experimental, numerical or analytical methods.

Ship impacts on complete OWT jackets are mainly investigated with numerical analyses that provide a good understanding of the collided jacket structural response and allow to identify the main governing parameters. As discussed, FE simulations provide accurate results but they are time-demanding.

Experimental tests are expensive and can hardly be performed to design a jacket against ship impacts. As only few ship collisions on OWT jackets have been recorded, empirical laws have not been developed.

Today, numerical methods seem therefore to be the main approach to assess the crashworthiness of an OWT jacket.

However, hundreds or thousands of collision scenarios have to be investigated to perform a complete collision risk analysis. In a pre-design stage, the geometrical and mechanical properties of the jacket are still to be defined, and all the collision scenarios have to be computed for several jacket designs. FE simulations are thus not convenient for this pre-design stage, as the computation time required would be too long.

It appears that a tool able to assess quickly the crashworthiness of an OWT jacket is missing. The purpose of this thesis is to answer this issue by developing a simplified method based an analytical approach to assess quickly the resistance of such collided structures. This method has to be suitable for a pre-design process and to identify the most critical collision scenarios for a given jacket design. Those scenarios could be then investigated in more details with FE models. The purpose of this tool is not to replace other design methods, such as FE analyses, but is a useful complement during the first design steps.

DNV standard [21] requires to investigate collisions of 14 MJ (sideways impact) or 11 MJ (bow or stern impact), which is much lower than the collisions reported by Kvitrud [43] going up to 70 MJ. For the present thesis, it was decided to consider collisions up to 75 MJ corresponding to a ship with a $6,000$ tons displacement and an initial velocity of 5 m/s. To be conservative with regard to the jacket, the striking ship will be considered as rigid, such as all the initial ship kinetic energy is dissipated by the collided OWT jacket alone.

The developed method is based on the upper-bound theorem associated with a plastic limit analysis. Assumptions on the deformation pattern of the impacted structure are required to use this theorem. FE simulations are thus performed to analyse the structural behaviour of the jacket and to identify the main deformation modes.

Closed-form expressions can then be derived to assess the resistance with regard to the ship penetration for all the identified deformation modes. The developed expressions are validated with FE simulations performed with *LS-DYNA*.

As the four identified deformation modes may occur simultaneously during a collision, an algorithm based on the so-called "continuous element method" has to be implemented to compute the total resistance of the jacket and take into account the interactions between all of them. The validation of the algorithm is achieved by comparing the results with FE simulations.

Several articles have been published by the author regarding the developed method, including the analytical developments used to describe the behaviour of some jacket component such as the impacted tubular members (Buldgen et al. [14]), the deformation due to punching (Pire et al. [62]) or the deformation at the base of the jacket (Pire et al. [61, 62]), the global algorithm (Pire et al. [60] and Le Sourne et al. [46]), or the numerical validation (Pire et al. [60]).

The same approach is followed by several researchers in the University of Liège (Belgium) and ICAM Engineering School in Nantes (France), under the supervision of Prof. Philippe Rigo and Prof. Hervé Le Sourne. Ship collisions on OWT monopiles and on floating OWT are investigated by Ms. Andreea Bela [8, 9] and Ms. Sara Echeverry Jaramillo [22] respectively. Several Master Thesis related to ship collisions on offshore structures were also achieved in these two institutions, such as Mr. Andres Barrera Arenas [7], Mr. Jose Babu Maliakel [49], Ms. Jing-Ru Hsieh [36], Mr. Pierre Berthonneau [10], Mr. Anthony Soret [72] and Mr. Pyae Sone Oo Yeye [89].

1.4 Structure of the thesis

The present thesis is divided into 9 Chapters, each of them having its own bibliography.

Chapter 1 **Introduction and state of the art:**
This Chapter presents the context of the research and describes the existing scientific work related to ship collisions. Based on the state of the art, the objectives of the thesis are defined and the structure of the thesis is described.

Chapter 2 **Collision risk analysis for offshore structures:**
This Chapter provides the theoretical background of both methods used in this thesis, namely the FE method and the analytical method.

Chapter 3 **Ship collision on offshore wind turbine analysis:**
The geometrical description of both the collided jacket and the striking ship is detailed. The numerical assumptions to model the collision are discussed. Finally, four deformation modes of the collided jacket are identified and described.

Chapter 4 **Local crushing of impacted tubular members:**
The analytical developments performed to assess the crushing force and the dissipated energy of the tubular members impacted by the ship stem or bulb are detailed and validated by comparison with FE simulations.

Chapter 5 **Global deformation of the whole jacket:**
This Chapter describes the algorithm, similar to FE one, developed to compute the deformation of the whole impacted jacket, including the buckling of the compressed tubular members. The results are validated by comparison with FE simulations.

Chapter 6 **Punching of legs by compressed braces:**
Semi-analytical expressions are derived to compute the resistant force and dissipated energy of a leg punched by a compressed brace. The methodology used to consider the punching process on the whole jacket is also detailed. Similarly, a validation process is performed.

Chapter 7 **Deformation at the base of the jacket:**
During a collision, a significant part of energy is dissipated near the foundation level, which is investigated in this Chapter. As for the other deformation modes, validation is performed.

Chapter 8 **General algorithm to assess the crashworthiness of an OWT jacket:**
The general algorithm used to compute the total resistance of the collided OWT jacket is fully described. It combines all four deformation modes and their interactions. Validation is finally performed by comparison with FE simulations.

Chapter 9 **Conclusions and perspectives:**
This Chapter summarises the thesis and lists my personal contributions. Some perspectives of research are also discussed.

Bibliography

[1] Y Akita, N Ando, Y Fujima, and K Kitamura. Studies on Collision-protective Structures in Nuclear Powered Ships. *Nuclear Engineering*, (19), 1972.

[2] J Amdahl. *Energy absorption in ship-platform impact.* PhD thesis, Norwegian Institute of Technologies, Trondheim, 1982.

[3] J Amdahl and T Holmas. High energy ship collisions with jacket supported offshore wind turbines. In *International Conference on Computational Methods in Marine Engineering*, 2011.

[4] J Amdahl and A Johansen. High-energy ship collision with jacket legs. In *Proceedings of the 11th International Offshore and Polar Engineering Conference*, Stavanger, Norway, 2001.

[5] American Petroleum Institute. *Recommended Practice for Planning, Designing and Constructing Fixed Offshore Platforms — Working Stress Design*, October 2007.

[6] Bard College. Offshore wind: What lies beneath? `http://www.bard.edu/cep/blog/?p=9240`, visited on January 31, 2018.

[7] A Barrera Arenas. Collision study of rigid ship models with a deformable offshore wind turbine jacket structure. Master's thesis, ICAM Nantes, 2014.

[8] A Bela, H Le Sourne, L Buldgen, and P Rigo. Numerical crashworthiness analysis of an offshore wind turbine monopile impacted by a ship. In *Proceedings of the MARSTRUCT 2015 5th International Conference on Marine Structures*, pages 661–669, 2015.

[9] A Bela, H Le Sourne, L Buldgen, and P Rigo. Ship collision analysis on offshore wind turbine monopile foundations. *Marine Structures*, (51):220–241, 2017.

[10] P Berthonneau. Etude analytique et numérique de la résistance aux collisions d'étraves de navires. Master's thesis, Université de Liège, Belgium, 2016.

[11] F Biehl. Collision safety analysis of offshore wind turbines. In *5th LS-DYNA Anwenderforum*, Bamberg, Germany, 2005.

[12] L Buldgen, P Berthonneau, and H Le Sourne. Investigation of bulbous bow resistance during oblique collisions against tubes or plane walls. In *International Conference on Ships and Offshore Structures ICSOS 2016*, Hamburg, Germany, 2016.

[13] L Buldgen, H Le Sourne, N Besnard, and P Rigo. Extension of the super-element method to the analysis of the oblique collision between two ships. *Marine Structures*, (29):22–57, 2012.

[14] L Buldgen, H Le Sourne, and T Pire. Extension of the super-elements method to the analysis of a jacket impacted by a ship. *Marine Structures*, (38):44–71, 2014.

[15] L Buldgen, H Le Sourne, and P Rigo. A simplified analytical method for estimating the resistance of lock gates to ship impacts. *Journal of Applied Mathematics*, (2012):1–39, 2012.

[16] L Buldgen, H Le Sourne, and P Rigo. Fast strength assessment of mitre gates to ship impact. *International Journal of Crashworthiness*, (18):423–443, 2013.

[17] MAG Calle, RE Oshiro, and M Alves. Ship collision and grounding: Scaled experiments and numerical analysis. *International Journal of Impact Engineering*, (103):195–210, 2017.

[18] BC Cerik, HK Shin, and SR Cho. A comparative study on damage assessment of tubular members subjected to mass impact. *Marine Structures*, (46):1–29, 2016.

[19] SR Cho, BS Seo, BC Cerik, and HK Shin. *Collision and grounding of ships and offshore structures*, chapter Experimental and numerical investigations on the collision between offshore wind turbine support structures and service vessels, pages 281–287. London: CRC Press, 2013.

[20] J de Oliveira, T Wiersbicki, and W Abramowicz. Plastic behavior of tubular members under lateral concentrated load. Technical Report n° 82-0708, DNV, 1982.

[21] Det Norske Veritas. *Offshore Standard DNV-OS-A101 - Safety Principles and arrangements*, April 2011.

[22] S Echeverry Jaramillo, H Le Sourne, A Bela, T Pire, and P Rigo. Design methods to assess the resistance of offshore wind turbine structures impacted by a ship. In *Proceedings of the 7th European African Conference on Wind Engineering (EACWE 2017)*, 2017.

[23] EDF. Une brève histoire de l'éolienne. `https://www.edf.fr/edf/accueil-magazine/une-breve-histoire-de-l-eolienne`, visisted on 6th March 2018.

[24] S Ehlers. The influence of the material relation on the accuracy of collision simulations. *Marine Structures*, (23):462–474, 2010.

[25] S Ehlers. Strain and stress relation until fracture for finite element simulations of a thin circular plate. *Thin-Walled Structures*, (48):1–8, 2010.

[26] S Ehlers, J Broekhuijsen, HS Alsos, F Biehl, and K Tabri. Simulating the collision response of ship side structures: a failure criteria benchmark study. *International Shipbuilding Progress*, (55):127–144, 2008.

[27] S Ehlers and K Tabri. A combined numerical and semi-analytical collision damage assessment procedure. *Marine Structures*, (28):101–119, 2012.

[28] S Ehlers and P Varsta. Strain and stress relation for non-linear finite element simulations. *Thin-Walled Structures*, (47):1203–1217, 2009.

[29] CP Ellinas. Ultimate strength of damaged tubular bracing members. *Journal of Structural Engineering*, (110(2)):245–259, 1984.

[30] CP Ellinas and AC Walker. Damage on tubular bracing members. In *Proceedings of IABSE colloquium on ship collision with bridges and offshore structures*, pages 253–261, Copenhagen, Denmark, 1983.

[31] European Wind Energy Association. *The European offshore wind industry - Key trends and statistics 2015*, 2016.

[32] European Wind Energy Association. *Wind in power - 2015 European Statistics*, 2016.

[33] Global Wind Energy Council. *Global wind report - Annual Market Update 2015*, 2016.

[34] K Hagiwara, H Takanabe, and H Kawano. A proposed method for predicting ship collision damage. *International Journal of Impact Engineering*, (1(3)):257–379, 1983.

[35] MS Hoo Fatt and T Wierzbicki. Damage of plastic cylinders under localized pressure loading. *International Journal of Mechanical Sciences*, 33:999–1016, 1991.

[36] JR Hsieh. Analytical formulations for ship offshore wind turbine collisions. Master's thesis, ICAM Nantes, 2015.

[37] Intergovernmental Panel on Climate Change. *Climate Change 2014 - Synthesis report*. Cambridge University Press, 2014.

[38] H Ito, K Kondo, N Yoshimura, M Kawashima, and S Yamamoto. A simplified method to analyze the strength of double hulled structured in collision. *Journal of SNAJ*, (156):299–312, 1984.

[39] N Jones. *Structural impact*. Cambridge: Cambridge University Press, 1997.

[40] N Jones, SE Birch, RS Birch, L Zhu, and M Brown. An experimental study on the lateral impact of fully clamped mild steel pipes. *Proceedings of the Institution of Mechanical Engineers, Part E: Journal of Process Mechanical Engineering*, (206):111–127, 1992.

[41] UB Karlsson, JW Ringsberg, E Johnson, M Hoseini, and A Ulfvarson. Experimental and numerical investigation of bulb impact with a ship side-shell structure. *Marine Technology*, (46(1)):16–26, 2009.

[42] MR Khedmati and M Nazari. A numerical investigation into strength and deformation characteristics of preloaded tubular members under lateral impact loads. *Marine Structures*, (25):33–57, 2012.

[43] A Kvitrud. Collisions between plastforms and ships in norway in the period 2001-2010. In *Proceedings of the ASME 2011 30th International Conference on Ocean, Offshore and Arctic Engineering - OMAE2011*, 2011.

[44] H Le Sourne, A Barrera, and JB Maliakel. Numerical crashworthiness analysis of an offshore wind turbine jacket impacted by a ship. *Journal of Marine Science and Technology*, (23(5)):694–704, 2015.

[45] H Le Sourne, N Besnard, C Cheylan, and N Buannic. A ship collision analysis program based on upper bound solutions and coupled with a large rotational ship movement analysis tool. *Journal of Applied Mathematics*, (2012), 2012.

[46] H Le Sourne, T Pire, JR Hsieh, and P Rigo. New analytical developments to study local and global deformations of an offshore wind turbine jacket impacted by a ship. In *Proceedings of the ICCGS 2016, University of Ulsan, Korea*, 2016.

[47] B Liu and C Guedes Soares. Experimental and numercial analysis of the crushing behaviour of stiffened web girders. *International Journal of Impact Engineering*, (88(6)):22–38, 2016.

[48] M Lützen. *Ship collision damage*. PhD thesis, Technical University of Denmark, Copenhagen, 2001.

[49] JB Maliakel. Collision damage analysis of ship-offshore jacket collisions using non-linear FEM analysis. Master's thesis, ICAM Nantes, 2014.

[50] VU Minorsky. An analysis of ship collision with reference to protection of nuclear power ships. *Journal of Ship Research*, (3(2)):1–4, 1959.

[51] D Moulas, M Shafiee, and A Mehmanparast. Damage analysis of ship collisions with offshore wind turbine foundations. *Ocean Engineering*, (143):149–162, 2017.

[52] Offshore Wind. Deutsche Windtechnik to Service Senvion's Alpha Ventus Turbines. `https://www.offshorewind.biz/2016/09/27/deutsche-windtechnik-to-service-senvions-alpha-ventus-turbines/`, visited on 9th March 2018.

[53] JK Paik. Practical techniques for finite element modelling to simulate structural crashworthiness in ship collisions and grounding (part i: Theory). *Ships and Offshore Structures*, (2(1)):81–85, 2007.

[54] JK Paik and PT Pedersen. Modelling of the internal mechanics in ship collisions. *Ocean Engineering*, (23(2)):107–142, 1996.

[55] JK Paik, BC Shin, and CY Kim. Damage estimation for offshore tubular members under quasi-static loading. *Journal of the Society of Naval architect of Korea*, (26(4)):81–93, 1989.

[56] JK Paik and AK Thayamballi. *Ultimate Limit State Design of Steel-Plated Structures*. John Wiley & Sons, LTD, 2002.

[57] JK Paik and AK Thayamballi. A concise introduction to the idealized structural unit method for nonlinear analysis of large plated structures and its application. *Thin-walled Structures*, (41):329–355, 2003.

[58] PT Pedersen, S Valsgaard, D Olsen, and S Spangenbeg. Ship impacts: bow collisions. *International Journal of Impact Engineering*, (13):163–187, 1993.

[59] Z Pei, K Iijima, M Fujikubo, S Tanaka, S Okazawa, and T Yao. Simulation on progressive collapse behaviour of whole ship model under extreme waves using idealized structural unit method. *Marine Structures*, (40):104–133, 2015.

[60] T Pire, S Echeverry, P Rigo, L Buldgen, and H Le Sourne. Validation of a simplified method for the crashworthiness of offshore wind turbine jackets using finite elements simulations. In C Guedes Soares and Y Garbatov, editors, *Progress in the Analysis and Design of Marine Structures, Proceedings of the 6th international conference on Marine Structures (MARSTRUCT 2017), Lisbon, Portugal, 8-10 May 2017*, pages 497–505. CRC Press, 2017.

[61] T Pire, H Le Sourne, S Echeverry, and P Rigo. Analytical formulations to assess the energy dissipated at the base of an offshore wind turbine jacket impacted by a ship. *Marine Structures*, (59):192–218, 2018.

[62] T Pire, H Le Sourne, and P Rigo. Assessment of the deformation by punching and at the base of an offshore wind turbine jacket impacted by a ship, 2017. BERA PhD Day.

[63] F Princiotta. *Global Climate Change - The Technology Challenge*. Springer, 2011.

[64] S Qvist, QB Nielsen, MH Schmidt, and SH Madsen. Ship collision: experimental and numerical analysis of double hull models. In *Proceeding of the Ninth Technical Conference on Material and Structural Modelling in Collision Research, Munich, Germany*, 1995.

[65] South Baltic Offshore Wind Energy Regions. Wind energy regions: Denmark. `http://www.southbaltic-offshore.eu/regions-denmark.html`, visited on 9th March 2018.

[66] JK Robson. Ship/platform collision incident database (2001). Technical report, Serco Assurance for Health and Safety Executive, 2003.

[67] BC Simonsen. Ship grounding on rock: Part I and II. *Marine Structures*, (10):519–584, 1997.

[68] BC Simonsen and H Ocakli. Experiments and theory on deck and girder crushing. *Thin Walled Structures*, (34):195–216, 1999.

[69] TH Soreide and J Amdahl. Deformation characteristics of tubular members with reference to impact loads from collision and dropped objects. *Norwegian Maritime Research*, (10(2)):3–12, 1982.

[70] TH Soreide, J Amdahl, E Eberg, T Holmas, and O Hellan. *USFOS: A computer program for progressive collapse analysis of steel offshore structures*. SINTEF, 1993.

[71] TH Soreide and D Kavlie. *Shell structures: stability and strength*, chapter Collision damages and residual strength of tubular members in steel offshore structure, pages 185–220. New York: Elsevier Applied Science Publishers, 1985.

[72] A Soret. Etude de la résistance à l'écrasement d'une étrave de navire. Master's thesis, Université de Liège, Belgium, 2016.

[73] MS Suh. *Plastic analysis of dented tubes subjected to combined loading.* PhD thesis, Cambridge: Massachusetts Institute of Technology, Department of Ocean Engineering, 1987.

[74] K Suzuki, H Ohtsubo, and C Sajit. Evaluation method of absorbed energy in collision of ships with anti-collision structure. In *International Conference of Ship Structure for the New Millennium: Supporting Quality in Shipbuilding*, Arlington, 2000.

[75] K Tabri, J Broekhuisen, J Matusiak, and P Varsta. Analytical modelling of ship collision based on full-scale experiments. *Marine Structures*, (22(1)):42–61, 2009.

[76] K Tabri, J Maattanen, and J Rante. Model-scale experiments of symmetric ship collisions. *Journal of Marine Science and Technology*, (13(1)):71–84, 2007.

[77] MT Tran. Effects of impacts from large supply vessels on jacket structures. Master's thesis, Faculty of Science and Technology, University of Stavanger, Norway, 2014.

[78] J Travanca and H Hao. Dynamics of steel platforms under ship impact. *Applied Ocean Research*, (47):352–372, 2014.

[79] J Travanca and H Hao. Numerical analysis of steel tubular member response to ship bow impacts. *International Journal of Impact Engineering*, (64):101–121, 2014.

[80] J Travanca and H Hao. Energy dissipation in high-energy ship-offshore jacket platform collisions. *Marine Structures*, (40):1–37, 2015.

[81] AW Vredeveldt and JHA Schipperen. Safe jacket configurations to resist boat impact. *Collision and Grounding of Ships and Offshore Structures*, 2013.

[82] G Wang and H Ohtsubo. Deformation of ship plate subjected to very large load. *Journal of Offshore Mechanics and Artic Engineering*, (119):173–180, 1997.

[83] AR Watson, SR Reid, W Johnson, and SG Thomas. Large deformations of thin-walled circular tubes under transverse loading-II: experimental study of the crushing of circular tubes by centrally applied opposed wedge-shaped indenters. *International journal of Mechanical Sciences*, (18(7-8)):387–397, 1976.

[84] AR Watson, SR Reid, W Johnson, and SG Thomas. Large deformations of thin-walled circular tubes under transverse loading-III: further experiments on the bending of simply supported tubes. *International journal of Mechanical Sciences*, (18(9-10)):501–509, 1976.

[85] LJ Wevers, AW Vredeveldt, TNO Building, and Construction Research Netherlands Institute for Maritime Research. *Full Scale Ship Collision Experiments 1998: Test of New Type Ship Side Structure, Royal Schelde, the Netherlands.* TNO, 1999.

[86] T Wierzbicki and W Abramowicz. On the crushing mechanics of thin-walled structures. *Journal of Applied Mechanics*, (50):727–734, 1983.

[87] T Wierzbicki and MS Suh. Indentation of tubes under combined loading. *International Journal of Mechanical Sciences*, 30:229–248, 1988.

[88] G Woisin. Design against collision. *Shiff & Hafen*, (31(2)):1059–1069, 1985.

[89] PSO Yeye. Numerical and analytical simulations of in-shore ships collisions within the scope of the A.D.N. regulations. Master's thesis, ICAM Nantes, 2017.

[90] X Yu. *Structural analysis with large deformations until fracture and with dynamic failure.* PhD thesis, University of Hamburg, Germany, 1996.

[91] U Yukio and SMH Rashed. The idealized structural unit method and its application to deep girder structures. *Computers and Structures*, (18(2)):277–283, 1984.

[92] M Zeinnoddini, JE Harding, and GAR Parke. Effect of impact damage on the capacity of tubular steel members of o¤shore structures. *Marine Structures*, (11):141–157, 1998.

[93] M Zeinnoddini, JE Harding, and GAR Parke. Dynamic behaviour of axially pre-loaded tubular steel members of offshore structures subjected to impact damage. *Ocean Engineering*, (26):963–978, 1999.

[94] M Zeinnoddini, JE Harding, and GAR Parke. Axially pre-loaded steel tubes subjected to lateral impacts: an experimental study. *International journal of Impact Engineering*, (27(6)):669–690, 2002.

[95] M Zhang, JX Liu, and ZQ Hu. Experimental and numerical analysis of tanker double-hull structures punched by a wedge indenter. In C Guedes Soares and Y Garbatov, editors, *Progress in the Analysis and Design of Marine Structures, Proceedings of the 6th international conference on Marine Structures (MARSTRUCT 2017), Lisbon, Portugal, 8-10 May 2017*, pages 549–556. CRC Press, 2017.

[96] S Zhang. *The mechanics of ship collisions.* PhD thesis, Technical University of Denmark, Copenhagen, 1999.

Chapter 2

Collision risk analysis for offshore structures

Abstract:

As explained in the previous Chapter, a complete collision risk analysis has to be performed for each new offshore project. The notion of risk includes both the probability of a collision to occur and the damage caused by that collision.

Even if computing the probability of collision is not the purpose of the present thesis, the basic background is introduced.

Two methods for computing the resistance and the damage on the collided offshore wind turbine are used in the thesis, namely the finite element method and the plastic limit analysis (analytical approach). First, the use of finite element approach within the thesis is presented. Then, the theoretical background of the analytical developments is detailed.

2.1 Introduction

Collisions are becoming a main issue for the design of several transport vehicles. For years now, cars are designed to protect the driver, passengers and people hit by the vehicle, and advertisements related to the safety are often used to promote the car.

Collisions have also to be considered when designing offshore structures, and in our context OWT jackets. In the case of ship impact, the damage could be a minor local dent near the impact area but could lead to a collapse of the overall structure for a large energy impact. In addition to a loss of electricity production, human lives may be endangered and ecological damage may occur if the wind turbine tower collapses on the striking ship. For those reasons, a complete collision risk analysis has to be performed for each offshore wind farm project.

The notion of collision risk combines both the probability of having a collision and the damage caused by that collision for all the scenarios that could occur. A scenario with a low probability but high damage could have a similar risk than a scenario more likely to occur but leading to few damage.

$$risk = probability \times damage \tag{2.1}$$

The probabilistic aspect is not the purpose of the present thesis, only a quick overview will be given in Section 2.2. Computing the damage related to a given collision scenario corresponds to the research goals. This can be achieved by several methods that are reviewed and discussed in Section 1.2. Two of them used in the thesis, namely finite element and simplified analytical methods, are more detailed in Section 2.3.

2.2 Assessment of collision events probability

Collision risk is widely investigated by Vinnem [9] and a methodology to compute the probability of collision is described. The main features are exposed here.

As a first step to compute the probability of collision, the vessels categories that may navigate within a navigation lane close to the wind farm, as discussed in [7], have to be identified. One may note the merchant vessels, fishing vessels, offshore supply vessels (OSV), warships, submarines and floating units such as drilling rigs, crane vessels or barges, for example.

For each of them, the volume of passing vessels during a given period can be estimated based on observations. Even if traffic lanes are defined for navigation, it could happen that a vessel deviates from this line due to technical problems (engine failure leading to drifting, navigation instruments errors, ...), human error or bad weather conditions (wind, waves, current, ...). Statistical data are here again available on the real position of vessels with regard to the navigation lanes (a normal distribution is given in Fig. 2.1 as an example [9]). OSV are treated

differently as they navigate within the wind farms to perform the maintenance operations on the turbines.

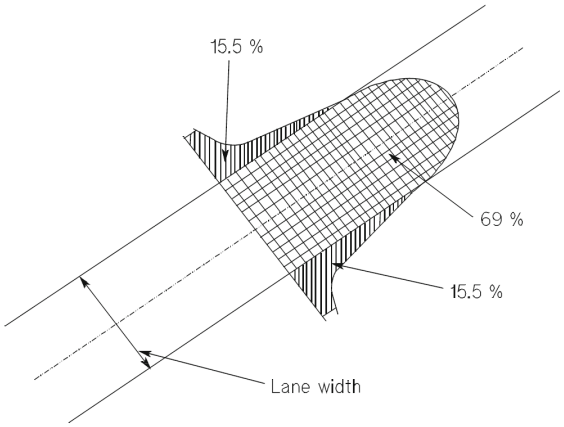

Figure 2.1: Lateral navigation patterns normal distribution [9]

At some point, the wind farm enters in the radar or visual coverage and the ship may recover a safe route. The ship recovery may fail due to three factors [9]:

- No reaction by the vessel crew;
- Erroneous action by the crew;
- Technical problem (engine, radar detection, ...).

For those three factors, probability of ship recovery failures are given based on statistical data, as illustrated in Fig. 2.2.

Recovery failure mode	Failure probabilities for recovery failure	
	By ship	From platform
Alcohol	1.1×10^{-4}	0.72
Asleep	2.3×10^{-3}	0.2
Accident	1.2×10^{-5}	0.75
Absent	9.5×10^{-4}	0.012
Distracted	9.5×10^{-4}	0.01
Radar	9.8×10^{-3}	0.18

Figure 2.2: Typical recovery failure probabilities [9]

Combining the volume of vessels around the wind farm, the distribution of route deviation with regard to the navigation lanes and the probability of recovery failure for each type of vessel, the probability of collision may be computed.

2.3 Existing methods to assess the crashworthiness

As described in Section 1.2, four types of design methods exist to assess the resistance of OWT jackets impacted by a ship.

In the framework of this thesis, experiments cannot be performed, and developing empirical laws is not the purpose of this research. Only FE and simplified analytical methods based on plastic limit analysis are considered and are discussed in the next Sections.

Those methods were already reviewed by Buldgen [1] in his PhD thesis. The main elements are reported here.

2.3.1 Finite element method

In the present thesis, FE simulations are used to validate the semi-analytical developments. The main theoretical background of the FE method in the framework of ship collisions is therefore introduced in Appendix A.

All the FE models are built using the pre-processor *PATRAN (MSC)* and solved with the commercial software *LS-DYNA (LSTC)*, which is widely used worldwide for collision simulations.

2.3.2 Plastic limit analysis approach

The theoretical background of the simplified analytical approach developed in the framework of this PhD thesis is based on an energy balance. It states that, at the end of the collision process, the whole initial kinetic energy of the striking ship has been dissipated into internal energy by the collided jacket. Mathematically, this equilibrium is expressed by Eq. 2.2

$$E_k = E_{int} \tag{2.2}$$

where E_k is the initial kinetic energy of the striking ship and E_{int} is the internal energy dissipated by the collided jacket.

Here, it is assumed that the striking ship is perfectly rigid. In practice, part of the energy is also dissipated by the ship deformation, as represented in Fig. 2.3. In this Figure, the impact force is represented on the vertical axis while the deformation is represented on the horizontal one, with the ship on the left and the collided structure, denoted as “Installation”, on the right. The energy dissipated corresponds to the grey area below the curve. The distribution of energy between the ship and the structure depends on their relative rigidity: the stiffer suffers less deformation and dissipate less energy.

Le Sourne et al. [5] performed FE simulations of ship collisions on OWT jackets with several types of striking ships and considering both the ship and the jacket as deformable. It was demonstrated that, when an OSV is considered, 80% of the energy is dissipated by the striking ship and only 20% by the struck jacket. On the other hand, when an ice class bulk carrier side shell collides the jacket, only 20% of the energy is dissipated by the ship and 80% by the jacket.

The validity of the assumption of rigid ship depends therefore on the type of striking ship and on its internal reinforcement. However, considering the ship as rigid is conservative with

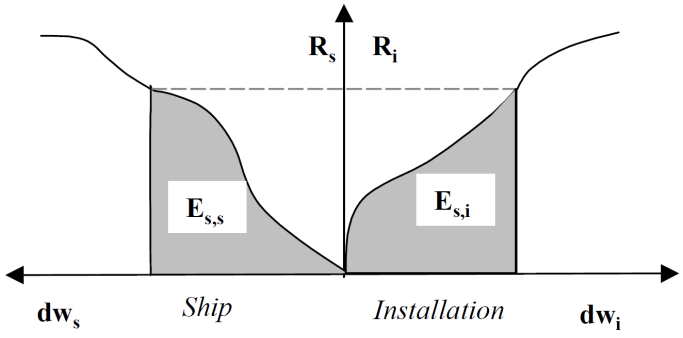

Figure 2.3: Energy dissipated by the ship and the structure [8]

regard to the jacket because this one has to dissipate the whole energy, without any contribution of the ship. Similar assumption of rigid ship was done by Buldgen et al. [2, 3] for ship collisions on plane and mitre gates.

The second assumption in Eq. 2.2 consists in stating that no other energy dissipation mode than jacket deformation occurs during the collision, such as for example friction between the ship and the jacket. Similarly to the first assumption, this hypothesis is conservative with regard to the jacket.

The two terms of Eq. 2.2 have now to be evaluated in order to develop analytical methods.

The value of the initial ship kinetic energy was discussed in Chapter 1. It is therefore decided to consider collision energies up to 75 MJ, which corresponds to a $6,000$ tons (added mass included) ship at a velocity of 5 m/s.

The energy dissipated plastically during a collision is computed using limit plastic analysis, as described by Jones [4]. The exact solution in terms of mechanics should satisfy three conditions, namely the equilibrium, the constitutive and compatibility equations. In practice, two methodologies are used:

- **The lower-bound method:**

  This method provides solutions that satisfy the equilibrium and the yield criteria and are called statically admissible. The internal energy computed with this method is lower than the exact energy. It is usually possible to find an infinity of solutions that meet both requirements.

- **The upper-bound method:**

  This method provides solutions that satisfy the equilibrium and the compatibility criteria and are called kinematically admissible. The internal energy computed with this method is larger than the exact energy. It is usually possible to find an infinity of solutions that meet both requirements.

In the next mathematical developments, based on the upper-bound method, additional assumptions are performed:

- The next theorem is valid for small displacements;
- The boundaries are assumed to be fixed. In the case of the collided jacket, it is therefore assumed that no displacements occur in the foundations.

We now consider a solid initially defined as Ω_0 moving to a configuration Ω during a collision (see Fig. 2.4). The displacement from Ω_0 to Ω is arbitrary chosen within all the kinematically admissible possible solutions. During the collision, the initial volume V becomes v.

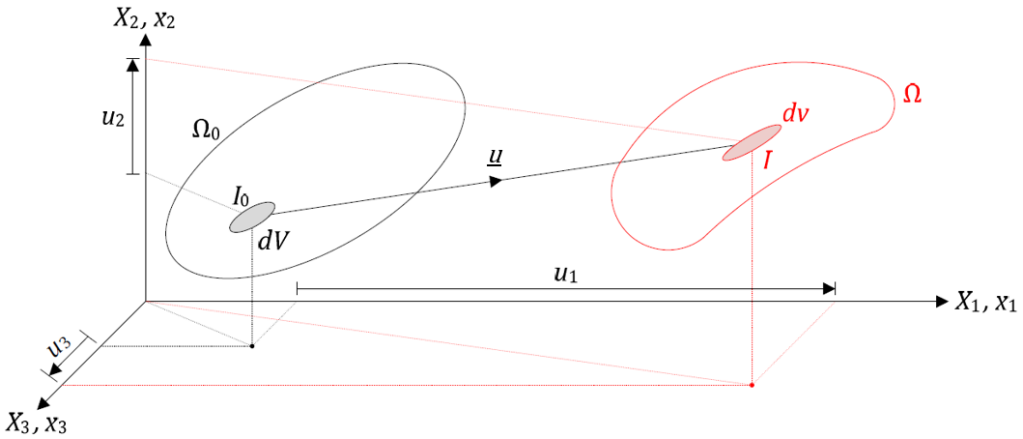

Figure 2.4: Solid kinematically admissible deformation during a collision [1]

The point I_0 in Ω_0 and with coordinates (X_1, X_2, X_3) moves to position I in Ω and its coordinates are (x_1, x_2, x_3). The displacement and velocity fields ($\underline{u}$ and $\underline{\dot{u}}$) between I_0 and I is assumed to be kinematically admissible. Their components u_i and $\dot{u}_i$ are defined in Eq. 2.3.

$$x_i = X_i + u_i(X_1, X_2, X_3) \Leftrightarrow \dot{x}_i = \dot{u}_i(X_1, X_2, X_3) \tag{2.3}$$

Ω is submitted to the forces acting at the boundaries and to the collision force denoted $\underline{P}$ (the force is a vector as it acts in 3 dimensions). As the boundaries are assumed to be fixed, no displacement occurs and no work is created. The only work acting on Ω is therefore due to the collision force $\underline{P}$. If we denote the ship velocity as $\underline{\dot{\delta}}$, the external work rate $\dot{W}$ is expressed in Eq. 2.4.

$$\dot{W} = \underline{P} \cdot \underline{\dot{\delta}} \tag{2.4}$$

The internal energy rate $\dot{E}_{int}$ of the solid is computed in Eq. 2.5.

$$\dot{E}_{int} = \iiint_v [\sigma] \cdot [\mathring{a}] \; dv \qquad \mathring{a}_{ij} = \frac{1}{2}\left(\frac{\partial \dot{u}_i}{\partial x_j} + \frac{\partial \dot{u}_j}{\partial x_i}\right) \tag{2.5}$$

where v is the volume of Ω, $[\sigma]$ is the Cauchy stress tensor and $[\mathring{a}]$ is the Rivlin-Eriksen rate of the Almansi strain tensor (see [1] for more details).

As discussed above, it is assumed that the whole initial kinetic energy is dissipated by the jacket alone. Therefore, one can write $\dot{W} = \dot{E}_{int}$ that allows to compute the collision force $\underline{P}$.

This theory is valid only for small displacements. However, in the event of a ship collision on an OWT jacket, the jacket will suffer displacements that cannot be assumed as small. In order to deal with finite displacements, the so-called upper-bound method was developed.

With regard to the theory presented above, the major difference consists in integrating the internal energy rate $\dot{E}_{int}$ on the initial volume V of Ω_0 instead of the deformed configuration Ω. This assumption will lead to formulations that can be solved analytically and provide closed-form solutions for the collision force. Working on the initial configuration of the structure requires also to choose consistent stress and strain tensors, as given in Eq. 2.6.

$$\dot{E}_{int} = \iiint_V [S] \cdot [\dot{E}] \; dV \qquad \dot{E}_{ij} = \frac{1}{2}\left(\frac{\partial \dot{u}_i}{\partial X_j} + \frac{\partial \dot{u}_j}{\partial X_i} + \frac{\partial u_k}{\partial X_i}\frac{\partial \dot{u}_k}{\partial X_j} + \frac{\partial u_k}{\partial X_j}\frac{\partial \dot{u}_k}{\partial X_i}\right) \tag{2.6}$$

where $[S]$ is the second Piola-Kirchhoff stress tensor and $[\dot{E}]$ is the Green strain rate tensor.

Using a real material stress-strain law, involving the elastic part, yielding, strain hardening and necking to rupture, in Eq. 2.6 would lead to expression that cannot be solved analytically. Additional hypothesis is therefore performed on the material behaviour; it is assumed that the material is rigid - perfectly plastic, as represented in Fig. 2.5. Doing so consists in neglecting all the elastic deformation.

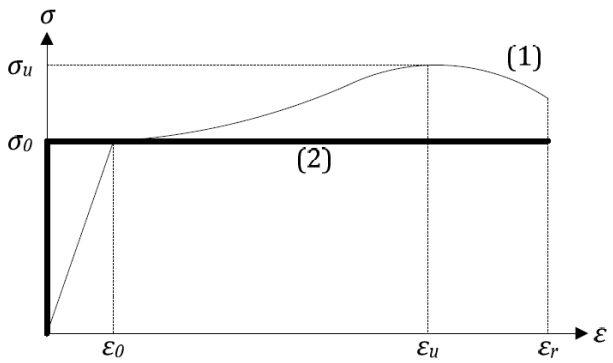

Figure 2.5: Real (1) and modelled (2) material law [1]

The flow stress can be considered as equal to the yielding stress σ_0. However, this assumption is too conservative for some authors, such as Zhang [10] or Lützen [6], who suggest to use the flow stress equal $(\sigma_0 + \sigma_u)/2$. With this assumption on the material law, Eq. 2.6 may be expressed using the equivalent Green-Lagrange strain rate $\dot{E}_p$, as done in Eq. 2.7.

$$\dot{E}_{int} = \iiint_V \sigma_0 \cdot \dot{E}_p \; dV \tag{2.7}$$

This final expression will be later used in the thesis to compute the collision resistant force.

Bibliography

[1] L Buldgen. *Simplified analytical methods for the crashworthiness and the seismic design of lock gates*. PhD thesis, Faculty of applied sciences, University of Liege, Belgium, 2014.

[2] L Buldgen, H Le Sourne, and P Rigo. A simplified analytical method for estimating the resistance of lock gates to ship impacts. *Journal of Applied Mathematics*, (2012):1–39, 2012.

[3] L Buldgen, H Le Sourne, and P Rigo. Fast strength assessment of mitre gates to ship impact. *International Journal of Crashworthiness*, (18):423–443, 2013.

[4] N Jones. *Structural impact*. Cambridge: Cambridge University Press, 1997.

[5] H Le Sourne, A Barrera, and JB Maliakel. Numerical crashworthiness analysis of an offshore wind turbine jacket impacted by a ship. *Journal of Marine Science and Technology*, (23(5)):694–704, 2015.

[6] M Lützen. *Ship collision damage*. PhD thesis, Technical University of Denmark, Copenhagen, 2001.

[7] Maritime Navigation Commission. Interaction between offshore wind farms and maritime navigation. Technical Report 161, PIANC, 2018.

[8] Standards Norway. *NORSOK n-004: Design of steel structures*, 2004.

[9] JE Vinnem. *Offshore Risk Assessment*. Springer, 2014. Third Edition.

[10] S Zhang. *The mechanics of ship collisions*. PhD thesis, Technical University of Denmark, Copenhagen, 1999.

Chapter 3

Ship collision on offshore wind turbine jacket analysis

Abstract:

Before developing the analytical formulations to assess the crashworthiness of an OWT jacket impacted by a ship, the structural behaviour has to be clearly identified, which is the aim of this Chapter. Numerical simulations are therefore performed with the *LS-DYNA* FE software.

First, the geometry of the striking ship, including its stem and bow, and of the jacket as well as the collision scenario definition are described. The numerical model is discussed and several simulations allow to determine that parameters, such as gravity loads, turbine and tower effect or the soil stiffness, have few influence on the jacket response to a collision.

Based on the results, four deformation modes are identified, which are further used as the basis for the main developments of the thesis.

Finally, a material failure criteria of a component is introduced in the material model to investigate the effect of rupture. This later is shown to have limited influence on the jacket structural behaviour to collision.

3.1 Introduction

The purpose of the present thesis is to provide analytical formulations in order to quickly assess the crashworthiness of an OWT jacket impacted by a ship. As a first step, the structural behaviour of such a structure collided by a ship has to be analysed and the most determinant parameters that govern the resistance have to be identified.

As discussed in Chapter 1, full-scale experiments cannot be performed, as any ship or jacket owner would not accept to cause voluntary damage on their structures. Physical scaled models are also difficult to perform as all the parameters (geometry, mechanical properties, mass, ...) cannot be adapted respecting all scaling rules. Therefore, numerical simulations, such as FEA, are the only way to model the jacket response to a ship collision (Fig. 3.1). Nevertheless, this methodology presents some limitations as some physical phenomena are difficult to model properly, such as for example the rupture or the presence of welding lines used to connect elements. However, it is agreed that using numerical models is quite reliable. In addition, the increasing power of computers allows admissible computation times.

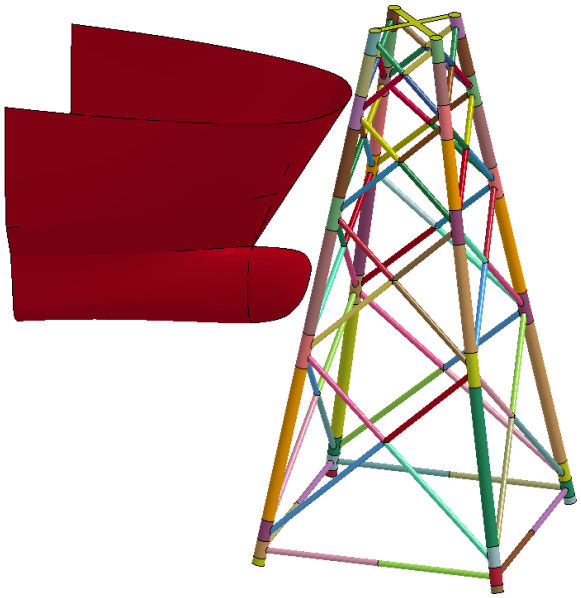

Figure 3.1: Example of a collision numerical simulation

Several authors performed FE simulations to model the collision of a ship on a part or on a complete offshore structure, amongst them Storheim and Amdahl [9], Vredeveldt et al. [13], Travanca et al. [11], Cho et al. [2] or Le Sourne et al. [6]. In this last reference [6], the influence of several parameters on the structural behaviour of the impacted offshore wind turbine jacket is investigated.

In Section 3.2, the striking ship and jacket numerical models used for this thesis are presented. Then, based on the researches performed by Le Sourne et al. [6], the determinant parameters for the jacket response to a collision are identified. A mesh size sensitivity analysis is then performed and discussed. The numerical simulations allow to identify four deformation modes

for which analytical formulations will be developed in Chapters 4 to 7. Finally, the effect of rupture criteria on the numerical results is investigated.

The data and results presented in this Chapter will be used as a reference in the next Chapters.

3.2 Collision description

The striking vessel, the collided OWT jacket and the collision scenario have to be defined before developing the analytical formulations to assess the crashworthiness.

3.2.1 Striking ship description

The ship stem (Fig. 3.2) is idealised at its upper deck as a parabola described by its two radii (p, q) and its center S. The stem and side angles are denoted by ϕ_b and ψ_b respectively while the height of the stem is denoted h_b.

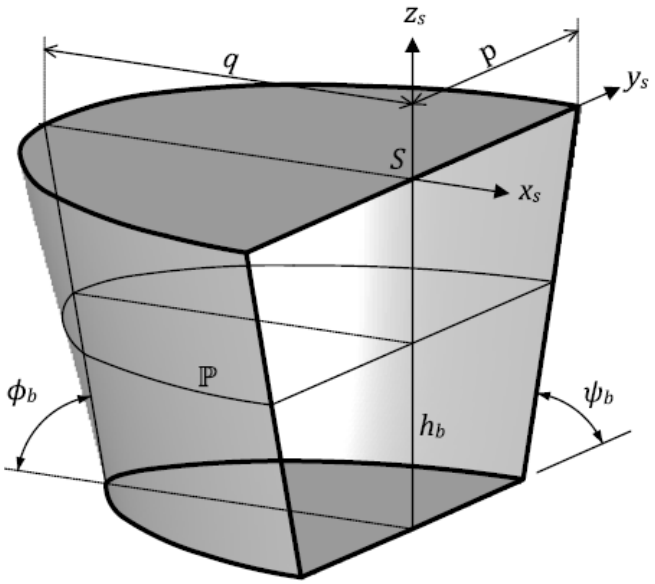

Figure 3.2: Striking ship stem dimensions

The equation of the parabola $\mathbb{P}$ corresponding to the intersection of the ship stem and the horizontal plane at the altitude z_s is given by Eq. 3.1.

$$\mathbb{P} \equiv \frac{x_s^2}{(q - z_s \cot \phi_b)^2} + \frac{y_s^2}{(p - z_s \cot \psi_b)^2} = 1 \qquad ; \qquad -h_b \leq z_s \leq 0 \tag{3.1}$$

The striking ship bulb is idealised as semi-ellipsoid, as can be seen in Fig. 3.3, with radii $(p_{bulb}, q_{bulb}, h_{bulb}/2)$. It is described with Eq. 3.2.

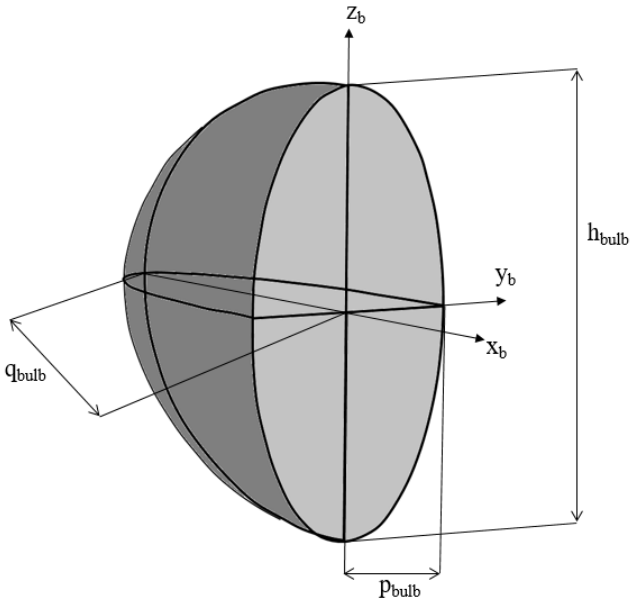

Figure 3.3: Striking ship bulb dimensions

$$\mathbb{B} \equiv \frac{x_b^2}{q_{bulb}^2} + \frac{y_b^2}{p_{bulb}^2} + \frac{z_b^2}{(h_{bulb}/2)^2} = 1 \tag{3.2}$$

The dimensions of a bulbous bow are represented in Fig. 3.4.

Table 3.1 lists all the data required to fully describe the striking ship geometry. The data followed by * are not required for non-bulbous bows.

Table 3.1: Input data for the striking ship (* not required for non-bulbous bows)

Description	Notation
Stem elliptic radius 1	p
Stem elliptic radius 2	q
Stem height	h_b
Stem angle	ϕ_b
Side angle	ψ_b
Bulb elliptic radius 1 *	p_{bulb}
Bulb elliptic radius 2 *	q_{bulb}
Bulb height *	h_{bulb}
Shift of bulb with regard to stem *	x_{bulb}
Ship total height *	h_{ship}

Both non-bulbous and bulbous ships corresponding to real OSVs, represented in Figs. 3.5 and 3.6 respectively, are considered in the present thesis. Their dimensions are given in Tables 3.2 and 3.3 respectively.

In all the simulations, the striking ship is considered as rigid. Describing the internal stiffening system is therefore useless.

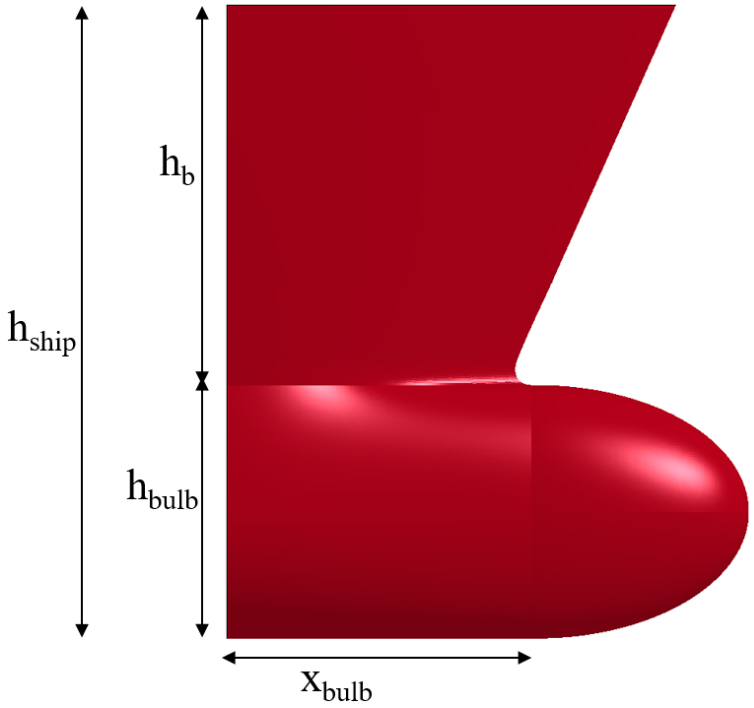

Figure 3.4: Bulbous bow dimensions

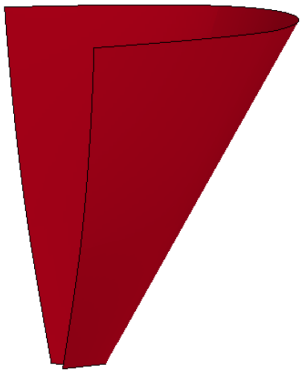

Figure 3.5: Non-bulbous bow finite element model

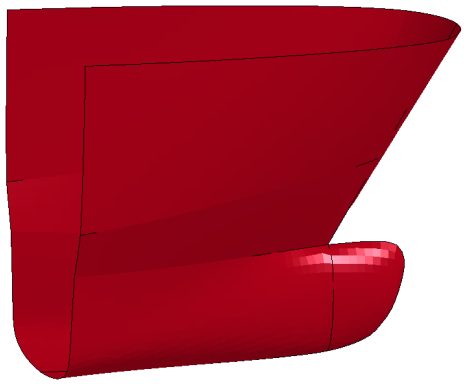

Figure 3.6: Bulbous bow finite element model

Table 3.2: Main dimensions of the non-bulbous striking ship stem

Property	Notation	Unit	Value
Elliptic radius 1	p	m	6
Elliptic radius 2	q	m	8
Total height 2	h_b	m	7
Stem angle	ϕ_b	deg	78
Side angle	ψ_b	deg	74

Table 3.3: Main dimensions of the bulbous striking ship

Property	Notation	Unit	Value
Stem elliptic radius 1	p	m	11.5
Stem elliptic radius 2	q	m	32
Stem height	h_b	m	16.8
Stem angle	ϕ_b	deg	59.7
Side angle	ψ_b	deg	82.9
Bulb elliptic radius 1	p_{bulb}	m	1.9
Bulb elliptic radius 2	q_{bulb}	m	6
Bulb height	h_{bulb}	m	9.1
Shift of bulb	x_{bulb}	m	22.5
Ship total height	h_{ship}	m	25.9

3.2.2 Collided offshore wind turbine jacket description

The jacket presented in Fig. 3.7 corresponds to a real structure designed and built by *STX France* [10]. Its geometrical and mechanical properties were provided by the company in the framework of the *CHARGEOL* project. The main dimensions of the jacket and its tubular members are given in Table 3.4.

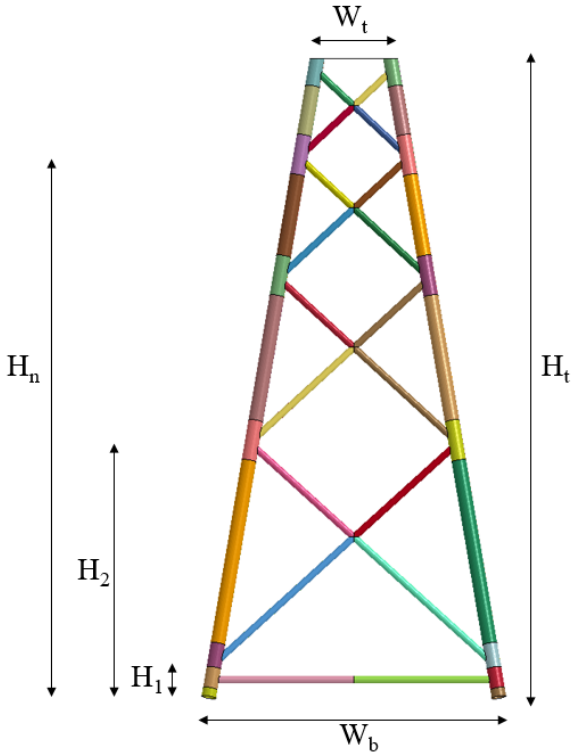

Figure 3.7: Dimensions of the collided OWT jacket

It is assumed that the foundation consists in piles installed into sleeves and connected with a cement grout, as depicted in Fig. 3.8. The model proposed in this Chapter does not take into account the elements located below the top level of the foundation, only the elements above the foundation are modelled.

Table 3.4: Dimensions of the investigated collided jacket

Property	Notation	Unit	Value
Total height	H_t	m	55
Width at bottom	W_b	m	25
Width at top	W_t	m	6.4
Altitude of braces - legs connections	$H_1, H_2, \ldots, H_n$	m	$2.5 - 22 - 36 - 46.5 - 55$
Ratio between external diameter and thickness of legs	$D_{e,leg}/t_{leg}$	$-$	26
Ratio between external diameter and thickness of braces	$D_{e,brace}/t_{brace}$	$-$	13

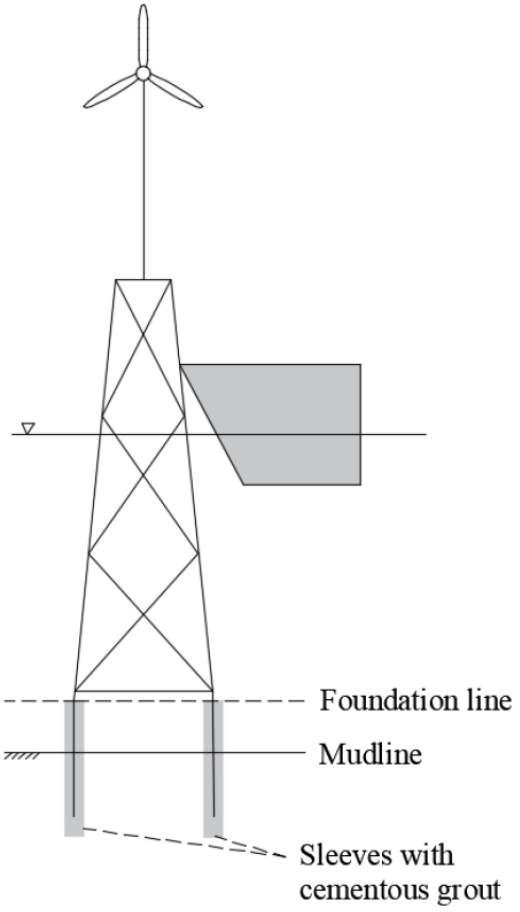

Figure 3.8: Ship - OWT jacket collision

The model of this structure was built for numerical simulations with *PATRAN* and with *MATLAB* for the analytical ones. Both are presented in Fig. 3.9 and show some differences.

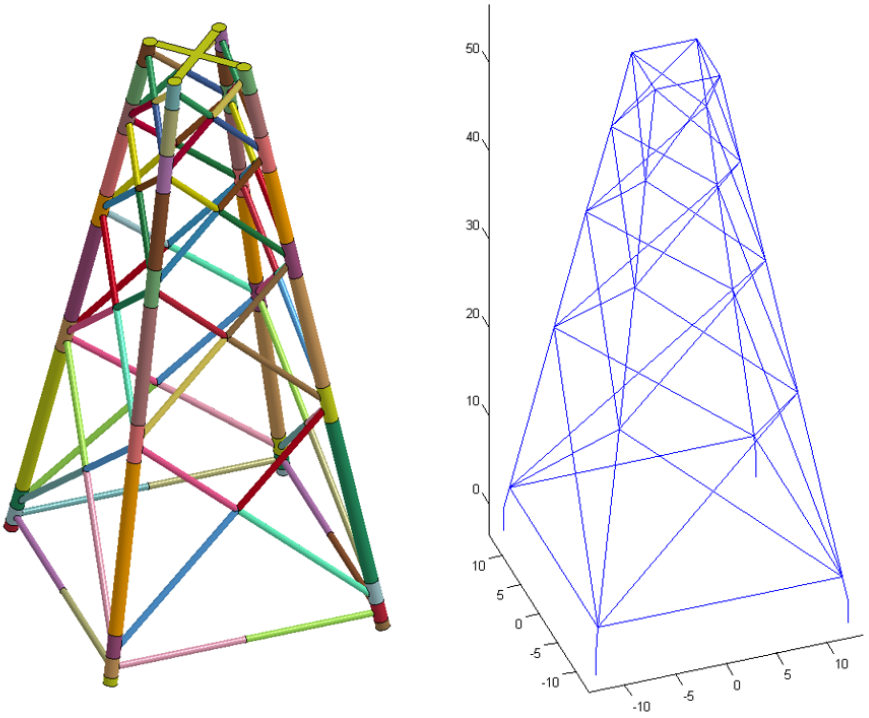

Figure 3.9: Collided OWT jacket *PATRAN* (left) and *MATLAB* (right) models

The first model was built with *PATRAN* in order to create a FE model that is then solved with *LS-DYNA*. This model is very close to the real structure in terms of geometrical and mechanical properties. The jacket is split into several parts, represented by different colors on the model (Fig. 3.9), allowing to provide specific mechanical properties for each of them and to post-process the results independently.

The second one is built with *MATLAB* and is used for the semi-analytical model, which is the purpose of the present thesis. The connections between legs and braces are slightly simplified as the gap between the connection of two braces on a leg is neglected. This assumption allows for a reduced number of elements and therefore a reduced computation effort to assess the global deformation of the whole jacket, as will be discussed later in Chapter 5. However, even if the gap is neglected for the global deformation, its value is used to compute the cross-section deformations due to punching in the leg - braces connections, as detailed in Chapter 6.

Three material laws are considered in the thesis, two for the semi-analytical model and one for the numerical validation:

- **Rigid-perfectly plastic**

  This material law, represented in Fig. 3.10, is used for the analytical developments presented in Chapters 4, 6 and 7. The choice of this material law is performed in order to obtain closed-form formulations. Indeed, as discussed in Section 2.3.2, considering either an elastic part or hardening would provide expressions that cannot be solved analytically.

- **Elastic-perfectly plastic**

  This material law is represented in Fig. 3.11 and is considered in Chapter 5 related to the overall motion of the structure. As will be discussed later on, the formulations can easily deal with the elastic part. In addition, the *overall motion* deformation mode will be the only one in which the elastic domain is considered.

- **Elastic-plastic with a power hardening model**

  This law, represented in Fig. 3.12, is considered for the numerical simulations used for the validation and aims to correspond to a realistic material behaviour (except that rupture of material is not included).

  The power hardening law is expressed in Eq. 3.3, with a strength parameter of 600 MPa and an exponent n of 0.21.

$$\sigma_h = k\left(\varepsilon_{yp} + \overline{\varepsilon}^p\right)^n \tag{3.3}$$

  where ε_{yp} is the elastic strain to yield and $\overline{\varepsilon}^p$ is the effective plastic strain (logarithmic).

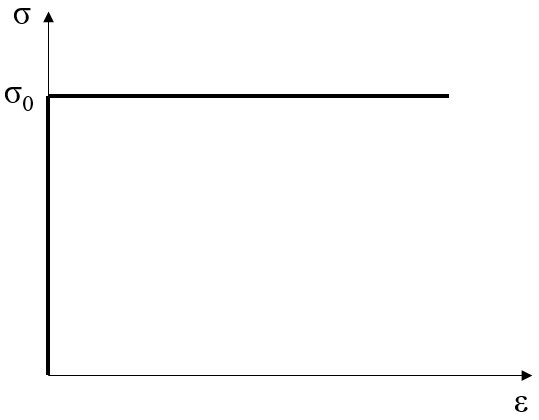

Figure 3.10: Rigid-plastic material law

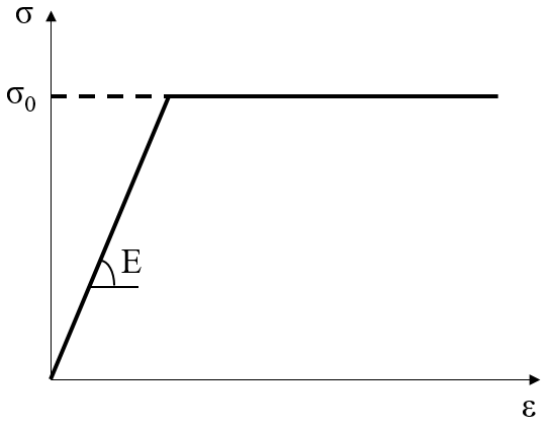

Figure 3.11: Elastic-plastic material law

In order to take into account hardening in the rigid-plastic and elastic-plastic material laws, the flow stress σ_0 is considered to be the mean value between the yielding stress $\sigma_y = 255\ MPa$ and the ultimate stress $\sigma_u = 380\ MPa$, i.e. $\sigma_0 = 317.5\ MPa$.

All the material parameters are summarised in Table 3.5.

3.2.3 Collision scenario description

The collision scenario between a given striking ship and the collided jacket is defined by the initial impact point and the direction of the ship.

The elevation of the contact point is defined in Fig. 3.13 by the parameter H. The ship trajectory is represented in Fig. 3.14 by the line described by an angle α and passing through a

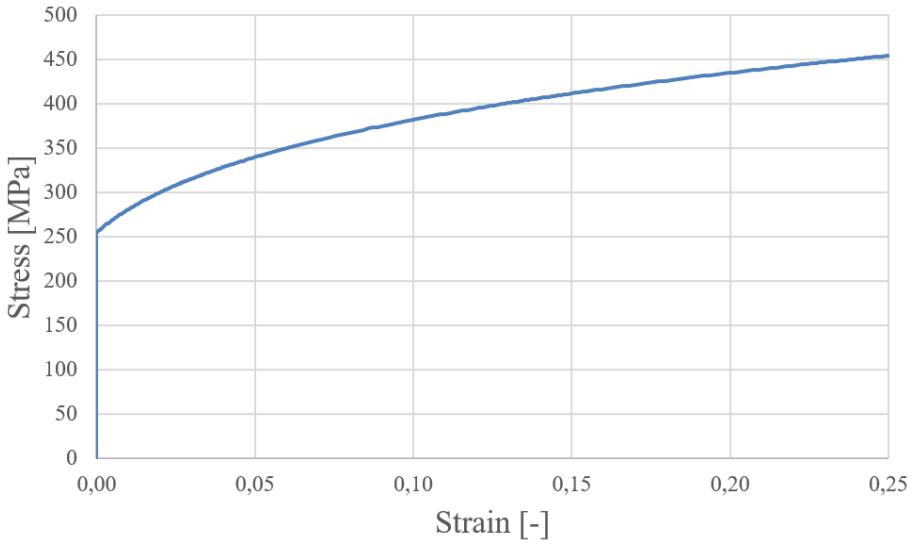

Figure 3.12: Elastic-plastic with a power hardening model material law

Table 3.5: Material laws parameters for the investigated collided jacket

Property	Notation	Unit	Value
Yielding stress	σ_0	MPa	255
Flow stress	σ_0	MPa	317.5
Ultimate stress	σ_u	MPa	380
Young modulus	E	MPa	$210,000$
Coulomb modulus	G	MPa	$81,000$
Poisson ratio	ν	–	0.3
Strength parameter	k	MPa	600
Strain hardening exponent	n	–	0.21

point P belonging to that trajectory. It is further assumed that the ship moves only in its surge direction, sway and heave are not considered in the present study (Fig. 3.15).

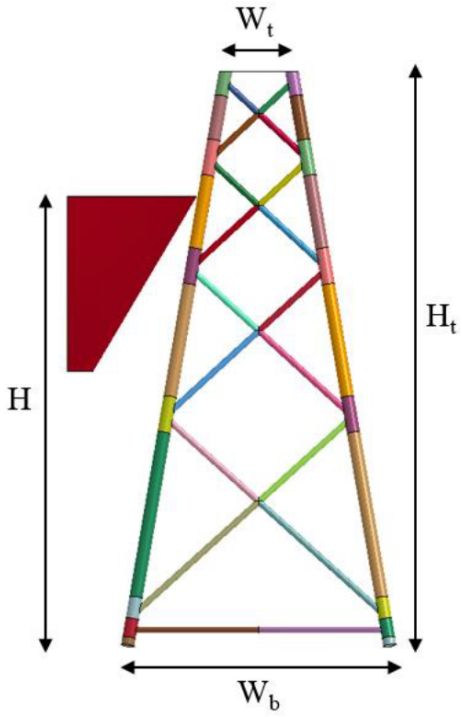

Figure 3.13: Definition of the collision elevation (H)

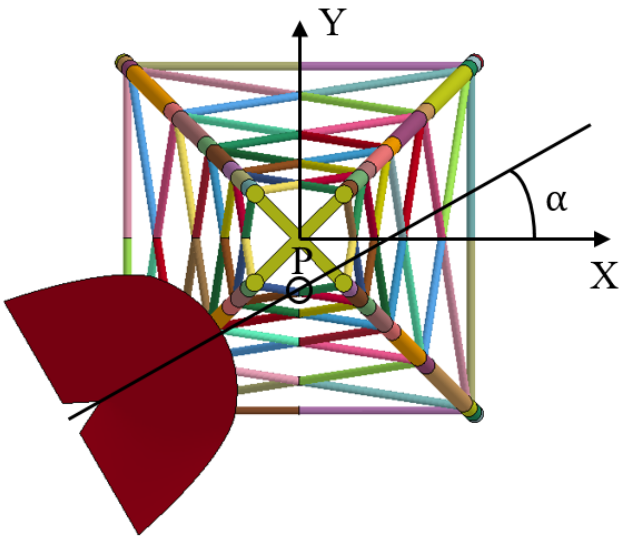

Figure 3.14: Definition of the collision angle α

The data required to describe the collision scenario are listed in Table 3.6.

Table 3.6: Data required to describe the collision scenario

Property	Notation	Unit
Ship altitude	H	m
Ship trajectory angle	α	deg
Coordinates in horizontal plane of point P belonging to the trajectory	X_P, Y_P	m
Ship mass	m_{ship}	kg
Ship initial velocity	$v_{ship,init}$	m/s

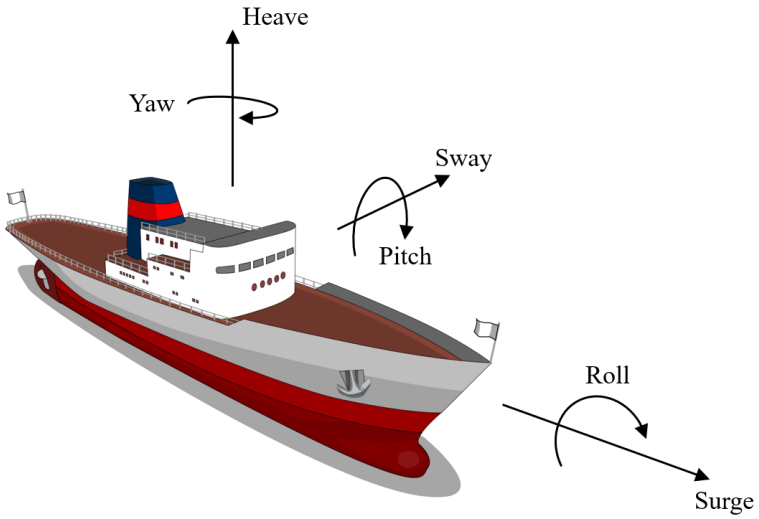

Figure 3.15: Ship displacements and rotations

3.3 Key parameters governing the jacket crashworthiness

Le Sourne et al. [6] investigated the main parameters that govern the structural behaviour of an OWT jacket impacted by a ship. Therefore, several FE collision simulations were performed, including or not those parameters. It is worth mentioning that all the simulations are performed without considering rupture of material.

The results were then compared to a FE reference model that consists in a jacket with four legs considered as perfectly clamped at the foundation level, impacted by a ship at a given point. Both the tower and the nacelle are not included in the model but their masses are represented by a punctual mass connected to the center of the transition piece. Gravity, wind and wave loads are neglected in this first model.

As this paper [6] was published in the framework of the *CHARGEOL* project, the OWT jacket modelled is exactly the same as the one described in Section 3.2.2.

3.3.1 Gravity loads effect

The first investigated parameter was the gravity load. The numerical simulations were performed in two steps:

1. **Gravity loads:**
   Gravity is first applied on the model as a pre-load using an implicit calculation. The self-weight includes the weight of the jacket itself, as well as the weight of the turbine (573 tons) and of the transition piece (66 tons), applied on top of the jacket.
   This first step provides initial state of stress and strain in the structure that is used for the second step.

2. **Crushing loads:**
   Then, considering the state of stress and strain resulting from the first step, the collision process in computed with an explicit calculation.

For several striking ship initial velocities (2 m/s and 6 m/s), it appeared that the plastic strain, the crushing force and the internal energy are similar, whatever gravity loads are taken into consideration or not.

It can be therefore concluded that gravity loads can be neglected to compute the crashworthiness of an OWT jacket impacted by a ship during the collision phase.

It is however worth mentioning that gravity has to be considered to assess the potential tower collapse process after the collision.

3.3.2 Turbine and tower effect

The tower and nacelle influence was also investigated by taking them into account explicitly. The tower was modelled with shell elements and connected to the transition piece. The rotating turbine induces loads and moments that were included in the model. Finally, the mass and inertia of the turbine were applied at the top of the tower and considered to be punctual. Gravity loads are first applied with an implicit computation, as detailed in Section 3.3.1, before starting the collision simulation.

The tower and nacelle have a very low influence on the jacket deformation itself. They can be therefore neglected as long as we are focussing on the jacket deformation only. However, modelling them properly provides relevant data on the displacement and acceleration of the turbine.

3.3.3 Soil stiffness effect

Previous simulations were performed considering the four legs perfectly clamped at the foundation level, which is conservative with regard to the jacket. Indeed, all the striking ship initial kinetic energy has to be fully dissipated by the structure, without any contribution of the soil.

The soil stiffness influence was also investigated to check if this assumption is realistic. From in-situ geotechnical measurements, soil stiffnesses in translation and rotation at the foundation level were determined.

The soil stiffness was thus modelled using 6 (3 for translation, 3 for rotation) linear springs connected to a point at the middle of each leg and at the foundation level, this point being itself connected to the leg extremities by rigid beams, as can be seen in Fig. 3.16.

For this simulation, the tower and the nacelle are modelled as described in Section 3.3.2, and gravity loads are applied before the collision, as explained in Section 3.3.1.

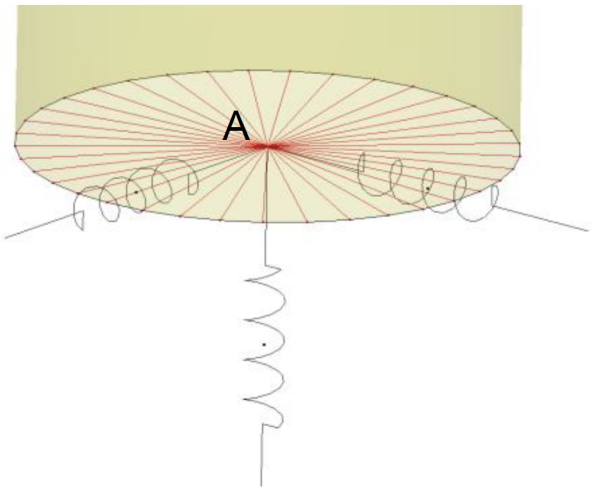

Figure 3.16: Rotational and translational springs and connections to model the soil stiffness [6]

The results show that considering the soil as infinitely rigid (assumptions of legs perfectly clamped) or with a finite stiffness (based on the stiffnesses obtained from in-situ measurements) provides similar results regarding the jacket crashworthiness. The assumption of perfectly clamped legs will thus be done for all the simulations presented in this thesis.

3.4 Finite element analysis of an offshore wind turbine jacket impacted by a ship

Before developing the analytical formulations to compute the crashworthiness of an OWT jacket, the collided jacket structural behaviour has to be studied. As real size experiments could not be performed for this research, nonlinear FE simulations were performed using the *LS-DYNA* FE solver.

3.4.1 Collisions assumptions

Both the striking ship, and the collided jacket are described in Section 3.2. For all the numerical simulations performed in the present thesis, the striking ship is considered as rigid. As discussed previously, this assumption is conservative with regard to the jacket as the whole ship initial kinetic energy is dissipated by the jacket itself, without any contribution of the ship.

Based on the researches performed by Le Sourne et al. [6], the most determinant parameters that govern the jacket structural response have been identified (Section 3.3). Based on this study, the following assumptions are performed:

- Gravity loads are not included in the model.
- The tower and the nacelle are not modelled.
- All four legs are assumed to be perfectly clamped at the foundation level.

3.4.2 Mesh size sensitivity analysis

For every numerical simulation, a mesh size sensitivity analysis has to be performed to identify the optimal mesh size. Considering small element size provides accurate results but is also time-demanding. On the contrary, large element size requires less computational effort but reduces the results accuracy.

Therefore, a collision scenario was investigated for several mesh sizes for the offshore wind turbine jacket, with mean element sizes varying from 8 to 20 cm.

The model is built with *PATRAN* based on the jacket dimensions described in Section 3.2.2. All the tubular members are meshed with Reduced Integrated Belytschko-Tsay shell elements [1, 4] (bilinear four-node quadrilateral shell with one point of integration).

The material law used for the collided jacket corresponds to the elastic-plastic with a power hardening model law, as described in Section 3.2.2.

The considered rigid striking ship corresponds to the non-bulbous OSV presented in Fig. 3.5. For the simulations presented in this Section, the ship is given a mass of $6,000$ tons (added mass included) and an initial velocity of 5 m/s in its surge direction, leading to a initial kinetic energy of 75 MJ.

The collision case investigated to determine the optimal mesh size is presented in Fig. 3.17. Here, a leg is collided between two connections with braces.

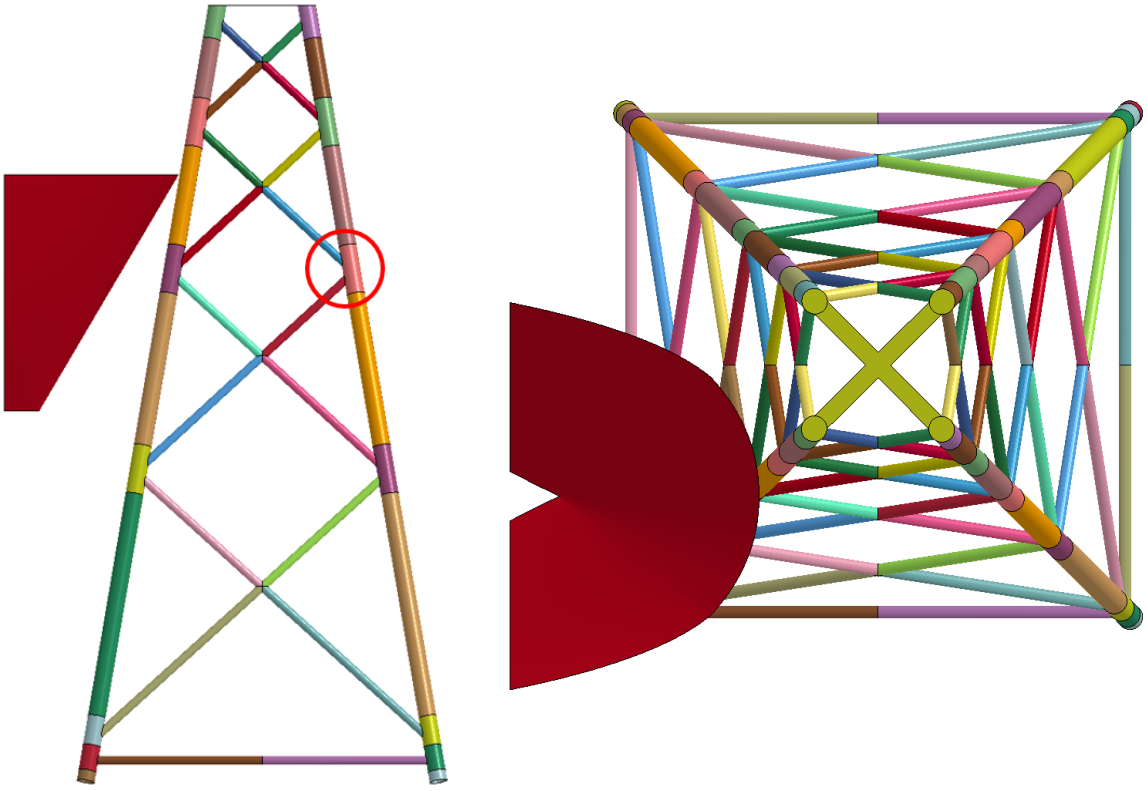

Figure 3.17: Collision scenario used to performed the mesh sensitivity analysis

In *LS-DYNA*, the contact between the striking ship and the jacket is computed with the card (i.e. command) AUTOMATIC_SURFACE_TO_SURFACE [4] described in Section A.3.

The collision scenario depicted in Fig. 3.17 was simulated for several mesh sizes, namely 8, 10, 12, 14, 16 and 20 *cm*. Zooms on the meshes taken near the connection circled in red in Fig. 3.17 is proposed in Figs. 3.18 to 3.23 for all the mesh sizes investigated.

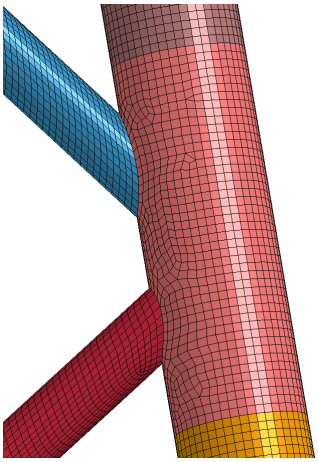

Figure 3.18: Mesh size 8 *cm*

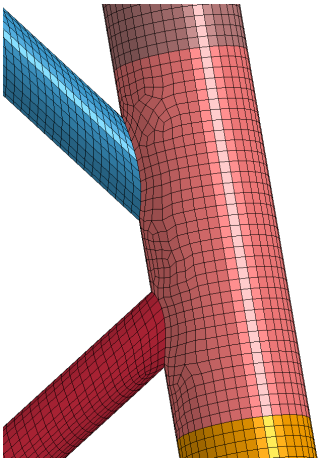

Figure 3.19: Mesh size 10 *cm*

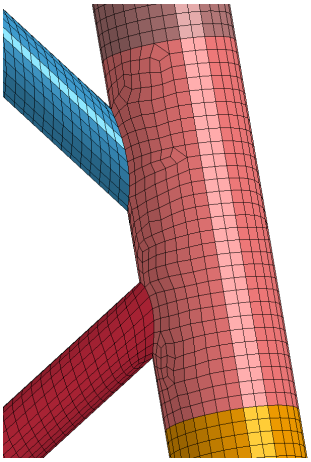

Figure 3.20: Mesh size 12 *cm*

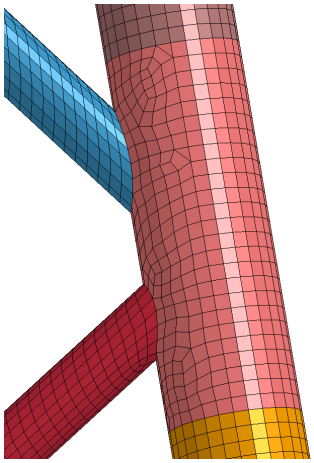

Figure 3.21: Mesh size 14 *cm*

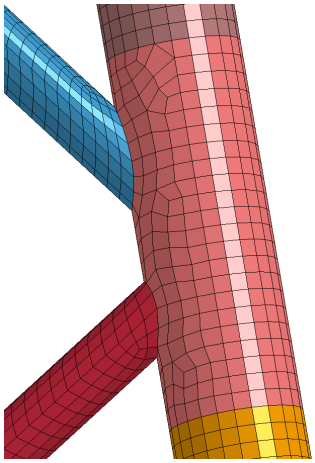

Figure 3.22: Mesh size 16 *cm*

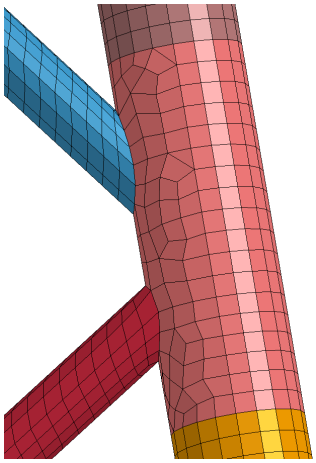

Figure 3.23: Mesh size 20 *cm*

The time evolution of the resistant force for the considered collision scenario is plotted in Fig. 3.24 for mesh sizes equal to 14, 12, 10 and 8 *cm* and a zoom on the maximum force period is given in Fig. 3.25. It appears from those Figures that the curves corresponding to mesh sizes 10 and 8 *cm* are close and tend to converge.

In addition, the number of shell elements and the ratio t_{simu}/t_{10cm}, where t_{simu} is the computation time required for the considered mesh size and t_{10cm} is the computation time for a mesh size of 10 *cm*, are given in Fig. 3.26. It is worth mentioning that all the simulations were performed using the same computational power.

As expected, the computational effort increases with the number of elements. Indeed, a smaller mesh size requires also a smaller time step in order to meet the Courant-Friedrichs-

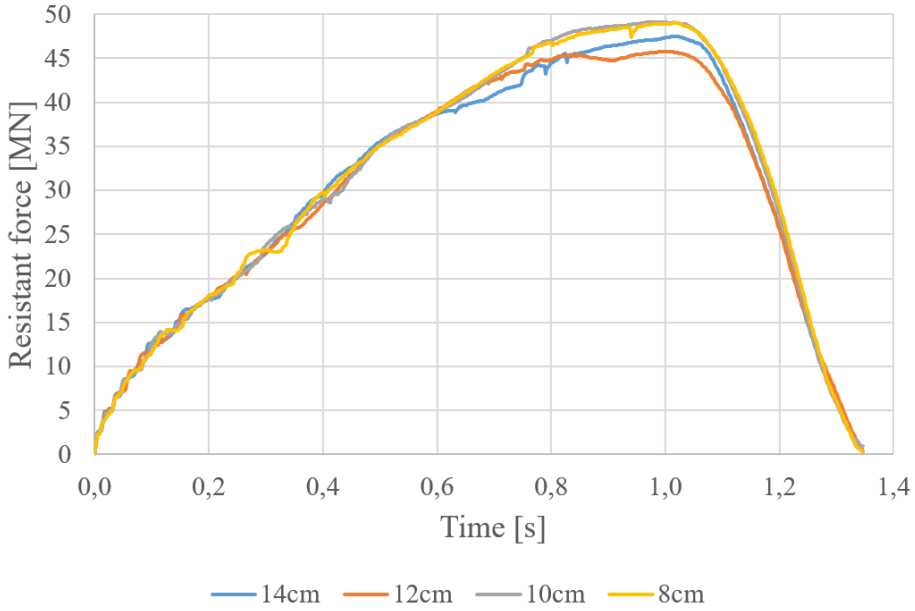

Figure 3.24: Time evolution of the resistant force for the investigated mesh sizes for the given collision scenario

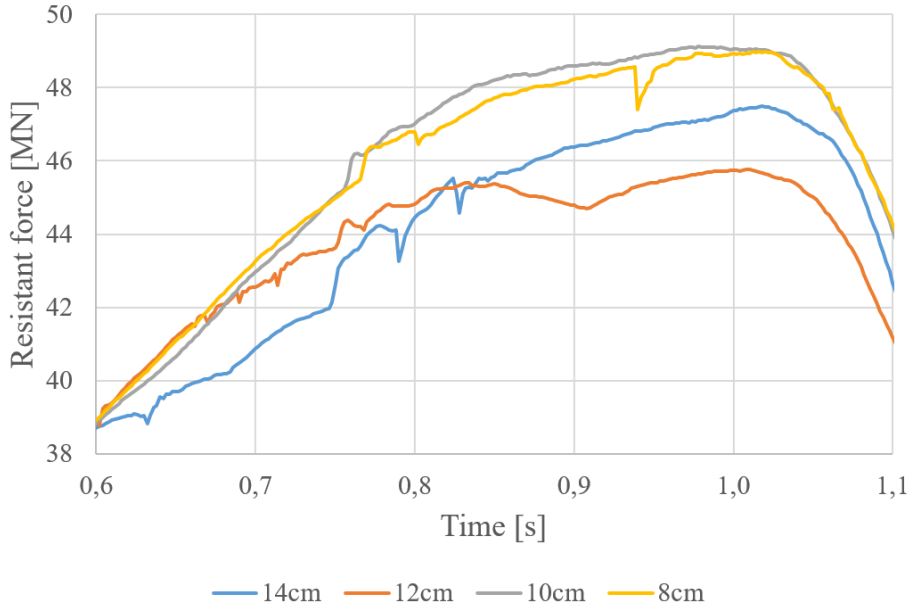

Figure 3.25: Time evolution of the resistant force for the investigated mesh sizes for the given collision scenario (zoom on the time interval where the force is maximum)

Lewy [3] condition (CFL). In addition, the contact is evaluated in *LS-DYNA* by computing the distance between the striking ship nodes and the jacket ones. Obviously, an increased number of nodes induces a larger number of node distances to compute at each iteration.

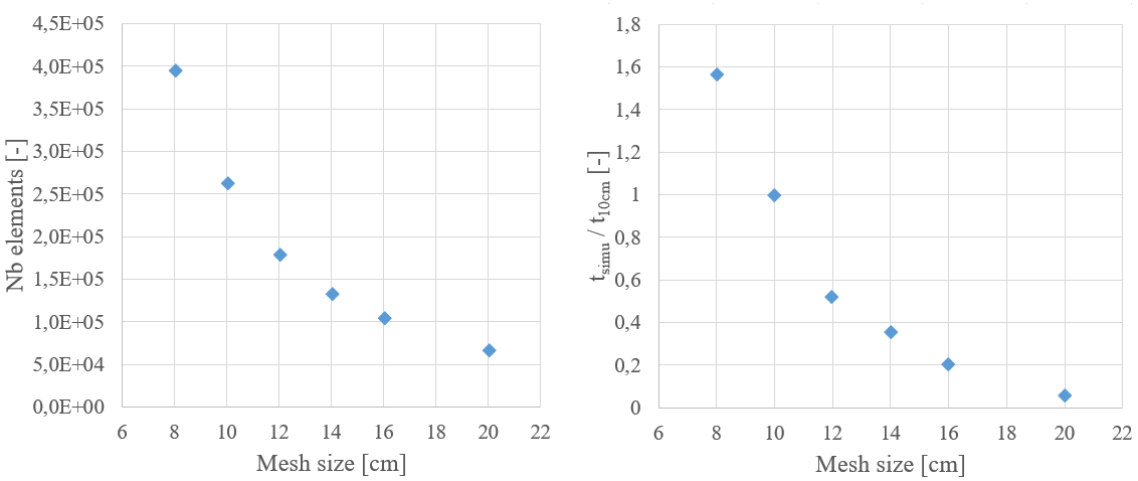

Figure 3.26: Number of jacket shell elements and computation time ratio for the investigated mesh sizes for the given collision scenario

From the presented results, it appears that a mesh size of 10 *cm* is the best compromise between results accuracy and computational effort.

3.5 Deformation modes of the impacted offshore wind turbine jacket

The collision scenario described in Fig. 3.17 was computed with *LS-DYNA* for an initial striking ship kinetic energy of 75 MJ, including all the numerical assumptions discussed in Section 3.4.

The corresponding effective plastic strain is given in Fig. 3.27, where all the areas depicted in red correspond to an effective plastic strain larger than 1%. This color code is similarly used in Figs. 3.28 to 3.32.

3.5.1 Description of the deformation modes

Based on the results obtained for this scenario and performing other numerical simulations considering other impact points and collision angles, four deformation modes are identified, each of them being treated independently in a dedicated Chapter, namely:

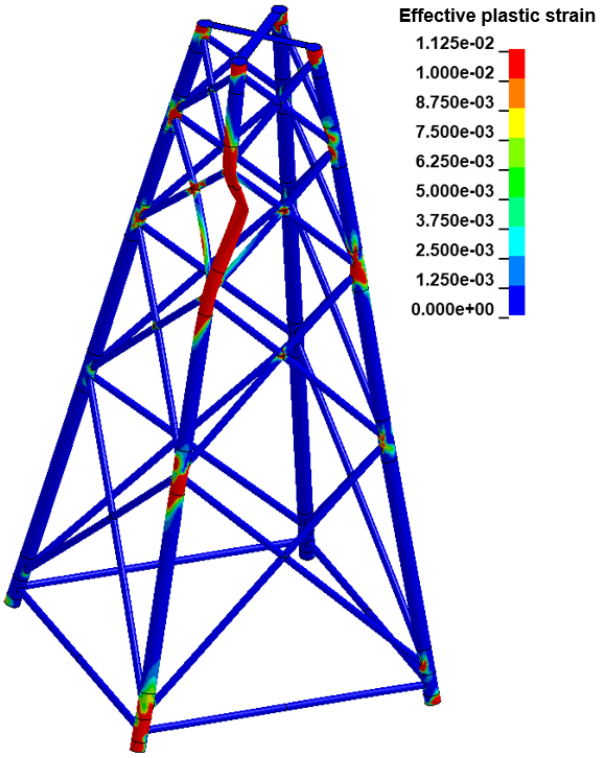

Figure 3.27: Effective plastic strain on the whole collided jacket

- Local crushing of impacted tubular members (Chapter 4);
- Global deformation of the whole jacket, including the buckling of compressed braces (Chapter 5);
- Punching of legs by compressed braces (Chapter 6);
- Deformation at the base of the jacket (Chapter 7).

The next Figs. 3.28 to 3.32 correspond to the collision scenario depicted in Fig. 3.17.

Local crushing of impacted tubular members

During a collision, the first deformation mode occurs near the contact area and consists in the local crushing of the impacted tubular member. The extent of the crushed area increases with the ship penetration, and plastic hinges appear both at the impact point and at the tubular member extremities for a given penetration.

Local crushing of the impacted tubular member can be seen in Fig. 3.28.

This deformation mode will be investigated in Chapter 4.

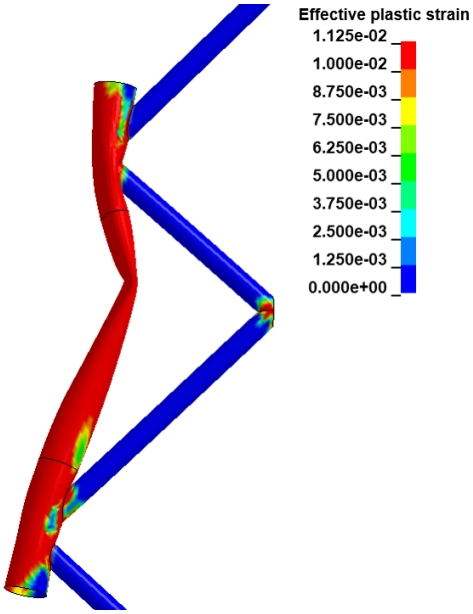

Figure 3.28: Local crushing of the impacted tubular member deformation mode

Global deformation of the whole jacket

The collided jacket will also suffer a global deformation. Indeed, all the tubular members are connected, and the crushing force is transmitted from the impact point to the foundations through all the tubular members that compose the jacket. Many braces are submitted to compressive forces and may buckle.

An overall motion of the whole structure therefore occurs, as can be seen in Fig. 3.29 in a jacket top view before and after the collision (displacement scale factor of 5, impacted tubular member removed from the Figure). As can be seen, the top part of the jacket, corresponding to the transition piece, rotates during the impact.

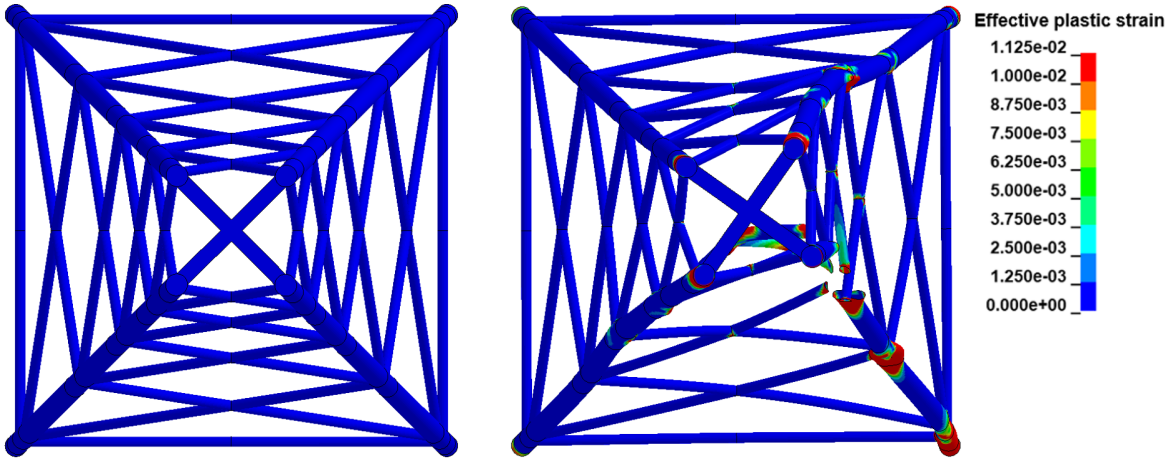

Figure 3.29: Initial position of the jacket (left) and global displacements after the collision (right)

The global deformation of the structure will be treated in Chapter 5.

Punching of legs by compressed braces

From the numerical results, it appears that local deformation, namely punching, may occur on a leg near the connection with compressed braces (see Fig. 3.30), on both impacted or rear legs. Several connections may be affected during one single collision, as can be seen in Fig. 3.31, where the areas circled in red on the legs are punched.

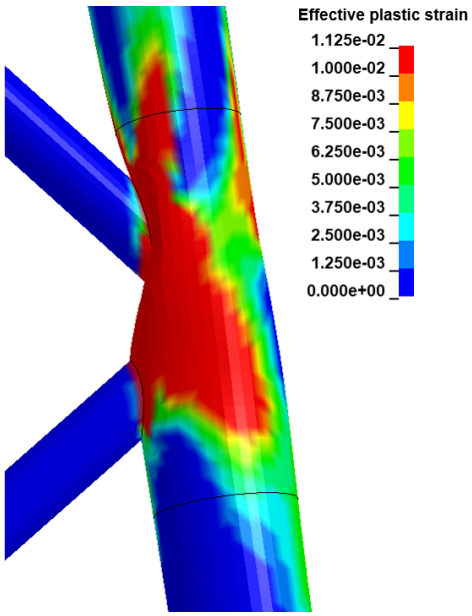

Figure 3.30: Punching of leg by compressed brace deformation mode

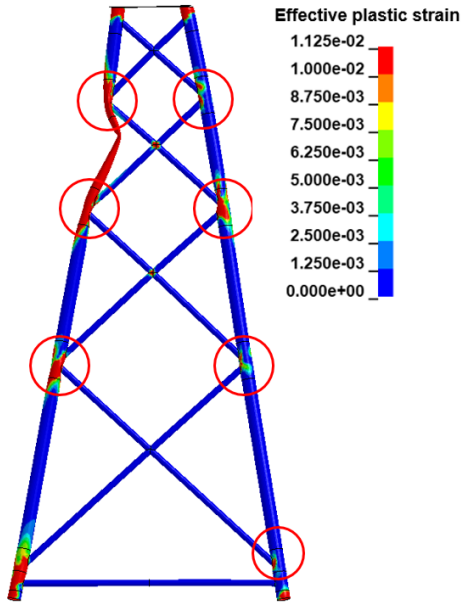

Figure 3.31: Punching on the whole collided jacket

The analytical formulations for the punching deformation mode are developed in Chapter 6. The characterisation of the punching process at one connection and the distribution of punching over the whole jacket are also described in Chapter 6.

Deformation at the base of the jacket

Looking at the numerical results, large effective plastic strain appear near the foundation level. On the rear leg, local buckling occurs and the resulting deformed leg has a shape looking like an "elephant foot", as can be seen in Fig. 3.32 (displacement amplification factor of 5). Significant elongation appears on the impacted leg.

This deformation mode is investigated in Chapter 7.

3.5.2 Discussion on the braces properties

As given in Table 3.4, the braces of the studied jacket have a ratio external diameter / thickness equal to 13. In literature, it appears that this ratio could go over 50 for other offshore wind turbine jackets, amongst others the structures studied by Travanca et al. [12] or Jin et al. [5].

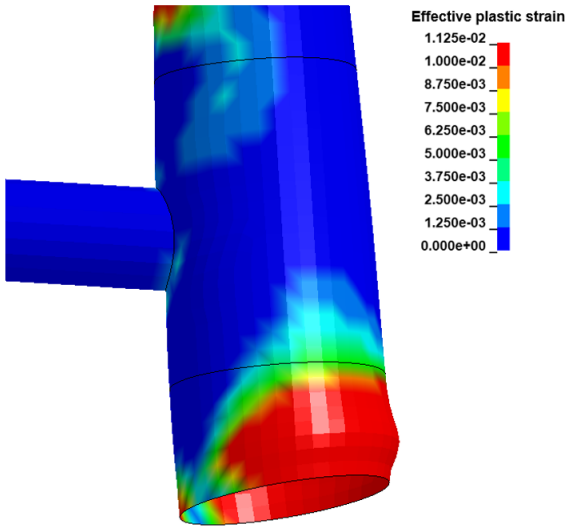

Figure 3.32: Deformation at the foundation level on the rear leg ("elephant foot")

The tubular members with the largest ratio D_e/t are the most likely to buckle for a given length and boundary conditions. With the investigated jacket properties, the ratio is low, which makes the braces more resistant to buckling.

In addition, the connections between the braces and the legs are not stiffened. This allows to limit the complexity of building the jacket and therefore its cost.

Finally, it appears that the braces are stronger than the connections. In this situation, punching of a leg by a compressed brace appears before the buckling of this brace.

In the case of connections stronger than the braces, buckling would occur first for compressed braces. For similar stiffnesses, both deformation modes could occur.

3.6 Effect of rupture criteria

The effect of rupture of the impacted leg during the collision event was investigated by the author [8].

Rupture was intentionally not considered in the numerical simulations presented previously. In order to determine the importance of this phenomenon, an erosive shear strain criterion is considered in the elastic - plastic material law used for the jacket.

The strain threshold defined by Lehmann and Peschmann [7] is given in Eq. 3.4.

$$\varepsilon_f = \varepsilon_g + \varepsilon_e \frac{t}{l_e} \tag{3.4}$$

where ε_f is the failure strain, ε_g is the uniform strain, ε_e is the necking strain and t/l_e is the thickness/element size ratio. For mild steel, common values are $\varepsilon_g = 0.056$ and $\varepsilon_e = 0.54$. As the element size l_e is 10 cm and the thickness t is 5 cm, the failure strain has a value of $\varepsilon_f = 0.33$.

The failure criteria presented in Eq. 3.4 is valid only for membranes under tension, and no other failure law for other stress states is available in the commercial code *LS-DYNA*. Therefore, this failure criteria is applied only to the tubular members submitted mainly to tension.

As can be seen in Fig. 3.9, the jacket is split into several parts, and each of them can be given a different material law.

The parts subjected to tension are located on the impacted leg, between connections of braces on the leg. Those are the only parts where the failure criteria is considered. Indeed, the rear leg is mainly submitted to compression. The area around the impact point suffers large deformations that involve a complex internal efforts distribution, and the failure criteria is therefore not applied in that zone. Finally, the parts located near the connections are punched during the collision process, which corresponds to a large amount of shear.

Several collision scenarios for different α collision angles (0°, 30° and 45°) (see Fig. 3.14) at the elevation given in Fig. 3.17 were performed. Considering a 75 MJ impact energy for each of them, failure never occurred in the impacted leg whatever the collision scenario.

The effective plastic strain given in Fig. 3.27 corresponds to the collision scenario described in Fig. 3.17 in which rupture is intentionally not considered. At the connections, the effective plastic strain is about 20% but it reaches 80% near the impact point. Rupture is therefore expected to occur in that zone.

Even if the internal forces distribution is more complex than pure tension in that area, an additional numerical simulation considering the erosive shear strain criterion described by Eq. 3.4 for the collided part is performed. A rupture strain equal to $\varepsilon_r = 0.33$ is still considered. The corresponding effective plastic strain is plotted in Fig. 3.33.

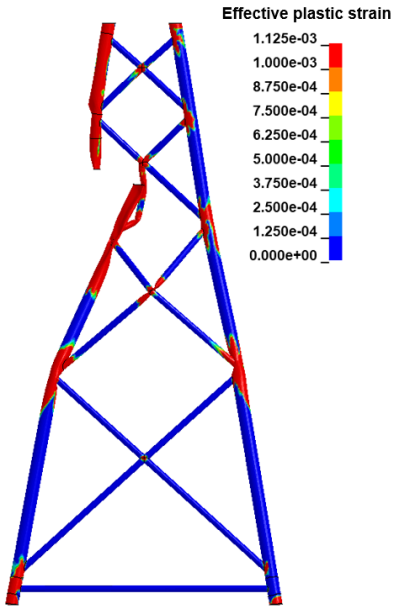

Figure 3.33: Plastic strain of one plane of an impacted jacket including rupture

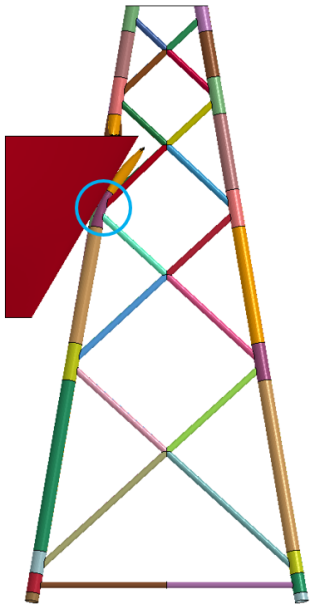

Figure 3.34: Contact between the bow and the connection below the impact point

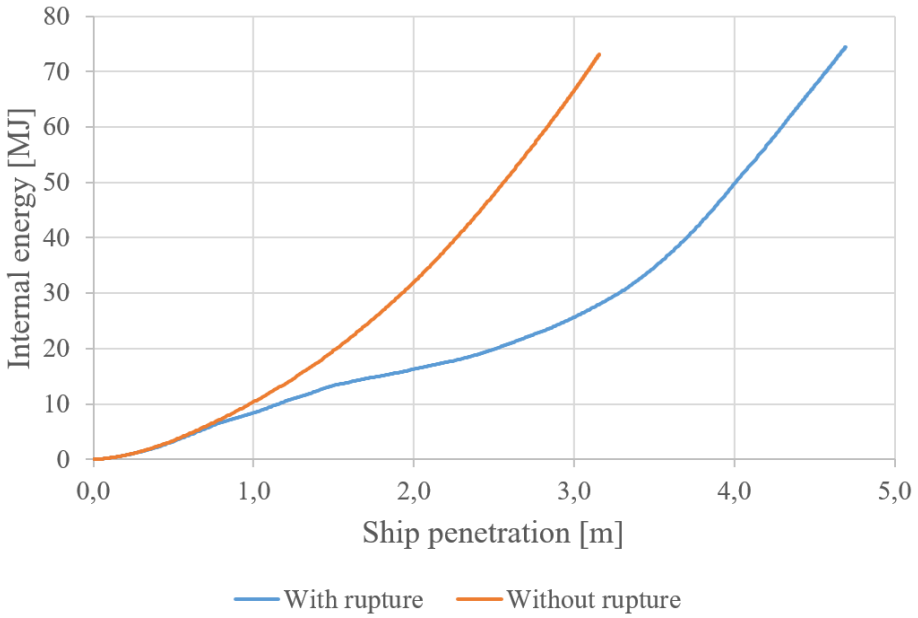

Figure 3.35: Evolution of internal energy for models with and without rupture

Considering rupture has few influence on the deformation due to punching and at the base of the jacket. Indeed, once the impacted element fails, the ship moves forward with only few resistance and few loss of kinetic energy. Then, the bow collides the connection located below the impact point, as highlighted in the blue circle in Fig. 3.34. The collision force is transmitted to the foundation system similarly to the scenarios without rupture.

However, for a given collision scenario, the ship penetration is larger when rupture is considered in the model. In the present case, the ship penetrations are equal to 3.16 m and 4.69 m without and with rupture considered in the model respectively, as can be seen in Fig. 3.35.

Finally, it appears that the ship penetration may vary if rupture is considered or not in the model, but the deformation modes are identical in both cases.

3.7 Conclusions

In this Chapter, FE simulations are performed in order to analyse the structural behaviour of an OWT jacket impacted by a ship.

First of all, the FE models are detailed in terms of geometrical properties. For the ship, mathematical expressions are given to fully describe both the stem, with a parabola at the upper deck, and the bulb, as a semi-ellipsoid. Even if those shapes are idealised, they are quite close to real ships bows and such geometrical assumptions remain valid for this research. The jacket corresponds to a real jacket, designed and built by *STX France*, and it is modelled according to the drawings provided by *STX France* in the framework of the *CHARGEOL* project.

Using FE simulations, Le Sourne et al. [6] investigated the effect of several parameters on the jacket response. It appeared that gravity has a negligible effect on the jacket deformation

during the collision process, but has a major influence in case of post-collision collapse. It was also demonstrated that the tower and the nacelle may be omitted in the model, as long as only the crashworthiness of the jacket is investigated. Finally, the soil-stiffness interaction with the structure is studied, and the results showed that considering the soil as infinitely rigid, which corresponds to consider the four legs as clamped at the foundation level, is a realistic assumption.

The jacket is modelled with Belytschko-Tsay shell elements [1, 4]. Their size is determined with a mesh size analysis, and the optimum mesh size is determined to be 10 cm.

Based on the several collision scenarios computed numerically, four deformation modes are identified, namely the local crushing of impacted tubular members, the global deformation of the whole jacket, the punching of legs by compressed braces and the deformation at the base of the jacket. For each of them, analytical formulations will be developed in the next Chapters.

Finally, failure is investigated by considering an erosive shear strain law and performing several simulations with collision energies of 75 MJ. The results showed that the ship penetration is larger when rupture is considered in the model, but the deformation modes identified remain the same with and without taking rupture into account in the material law.

Bibliography

[1] T Belytschko, I Lin, and CS Tsay. Explicit algorithms for the nonlinear dynamics of shells. *Computer Methods in Applied Mechanics and Engineering*, (42):225–251, 1984.

[2] SR Cho, BS Seo, BC Cerik, and HK Shin. Experimental and numerical investigations on the collision between offshore wind turbine support structures and service vessels. In Leira J, editor, *Collision and Grounding of Ships and Offshore Structures*, 2013.

[3] R Courant, K Friedrichs, and H Lewy. Über die partiellen differenzengleichungen der mathematischen physik. *Mathematische Annalen*, (100(1)):32–74, 1928.

[4] JO Hallquist. LS-DYNA theoretical manual. Technical report, Livermore Software Technology Corporation, 2006.

[5] WL Jin, J Song, SF Gong, and Y Lu. Evaluation of damage to offshore platform structures due to collision of large barge. *Engineering Structures*, (27):1317–1326, 2005.

[6] H Le Sourne, A Barrera, and JB Maliakel. Numerical crashworthiness analysis of an offshore wind turbine jacket imapcted by a ship. *Journal of Marine Science and Technology*, (23(5)):694–704, 2015.

[7] E Lehmann and J Peschmann. Energy absorption by the steel structure of ships in the event of collisions. *Marine Structures*, (15):429–441, 2002.

[8] T Pire, S Echeverry Jaramillo, P Rigo, L Buldgen, and H Le Sourne. Validation of a simplified method for the crashworthiness of offshore wind turbine jackets using finite elements simulations. In C Guedes Soares and Y Garbatov, editors, *Progress in the Analysis and Design of Marine Structures, Proceedings of the 6th international conference on Marine Structures (MARSTRUCT 2017), Lisbon, Portugal, 8-10 May 2017*, pages 497–505. CRC Press, 2017.

[9] M Storheim and J Amdahl. Design of offshore structures against accidental ship collisions. *Marine Structures*, (37):135–172, 2014.

[10] STX France. Energies marines. `http://stxfrance.fr/bu-energies-marines/`, visited on 5th March.

[11] J Travanca and H Hao. Dynamics of steel offshore platforms under ship impact. *Applied Ocean Research*, (47):352–372, 2014.

[12] J Travanca and H Hao. Energy dissipation in high-energy ship-offshore jacket platform collisions. *Marine Structures*, (40):1–37, 2015.

[13] AW Vredeveldt, JHA Schipperen, QHA Nassar, and CA Spaans. Safe jacket configurations to resist boat impact. In Leira J, editor, *Collision and Grounding of Ships and Offshore Structures*, 2013.

Chapter 4

Local crushing of impacted tubular members

Abstract:

The aim of this Chapter is to present a simplified analytical method for estimating the crushing resistance of a tubular member impacted by the stem of a striking ship. The collision angle of the vessel is arbitrary, i.e. oblique collisions are also considered. The two extremities of the tube are assumed to be clamped.

To achieve this goal, closed-form expressions are first derived for the particular situations of horizontal and vertical tubular members by applying the upper-bound method. An interpolation formula is then proposed to get the resistance opposed by the cylindrical member for any inclination angle.

In order to validate these theoretical developments, comparisons are made with FE simulations. These latter are performed using the *LS-DYNA* FE software. In almost all cases, the analytical prediction of the resistance is found to be in quite good agreement with the numerical ones.

Then, comparison is made by simulating an Offshore Supply Vessel (OSV) collision with a full jacket. In this case, the theoretical model is found to be insufficient for large impact energies and points out the need of additional deformation modes.

Finally, the model is extended and validated for collisions of a striking ship bulb on inclined tubular members.

Reference paper:

L Buldgen, H Le Sourne and T Pire. Extension of the super-elements method to the analysis of a jacket impacted by a ship. *Marine Structures*, (38):44-71, 2014.

4.1 Introduction

From Chapter 3, four deformation modes of an OWT jacket impacted by a ship were identified, namely:

- local crushing of impacted tubular members (present Chapter);
- global deformation of the whole jacket (Chapter 5);
- punching of legs by compressed braces (Chapter 6);
- deformation at the base of the jacket (Chapter 7).

A quick look into numerical simulations results tends to suggest that most of the initial kinetic energy of the striking ship is first dissipated by local crushing. Therefore, this deformation mode is first investigated. The jacket is idealised as a set of individual tubes (Fig. 4.1) with particular connections at their extremities. It is assumed here that the deformations only take place on the tubular members in contact with the bow, all the adjacent ones being unaffected. This hypothesis is the single restriction postulated in the present developments.

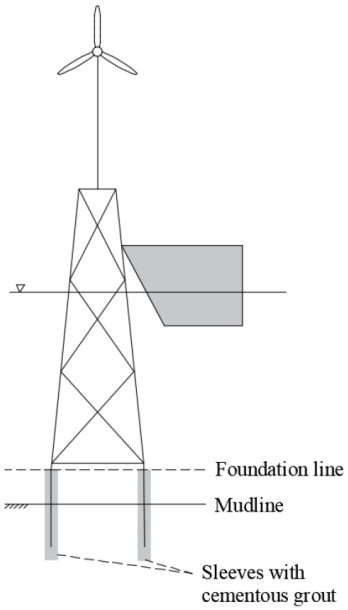

Figure 4.1: Ship - OWT jacket collision

The problem of an impact occurring on a tubular member has already been treated in the literature by Hoo Fatt and Wierzbicki [6], Wierzbicki and Suh [11] or Zeinoddini, Harding and Parke [12], amongst others. All these authors have considered the case of a concentrated load acting at the mid-length of a tubular member having a length L and a radius R (Fig. 4.2(a)). Nevertheless, this work is insufficient, as the analysis of a jacket component impacted by a ship (Fig. 4.2(b)) is similar to the one of an eccentric oblique impact, initially located at a distance L_1 from the left support, occurring on a tubular member having an inclination χ and where the striking direction is characterised by an angle α. Moreover, the bow shape may also have an

influence on the deformation pattern, which is not necessarily the same as for a concentrated force. The work detailed in this Chapter goes one step further by accounting for all these particularities and aims to be a generalisation of what has already been done by many authors.

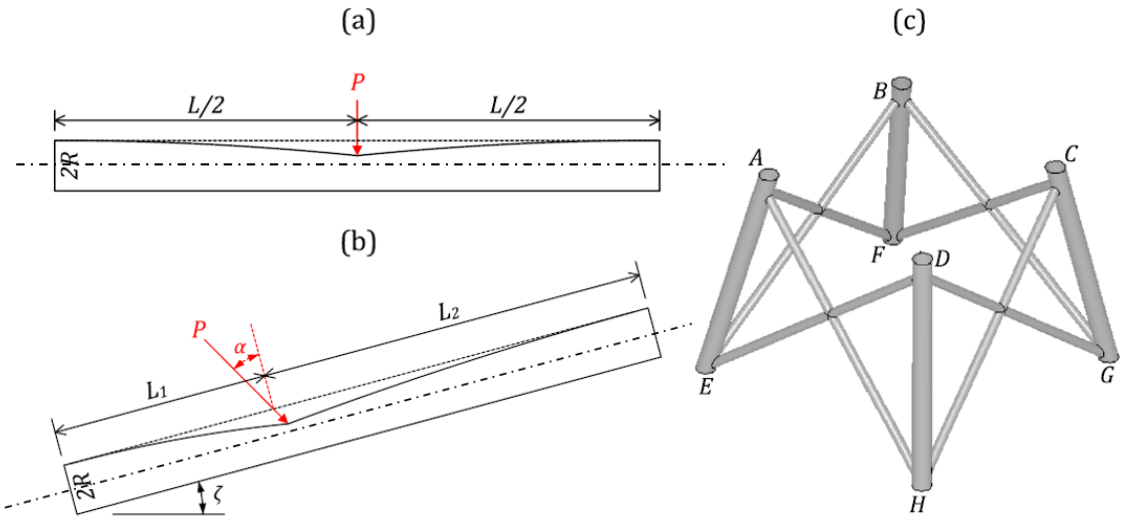

Figure 4.2: Description of the collision configuration

After describing the collision scenarios and introducing all variables, the analytical developments are fully described. In order to get closed-form expressions of the force - penetration curve, two particular collision scenarios are considered, namely an impact on a vertical and on a horizontal tubular member. The case of an arbitrary collision is treated by interpolating the results from both previously cited particular cases. Validations of the obtained results is achieved by comparing them with numerical simulations performed with the FE software *LS-DYNA*, considering both single isolated tubular members and full jacket. Finally, the model is extended to the case of an impact of a bulb on a cylindrical member.

4.2 Description of the collision scenario

When a ship collides the jacket of an OWT, the direction followed by the vessel and the inclination of the struck tubular member are arbitrary. The collision scenario is therefore defined by the relative position between the ship and the impacted tubular member.

Let us first consider the portion of the jacket depicted in Fig. 4.2(c) and suppose that the cylindrical member CH is collided by the stem. By denoting C' the vertical projection of point C over the horizontal plane $EFGH$ (Fig. 4.3(a)), the vertical plane CHC' (Fig. 4.3(a) and (b)) containing CH is used for locating the vessel with respect to the struck cylindrical member. A new reference frame (X, Y, Z) is defined to characterise the position of the vessel, having its origin in C and oriented so that the horizontal X axis is normal to CHC' and Z is vertical.

The ship stem is described in Section 3.2.1 and its relative position with regard to the impacted tubular member is represented in Fig. 4.4.

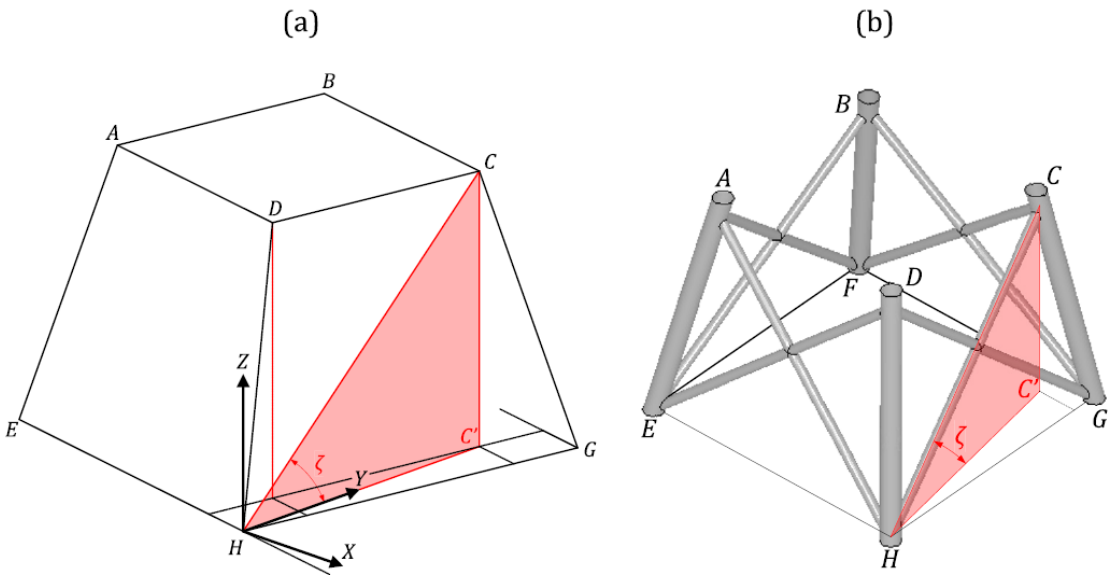

Figure 4.3: Three dimensional view of the vertical plan containing the impacted tubular member

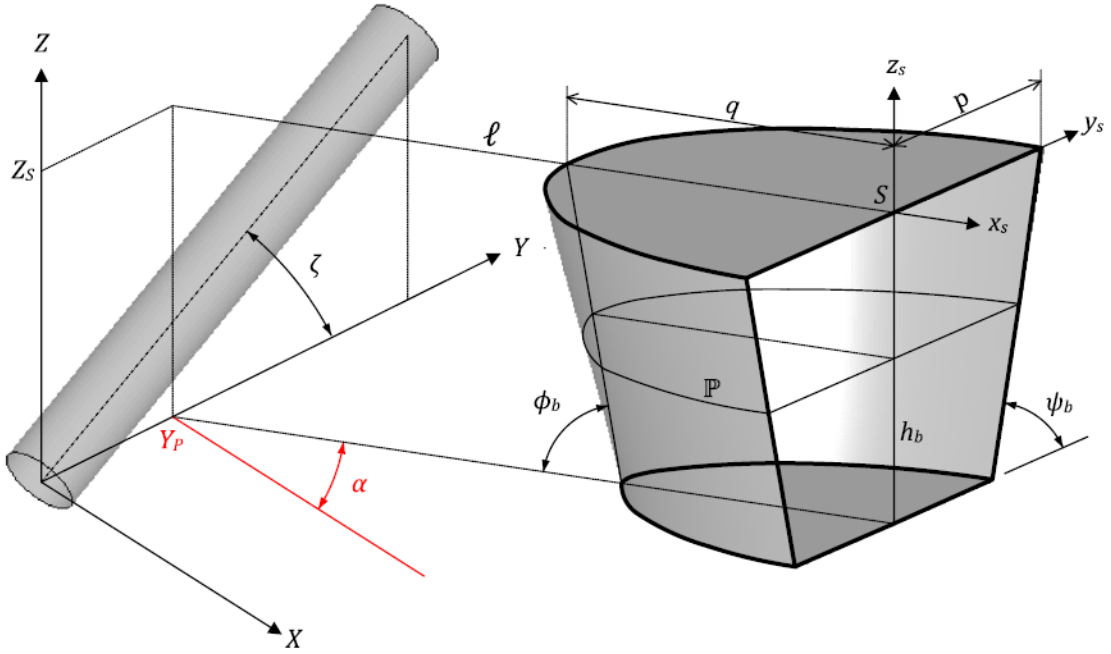

Figure 4.4: Relative position of the striking vessel with respect to the tubular member

It is now possible to further define the trajectory of the stem in the reference frame (X, Y, Z) by following the point S, center of the uppermost deck parabola. In fact, the vessel is supposed to move along an oblique straight line l (Fig. 4.4), making an angle α with the horizontal X axis and crossing the plane (Y, Z) located at Y_P. The parameters Y_P and α are sufficient to locate the point S along X and Y axes, but its position along vertical Z axis is still unknown. This latter will be simply denoted by Z_S, so that the three parameters (α, Y_P, Z_S) are the data required to completely define the relative position of the bow with respect to the cylindrical member.

The tubular member geometry is finally described by its radius R, its thickness t_p, its length L and its inclination angle ξ with respect to the horizontal plane (X, Y), as depicted in Figs. 4.3 and 4.4.

4.3 Impact on a vertical tubular member

4.3.1 Deformation mechanism

As a first step, let us start by analysing the particular case of an impact on a vertical tubular member, i.e. for which $\zeta = \pi/2$. The collision configuration of Fig. 4.5 shows that the tubular member is first impacted by the uppermost deck. The impact kinematics is therefore analysed in the horizontal plane located at $Z = Z_S$ (or $z_s = 0$). Fig. 4.6 presents a top view of the relative position occupied by the vessel and the tubular member when the first contact appears. For clarity, the dimensions of the tube have been intentionally exaggerated with respect to those of the ship.

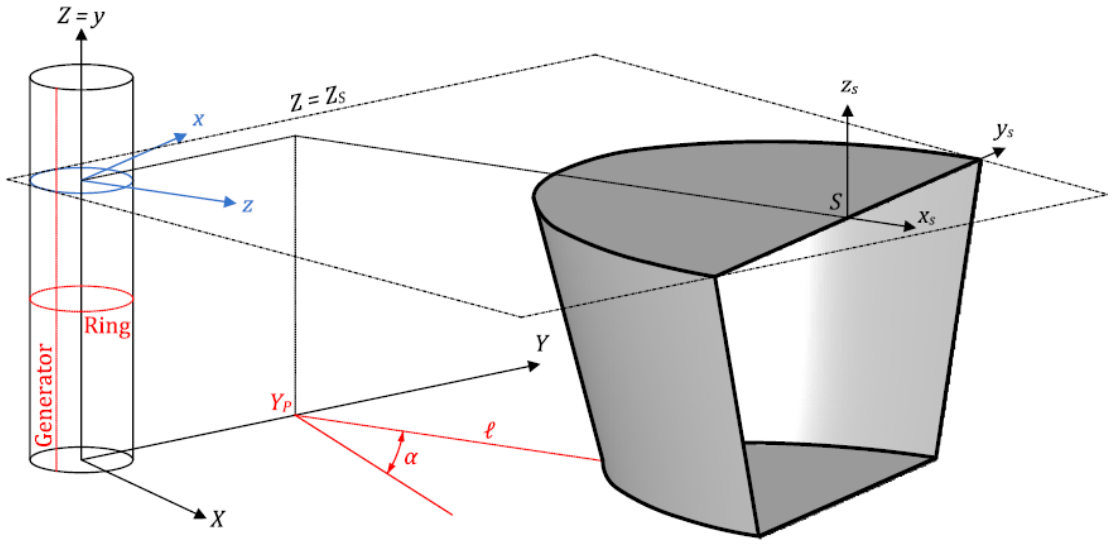

Figure 4.5: Collision configuration for an impact on a vertical tubular member

For convenience, a new reference frame (x, y, z) located at the center of the tubular member and parallel to (x_s, y_s, z_s) is introduced. If we denote by (x_S, y_S) the coordinates of point S with

respect to (x, y, z), then the equations of curves $\mathbb{P}$ and $\mathbb{C}$ respectively describing the stem and the tubular member in the horizontal plane $z_s = 0$ may be obtained from Eq. 3.1:

$$\mathbb{P} \equiv \frac{(x - x_s)^2}{p^2} + \frac{(z - z_s)^2}{q^2} = 1 \qquad \mathbb{C} \equiv \frac{x^2}{R^2} + \frac{z^2}{R^2} = 1 \tag{4.1}$$

By expressing that $\mathbb{C}$ and $\mathbb{P}$ are initially tangent (Fig. 4.6), the coordinates (x_I, z_I) of the first contact point I can be calculated and Eq. 4.1 gives the initial position (x_S, z_S) of point S.

When the ship is moving forwards, for a given value of the penetration δ, the section of the tubular member is crushed by an amount $a(\delta) = \overline{AI} \leq \delta$. From Fig. 4.6, the crushing distance $a(\delta)$ is found by calculating the intersection A between the current position of the stem $\mathbb{P}(\delta)$ and the straight line OI relating the origin O to the initial contact point I. The equation of $\mathbb{P}(\delta)$ may be directly derived from Eq. 4.1:

$$\mathbb{P}(\delta) \equiv z = -\frac{q}{p}\sqrt{p^2 - (x - x_s)^2} + z_s - \delta \qquad OI \equiv z = x \cot\beta \tag{4.2}$$

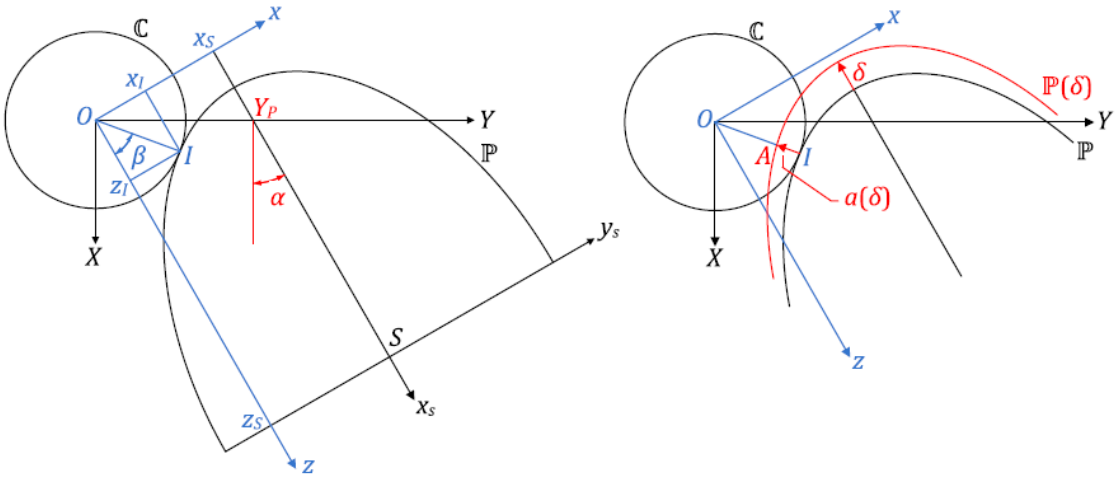

Figure 4.6: Collision configuration in the horizontal plane $Z = Z_S$

The coordinates (x_A, z_A) of point A are the particular values for which the two equations mentioned in Eq. 4.2 are simultaneously satisfied and it can be shown so x_A is given by:

$$x_A = \frac{q^2 x_s - p^2(\delta - z_s)\cot\beta - pq\,\mathrm{sign}(x_s)\sqrt{q^2 + p^2\cot^2\beta - (x_s\cot\beta + \delta - z_s)^2}}{q^2 + p^2\cot^2\beta} \tag{4.3}$$

which may be used to calculate $a(\delta) = |(x_I - x_A)/\sin\beta|$. As soon as the crushing distance is known, the next step consists in imagining a realistic deformation pattern for the tubular member cross-section. To do so, let us consider the straight line d that is tangent to $\mathbb{P}$ (Fig. 4.7(a)). When $\delta = 0$, d is going through the initial contact point I and is tangent to both $\mathbb{C}$ and $\mathbb{P}$. However, as the ship is moving forwards ($a(\delta) > 0$), d remains tangent to $\mathbb{P}(\delta)$ and goes through the intersection point A (Fig. 4.7(a)). The angle made by d and the horizontal

x axis, denoted by γ, is used for defining the deformation pattern of the tube cross-section. Moreover, as detailed hereafter, considering the tangent line d and the inclination angle γ is an approximate manner of accounting for the shape of striking stem. The expression of γ is found by considering the equation of $\mathbb{P}(\delta)$ given by Eq. 4.2, i.e.:

$$\tan\gamma = \left[\frac{\partial z}{\partial x}\right]_{x=x_A} \quad \Leftrightarrow \quad \gamma = atan\left(\frac{p}{q}\frac{x_s - x_A}{\sqrt{p^2-(x_A-x_s)^2}}\right) \tag{4.4}$$

where x_A is given by Eq. 4.3 and x_S by the initial position of the ship at the beginning of the impact. The assumed deformation pattern related to γ is depicted in Fig. 4.7(a), where the tubular member section is shown to be crushed over a distance $a(\delta) = \overline{AI}$. The deformation pattern associated with $a(\delta)$ is then defined with help of the tangent line $d \equiv BC$ and the inclination angle γ introduced here above.

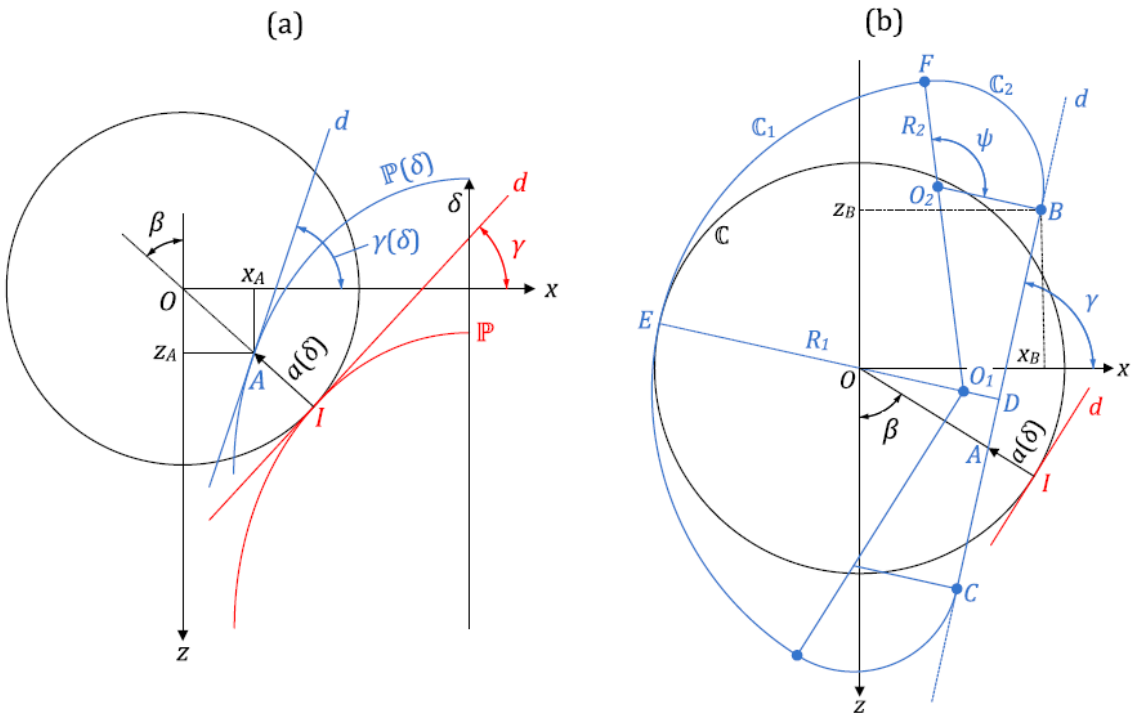

Figure 4.7: Deformation pattern of the tubular member cross-section

Let us start by considering the straight line ED perpendicular to BC and such that $\overline{BD} = \overline{CD}$. In fact, ED is the bisection of BC and E is located at the intersection of the initial tubular member cross-section $\mathbb{C}$ (Fig. 4.7(b)). By imposing symmetry condition with respect to ED, we can simply analyse the upper half $EFBD$ of the deforming cross-section, which may be split into three different portions:

- The circular arc $\mathbb{C}_1 \equiv EF$, characterised by its radius R_1 and its center O_1. For a given value of δ, the current opening of $\mathbb{C}_1$ is equal to $\pi - \psi$.

- The circular arc $\mathbb{C}_2 \equiv BF$, characterised by its radius R_2 and its center O_2. For a given value of δ, the current opening of $\mathbb{C}_2$ is equal to ψ.
- The straight segment BD having the same inclination γ than the tangent line d and characterised by a total length equal to $(R_1 - R_2)\sin\psi$.

Considering such a deformation pattern requires the calculation of R_1, R_2 and ψ for defining correctly the deformed cross-section. To do so, we can start by deriving the coordinates (x_B, z_B) of point B. From Fig. 4.7(b), it can be shown that:

$$\begin{aligned} x_B &= (R_1 - R)\cos\gamma + (R_1 - R_2)\cos(\gamma + \psi) \\ z_B &= (R_1 + R_2 - R)\cos\gamma + (R_1 - R_2) + (R_1 - R_2)\cos(\gamma + \psi) \end{aligned} \tag{4.5}$$

On the other hand, as d has an inclination γ and is going through the point A, its equation may be written as follow:

$$d \equiv z = x_A \cot\beta - (x - x_A)\tan\gamma \tag{4.6}$$

where x_A and γ are respectively given by Eqs. 4.3 and 4.4. The angle β is defined on Figs. 4.6 and 4.7(b) with help of the initial contact point I. As $B \in d$, the coordinates (x_B, z_B) given in Eq. 4.5 have to satisfy Eq. 4.6, which allows us to find a first relation between R_1, R_2 and ψ:

$$R_2 = \frac{R + x_A(\cot\beta\cos\gamma + \sin\gamma) - R_1(1 - \cos\psi)}{1 - \cos\psi} \tag{4.7}$$

An additional relation may be found by assuming, as done in references [11, 12], that the initial perimeter of $\mathbb{C}$ remains unchanged during the crushing process. This may be mathematically translated by the following relation:

$$R_1(\pi - \psi) + R_2\psi + \overline{BD} = \pi R \quad \Leftrightarrow \quad R_1(\pi - \psi) + R_2\psi + (R_1 - R_2)\sin\psi = \pi R \tag{4.8}$$

Substituting Eq. 4.7 in Eq. 4.8 leads to an explicit expression for R_1 as a function ψ. It may be shown that:

$$R_1 = \frac{\pi R(1 - \cos\psi) - (\psi - \sin\psi)(R + x_A(\cot\beta\cos\gamma + \sin\gamma))}{\pi(1 - \cos\psi) - 2(\psi - \sin\psi)} \tag{4.9}$$

From Fig. 4.7(b), it appears that $\psi = \pi$ when the section is completely crushed. If we denote by ψ_0 the initial value of ψ when $\delta = 0$, we may adopt the subsequent linear variation of ψ with the penetration δ:

$$\psi = \psi_0 + (\pi - \psi_0)\frac{\delta}{\delta_f} \tag{4.10}$$

where δ_f is the final value of δ for which the section is completely crushed. The value of ψ_0 is still unknown but will be fixed later on. The deforming pattern depicted in Fig. 4.7(b) is entirely characterised with help of Eqs. 4.7, 4.9 and 4.10 and the next step consists in deriving the displacement field associated to this mechanism.

4.3.2 Definition of the displacement field

The goal of this Section is to define the displacement field associated with the deformation pattern depicted in Fig. 4.7(b) and reproduced in Fig. 4.8(a), where ED is still a line of symmetry and H is the intersection between ED and $\mathbb{C}$. Let us now consider any point M belonging to $\mathbb{C}$ and having the coordinates $(x_M, z_M) = (R\cos\theta, R\sin\theta)$. In the deformed configuration $\mathbb{C}'$ depicted in Fig. 4.8(a), M is moved to another point N located in (x_N, z_N). The perimeter of the cross-section remaining constant, the length of HM measured along $\mathbb{C}$ is equal to the length of DN in the deformed configuration $\mathbb{C}'$, which writes:

$$\overline{DN} = R(\theta + \gamma - \pi/2) \tag{4.11}$$

where $\overline{DN}$ is the curvilinear length between D and N measured along $\mathbb{C}'$. By developing the previous equation, it is possible to find (x_N, z_N) and to calculate the displacement $w(\theta, \delta)$ of point M, i.e. the distance $\overline{MN}$ (Fig. 4.8(a)):

$$w(\theta, \delta) = \sqrt{(x_N - x_M)^2 + (z_N - z_M)^2} \tag{4.12}$$

Additional information related to the mathematical derivation of $w(\theta, \delta)$ may be found in references [4, 9, 11]. By taking the time derivative of Eq. 4.12, we get the velocity field $\dot{w}(\theta, \delta)$.

So far, only the displacements taking place in the horizontal plane $Z = Z_S$ (Fig. 4.5) have been considered. Nevertheless, it is clear that the entire tubular member is deforming during the impact, so we need to extrapolate the velocity $\dot{w}(\theta, \delta)$ along the vertical y axis.

This can be achieved by proceeding in a similar way than Wierzbicki and Suh [11], who considered that the deforming portion of the tube is progressively growing with the indentation δ. Consequently, looking at the deformation in the plane $x = 0$ (Fig. 4.8(b)), we can imagine that the tubular member is linearly indented over the portion $-\xi_2 \leq y \leq \xi_1$, while the other parts $-L_2 \leq y < \xi_2$ and $\xi_1 < y \leq L_1$ are assumed to remain undamaged:

$$\begin{aligned}
&\dot{W}(\theta, \delta, y) = \dot{w}(\theta, \delta)\left(1 - \tfrac{y}{\xi_1(\delta)}\right) && \text{if } y \in [0; \xi_1(\delta)] \\
&\dot{W}(\theta, \delta, y) = \dot{w}(\theta, \delta)\left(1 + \tfrac{y}{\xi_2(\delta)}\right) && \text{if } y \in [-\xi_2(\delta); 0] \\
&\dot{W}(\theta, \delta, y) = 0 && \text{if } y \in [L_2; -\xi_2(\delta)[\cup]\xi_1(\delta); L_1]
\end{aligned} \tag{4.13}$$

where $\xi_1 \leq L_1$ and $\xi_2 \leq L_2$ will be fixed later on.

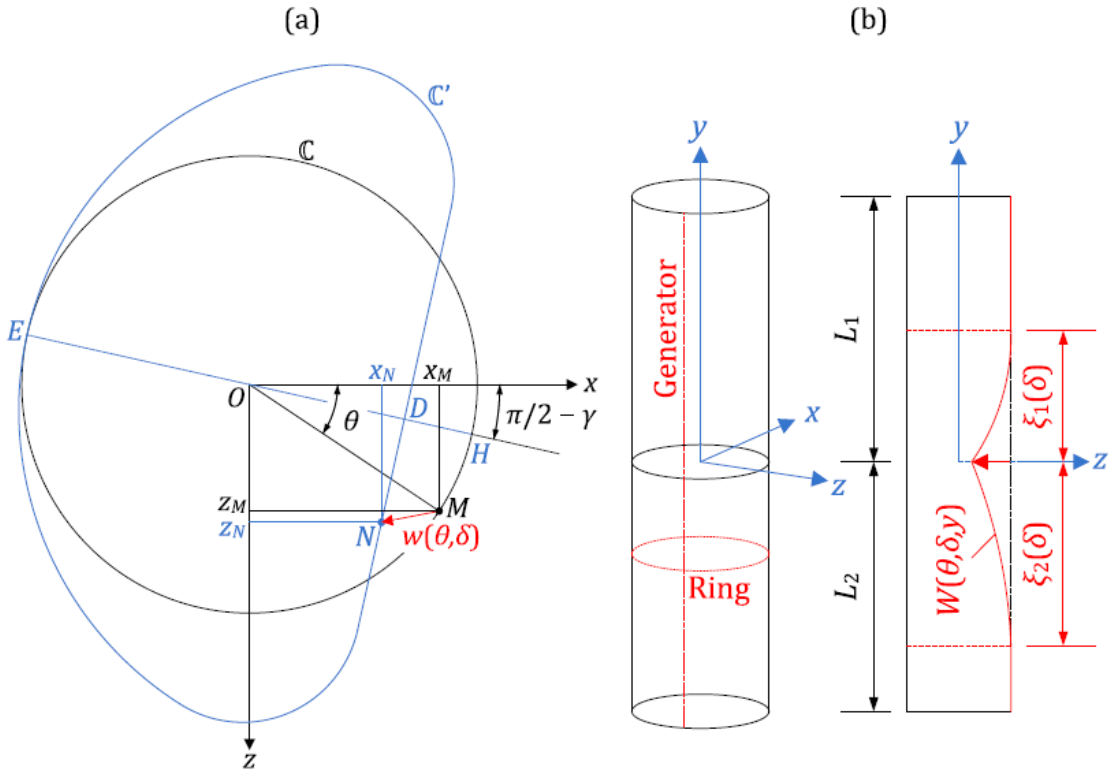

Figure 4.8: Definition of the displacement field

4.3.3 Local crushing resistance

To derive analytically the crushing resistance, the basic idea is to apply the upper-bound theorem (see Jones [7] for more details), by supposing that the tubular member is made of a rigid-plastic material characterised by a flow stress σ_0.

As a first step, similarly to Wierzbicki and Suh [11], we suppose that the impacted tubular member is composed of generators supported by independent rings that are free to slide on each other without shearing (see Figs. 4.5 and 4.8(b)). As a consequence, the total energy rate $\dot{E}$ of the crushing mechanism is simply given by:

$$\dot{E} = \dot{E}_r + \dot{E}_g \tag{4.14}$$

where $\dot{E}_r$ and $\dot{E}_g$ are the energy rates of the rings and the generators respectively.

4.3.3.1 Energy rate of the rings

Let us start by considering the energy rate $\dot{E}_b$ related to the deformation of the central section depicted in Fig. 4.7(b). The expression of $\dot{E}_b$ can be derived by following a very similar procedure than the one exposed in references [11, 12]. As justified by Wierzbicki in [11], $\dot{E}_b$ is mainly due to bending effects taking place over the cross-section. Fig. 4.7(b) shows that the curvatures χ_1 and χ_2 characterising the circular arcs $\mathbb{C}_1$ and $\mathbb{C}_2$ are not the same, as we have $\chi_1 = 1/R_1$ and

$\chi_2 = 1/R_2$. The curvature is therefore discontinuous at the junctions $\mathbb{C}_1 \cap \mathbb{C}_1$ and $\mathbb{C}_2 \cap BD$, which implies moving plastic hinges to be located at points B and F. Consequently, the energy dissipation is due to both the modification of the curvature along $\mathbb{C}_1$ and $\mathbb{C}_2$, and the bending effects occurring inside the moving plastic hinges, so we have:

$$\dot{E}_b = 2m_0 \left(\frac{V_B}{R_2} + \left(\frac{1}{R_2} - \frac{1}{R_1} \right) V_F + \int_F^E \dot{\chi}_1 dl + \int_D^F \dot{\chi}_2 dl \right) \tag{4.15}$$

where $m_0 = \sigma_0 t_p^2/4$ is the tubular member bending capacity per unit of length. The first and second terms of Eq. 4.15 correspond to the energy dissipated inside the hinges B and F. These latter are characterised by the velocities V_B and V_F and it can be demonstrated from Fig. 4.7(b) that:

$$\begin{aligned} V_B &= (R_1 - R_2)\dot{\chi} - (\pi - \psi)\dot{R}_1 - \psi \dot{R}_2 = \left((R_1 - R_2)\frac{\partial \psi}{\partial \delta} - (\pi - \psi)\frac{\partial R_1}{\partial \delta} - \psi \frac{\partial R_2}{\partial \delta} \right) \dot{\delta} \\ V_F &= R_1 \dot{\chi} - (\pi - \psi)\dot{R}_1 = \left(R_1 \frac{\partial \psi}{\partial \delta} - (\pi - \psi)\frac{\partial R_1}{\partial \delta} \right) \dot{\delta} \end{aligned} \tag{4.16}$$

Similarly, the third and fourth terms of Eq. 4.15 describe the change of curvature occurring in $\mathbb{C}_1$ and $\mathbb{C}_2$ respectively. As $\chi_1 = 1/R_1$ and $\chi_2 = 1/R_2$, these curvilinear integrals are quite easy to evaluate and may be written as:

$$\int_F^E \dot{\chi}_1 dl = \frac{\pi - \psi}{R_1} \frac{\partial R_1}{\partial \delta} \dot{\delta} \qquad ; \qquad \int_D^F \dot{\chi}_2 dl = \frac{\psi}{R_2} \frac{\partial R_2}{\partial \delta} \dot{\delta} \tag{4.17}$$

By introducing Eqs. 4.16 and 4.17 in Eq.4.15, a closed-form expression of $\dot{E}_b$ is derived, where $\partial R_1/\partial \delta$, $\partial R_2/\partial \delta$ and $\partial \psi/\partial \delta$ are obtained by derivation of Eqs. 4.9, 4.7 and 4.10 respectively.

The theoretical developments performed here above are only valid for the central cross-section located in the horizontal plane $y = 0$ (Fig. 4.5), but a similar procedure should be followed for all the rings located along the vertical y axis. Nevertheless, if we want to analyse the situation for $y \neq 0$, it is clear that the deformation pattern of Fig. 4.7(b) is not valid any more because the crushing distance is not equal to $a(\delta)$ in this case. In fact, if $y \neq 0$, the penetration has to be found by integrating the velocity field postulated in Eq. 4.13 with the particular initial condition $W(\theta, \delta, y) = 0$ for $\delta = 0$. Unfortunately, it is impossible to apply such an approach if we want to obtain a closed-form solution. As suggested in [11], an approximate solution is derived by calculating the bending dissipation in a section located at $y \neq 0$ through a linear interpolation of $\dot{E}_b$. The total energy rate $\dot{E}_r$ of the rings located along the vertical y axis is then given by:

$$\dot{E}_r = \int_{-\xi_2}^0 \dot{E}_b \left(1 + \frac{y}{\xi_2} \right) dy + \int_0^{\xi_1} \dot{E}_b \left(1 - \frac{y}{\xi_1} \right) = \dot{E}_b \frac{\xi_1 + \xi_2}{2} \tag{4.18}$$

where $\dot{E}_b$ is obtained by using Eq. 4.15.

4.3.3.2 Energy rate of the generators

As mentioned here above, the displacement field $W(\theta, \delta, y)$ acting on a generator may be found by integrating the velocity profile. Eq. 4.13 shows that both the length and the curvature of the generator change when $W(\theta, \delta, y)$ increases, which implies membrane and bending effects that are difficult to evaluate analytically. A conservative hypothesis is then to neglect the flexural energy, which means that the dissipation is entirely coming from the membrane strains developing inside the generator. As each generator is supposed to slide freely on the rings without shearing, the only contribution to the membrane energy rate comes from an axial elongation. The corresponding deformation rate $\dot{\varepsilon}_m$ is given by:

$$\dot{\varepsilon}_m(\theta, \delta, y) = \frac{\partial W}{\partial y}\frac{\partial \dot{W}}{\partial y} \tag{4.19}$$

Consequently, the total membrane energy rate $\dot{E}_m$ associated to a particular generator located at the angular position θ is calculated by integrating $\dot{\varepsilon}_m$ along the deforming part of the tubular member:

$$\dot{E}_m(\theta, \delta) = n_0 \int_{-\xi_2}^{\xi_1} \dot{\varepsilon}_m(\theta, \delta, y) dy = n_0 \dot{\delta} \left(\frac{1}{\xi_1} + \frac{1}{\xi_2}\right) w(\theta, \delta) \frac{\partial w}{\partial \delta} \tag{4.20}$$

where $n_0 = \sigma_0 t_p$ is the axial resistance of the tubular member per unit of length. Here, $w(\theta, \delta)$ is the displacement field of the central cross-section given by Eq. 4.12 and $\partial w/\partial \delta$ is the corresponding velocity. It is worth noting that $\dot{E}_m$ corresponds to a single generator located at a certain angular position θ. So calculating $\dot{E}_g$ requires to account for all the generators, i.e.:

$$\dot{E}_g = \int_{\mathbb{C}} \dot{E}_m(\theta, \delta) dl = 2Rn_0\dot{\delta} \left(\frac{1}{\xi_1} + \frac{1}{\xi_2}\right) \int_0^{2\pi} w(\theta, \delta) \frac{\partial w}{\partial \delta} d\theta = \left(\frac{1}{\xi_1} + \frac{1}{\xi_2}\right) \dot{E}'_m \tag{4.21}$$

Since it is practically impossible to find a closed-form for $\dot{E}'_m$, Eq. 4.21 is solved by numerical integration.

4.3.3.3 Virtual work principle

Once all the contributions have been calculated, Eqs. 4.14, 4.18 and 4.21 are used to find the total energy rate:

$$\dot{E} = \dot{E}_b \frac{\xi_1 + \xi_2}{2} + \left(\frac{1}{\xi_1} + \frac{1}{\xi_2}\right) \dot{E}'_m \tag{4.22}$$

According to the virtual velocity principle ([7] for more details), the internal energy rate is equated to the external power developed by the crushing resistance $P_l(\delta)$ of the vertical tubular member. As depicted in Fig. 4.7(a), for a given penetration δ, the displacement of the contact

point I is equal to $a(\delta)$. Consequently, applying the virtual work principle leads to:

$$\begin{aligned} P_l(\delta)\dot{a}(\delta) &= \dot{E}_b\frac{\xi_1+\xi_2}{2} + \left(\frac{1}{\xi_1}+\frac{1}{\xi_2}\right)\dot{E}'_m \\ \Leftrightarrow P_l(\delta) &= \left(E_b\frac{\xi_1+\xi_2}{2} + \left(\frac{1}{\xi_1}+\frac{1}{\xi_2}\right)E'_m\right)\left(\frac{\partial a}{\partial \delta}\right)^{-1} \end{aligned} \tag{4.23}$$

where $E_b = \dot{E}_b/\delta$ and $E'_m = \dot{E}'_m/\delta$. The last step is then to evaluate ξ_1 and ξ_2. This can be achieved by minimising Eq. 4.23:

$$\begin{aligned} &\frac{\partial P_l}{\partial \xi_1} = 0 \quad ; \quad \frac{\partial P_l}{\partial \xi_2} = 0 \\ &\Leftrightarrow \xi_1(\delta) = \min\left(\sqrt{2E'_m/E_b}; L_1\right) \quad ; \quad \xi_2(\delta) = \min\left(\sqrt{2E'_m/E_b}; L_2\right) \end{aligned} \tag{4.24}$$

As a final remark, it is worth bearing in mind that there is still one undefined parameter. Indeed, if we go back to Eq. 4.10, we see that the initial value ψ_0 of the angle ψ remains unknown. By comparisons with numerical simulations (see Section 4.5.2), this one is fixed to $3\pi/4$. This value is quite close to the one recommended in Refs. [4, 11, 12].

4.3.4 Global crushing resistance

All the theoretical developments presented in Sections 4.3.1 - 4.3.3 were carried out with the objective of modelling a localised indentation of the cylindrical member. In other words, this means that the tubular member is supposed to be crushed without exhibiting any beam-like behaviour. In this case, we say that the resistance $P_l(\delta)$ is said to be provided through a *local* deforming mode. However, droptests on tubular members show that for a given penetration, the member is forced into an overall bending motion [3]. The deformations are not any longer confined in a localised area near the impact point but affect the entire tubular member. In that case, we say that the resistance $P_g(\delta)$ is said to be provided through a *global* deforming mode.

FE simulations of full-scale ship-jacket collisions show that at the beginning of the impact, the crushing resistance of a leg or a brace is essentially coming from the local mode [8]. But as the ship is moving forwards, the global mode is progressively activated. Consequently, there is a switch in the behaviour of the cylindrical member. In reality, this transition is quite smooth but in our mathematical model, the activation of the global deforming mode is supposed to occur abruptly, for a particular value δ_t of the penetration. As depicted in Fig. 4.9(a), the final resistance $P_v(\delta)$ is evaluated as follow:

$$P_v(\delta) = P_l(\delta) \text{ if } \delta \leq \delta_t \quad ; \quad P_v(\delta) = P_g(\delta) \text{ if } \delta > \delta_t \tag{4.25}$$

The final step to get $P_v(\delta)$ is then to evaluate $P_g(\delta)$. In fact, the global behaviour of the tubular member may be studied with the classical theory of beams. If the extremities of the tubular member are totally restrained, then the global resistance $P_g(\delta)$ is derived under the

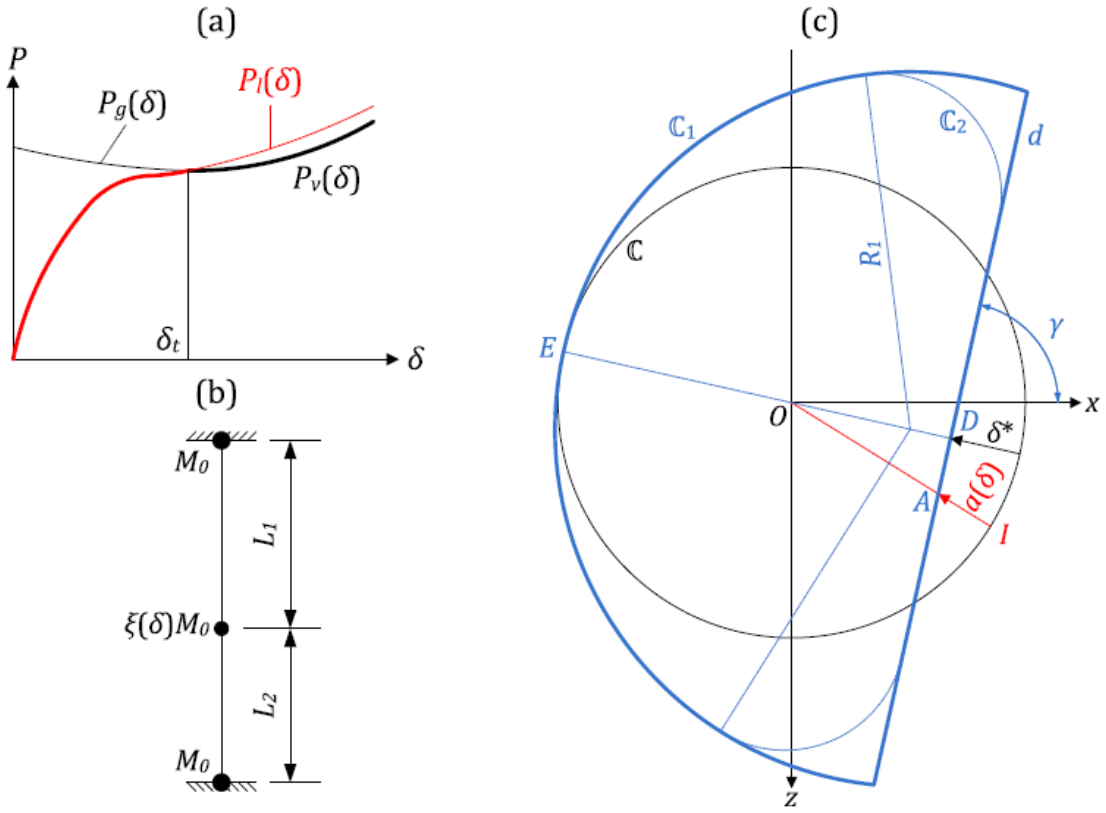

Figure 4.9: (a) Evaluation of the total resistance; (b) Activation of the global plastic mechanism for a given penetration d; (c) Reduced cross-section

assumption of a three plastic hinges mechanism. This one is represented in Fig. 4.9(b), where M_0 is the fully plastic bending moment of the initial circular cross-section $\mathbb{C}$. The thickness t_p being small in comparison with the radius R, we have $M_0 = 4R^2\sigma_0 t_p$. At the beginning of the global mode, M_0 has to be reached at the two extremities of the tube, as the corresponding sections are supposed to be undamaged. However, this is not the case for the central cross-section, where only a reduced value $\xi(\delta)M_0 \leq M_0$ can be reached because of the crushing of the cross-section. In fact, $\xi(\delta)M_0$ is the plastic bending moment calculated by considering the deformed cross-section depicted in Fig. 4.7(b) for a given value of δ. So the main issue is now to evaluate the reduction factor $\xi(\delta)$, which is a quite arduous task.

Considering the deformed tubular member section depicted in Fig. 4.7(b), it is difficult to evaluate precisely the reduction factor $\xi(\delta)$. As suggested by De Oliveira [4], $\xi(\delta)$ may be derived for an approximate cross-section, obtained by neglecting $\mathbb{C}_2$ and extending $\mathbb{C}_1$ till the tangent line d. Doing so, we get the semi-circular section depicted in Fig. 4.9(c) for which it is much easier to evaluate the plastic bending moment. Following the methodology of De Oliveira [4], the derivation of $\xi(\delta)$ provides:

$$\xi(\delta) = \frac{1}{2}\left(\left(\frac{\delta^\star}{2R}\right)^2 - 1\right)\left(\frac{\delta^\star}{2R} - 2\right) \quad ; \quad \delta^\star = R - (R - a(\delta))\cos(\gamma - \beta) \tag{4.26}$$

where $\delta^\star$ is the displacement of the symmetry point D (Fig. 4.9(c)). For a given local indentation δ, the crushing force required for activating the plastic mechanism depicted in Fig. 4.9(b) is derived by applying the classical theory of beams:

$$P_g(\delta) = \frac{L_1 + L_2}{L_1 L_2}(1 + \xi(\delta))M_0 \tag{4.27}$$

As shown by Eq. 4.26, $\xi(\delta)$ is a decreasing function of the penetration δ, which explains the decrease of $P_g(\delta)$ before the transition occurring at δ_t (Fig. 4.9(a)).

As mentioned earlier, a transition is assumed to happen when the local resistance reaches the value required for activating the mechanism of Fig. 4.9(b). According to Eq. 4.27, the crushing resistance writes at this moment:

$$P_l(\delta_t) = P_g(\delta_t) = \frac{L_1 + L_2}{L_1 L_2}(1 + \xi_t)M_0 \quad ; \quad \xi_t = \xi(\delta_t) \tag{4.28}$$

which means that the global mode is characterised by a central cross-section having a reduced plastic bending moment of $\xi_t M_0$, with $\xi_t = \xi(\delta_t)$.

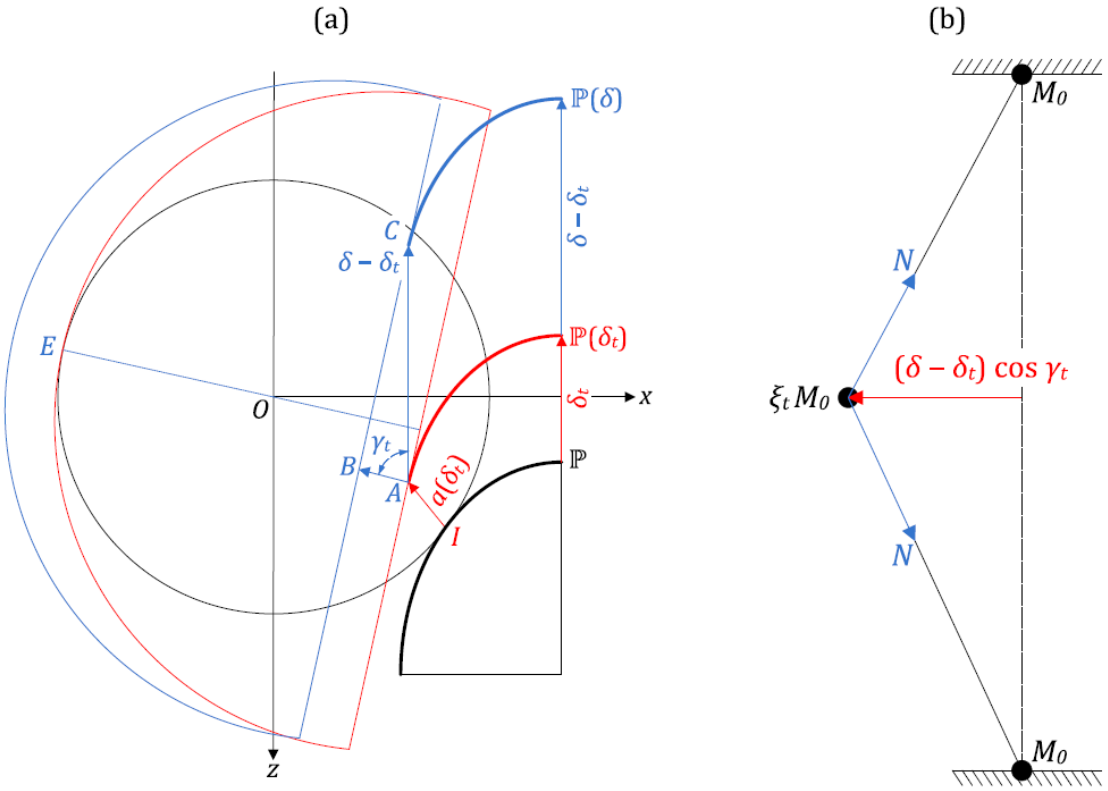

Figure 4.10: Displacement of the central section during the global mode

In order to derive the resistance $P_g(\delta)$ when $\delta > \delta_t$ and to define the displacements during the overall motion of the beam, we consider the situation depicted in Fig. 4.10(a), where for clarity, the tubular member radius has been intentionally exaggerated in comparison with the vessel size. From this Figure, it appears that initially (i.e. for $\delta = 0$), the first contact between

the stem $\mathbb{P}$ and the ship occurs at point I. The local mode is then activated, and for $\delta \leq \delta_t$, the section is deformed in accordance with the pattern drawn on Fig. 4.7(b). When $\delta = \delta_t$, the local resistance $P_l(\delta_t)$ is sufficient for activating the global mode. At this moment, the crushing penetration is $a_t = a(\delta_t)$, the inclination angle is $\gamma_t = \gamma(\delta_t)$ and the approximate plastic bending moment of the corresponding deformed cross-section is equal to $\xi_t M_0$.

When $\delta > \delta_t$, the local crushing process is stopped and the section starts moving as a whole. Fig. 4.10(a) shows that for a given value of δ, point A is moving to C such that $\overline{AC} = \delta - \delta_t$, which causes the section to move aside. This displacement is characterised by $\overline{AB} = (\delta - \delta_t)\cos\gamma_t$ and the global deforming mode may be studied using the classical beam theory applied to the structure depicted in Fig. 4.10(b).

During the overall motion represented in Fig. 4.10(b), the resistance $P_g(\delta)$ comes from both bending and membrane effects. These latter are due to the development of normal tensile forces N associated with the axial lengthening of the beam. A criterion is therefore needed to define how the flexural and extensional contributions are interacting. According to De Oliveira [4], the relation between the bending moment M and the normal force N in the plastic hinges may be written as:

$$M = M_0\left(1 - \frac{N^2}{N_0^2}\right) \quad \text{or} \quad M = \xi_t M_0\left(1 - \frac{N^2}{N_0^2}\right) \tag{4.29}$$

where $N_0 = 2\pi R\sigma_0 t_p$ is the plastic tensile capacity of the cylindrical member. The first of Eq. 4.29 is valid for the two extreme cross-sections, while the second has to be applied to the central one. Using this relation and applying the classical beam theory, a closed-form expression of $P_g(\delta)$ is obtained (Jones [7] for more details):

$$\begin{aligned} P_g(\delta) &= \frac{L_1 + L_2}{L_1 L_2}\left((1 + \xi(\delta))M_0\left(1 - \frac{N(\delta)^2}{N_0^2}\right) + N(\delta)(\delta - \delta_t)\cos\gamma_t\right) \\ \text{with: } N(\delta) &= \min\left(\frac{N_0^2(\delta - \delta_t)\cos\gamma_t}{2(1 + \xi_t)M_0}; N_0\right) \end{aligned} \tag{4.30}$$

As a conclusion, the resistance $P_v(\delta)$ developed during the impact of a vertical tubular member is calculated by applying Eq. 4.25, in which $P_l(\delta)$ and $P_g(\delta)$ are respectively given by Eqs. 4.23 4.30.

4.4 Impact on a horizontal tubular member

4.4.1 Deformation mechanism

Let us now investigate the particular case of an impact occurring on a horizontal tubular member, i.e. for which the inclination angle $\zeta = 0$ (Fig. 4.4). Fig. 4.11 presents the collision configuration,

where the striking vessel is travelling along the line l, making an angle α with the horizontal X axis and strikes the tubular member at a point I defined by its coordinates (X_I, Y_I, Z_I).

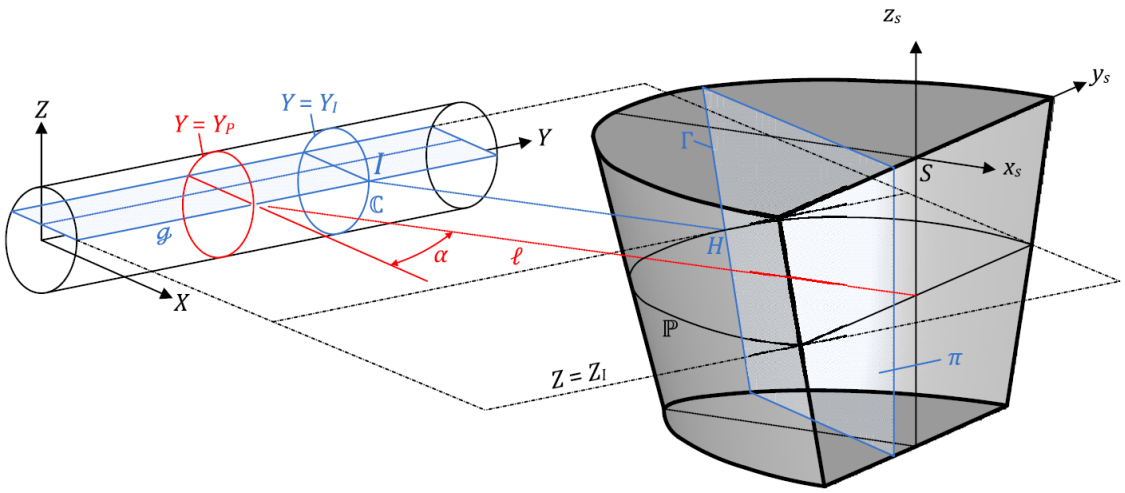

Figure 4.11: Collision configuration for an impact on a horizontal tubular member

$\mathbb{P}$ being the intersection curve between the stem and the horizontal plane located at $Z = Z_I$, it is possible to find a point H such that the tangent line to $\mathbb{P}$ is parallel to the horizontal Y axis. Fig. 4.11 shows that when the ship is moving along the line l, the points H and I tend to come closer and finally occupy the same position at the beginning of the penetration. At this moment, $\mathbb{P}$ is tangent to the generator g of the tubular member and Fig. 4.12(a) presents the corresponding configuration in the horizontal plane $Z = Z_I$.

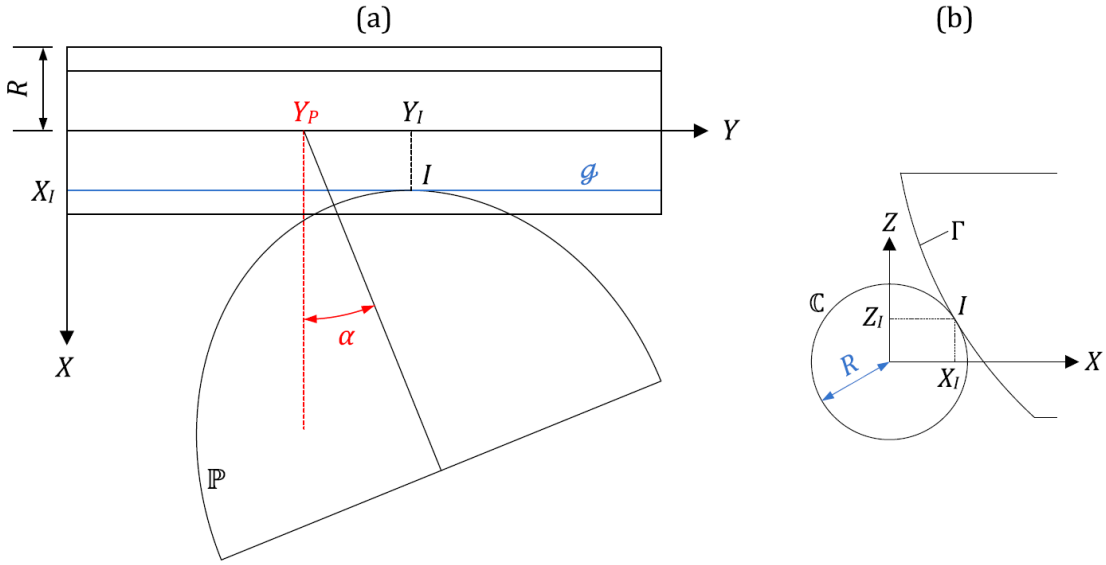

Figure 4.12: Initial position of the stem in a horizontal and in a vertical plane

Let us also consider the vertical plane π parallel to (X, Z) and passing through H. The intersection curve Γ between this plane and the stem is not necessarily a straight line, unless $\alpha = 0$. Similarly, when the striking vessel travels along the line l, Γ comes closer to the ring $\mathbb{C}$ of the tubular member and touches $\mathbb{C}$ at point I at the beginning of the impact (Fig. 4.12(b)).

Fig. 4.12 shows that closed-form solutions for Y_I, Z_I and X_I may be found by imposing a tangency condition between $\mathbb{P}$ and g, but also between Γ and $\mathbb{C}$. Since the resulting mathematical expressions are quite complex, they are solved numerically by using a Newton-Raphson method.

As the crushing process is concerned, although the impact on a horizontal cylindrical member can be treated similarly than the vertical one (Section 4.3), it is important to account for some particularities. For a given penetration δ, the relative position between the ship and the tubular member is depicted in Fig. 4.12. Considering the horizontal plane $Z = Z_I$, Fig. 4.12(a) shows that the current position I' of point I is located at the ordinate $Y_I - \delta \sin\alpha$ and that the displacement of $\mathbb{P}$ along the X axis is only $\delta \cos\alpha$. Consequently, the collision process may be formally modelled by considering that the tubular member section located in the vertical plane $Y = Y_I \sin\alpha$ is simply crushed by the curve Γ with a penetration of $\delta \cos\alpha$, as illustrated in Fig. 4.12(b).

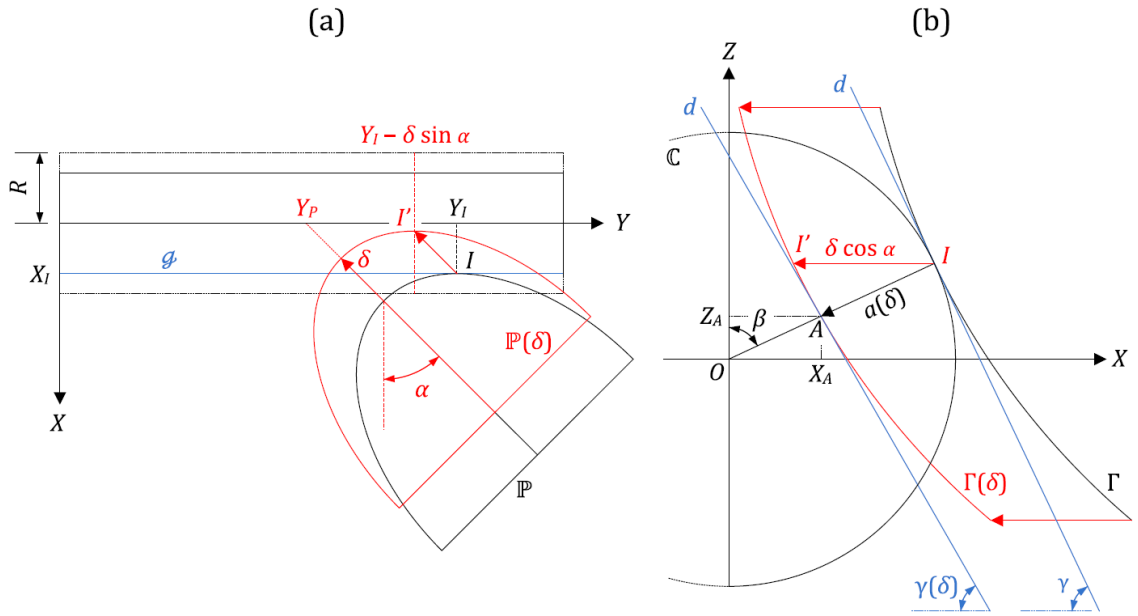

Figure 4.13: Relative position of the stem and the tube for a given penetration

Comparing Fig. 4.13(b) with Fig. 4.7(a), the two situations are seen to be nearly similar, but this time, the coordinates (X_A, Z_A) of point A have to be derived by calculating the intersection of Γ with the straight line OI. Similarly, the inclination angle γ has also to be found by considering the tangent line d to the curve Γ. The determination of X_A, Z_A and γ may be achieved by assuming that the stem is sufficiently large to consider Γ as a straight line and therefore very close to d. Consequently, as γ is now constant for all values of δ and equal to the initial inclination β, we simply have the following relations:

$$\gamma = \beta = \arctan(X_I/Z_I) \qquad ; \qquad X_A = X_I - \delta \cos\alpha \sin^2\beta \tag{4.31}$$

in which the coordinates (X_I, Z_I) are determined from the initial position of the striking vessel. This result allows for the evaluation of the crushing penetration: $a(\delta) = |(X_I - X_A)/\sin\beta|$.

Once γ and $a(\delta)$ have been obtained, it is possible to define how the tubular member cross-section located in the plane $Y = Y_I - \delta \sin\alpha$ is likely to deform. To do so, we can imagine that the deformation pattern of Fig. 4.7(b) is supposed to be still valid, but this time γ and X_A are evaluated by considering Eq. 4.31 instead of Eqs. 4.3 and 4.4. The three parameters R_1, R_2 and ψ used for characterising the crushed section are then given by Eqs. 4.9, 4.7 and 4.10 respectively.

4.4.2 Definition of the displacement field

As the deformation mechanism of the ring located in the vertical plane $Y = Y_I - \delta \sin\alpha$ is formally identical to the one considered for the case of a vertical tubular member, the displacement field $w(\theta, \delta)$ affecting this cross-section is the same than the one depicted in Fig. 4.8(a).

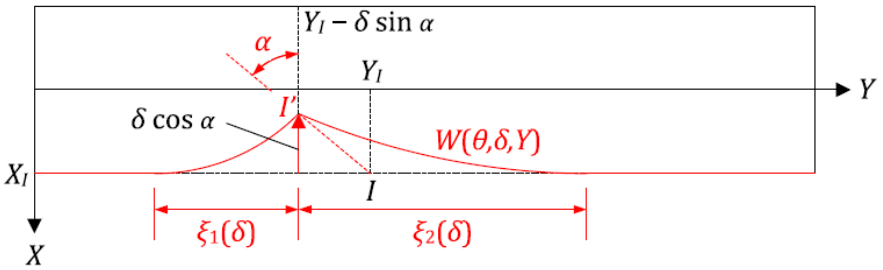

Figure 4.14: Extrapolation of the displacement field for any section located along the Y axis

Therefore, Eq. 4.12 still holds for deriving $w(\theta, \delta)$, but the extrapolation described by Eq. 4.13 to get the velocity $\dot{W}(\theta, \delta, Y)$ over the entire cylindrical member is not valid any more. Indeed, if we refer to Fig. 4.14, the formulas given in Eq. 4.13 have to be modified in the following way:

$$\begin{aligned}
&\dot{W}(\theta,\delta,y) = 0 && \text{if } Y \in [0; Y_I - \delta\sin\alpha - \xi_1(\delta)] \\
&\dot{W}(\theta,\delta,y) = \dot{w}(\theta,\delta)\left(1 + \tfrac{Y - Y_I + \delta\sin\alpha}{\xi_1(\delta)}\right) && \text{if } Y \in [Y_I - \delta\sin\alpha - \xi_1(\delta); Y_I - \delta\sin\alpha] \\
&\dot{W}(\theta,\delta,y) = \dot{w}(\theta,\delta)\left(1 - \tfrac{Y - Y_I + \delta\sin\alpha}{\xi_2(\delta)}\right) && \text{if } Y \in [Y_I - \delta\sin\alpha; Y_I - \delta\sin\alpha + \xi_2(\delta)] \\
&\dot{W}(\theta,\delta,y) = 0 && \text{if } Y \in [Y_I - \delta\sin\alpha + \xi_2(\delta); L]
\end{aligned} \tag{4.32}$$

Here again, ξ_1 and ξ_2 are two parameters that will be fixed by minimising the crushing resistance, but it is already clear that we should have $\xi_1 \leq Y_I - \delta\sin\alpha$ and $\xi_2 \leq L - Y_I + \delta\sin\alpha$.

4.4.3 Local crushing resistance

The evaluation of the crushing resistance may be achieved by following the procedure detailed in Section 4.3.3. The tubular member may also be considered as a set of horizontal generators slightly connected to vertical circular rings (Fig. 4.15), so that the total crushing energy rate $\dot{E}$ is still given by Eq. 4.14.

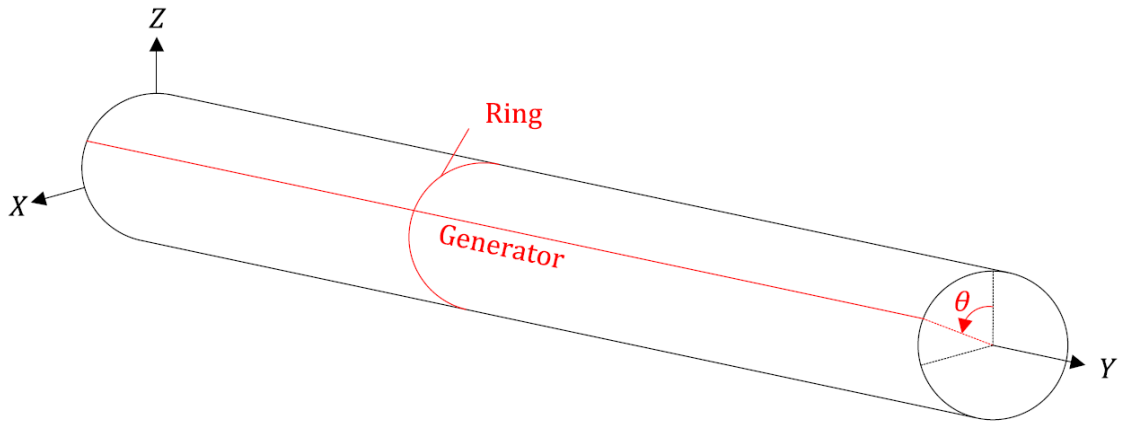

Figure 4.15: Ring and generator of a horizontal tubular member

Furthermore, as $w(\theta, \delta)$ is defined in a similar way than for a vertical tubular member, the mathematical derivation of $\dot{E}_b$ leads again to Eq. 4.15 - 4.17. The interpolation 4.18 to get the total contribution of the rings $\dot{E}_r$ is therefore still valid, as it is done in accordance with Fig. 4.14. Similarly, the total contribution $\dot{E}_g$ of the generators is also given by Eq. 4.21 and Eq. 4.22 is also used to get $\dot{E}$. Once the internal energy has been calculated, the virtual work principle is applied. This latter states that $\dot{E}$ equals the external work rate of the crushing resistance $P_h(\delta)$. As depicted in Fig. 4.13(b), for a given penetration δ, the contact point is moving from I to A, so that the corresponding work rate performed by $P_l(\delta)$ is simply $P_l(\delta)\dot{a}(\delta)$. Therefore, by accounting for Eq. 4.31, we have:

$$\begin{aligned} P_l(\delta)\dot{a}(\delta) &= \dot{E}_b \frac{\xi_1 + \xi_2}{2} + \left(\frac{1}{\xi_1} + \frac{1}{\xi_2}\right) \dot{E}'_m \\ \Leftrightarrow P_l(\delta) &= \left(E_b \frac{\xi_1 + \xi_2}{2} + \left(\frac{1}{\xi_1} + \frac{1}{\xi_2}\right) E'_m\right) \Big/ \sin\beta \cos\alpha \end{aligned} \tag{4.33}$$

The derivation of ξ_1 and ξ_2 is achieved by minimising Eq. 4.33, so Eq. 4.24 have to be corrected to account for the obliquity of the impact:

$$\begin{aligned} \xi_1(\delta) &= \min\left(\sqrt{E'_m/E_b}; Y_I - \delta \sin\alpha\right) \\ \xi_2(\delta) &= \min\left(\sqrt{E'_m/E_b}; L - Y_I + \delta \sin\alpha\right) \end{aligned} \tag{4.34}$$

This Eq. 4.34 may be used in conjunction with Eqs. 4.18, 4.21 and 4.33 to get $P_l(\delta)$, but this has to be done in accordance with the particularities detailed in Eq. 4.31 for $\zeta = 0$.

4.4.4 Global crushing resistance

The derivation of the resistance $P_g(\delta)$ during the global deforming mode for a horizontal tubular member can be performed by following the same procedure than the one described in Section 4.3.4. For a given value of δ, the plastic mechanism related to the overall motion of the

tubular member is depicted in Fig. 4.16(a), where the central plastic hinge is also characterised by a lower plastic bending moment $\xi(\delta)M_0$.

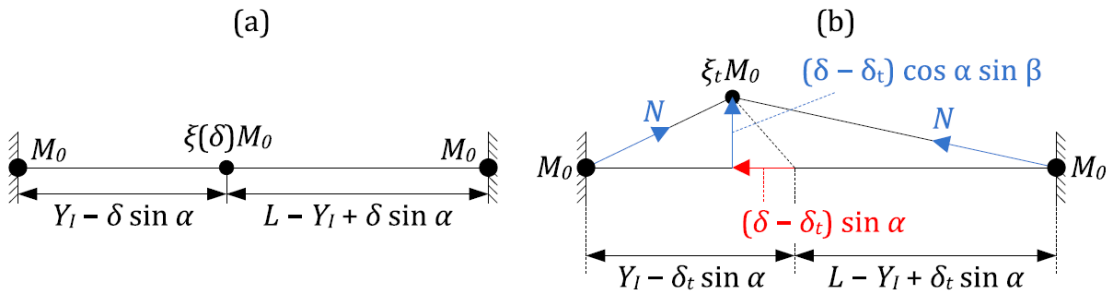

Figure 4.16: Global plastic mechanism for a horizontal tubular member

As for the case of a vertical tubular member, the reduction coefficient $\xi(\delta)$ may be found by applying Eq. 4.26, but we should account here for the particular definition of $a(\delta)$ as detailed in Eq. 4.31:

$$\xi(\delta) = \frac{1}{2}\left(\left(\frac{\delta \cos\alpha \sin\beta}{2R}\right)^2 - 1\right)\left(\frac{\delta \cos\alpha \sin\beta}{2R} - 2\right) \tag{4.35}$$

Similarly, for a given value of δ, the global resistance required to activate the plastic mechanism of Fig. 4.16(a) can be calculated by modifying Eq. 4.27 to account for the inclination angle α. Therefore, in Eq. 4.27, L_1 and L_2 simply have to be replaced by $Y_I - \delta \sin\alpha$ and $L - Y_I + \delta \sin\alpha$ to get the following result:

$$P_g(\delta) = \frac{L \sin\beta}{(Y_I - \delta \sin\alpha)(L - Y_I + \delta \sin\alpha)}(1 + \xi(\delta))M_0 \tag{4.36}$$

The transition from local to global deforming mode occurs when $\delta = \delta_t$. At this moment, the local crushing resistance is equal to the global one calculated by applying Eq. 4.36:

$$P_l(\delta_t) = P_g(\delta_t) = \frac{L \sin\beta}{(Y_I - \delta_t \sin\alpha)(L - Y_I + \delta_t \sin\alpha)}(1 + \xi(\delta_t))M_0 \quad ; \quad \xi_t = \xi(\delta_t) \tag{4.37}$$

which means that the value reached by $P_l(\delta)$ is sufficient for activating the global mode depicted in Fig. 4.16(a). Once the transition has occurred, i.e. when $\delta > \delta_t$, the resistance $P_g(\delta)$ is no longer given by Eq. 4.36 because normal tensile forces N appear inside the two arms of the deforming beam (Fig. 4.16(b)). In fact, when the structure is forced into the overall motion, an axial lengthening is added to the bending effects. In the vertical case, the main difficulty is to account for the oblique trajectory followed by the vessel ($\alpha \neq 0$). This problem has been treated by some authors, such as Tin Loi [10] or Buldgen [2]. By following the approximate theoretical

procedure described in Ref. [2] for example, it is possible to establish the subsequent results:

$$
\begin{aligned}
P_g(\delta) &= \frac{L\sin\beta}{l_1(\delta)l_2(\delta)}\left(M_0(1+\xi_t)\left(1-\frac{N(\delta)^2}{N_0^2}\right)+N(\delta)(\delta-\delta_t)\cos\alpha\sin\beta\right) \\
\text{with: } N(\delta) &= \frac{N_0^2}{2(1+\xi_t)M_0}\frac{(\delta-\delta_t)\cos\alpha\sin\beta}{2}\left(1+\frac{l_1(\delta)l_2(\delta)L}{l_1(\delta_t)l_2(\delta)^2+l_2(\delta_t)l_1(\delta)^2}\right) \\
l_1(\delta) &= Y_I-\delta\sin\alpha \quad ; \quad l_1(\delta) = L-Y_I+\delta\sin\alpha
\end{aligned}
\tag{4.38}
$$

As a conclusion, the crushing resistance $P_h(\delta)$ of a horizontal tubular member during the collision may be derived in the same way than Eq. 4.25, but $P_l(\delta)$ and $P_g(\delta)$ have to be calculated by applying Eq. 4.33 and Eq. 4.38 respectively.

4.5 Impact on an oblique tubular member

4.5.1 Crushing resistance

It is quite difficult to handle with the mathematical expressions of the stem and of the tubular member in the oblique case. Indeed, when $\zeta \neq 0$ and $\zeta \neq \pi/2$, it is difficult to postulate a consistent displacement field $W(\theta, \delta, y)$ representative of the cross-section deformation during the crushing process. The main difficulty comes from the fact that the rings have an elliptic shape and not a circular one (Fig. 4.17), so it is not easy to imagine how this section is likely to deform when it is impacted by the stem.

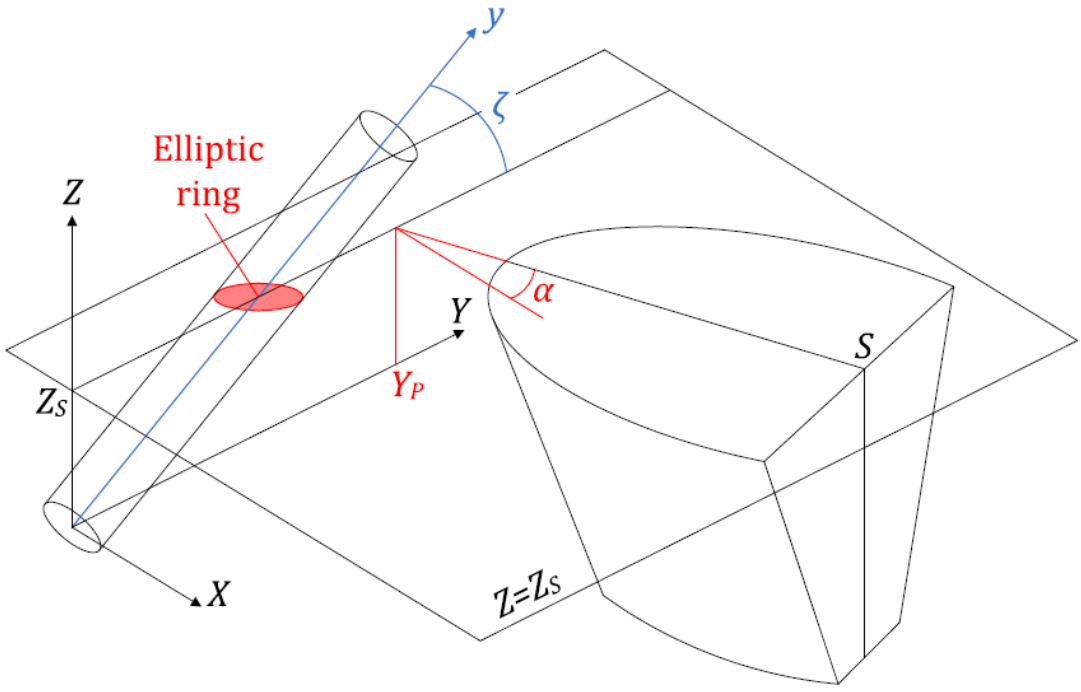

Figure 4.17: Configuration of an oblique impact occurring on an inclined tubular member

In this thesis, this issue is not solved analytically. Nevertheless, in order to evaluate the crushing resistance $P(\delta)$ in the case of an oblique tubular member, we will simply admit that this one can be calculated by performing a linear interpolation between the two particular solutions $P_v(\delta)$ and $P_h(\delta)$ derived in Sections 4.3 and 4.4. In other words, we postulate that:

$$P(\delta) = \left(1 - \frac{2\zeta}{\pi}\right) P_h(\delta) + \frac{2\zeta}{\pi} P_v(\delta) \tag{4.39}$$

4.5.2 Numerical validation

In order to validate the mathematical developments exposed in the previous Sections, we can check if the theoretical prediction $P(\delta)$ given by Eq. 4.39 is in accordance with numerical solutions. To do so, some numerical simulations are carried out using the FE software *LS-DYNA*. Two different tubular members, whose properties are listed in Table 4.1, are studied. For the first one, typical dimensions of a jacket leg are considered, while the second may be assimilated to a classical brace. Only two different inclinations (60° and 90°) are considered for the leg because it is quite uncommon to have $\zeta < 60°$ for this kind of structure. Similarly, for the brace, it seems reasonable to keep ζ lower than 45°. Both tubular members are supposed to be perfectly restrained at their extremities.

Table 4.1: Properties of the two tubular members used for the numerical simulations

Property	Notation	Unit	Leg	Brace
Radius	R	m	0.65	0.35
Length	L	m	10	8
Thickness	t_p	m	0.038	0.0127
Inclination	ζ	deg	$60; 90$	$0; 30; 45$

For the purpose of numerical simulations, the leg and the brace are respectively modelled with 9100 and 7040 Belytschko-Tsay shell elements [1, 5]. The mesh is regular, with an average element dimension of 5 $cm \times 5$ cm. The elastic-plastic material behaviour is described by the bilinear stress-strain curve depicted in Fig. 4.18 and by using the properties listed in Table 4.2. At the end of the elastic phase (i.e. for $\sigma = \sigma_0$), the material is submitted to a slow hardening characterised by the tangent modulus E_T. In reality, this phase ends by the rupture of the material, which is not considered in the present work.

Table 4.2: Material law used for the numerical simulations

Property	Notation	Unit	Value
Young modulus	E	MPa	$210,000$
Poisson ratio	ν	$-$	0.3
Flow stress	σ_0	MPa	240
Tangent modulus	E_T	MPa	$1,018$

These two tubular members are impacted by a stem assumed to be perfectly rigid. The main dimensions of the striking vessel are presented in Table 3.2.

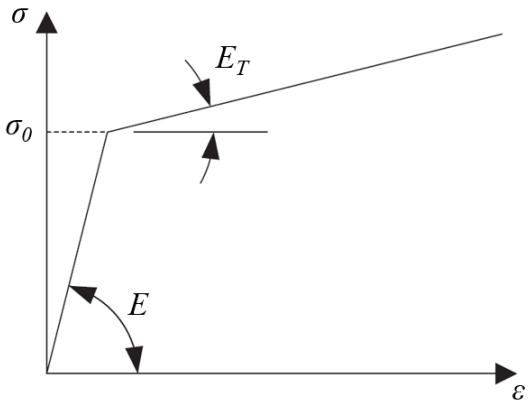

Figure 4.18: Stress-strain curve used for the numerical simulations

The relative position between the stem and the tubular member is defined by the parameters $(Y_P; Z_S; \alpha)$, as depicted in Fig. 4.4. In order to check the validity of Eq. 4.39, different configurations associated with various values have been investigated.

4.5.2.1 Impact on a leg

A lot of numerical simulations were performed in order to assess the crushing resistance of a leg for different values of ζ, α, Y_P and Z_S. Five scenarios described in Table 4.3 are presented here. For the case of a vertical tubular member ($\zeta = 90°$), there is no need to specify a value for because the impact problem is axisymmetric.

Table 4.3: Collision configurations for an impact on a leg

Scenario	ζ $[deg]$	α $[deg]$	Y_P $[m]$	Z_S $[m]$
1.1	60	0	3	6
1.2	60	30	1	6
1.3	60	45	-1	5
2.1	90	/	0	6
2.2	90	/	4	6

For each scenario, the curves showing the evolution of $P(\delta)$ as predicted by Eq. 4.39 are compared in Figs. 4.19 to 4.23 together with the ones calculated by *LS-DYNA*. The simulations were arbitrarily stopped after reaching a penetration of 1 m. These Figures show a quite good accordance between numerical and analytical results. Moreover, in almost all cases, the analytical derivation was found to be conservative as it tends to underestimate the crushing resistance. In fact, the maximal discrepancy was observed for scenario 2.1 (Fig. 4.22), for which an underestimation of 25% of $P(\delta)$ was found when $\delta = 1$ m. This may be explained by the fact that the theoretical model tends to activate the global mode a bit too early.

As shown by some of the above Figures, the slope of the analytical curve may change suddenly, reflecting the transition from the local to the global deforming mode. Indeed, it is worth recalling that the theoretical models first postulate a local crushing of the tubular member. During this phase, the rigidity is quite important and explains why the force is rapidly growing.

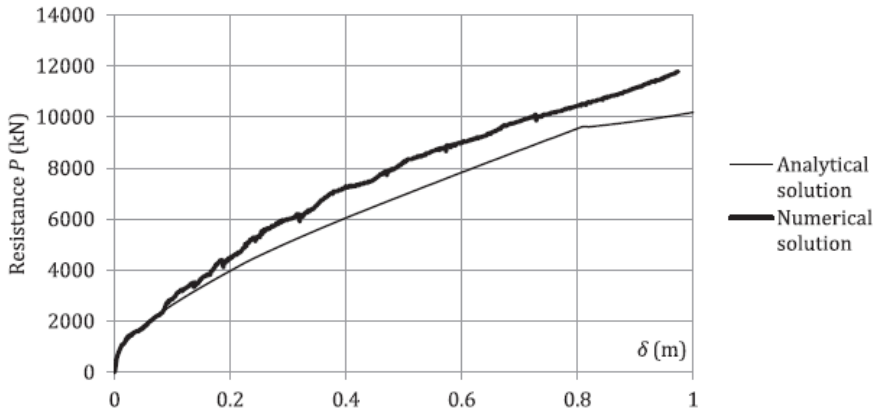

Figure 4.19: Comparison of the analytical leg resistance to the numerical one for scenario 1.1

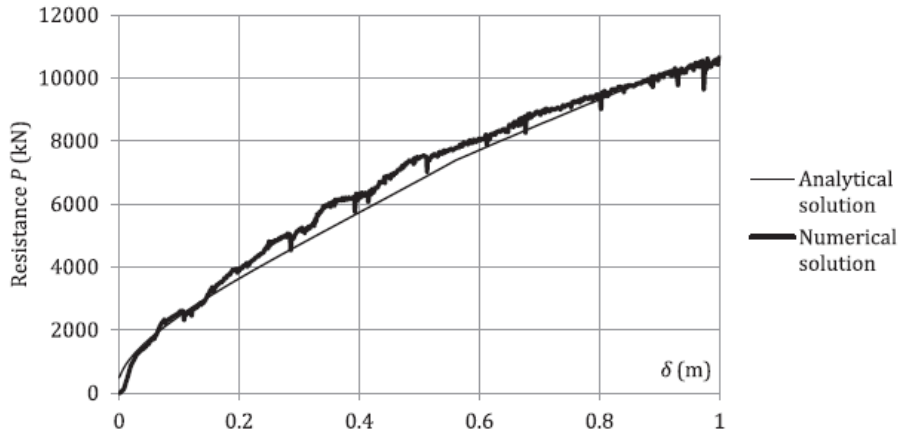

Figure 4.20: Comparison of the analytical leg resistance to the numerical one for scenario 1.2

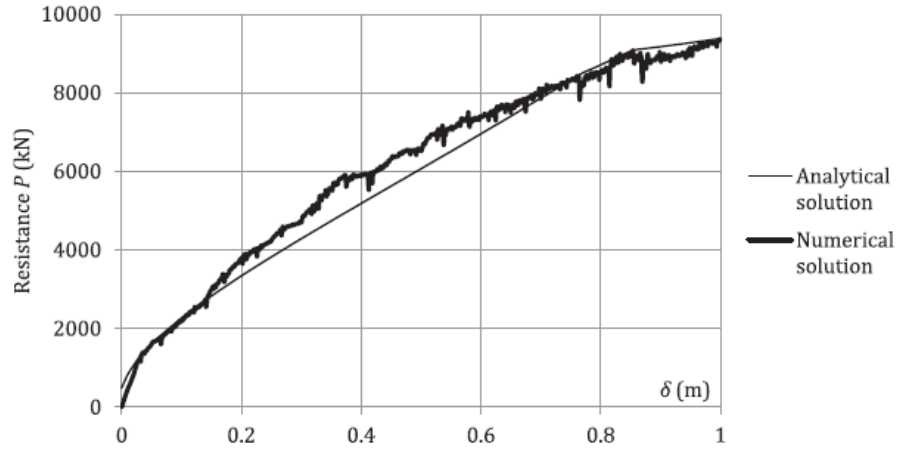

Figure 4.21: Comparison of the analytical leg resistance to the numerical one for scenario 1.3

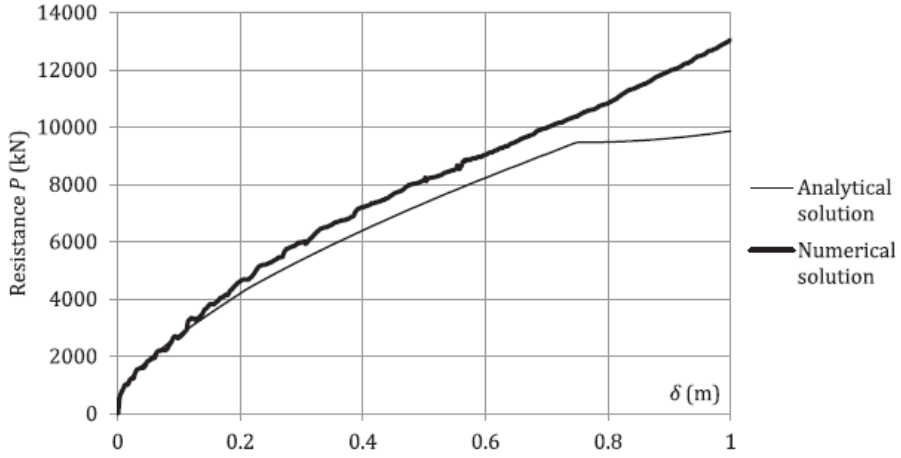

Figure 4.22: Comparison of the analytical leg resistance to the numerical one for scenario 2.1

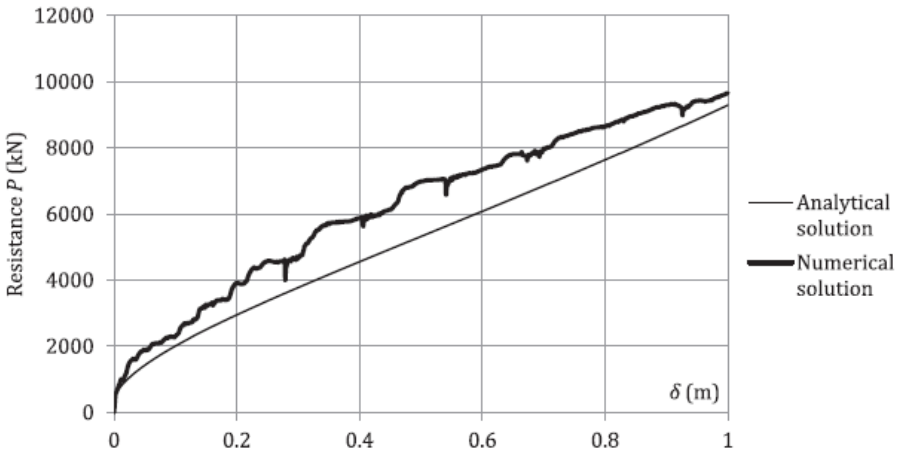

Figure 4.23: Comparison of the analytical leg resistance to the numerical one for scenario 2.2

This denting process ends with the development of an overall bending motion of the tubular member, which is a more flexible deformation process and is responsible for an inflection of the resistance curve. This change in the tube behaviour may be illustrated by Fig. 4.24, which presents some results obtained numerically with *LS-DYNA*. Fig. 4.24(a) shows the deformation of a tubular member cross-section located near the initial contact point. For a given penetration δ of the striking vessel, a global backward movement (quantified by δ_g) occurs. On Fig. 4.24(b), the total indentation δ is quite small, so the crushing process is only characterised by a local denting δ_l, the rear edge of the tube remaining straight. Fig. 4.24(c) is obtained for a larger value of δ and shows that the global mode has already been activated.

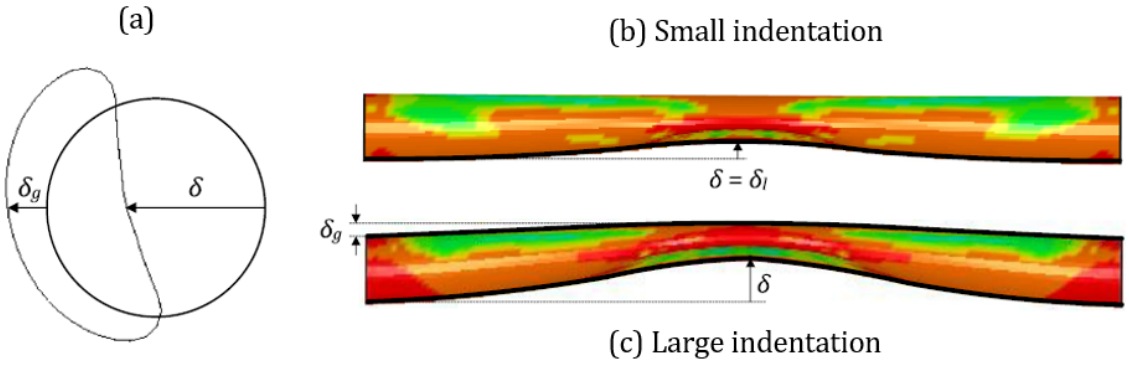

Figure 4.24: Local and global deforming modes

4.5.2.2 Impact on a brace

We also performed a great number of collisions involving the brace and the vessel described above. The results obtained for the scenarios listed in Table 4.4 are presented. The corresponding curves are depicted in Figs. 4.25 to 4.27.

Table 4.4: Collision configurations for an impact on a brace

Scenario	ζ $[deg]$	α $[deg]$	Y_P $[m]$	Z_S $[m]$
3	0	45	-1	1
4	30	30	1	5
5	45	0	2	6

As shown by these Figures, the conclusions drawn for a leg are also valid for a brace. Here again, the agreement between analytical and numerical solutions seems to be satisfactory. Moreover, in all cases, the theoretical approximation tends to be conservative. The maximal discrepancy is equal to 25% and is observed for scenario 3 (Fig. 4.25).

As for the case of an impact on a leg (Section 4.5.2.1), the sudden slope change appearing on the analytical curves is also due to the theoretical transition from local to global resisting mode. It is worth noting that this switch is occurring sooner for braces because of a smaller radius R compared with the legs one.

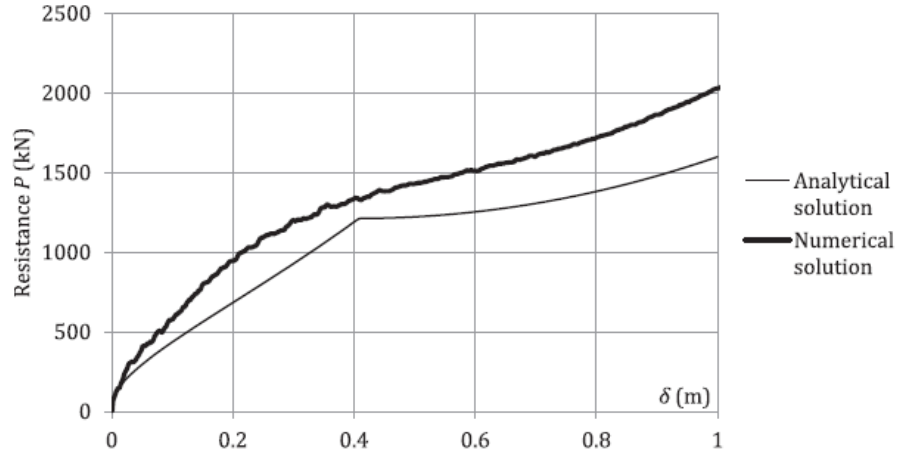

Figure 4.25: Comparison of the analytical brace resistance to the numerical one for scenario 3

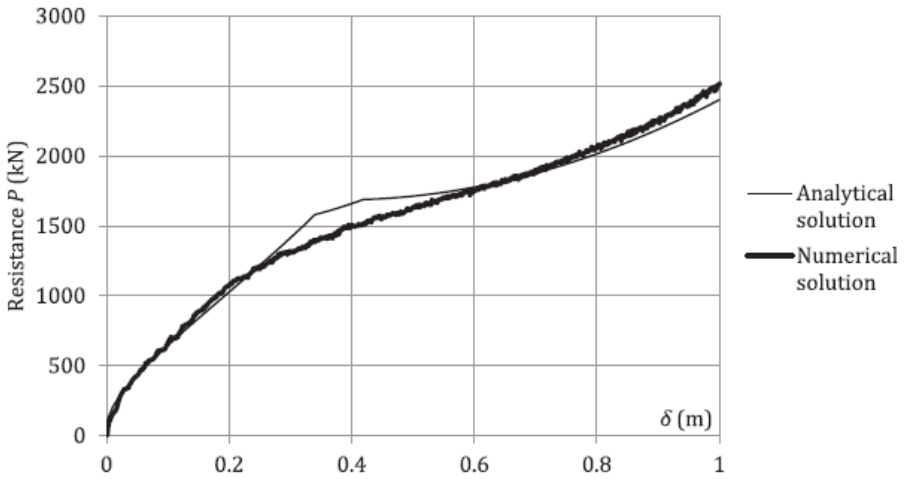

Figure 4.26: Comparison of the analytical brace resistance to the numerical one for scenario 4

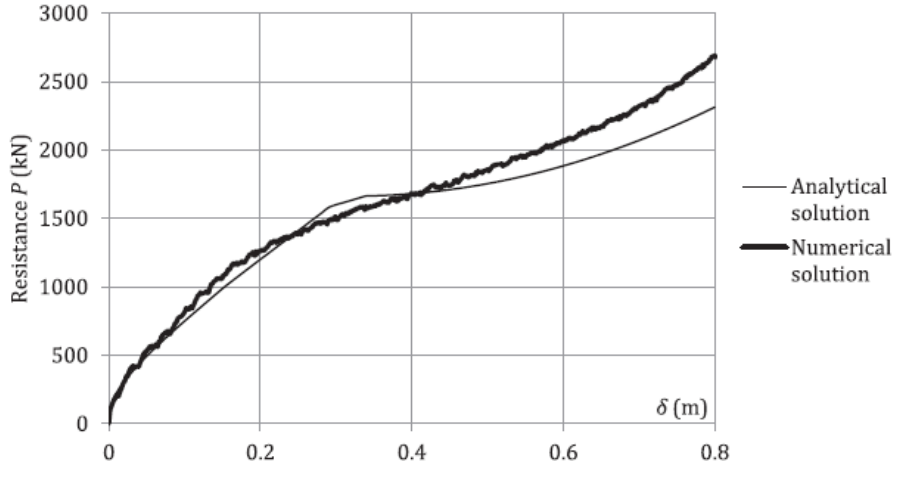

Figure 4.27: Comparison of the analytical brace resistance to the numerical one for scenario 5

4.6 Impact on a full-scale jacket

In order to have a better insight of what happens during an impact on an OWT jacket, the FE software *LS-DYNA* was used to simulate a collision occurring near the top of the structure (Fig. 4.28). The tubular members constituting the jacket described in Section 3.2.2 are modelled with Belytschko-Tsay shell elements [1, 5] associated with an elastic-plastic material law described by a similar curve than the one of Fig. 4.18. The assumptions related to the jacket model are presented in Section 3.4.1.

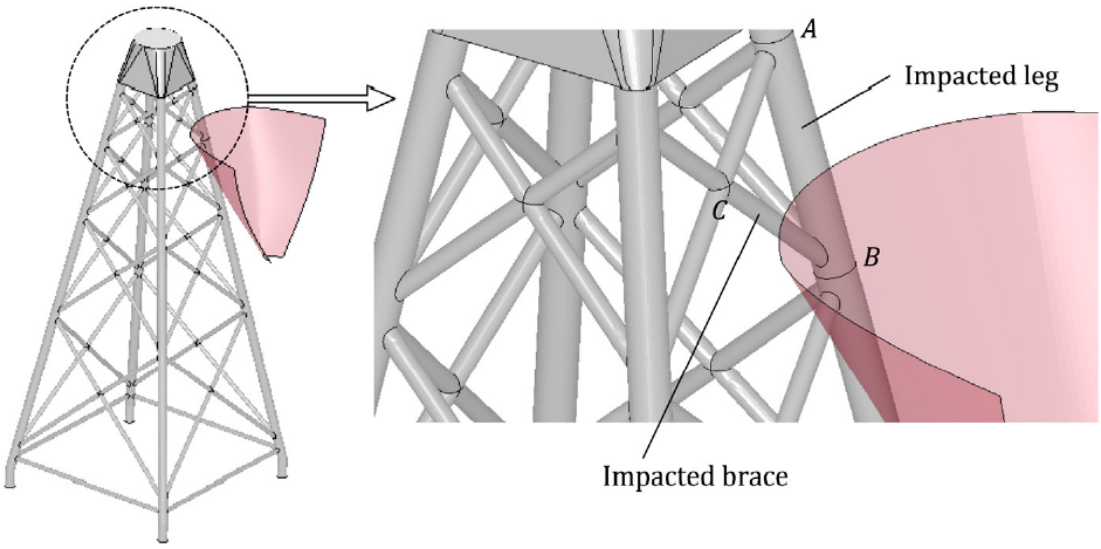

Figure 4.28: Collision scenario for the impact on a full-scale jacket

The striking stem is considered as being perfectly rigid, which implies that all the collision energy is dissipated by the support. Its total mass is close to $5,000$ tons and two different initial velocities of 2 m/s and 5 m/s are considered for the simulations.

For an initial striking velocity of 2 m/s, only the leg is impacted by the stem (see Fig. 4.28). In order to obtain a rapid estimation of the crushing resistance, the simplified method described previously is applied by assuming that the collision takes place on an individual tubular member AB characterised by the geometrical parameters introduced in Fig. 4.4. Applying the above-mentioned mathematical approach to this isolated cylindrical member, the resistance $P(\delta)$ is assessed for each value of the vessel penetration δ. This is achieved by applying the interpolation Eq. 4.39 and leads to the analytical curve shown Fig. 4.29(b). Similarly, the internal energy dissipated by the tubular member is also computed, as depicted in Fig. 4.29(a). If we compare the present analytical curves with the ones given by *LS-DYNA*, we see from Fig. 4.29 that the agreement is quite satisfactory. Even if the resistant force is underestimated at the end of the simulation, the energy dissipation is almost correctly reproduced.

Let us now investigate the case of an initial striking velocity of 5 m/s. In such a scenario, both the leg and the brace of Fig. 4.28 are impacted by the rigid stem. Once again, these tubular members can be seen as isolated elements and Eq. 4.39 may be applied to get an approximation

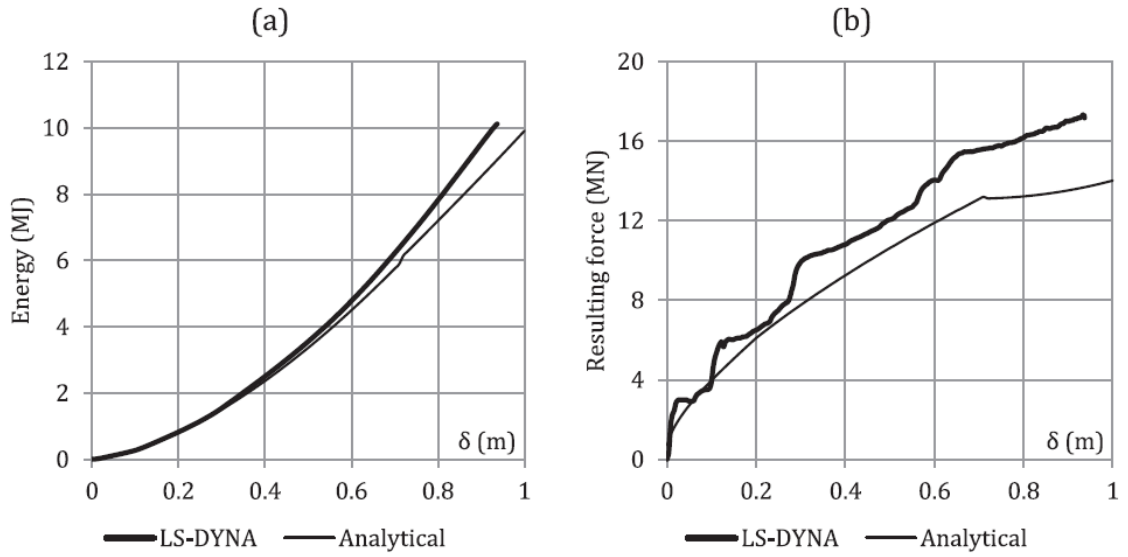

Figure 4.29: Comparison of (a) the internal energy and (b) the total crushing force obtained analytically and numerically for an initial velocity of 2 m/s

of the collision resistance. Doing so leads to the curves presented in Fig. 4.30. This time, there is a large discrepancy with the numerical solution given by *LS-DYNA*, as the theoretical model drastically overestimates the energy dissipation and the collision resistance.

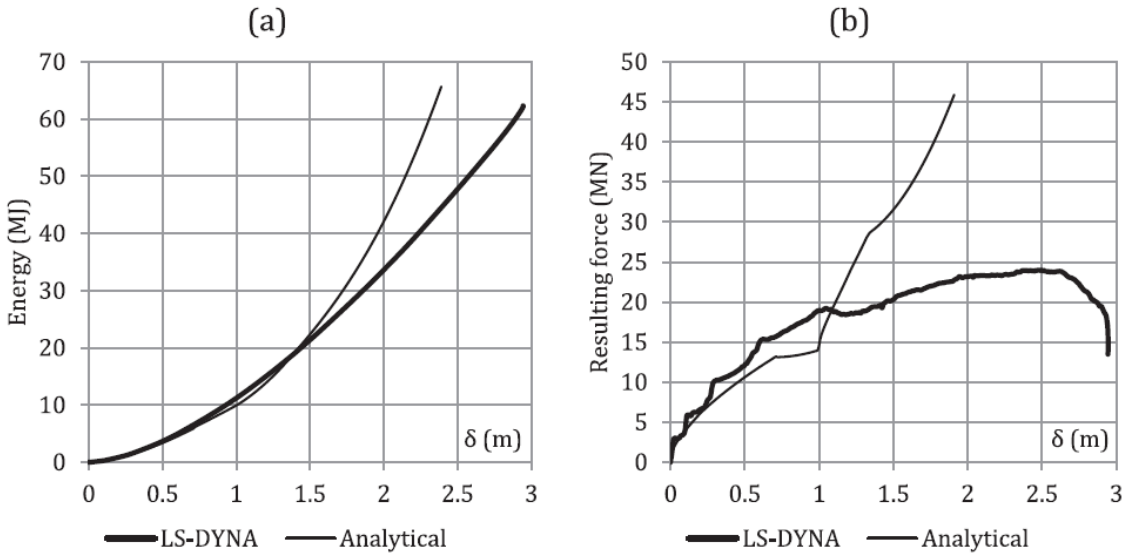

Figure 4.30: Comparison of (a) the internal energy and (b) the total crushing force obtained analytically and numerically for an initial velocity of 5 m/s

This important discrepancy may be explained by the boundary conditions assumed for the analytical derivation. Indeed, as detailed in the previous Sections, we consider that both extremities of the tubular member are strongly clamped and therefore do not move during the collision. In other words, the hypothesis is made that the nodes A, B and C of Fig. 4.28 are fixed. Nevertheless, this is obviously not the case as the jacket is also forced into an overall

flexural and torsional movement (Fig. 4.31). For the smaller velocity of 2 m/s, these motions remains quite small, which explains the quite good agreement.

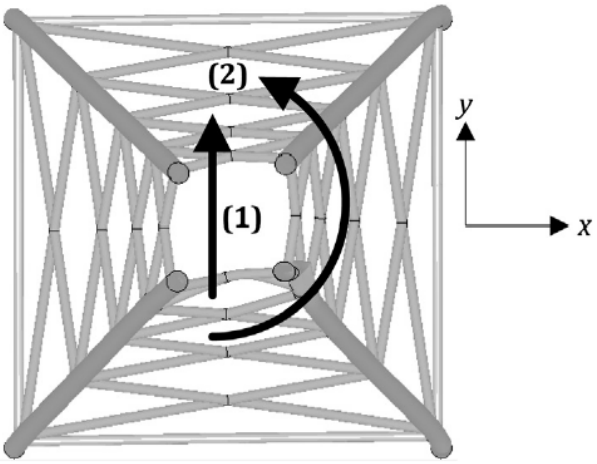

Figure 4.31: Overall flexural (1) and torsional (2) movement of the jacket for a velocity of 5 m/s

Please note that, for a ship penetration up to 1 m, the FE curves computed for initial velocities of 2 m/s (Fig. 4.29) and 5 m/s (Fig. 4.30) are similar, validating the assumption of neglecting inertia effects and developing quasi-static formulations.

4.7 Extension to bulb-tubular member collision

4.7.1 Collision description

A jacket tubular member may also be impacted by the bulb of a striking bulbous bow. The analytical developments presented above have to be adapted to this different colliding shape and then validated.

The bulb is described in Section 3.2.1 and its relative position with regard to the impacted tubular member can be seen in Fig. 4.32.

In Fig. 4.4, the angles ϕ_b and ψ_b are used to define the colliding bow. Equivalent angles ϕ_{bulb} and ψ_{bulb} have to be identified in the case of collisions with a bulb. Therefore, the initial collision point between the bulb and the tubular member has to be computed. This is achieved by decomposing both the bulb and the tubular member into several horizontal slices, as shown in Fig. 4.33. The bulb is considered to be initially far enough from the tubular member and is then displaced by small steps until contact occurs for one of the defined slices.

Both the bulb and the tubular member have to be expressed in a common frame (X, Y, Z) where Z is the vertical axis and X, Y define a horizontal plane. We denote by $(\Delta X_b, \Delta Y_b, \Delta Z_b)$ and $(\Delta X_c, \Delta Y_c, \Delta Z_c)$ the distance between the bulb reference coordinate system and tubular member coordinate reference system with regard to the common reference coordinate system respectively.

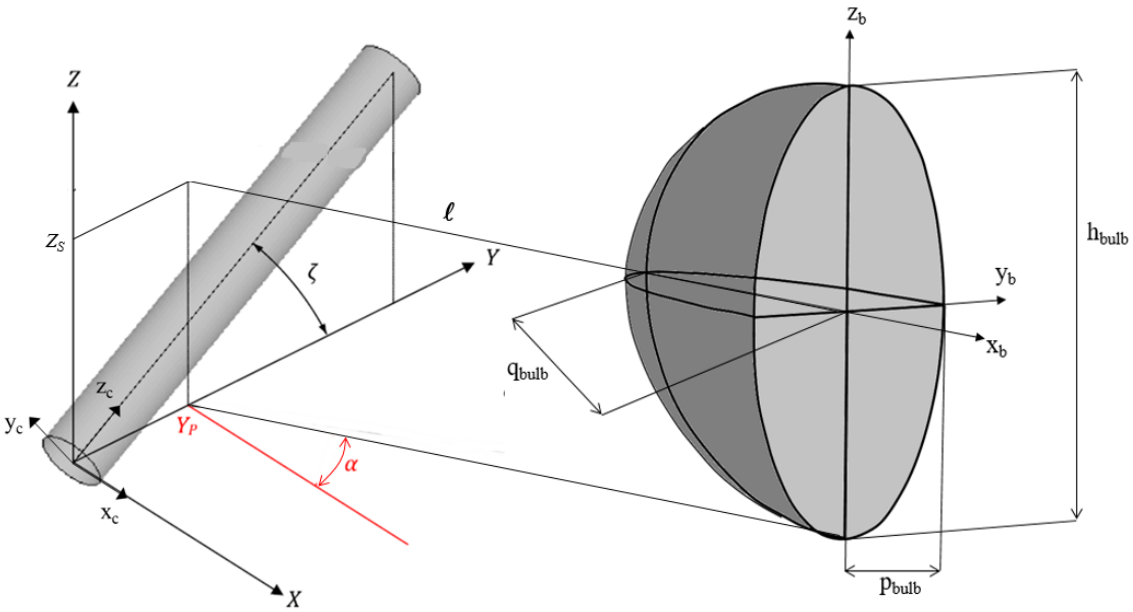

Figure 4.32: Relative position of the striking bulb with respect to the tubular member

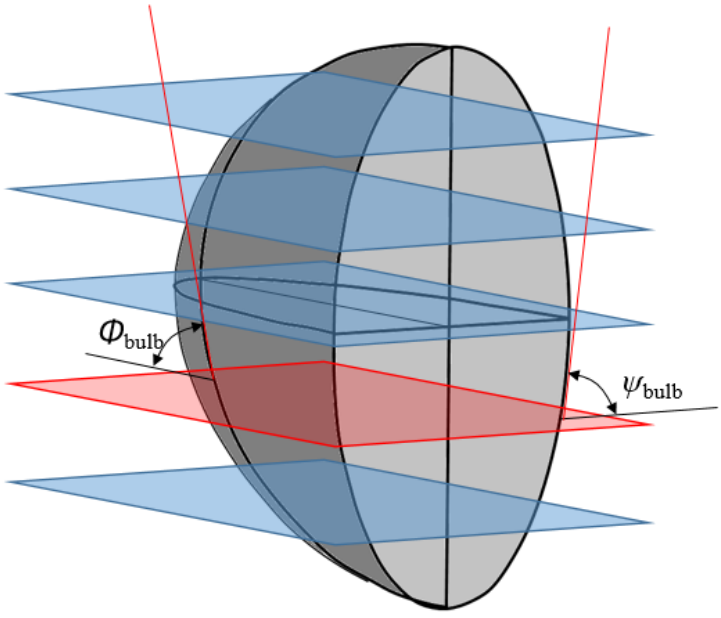

Figure 4.33: Decomposition of the bulb into several slices

For the bulb, it comes:

$$\begin{cases} x_b = (X - \Delta X_b)\cos\alpha_s + (Y - \Delta Y_b)\sin\alpha_s \\ y_b = -(X - \Delta X_b)\sin\alpha_s + (Y - \Delta Y_b)\cos\alpha_s \\ z_b = Z - \Delta Z_b \end{cases} \tag{4.40}$$

and Eq. 3.2 becomes:

$$\begin{aligned} \mathbb{B} \equiv & \left[\frac{(X - \Delta X_b)\cos\alpha_s + (Y - \Delta Y_b)\sin\alpha_s}{q_{bulb}}\right]^2 \\ & + \left[\frac{-(X - \Delta X_b)\sin\alpha_s + (Y - \Delta Y_b)\cos\alpha_s}{p_{bulb}}\right]^2 + \left[\frac{Z - \Delta Z_b}{h_{bulb}/2}\right]^2 - 1 = 0 \end{aligned} \tag{4.41}$$

The tubular member has a coordinate system (x_c, y_c, z_c), with z_c the main axis and x_c being in the horizontal plane defined by X, Y axes. In its local frame, the tubular member expression is:

$$\mathbb{B} \equiv \frac{x_c^2}{R^2} + \frac{y_c^2}{R^2} = 1 \tag{4.42}$$

In the global frame, it comes:

$$\begin{cases} x_c = (X - \Delta X_c)\cos\alpha_e\sin\zeta + (Y - \Delta Y_c)\sin\alpha_e\sin\zeta - (Z - \Delta Z_c)\cos\zeta \\ y_c = -(X - \Delta X_c)\sin\alpha_e + (Y - \Delta Y_c)\cos\alpha_e \\ z_c = (X - \Delta X_c)\cos\alpha_e\cos\zeta + (Y - \Delta Y_c)\sin\alpha_e\cos\zeta + (Z - \Delta Z_c)\sin\zeta \end{cases} \tag{4.43}$$

and Eq. 4.42 becomes:

$$\begin{aligned} \mathbb{C} \equiv & \left[\frac{(X - \Delta X_c)\cos\alpha_e\sin\zeta + (Y - \Delta Y_c)\sin\alpha_e\sin\zeta - (Z - \Delta Z_c)\cos\zeta}{R}\right]^2 \\ & + \left[\frac{-(X - \Delta X_c)\sin\alpha_e + (Y - \Delta Y_c)\cos\alpha_e}{R}\right]^2 - 1 = 0 \end{aligned} \tag{4.44}$$

For each slice, the values of Z is defined by the elevation of the considered slice. The remaining task is to compute X and Y, which is done with a Newton-Raphson method. Those are initiated as X_i and Y_i and are updated according to the following expression until convergence:

$$\begin{Bmatrix} X_{i+1} \\ Y_{i+1} \end{Bmatrix} = \begin{Bmatrix} X_i \\ Y_i \end{Bmatrix} - \begin{bmatrix} \frac{\partial\mathbb{B}}{\partial X} & \frac{\partial\mathbb{B}}{\partial Y} \\ \frac{\partial\mathbb{C}}{\partial X} & \frac{\partial\mathbb{C}}{\partial Y} \end{bmatrix}^{-1} \begin{Bmatrix} \mathbb{B} \\ \mathbb{C} \end{Bmatrix} \tag{4.45}$$

with

$$\begin{aligned}\frac{\partial \mathbb{B}}{\partial X} = 2\frac{(X-\Delta X_b)\cos\alpha_s + (Y-\Delta Y_b)\sin\alpha_s}{q_{bulb}}\frac{\cos\alpha_s}{q_{bulb}} \\ -2\frac{-(X-\Delta X_b)\sin\alpha_s + (Y-\Delta Y_b)\cos\alpha_s}{p_{bulb}}\frac{\sin\alpha_s}{p_{bulb}}\end{aligned} \tag{4.46}$$

$$\begin{aligned}\frac{\partial \mathbb{B}}{\partial Y} = 2\frac{(X-\Delta X_b)\cos\alpha_s + (Y-\Delta Y_b)\sin\alpha_s}{q_{bulb}}\frac{\sin\alpha_s}{q_{bulb}} \\ +2\frac{-(X-\Delta X_b)\sin\alpha_s + (Y-\Delta Y_b)\cos\alpha_s}{p_{bulb}}\frac{\cos\alpha_s}{p_{bulb}}\end{aligned} \tag{4.47}$$

$$\begin{aligned}\frac{\partial \mathbb{C}}{\partial X} = 2\frac{(X-\Delta X_c)\cos\alpha_e\sin\zeta + (Y-\Delta Y_c)\sin\alpha_s\sin\zeta - (Z-\Delta Z_c)\cos\zeta}{R}\frac{\cos\alpha_e\sin\zeta}{R} \\ -2\frac{-(X-\Delta X_c)\sin\alpha_e + (Y-\Delta Y_c)\cos\alpha_e}{R}\frac{\sin\alpha_e}{R}\end{aligned} \tag{4.48}$$

$$\begin{aligned}\frac{\partial \mathbb{C}}{\partial Y} = 2\frac{(X-\Delta X_c)\cos\alpha_e\sin\zeta + (Y-\Delta Y_c)\sin\alpha_s\sin\zeta - (Z-\Delta Z_c)\cos\zeta}{R}\frac{\sin\alpha_e\sin\zeta}{R} \\ +2\frac{-(X-\Delta X_c)\sin\alpha_e + (Y-\Delta Y_c)\cos\alpha_e}{R}\frac{\cos\alpha_e}{R}\end{aligned} \tag{4.49}$$

Once the elevation Z_{FI} of the first contact point is identified, the angles ϕ_{bulb} and ψ_{bulb} are defined as tangent to the bulb at the considered slice (see Fig. 4.33):

$$\begin{aligned}\phi_{bulb} &= \arctan\left(\frac{\partial \mathbb{B}}{\partial Z}\right)_{Z=Z_{FI};Y=0} \\ \psi_{bulb} &= \arctan\left(\frac{\partial \mathbb{B}}{\partial Z}\right)_{Z=Z_{FI};X=0}\end{aligned} \tag{4.50}$$

4.7.2 Numerical validation

Following the same methodology as in Section 4.5.2, several collision scenarios are investigated to validate the analytical developments. The bulb is likely to hit tubular members located lower than the ones impacted by the bow. The impacted elements are therefore longer than the one used in the previous numerical validation, and its properties are given in Table 4.5.

Table 4.5: Properties of the tubular member used for the numerical simulations (bulb impact)

Property	Notation	Unit	Value
Radius/thickness	R/t	$-$	13
Length	L	m	20
Inclination	ζ	deg	$45; 60; 90$

The numerical assumptions are identical to the ones performed for the validations of stem impacts on tubular members and are detailed in Section 4.5.2.

The bulb properties are given in Table 4.6, referring to Fig. 4.32.

Table 4.6: Main dimensions of the striking bulb

Property	Notation	Unit	Value
Elliptic radius 1	p_{bulb}	m	2.5
Elliptic radius 2	q_{bulb}	m	8
Total height	h_{bulb}	m	10

Four collision scenarios are investigated to validate the analytical formulations in case of an impact occurring between a bulb and a tubular member. They are listed in Table 4.7.

Table 4.7: Collision configurations for a bulb impact

Scenario	ζ (deg)	α (deg)	Y_P (m)	Z_S (m)
6.1	90	/	0	13
6.2	90	/	1	10
7	60	30	6	10
8	45	30	6	7

The evolutions of both dissipated energy and crushing force for a maximum penetration of 2 m are plotted in Figs. 4.34 to 4.37.

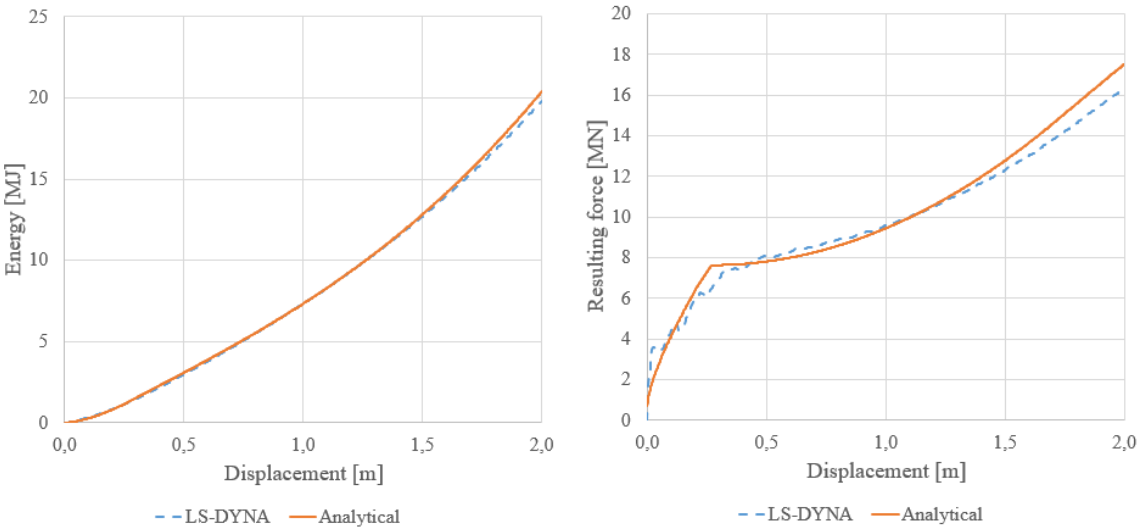

Figure 4.34: Comparison of analytical and numerical results for scenario 6.1

As for bow - tubular members collisions, curves show a good accordance between the numerical and the analytical models. The maximum discrepancy in term of dissipated energy for a penetration of 2 m is 3%, 12%, 19% and 5% for scenarios 6.1, 6.2, 7 and 8 respectively.

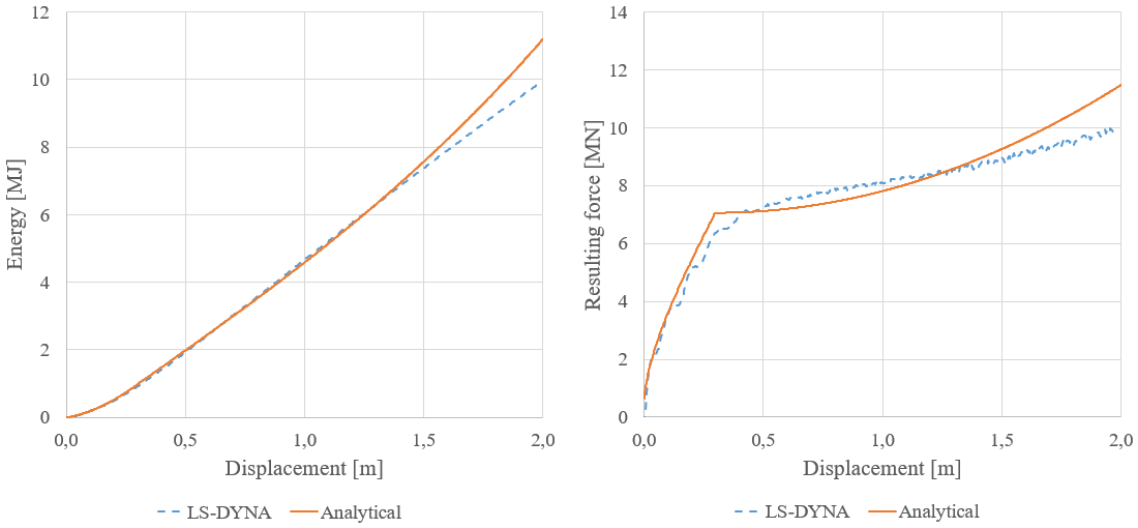

Figure 4.35: Comparison of analytical and numerical results for scenario 6.2

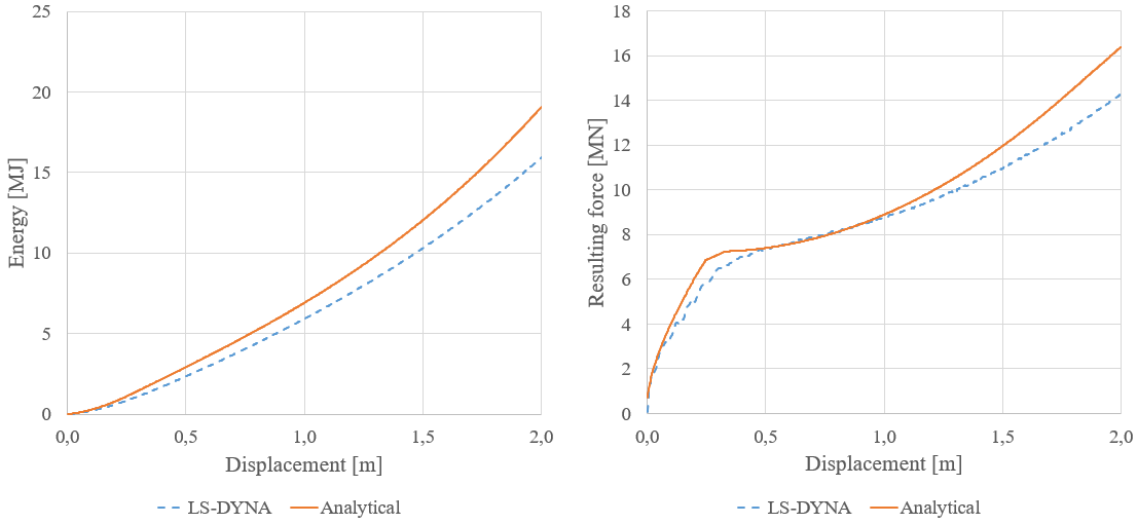

Figure 4.36: Comparison of analytical and numerical results for scenario 7

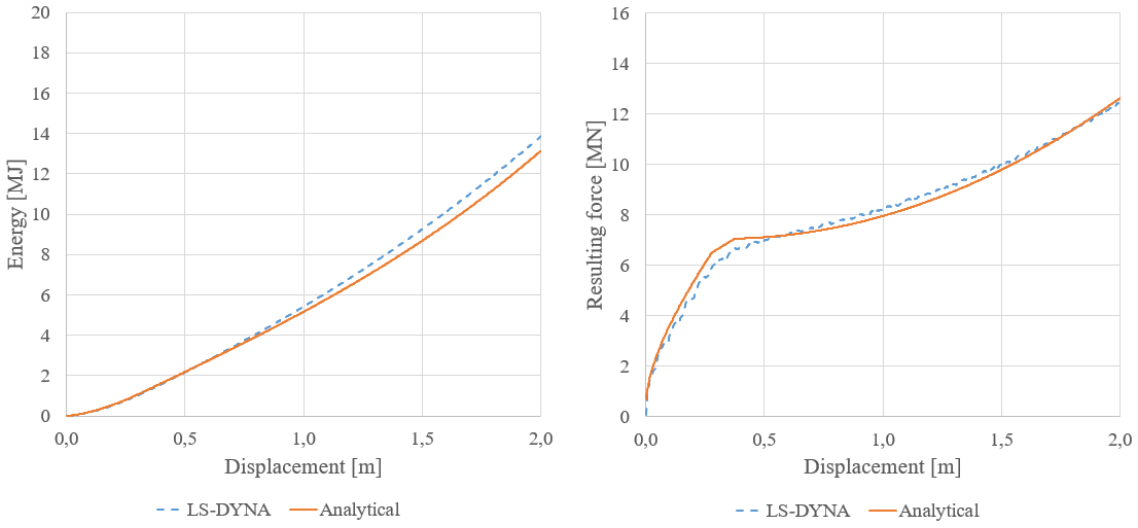

Figure 4.37: Comparison of analytical and numerical results for scenario 8

4.8 Conclusions

In this Chapter, a closed-form expression for evaluating the resistance opposed by an inclined tubular member submitted to a collision with the stem or the bulb of a given ship is developed. This is done by accounting for the shape of the colliding part and for different collision angles.

As a first step, the particular case of an impact occurring on a vertical tubular member is investigated. The analytical derivation is performed by applying the upper-bound method. To do so, we first imagine a displacement field that is compatible with the assumed shape of the striking vessel. To evaluate the impact resistance, the tubular member is idealised by a set of horizontal rings disconnected to vertical generators. Both of them are submitted to an assumed displacement profile and the virtual velocities principle is applied to get the corresponding crushing resistance.

As a second step, the situation of a horizontal tubular member is treated. The method is similar to the vertical case, but the assumed deformation pattern is of course somewhat different.

An interpolation formula is then proposed to evaluate the crushing resistance for any inclination of the cylindrical member. In order to validate the theoretical developments, the crushing force assessed analytically is compared with numerical results. In almost all the cases, the agreement between our simplified method and the results given by the *LS-DYNA* FE code are satisfactory, as the divergence never exceeds 25%. Moreover, the analytical procedure leads to conservative results, as the crushing force and the energy dissipated by the tubular member are always underestimated.

Impact on a full-scale jacket is also treated. Once again, the collision is simulated using *LS-DYNA* and the corresponding results are compared with the analytical predictions. The numerical simulations are performed by considering two different initial velocities for the striking vessel, i.e. 2 m/s and 5 m/s. In the first case, when the velocity is rather small, the agreement of the present theoretical derivation is quite satisfactory. Nevertheless, in the second case, when the velocity is increased, a significant discrepancy is observed. This one is due to the fact that the tubular members surrounding the impacted one are also deformed during the crash. This points out the necessity of accounting for a coupling between several deformation modes, which are considered in the next Chapters.

In the last part of this Chapter, the model is extended to bulb colliding on tubular members. For each collision scenario, the initial impact point is first identified. We virtually divide the bulb into horizontal slices. The bulb is first located away from the tubular member and approaches it by spatial steps. At each step, contact between the considered slice and the tubular member is checked, until the first contact point is identified. Elliptic radii are considered to be the ones corresponding to the slice, while the stem and side angles are considered to be tangent to the initial contact point. Using these assumptions and the formulations described for stem impacts provides accurate results, validating also the equations in case of bulb impacts.

Bibliography

[1] T Belytschko, I Lin, and CS Tsay. Explicit algorithms for the nonlinear dynamics of shells. *Computer Methods in Applied Mechanics and Engineering*, (42):225–251, 1984.

[2] L Buldgen, H Le Sourne, and P Rigo. Fast strength assessment of mitre gates to ship impact. *International Journal of Crashworthiness*, 18:423–443, 2013.

[3] BC Cerik, HK Shin, and SR Cho. A comparative study on damage assessment of tubular members subjected to mass impact. *Marine Structures*, (46):1–29, 2016.

[4] J de Oliveira, T Wiersbicki, and W Abramowicz. Plastic behavior of tubular members under lateral concentrated load. Technical Report n° 82-0708, DNV, 1982.

[5] JO Hallquist. LS-DYNA theoretical manual. Technical report, Livermore Software Technology Corporation, 2006.

[6] MS Hoo Fatt and T Wierzbicki. Damage of plastic cylinders under localized pressure loading. *International Journal of Mechanical Sciences*, 33:999–1016, 1991.

[7] N Jones. *Structural impact*. Cambridge: Cambridge University Press, 1997.

[8] H Le Sourne, A Barrera, and JB Maliakel. Numerical crashworthiness analysis of an offshore wind turbine jacket impacted by a ship. *Journal of Marine Science and Technology*, 23:694–704, 2015.

[9] MS Suh. *Plastic analysis of dented tubes subjected to combined loading*. PhD thesis, Cambridge: Massachusetts Institute of Technology, Department of Ocean Engineering, 1987.

[10] F Tin Loi. Post-yield behavior of a rigid-plastic beam with partial axial and rotational end fixities. *International Journal of Mechanical Sciences*, 32:623–630, 1990.

[11] T Wierzbicki and MS Suh. Indentation of tubes under combined loading. *International Journal of Mechanical Sciences*, 30:229–248, 1988.

[12] M Zeinoddini, JE Harding, and GAR Parke. Effect of impact damage on the capacity of tubular steel members of offshore structures. *Marine Structures*, 11:141–157, 1998.

Chapter 5

Global deformation of the whole jacket

Abstract:

This Chapter aims to detail the algorithm developed to compute the overall deformation of an OWT jacket impacted by a ship. The local cross-section deformations of all tubular members are not included here.

The global motion computation is achieved by dividing the jacket into large elements, each tubular member of the structure being one of them. Both extremities of each element has 6 degrees of freedom to describe its displacements. Using a methodology similar to the one used for FE approach, the elementary stiffness matrix is computed for each element, including the elastic regime and apparition of plastic hinges, second order geometrical effects and semi-rigid connections. The deformation of the collided jacket is controlled by the displacement of the impact point between the striking ship and the structure.

Validation of the algorithm is achieved by comparing our results with FE simulations performed with *LS-DYNA*. The results show a good agreement between both models, validating the developed algorithm.

5.1 Introduction

Numerical simulations using FE method were performed in Chapter 3 to understand the structural behaviour of OWT jackets impacted by a ship and four deformation modes were identified, namely:

- local crushing of impacted tubular members (Chapter 4);
- global deformation of the whole jacket (present Chapter);
- punching of legs by compressed braces (Chapter 6);
- deformation at the base of the jacket (Chapter 7).

This present Chapter focuses on the second one, the global deformation of the whole jacket. The ship collides the jacket locally and the displacement near the contact point affects all the elements of the structure until the crushing forces are transmitted to the foundation. The deformation of cross-sections (crushing or punching, for example) is not considered in the study of this deformation mode.

The methodology developed here uses a formulation similar to the one used for FE theory, considering each tubular member as one single element. In this way, the number of elements in the model is low (in FE models, each tubular member would be modelled with several beam elements), as well as the computational effort. This method is already used in *USFOS* software [8] for similar structures as our developments are close to that code.

Developing an algorithm to assess the overall deformation of the whole structure is achieved in several steps. First, the stiffness matrices is computed individually in elastic regime. They are then extended to the plastic regime by accounting for possible plastic hinges at several determined locations. The stiffness matrices are modified for the plastic regime, and nodal forces have to be added to ensure that the stress state remains on the plastic surface. Elementary stiffness matrices and force vectors are assembled to characterise the entire structure. The structural motion is governed by the ship impact point displacement. Additional computations are performed to evaluate the internal forces. The implementation of all the developed equations is given for each step. Finally, the validation of the algorithm is performed considering several collision scenarios.

This Chapter is based on various developments in the literature from several authors, all being cited in the bibliography. The main achievement consists in gathering all these works to get a consistent methodology to assess the overall motion of the impacted structure.

5.2 Description

The methodology used to describe the overall motion of the jacket is similar to the one used in FE approach. The structure is first divided into large structural units, which correspond here to tubular members. For each of them, the elastic elementary matrix is developed. Plasticity is then accounted for by considering plastic hinges that can occur only at three locations, i.e. at both extremities of the element and at midspan. Following the same methodology as for FE, the elementary matrices are assembled and the system is solved.

In the next sections, the vectors are simply underlined ($\underline{v}$) and the matrices doubly underlined ($\underline{\underline{M}}$).

5.2.1 Elementary elastic stiffness matrices

Every tubular member is modelled with a beam element with 6 degrees of freedom at each extremity, as can be seen in Fig. 5.1.

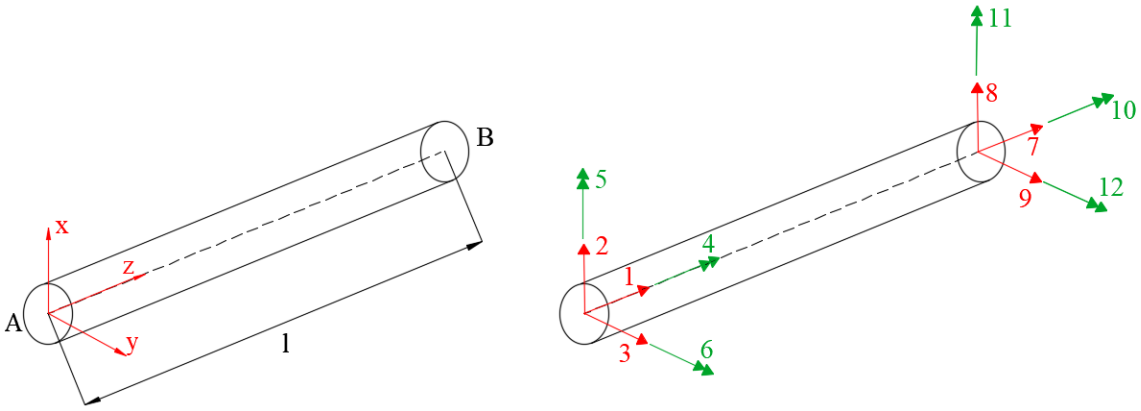

Figure 5.1: Axes and degrees of freedom for beam-elements

The elastic elementary stiffness matrices are derived from the formulation of Aristizabal-Ochoa [1] that includes semi-rigid connections (with a parameter allowing to consider connections from perfectly hinged to perfectly clamped) and second-order effects using Timoshenko stability functions [9].

The elastic elementary stiffness matrix is given under the form:

$$\underline{\underline{k}} = \begin{bmatrix} k_{1,1} & k_{1,2} & \cdots & \cdots & k_{1,12} \\ k_{2,1} & k_{2,1} & & & \vdots \\ \vdots & & \ddots & & \vdots \\ \vdots & & & \ddots & \vdots \\ k_{12,1} & \cdots & \cdots & \cdots & k_{12,12} \end{bmatrix} \tag{5.1}$$

The following expressions are fully detailed in [1] and are given here as a reminder. Please note that the degrees of freedom numbering used here and presented in Fig. 5.1 changes with regard to the Aristizabal-Ochoa's paper one presented in Fig. 5.2. The numbering correspondence is given in Table 5.1.

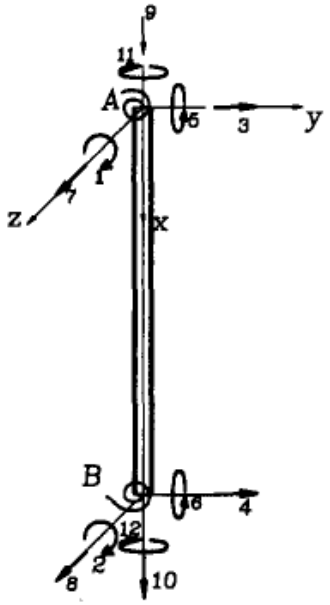

Figure 5.2: DOFs Numbering in Aristizabal-Ochoa's paper [1]

Table 5.1: Equivalence between the present thesis and Aristizabal-Ochoa's paper [1] degrees of freedom numbering

T. Pire's PhD thesis	1	2	3	4	5	6	7	8	9	10	11	12
Aristizabal-Ochoa's paper [1]	9	3	7	11	5	1	10	4	8	12	6	2

5.2.1.1 Flexural stiffness in one single plane

We define the fixity factor at node i as ρ_i and the rigidity index as R_i [11]. For a hinged connection, we have $\rho_i = 0$ and $R_i = 0$, while their values are equal to $\rho_i = 1$ and $R_i = \infty$ for a clamped connection. Both variables are linked by Eq. 5.2 [11].

$$\rho_i = \frac{1}{1 + \frac{3}{R_i}} \tag{5.2}$$

In the present thesis, it is assumed that all the tubular members are clamped at both extremities.

For prismatic column with rigid connections and submitted to an axial force P (positive in compression and negative in tension), Salmon and Johnson [7] defined the parameter u as:

$$u = \sqrt{\frac{P}{EI/l^2}} \tag{5.3}$$

with E the Young modulus, I, the flexural inertia and l the element length.

The following expressions are detailed for the deformation in one single plane, with degrees of freedom $2, 6, 8, 12$. The next equations are a reminder of the elementary matrix components given in [1]. The element ends are denoted A and B (see Fig. 5.1) and are then used in the subscripts.

Compression ($P > 0$)

If the column is submitted to compression, one has:

$$k_{6,6} = \frac{3\rho_A\left(1-\rho_B\right)u^2 + 9\rho_A\rho_B\left(1-u/\tan u\right)}{\left(1-\rho_A\right)\left(1-\rho_B\right)u^2 + 3\left(\rho_A+\rho_B-2\rho_A\rho_B\right)\left(1-u/\tan u\right) + 9\rho_A\rho_B\left[\tan(u/2)/(u/2)-1\right]}\frac{EI}{l} \tag{5.4}$$

$$k_{12,6} = \frac{9\rho_A\rho_B\left(u/\sin u-1\right)u^2}{\left(1-\rho_A\right)\left(1-\rho_B\right)u^2 + 3\left(\rho_A+\rho_B-2\rho_A\rho_B\right)\left(1-u/\tan u\right) + 9\rho_A\rho_B\left[\tan(u/2)/(u/2)-1\right]}\frac{EI}{l} \tag{5.5}$$

$$k_{12,12} = \frac{3\rho_B\left(1-\rho_A\right)u^2 + 9\rho_A\rho_B\left(1-u/\tan u\right)}{\left(1-\rho_A\right)\left(1-\rho_B\right)u^2 + 3\left(\rho_A+\rho_B-2\rho_A\rho_B\right)\left(1-u/\tan u\right) + 9\rho_A\rho_B\left[\tan(u/2)/(u/2)-1\right]}\frac{EI}{l} \tag{5.6}$$

No axial effort ($P = 0$)

When the axial effort applied on the element is equal to 0, the stiffness matrix coefficients are first-order coefficients:

$$k_{6,6} = \frac{12\rho_A}{4-\rho_A\rho_B}\frac{EI}{l} \tag{5.7}$$

$$k_{12,6} = \frac{6\rho_A\rho_B}{4-\rho_A\rho_B}\frac{EI}{l} \tag{5.8}$$

$$k_{12,12} = \frac{12\rho_B}{4-\rho_A\rho_B}\frac{EI}{l} \tag{5.9}$$

Tension ($P < 0$)

Finally, if the element is submitted to tension, one has:

$$k_{6,6} = \frac{-3\rho_A\left(1-\rho_B\right)u^2 + 9\rho_A\rho_B\left(1-u/\tanh u\right)}{-\left(1-\rho_A\right)\left(1-\rho_B\right)u^2 + 3\left(\rho_A+\rho_B-2\rho_A\rho_B\right)\left(1-u/\tanh u\right) + 9\rho_A\rho_B\left[\tanh(u/2)/(u/2)-1\right]}\frac{EI}{l} \quad (5.10)$$

$$k_{12,6} = \frac{9\rho_A\rho_B\left(u/\sinh u - 1\right)u^2}{-\left(1-\rho_A\right)\left(1-\rho_B\right)u^2 + 3\left(\rho_A+\rho_B-2\rho_A\rho_B\right)\left(1-u/\tanh u\right) + 9\rho_A\rho_B\left[\tanh(u/2)/(u/2)-1\right]}\frac{EI}{l} \quad (5.11)$$

$$k_{12,12} = \frac{-3\rho_B\left(1-\rho_A\right)u^2 + 9\rho_A\rho_B\left(1-u/\tanh u\right)}{-\left(1-\rho_A\right)\left(1-\rho_B\right)u^2 + 3\left(\rho_A+\rho_B-2\rho_A\rho_B\right)\left(1-u/\tanh u\right) + 9\rho_A\rho_B\left[\tanh(u/2)/(u/2)-1\right]}\frac{EI}{l} \quad (5.12)$$

Shear effect

The components $k_{6,6}$, $k_{12,12}$ and $k_{12,6}$ are affected by shear and have to be multiplied by $(1+\Phi/4)/(1+\Phi)$ for $k_{6,6}$ and $k_{12,12}$ and by $(1-\Phi/2)/(1+\Phi)$ for $k_{12,6}$ where

$$\Phi = \frac{12EI}{GA_s l^2} \quad (5.13)$$

and A_s the shear area of the cross-section [2].

Other coefficients

The remaining coefficients can be computed with regard to $k_{6,6}$, $k_{12,6}$ and $k_{12,12}$ with the following relations, whatever the value of P:

$$k_{6,2} = -k_{8,6} = \frac{k_{6,6}+k_{12,6}}{l} \quad (5.14)$$

$$k_{12,2} = -k_{12,8} = \frac{k_{12,12}+k_{12,6}}{l} \quad (5.15)$$

$$k_{2,2} = k_{8,8} = -k_{8,2} = \frac{k_{6,2}+k_{12,2}-P}{l} \quad (5.16)$$

By symmetry, one has:

$$k_{i,j} = k_{j,i} \quad (5.17)$$

with $i, j = 2, 6, 8, 12$ and $i \neq j$.

Finally, one can write:

$$k_{2,6,8,12} = \begin{bmatrix} k_{2,2} & & & \\ k_{6,2} & k_{6,6} & & \\ k_{8,2} & k_{8,6} & k_{8,8} & \\ k_{12,2} & k_{12,6} & k_{12,8} & k_{12,12} \end{bmatrix} \tag{5.18}$$

Similarly, in the other flexural plane, one has:

$$k_{3,5,9,11} = k_{2,6,8,12} \tag{5.19}$$

5.2.1.2 Axial stiffness

The classical first-order stiffness coefficient is $k = EA/l$. In order to take into account the flexural moments, this coefficient was modified by Ekhande et al. [2] to

$$k_{1,1} = k_{7,7} = -k_{7,1} = s_1 EA/l \tag{5.20}$$

with:

$$s_1 = \frac{1}{1 + (H_x + H_y)\,\frac{EA}{4P^3 l^2}} \tag{5.21}$$

where

$$u = \sqrt{\frac{P}{EI_y/l^2}} \qquad \text{and} \qquad v = u\sqrt{\frac{(EI)_y}{(EI)_x}} \tag{5.22}$$

H_x and H_y are computed as follows:

Compression ($P > 0$)

$$\begin{aligned} H_x = v\left(M_{xa}^2 + M_{xb}^2\right)\left(1/\tan v + v/\sin^2 v\right) - 2\left(M_{xa} + M_{xb}\right)^2 \\ +2vM_{xa}M_{xb}\left(1 + v\tan v\right)/\sin v \end{aligned} \tag{5.23}$$

$$\begin{aligned} H_y = u\left(M_{ya}^2 + M_{yb}^2\right)\left(1/\tan u + u/\sin^2 u\right) - 2\left(M_{ya} + M_{yb}\right)^2 \\ +2uM_{ya}M_{yb}\left(1 + u\tan u\right)/\sin u \end{aligned} \tag{5.24}$$

Tension ($P < 0$)

$$H_x = v\left(M_{xa}^2 + M_{xb}^2\right)\left(1/\tanh v + v/\sinh^2 v\right) - 2\left(M_{xa} + M_{xb}\right)^2 + 2vM_{xa}M_{xb}\left(1 + v\tanh v\right)/\sinh v \tag{5.25}$$

$$H_y = u\left(M_{ya}^2 + M_{yb}^2\right)\left(1/\tanh u + u/\sinh^2 u\right) - 2\left(M_{ya} + M_{yb}\right)^2 + 2uM_{ya}M_{yb}\left(1 + u\tanh u\right)/\sinh u \tag{5.26}$$

5.2.1.3 Torsional stiffness

The interactions between axial, flexural and torsional stiffness are neglected. According to Saint-Venant's theory, one has:

$$k_{4,4} = k_{10,10} = -k_{10,4} = \frac{GJ}{l} \tag{5.27}$$

where G is the Coulomb modulus and J the torsional inertia.

5.2.2 Stiffness reduction due to plastic hinges

The plastic surface F has to be defined, taking into account all the internal forces in one element node. In the Eurocode 3 [3], a formulation for circular cross-sections can be found and is written in Eq. 5.28.

$$F \equiv \left(\frac{M_x}{M_{pl}\left(1 - \left(\frac{N}{N_{pl}}\right)^2\right)}\right)^2 + \left(\frac{M_y}{M_{pl}\left(1 - \left(\frac{N}{N_{pl}}\right)^2\right)}\right)^2 - 1 = 0 \tag{5.28}$$

where M_x and M_y are the internal bending moments around x and y axes respectively, N is the internal axial force, M_{pl} and N_{pl} the plastic bending moment and the axial resistance force respectively. Such plastic resistances are computed in Eqs. 5.29 and 5.30.

$$N_{pl} = \pi\left(R_2^2 - R_1^2\right)\sigma_0 = A\sigma_0^2 \tag{5.29}$$

$$M_{pl} = 2\int_0^{2\pi} d\theta \int_{R_1}^{R_2} \sigma_0 r \sin\theta r dr = 4\sigma_0 \frac{R_2^3 - R_1^3}{3} \tag{5.30}$$

where A is the cross-section area, σ_0 the flow stress, R_1 and R_2 the internal and external radii of the tubular member respectively.

Considering the formulation of plastic surface expressed in Eq. 5.28, it is assumed that the internal shear force (V_x and V_y) is lower than half of the shear plastic resistance and can therefore be neglected and that the effect of torsion force (T) can be neglected with regard to bending and normal forces.

The orientation of the inertia axes for a tubular member is undefined, and considering a resulting bending moment could be relevant. However, the presented formulation is developed to compute the bending moments around the x and y axes independently, which is required for a further change from a local coordinate system (for each tubular member) to a global coordinate system (for the whole jacket), as discussed in Section 5.2.3.

This plastic surface may be derived with regard to the internal forces.

$$\underline{g}^T = \begin{bmatrix} \frac{\partial F}{\partial N} & \frac{\partial F}{\partial V_x} & \frac{\partial F}{\partial V_y} & \frac{\partial F}{\partial T} & \frac{\partial F}{\partial M_x} & \frac{\partial F}{\partial M_y} \end{bmatrix} \tag{5.31}$$

The components of Eq. 5.31 may be expressed as

$$\begin{aligned} \frac{\partial F}{\partial N} &= \frac{4N}{N_{pl}^2 \left(1 - \left(\frac{N}{N_{pl}}\right)^2\right)^3} \frac{M_x^2 + M_y^2}{M_{pl}^2} \\ \frac{\partial F}{\partial V_x} &= \frac{\partial F}{\partial V_y} = \frac{\partial F}{\partial T} = 0 \\ \frac{\partial F}{\partial M_x} &= \frac{2M_x}{\left[M_{pl}\left(1 - \left(\frac{N}{N_{pl}}\right)^2\right)\right]^2} \\ \frac{\partial F}{\partial M_y} &= \frac{2M_y}{\left[M_{pl}\left(1 - \left(\frac{N}{N_{pl}}\right)^2\right)\right]^2} \end{aligned} \tag{5.32}$$

In order to simplify the notation next, all the degrees of freedom related to the element node A are denoted with subscript A, similarly for node B. For example, the stiffness matrix given in Eq. 5.1 can be written in Eq. 5.33:

$$\underline{\underline{k}} = \begin{bmatrix} k_{1,1} & k_{1,2} & \cdots & \cdots & k_{1,12} \\ k_{2,1} & k_{2,1} & & & \vdots \\ \vdots & & \ddots & & \vdots \\ \vdots & & & \ddots & \vdots \\ k_{12,1} & \cdots & \cdots & \cdots & k_{12,12} \end{bmatrix} = \begin{bmatrix} k_{A,A} & k_{A,B} \\ k_{B,A} & k_{B,B} \end{bmatrix} \tag{5.33}$$

In this methodology, it is considered that the cross-section is fully elastic or fully yielded (corresponding to a plastic hinge), the transition between both states being defined by the plastic surface given in Eq. 5.28. The cross-section partial yielding, i.e. only a part of the cross-section is yielded while the rest is still is elastic domain, is not taken into account.

It is further assumed that plastic hinges may appear only at determined locations, i.e. at both extremities and at midspan. Those cases are studied in Sections 5.2.2.1 and 5.2.2.2 respectively.

5.2.2.1 Plastic hinge at element end

Elasto-plastic stiffness

From *USFOS* (all the details can be found in [8]), the incremental stiffness expression is given in Eq. 5.34.

$$\begin{Bmatrix} \Delta \underline{s}_A \\ \Delta \underline{s}_B \end{Bmatrix} = \begin{bmatrix} \underline{\underline{k}}^{ep}_{AA} & \underline{\underline{k}}^{ep}_{AB} \\ \underline{\underline{k}}^{ep}_{BA} & \underline{\underline{k}}^{ep}_{BB} \end{bmatrix} \begin{Bmatrix} \Delta \underline{v}_A \\ \Delta \underline{v}_B \end{Bmatrix} + \begin{bmatrix} \underline{\underline{p}}^{ep}_{AA} & \underline{\underline{p}}^{ep}_{AB} \\ \underline{\underline{p}}^{ep}_{BA} & \underline{\underline{p}}^{ep}_{BB} \end{bmatrix} \begin{Bmatrix} \Delta \underline{\bar{s}}_A \\ \Delta \underline{\bar{s}}_B \end{Bmatrix} \tag{5.34}$$

with

$$\underline{\underline{k}}^{ep}_{ij} = \underline{\underline{k}}_{ij} - \underline{\underline{k}}_{ik} \underline{k}_k \underline{\underline{h}}^T_{kj} \qquad i,j,k = A,B \tag{5.35}$$

and

$$\underline{\underline{p}}^{ep}_{ij} = \underline{\underline{\delta}}_{ij} - \underline{\underline{k}}_{ik} \underline{k}_k \underline{\underline{p}}^T_{kj} \qquad i,j,k = A,B \tag{5.36}$$

using Einsteins summation. Note that $\underline{\underline{\delta}}_{ij}$ is the identity matrix.

In Eq. 5.34, we have $\Delta \underline{S}_i$ the variation of internal force at node i expressed in Eq. 5.37, $\Delta \underline{v}_i$ the variation of displacement at node i expressed in Eq. 5.38 and $\Delta \underline{\bar{S}}_i$ the consistent nodal forces increments coming from concentrated and laterally distributed forces. In our present case, no concentrated loads or distributed loads are applied on the structure, such as $\Delta \underline{\bar{S}}_i = 0$ for any node of the collided jacket.

$$\underline{s}^T_i = \begin{bmatrix} N & V_x & V_y & T & M_x & M_y \end{bmatrix} \tag{5.37}$$

$$\underline{v}^T_i = \begin{bmatrix} u_z & u_x & u_y & \theta_z & \theta_x & \theta_y \end{bmatrix} \tag{5.38}$$

The remaining expressions of Eq. 5.34 are given in Eqs. 5.39, 5.40 and 5.41.

$$\begin{aligned}
\underline{\underline{h}}^T_{A,A} &= \frac{1}{det} \left\{ \left(\underline{g}^T_B \left(\underline{\underline{k}}_{B,B} + \underline{\underline{k}}^h_{B,B} + \underline{\underline{C}}_{B,B} \right) \underline{g}_B \right) \underline{g}^T_A \underline{\underline{k}}_{A,A} - \left(\underline{g}^T_A \underline{\underline{k}}_{A,B} \underline{g}_A \right) \underline{g}^T_A \underline{\underline{k}}_{B,A} \right\} \\
\underline{\underline{h}}^T_{A,B} &= \frac{1}{det} \left\{ \left(\underline{g}^T_B \left(\underline{\underline{k}}_{B,B} + \underline{\underline{k}}^h_{B,B} + \underline{\underline{C}}_{B,B} \right) \underline{g}_B \right) \underline{g}^T_A \underline{\underline{k}}_{A,B} - \left(\underline{g}^T_A \underline{\underline{k}}_{A,B} \underline{g}_A \right) \underline{g}^T_A \underline{\underline{k}}_{B,B} \right\} \\
\underline{\underline{h}}^T_{B,A} &= \frac{1}{det} \left\{ \left(\underline{g}^T_A \left(\underline{\underline{k}}_{A,A} + \underline{\underline{k}}^h_{A,A} + \underline{\underline{C}}_{A,A} \right) \underline{g}_A \right) \underline{g}^T_B \underline{\underline{k}}_{B,A} - \left(\underline{g}^T_B \underline{\underline{k}}_{B,A} \underline{g}_A \right) \underline{g}^T_A \underline{\underline{k}}_{A,A} \right\} \\
\underline{\underline{h}}^T_{B,B} &= \frac{1}{det} \left\{ \left(\underline{g}^T_A \left(\underline{\underline{k}}_{A,A} + \underline{\underline{k}}^h_{A,A} + \underline{\underline{C}}_{A,A} \right) \underline{g}_A \right) \underline{g}^T_B \underline{\underline{k}}_{B,B} - \left(\underline{g}^T_B \underline{\underline{k}}_{B,A} \underline{g}_A \right) \underline{g}^T_A \underline{\underline{k}}_{A,B} \right\}
\end{aligned} \tag{5.39}$$

$$\begin{aligned}
\underline{\underline{p}}^T_{A,A} &= \frac{1}{det}\left(\underline{g}^T_B\left(\underline{\underline{k}}_{B,B} + \underline{\underline{k}}^h_{B,B} + \underline{\underline{C}}_{B,B}\right)\underline{g}_B\right)\underline{g}^T_A \\
\underline{\underline{p}}^T_{A,B} &= \frac{1}{det}\left(-\underline{g}^T_A\underline{\underline{k}}_{A,B}\underline{g}_B\right)\underline{g}^T_B \\
\underline{\underline{p}}^T_{B,A} &= \frac{1}{det}\left(-\underline{g}^T_B\underline{\underline{k}}_{B,A}\underline{g}_A\right)\underline{g}^T_A \\
\underline{\underline{p}}^T_{B,B} &= \frac{1}{det}\left(\underline{g}^T_A\left(\underline{\underline{k}}_{A,A} + \underline{\underline{k}}^h_{A,A} + \underline{\underline{C}}_{A,A}\right)\underline{g}_A\right)\underline{g}^T_B
\end{aligned} \tag{5.40}$$

$$det = \left(\underline{g}^T_A\left(\underline{\underline{k}}_{A,A} + \underline{\underline{k}}^h_{A,A} + \underline{\underline{C}}_{A,A}\right)\underline{g}_A\right)\left(\underline{g}^T_B\left(\underline{\underline{k}}_{B,B} + \underline{\underline{k}}^h_{B,B} + \underline{\underline{C}}_{B,B}\right)\underline{g}_B\right) - \left(\underline{g}^T_A\underline{\underline{k}}_{A,B}\underline{g}_B\right)^2 \tag{5.41}$$

The matrix $\underline{\underline{k}}^h$ covers hardening effect while the matrix $\underline{\underline{C}}$ covers the deformation of the plastic surface.

Plastic correction

In plastic regime, the stress state moves tangentially to the plastic surface during a finite load increment. Therefore, the stress state does not remain on the plastic surface, which can be corrected by applying an equivalent load vector.

If we denote $\Delta\underline{\bar{f}}_i$ the deviation from the yield surface at node i, the equivalent force vector is written in Eq. 5.42

$$\begin{Bmatrix} \Delta\underline{s}^\star_A \\ \Delta\underline{s}^\star_B \end{Bmatrix} = -\begin{bmatrix} \underline{\underline{t}}^{ep}_{AA} & \underline{\underline{t}}^{ep}_{AB} \\ \underline{\underline{t}}^{ep}_{BA} & \underline{\underline{t}}^{ep}_{BB} \end{bmatrix}\begin{Bmatrix} \Delta\underline{\bar{f}}_A \\ \Delta\underline{\bar{f}}_B \end{Bmatrix} \tag{5.42}$$

with

$$\underline{\underline{t}}^{ep}_{ij} = -\underline{\underline{t}}_{ik}\ \underline{g}_k\ \underline{\underline{t}}_{kj} \tag{5.43}$$

and

$$\begin{aligned}
\underline{\underline{t}}^T_{A,A} &= \frac{1}{det}\left(\underline{g}^T_B\left(\underline{\underline{k}}_{B,B} + \underline{\underline{k}}^h_{B,B} + \underline{\underline{C}}_{B,B}\right)\underline{g}_B\right)\underline{g}^T_A \\
\underline{\underline{t}}^T_{A,B} &= \frac{1}{det}\left(-\underline{g}^T_A\underline{\underline{k}}_{A,B}\underline{g}_B\right)\underline{g}^T_B \\
\underline{\underline{t}}^T_{B,A} &= \frac{1}{det}\left(-\underline{g}^T_B\underline{\underline{k}}_{B,A}\underline{g}_A\right)\underline{g}^T_A \\
\underline{\underline{t}}^T_{B,B} &= \frac{1}{det}\left(\underline{g}^T_A\left(\underline{\underline{k}}_{A,A} + \underline{\underline{k}}^h_{A,A} + \underline{\underline{C}}_{A,A}\right)\underline{g}_A\right)\underline{g}^T_B
\end{aligned} \tag{5.44}$$

where *det* is defined in Eq. 5.41.

The distance from the stress state to the plastic surface has still to be computed. In our situation, the plastic surface is defined in Eq. 5.28 and is a function of three internal forces,

namely the axial force N and two bending moments M_x and M_y. In plastic regime, the stress state moves tangentially to the plastic surface. As this one is convex, the updated stress state is outside this plastic surface.

The distance between the actual stress state and the plastic surface is defined as the distance between the stress state and the intersection point between the plastic surface and the straight line normal to that surface passing through the stress state.

In two dimensions, this can be illustrated in Fig. 5.3 by a plastic surface defined in Eq. 5.45. The stress state is denoted by σ and the normal to the surface passing through σ is d.

$$F_{2D} \equiv \frac{M}{M_{pl,Rd}} + \left(\frac{N}{N_{pl,Rd}}\right)^2 - 1 = 0 \tag{5.45}$$

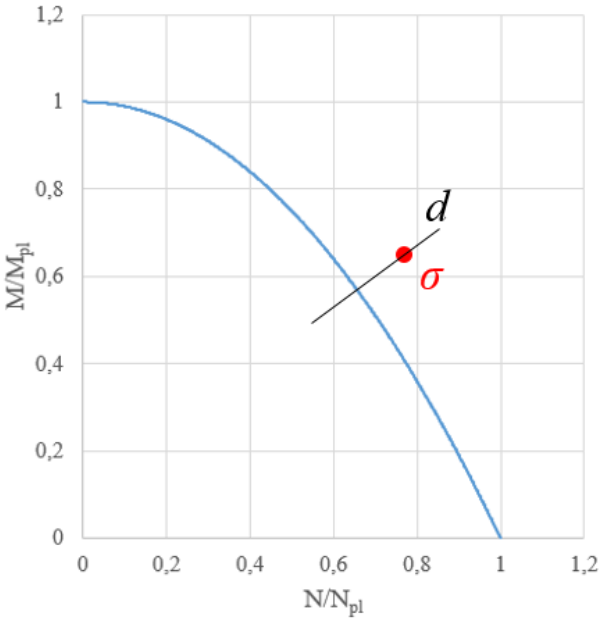

Figure 5.3: Line normal to plastic surface passing through the stress state

We need to compute the intersection point between the plastic surface and the straight line normal to that surface passing through the stress state. Mathematically, this point is:

- on the plastic surface F (Eq. 5.28);
- on the line d normal to the plastic surface passing through σ (Eq. 5.46).

$$\begin{cases} d_N \equiv \dfrac{\partial F}{\partial N} t + N_\sigma - N = 0 \\ d_{Mx} \equiv \dfrac{\partial F}{\partial M_x} t + M_{x,\sigma} - M_x = 0 \\ d_{My} \equiv \dfrac{\partial F}{\partial M_y} t + M_{y,\sigma} - M_y = 0 \end{cases} \tag{5.46}$$

Four unknowns N, M_x, M_y and t have to be found with the four equations given in Eq. 5.28 and 5.46. The problem is solved using a Newton-Raphson iterative method detailed in Eq. 5.47.

$$\begin{Bmatrix} N \\ M_x \\ M_y \\ t \end{Bmatrix}_{i+1} = \begin{Bmatrix} N \\ M_x \\ M_y \\ t \end{Bmatrix}_{i} - \begin{bmatrix} \frac{\partial F}{\partial N} & \frac{\partial F}{\partial M_x} & \frac{\partial F}{\partial M_y} & \frac{\partial F}{\partial t} \\ \frac{\partial d_N}{\partial N} & \frac{\partial d_N}{\partial M_x} & \frac{\partial d_N}{\partial M_y} & \frac{\partial d_N}{\partial t} \\ \frac{\partial d_{Mx}}{\partial N} & \frac{\partial d_{Mx}}{\partial M_x} & \frac{\partial d_{Mx}}{\partial M_y} & \frac{\partial d_{Mx}}{\partial t} \\ \frac{\partial d_{My}}{\partial N} & \frac{\partial d_{My}}{\partial M_x} & \frac{\partial d_{My}}{\partial M_y} & \frac{\partial d_{My}}{\partial t} \end{bmatrix}^{-1} \begin{Bmatrix} F \\ d_N \\ d_{Mx} \\ d_{My} \end{Bmatrix} \tag{5.47}$$

with $\frac{\partial F}{\partial N}$, $\frac{\partial F}{\partial M_x}$, and $\frac{\partial F}{\partial M_y}$ given in Eq. 5.32 and $\frac{\partial F}{\partial t} = 0$.

Then, one can compute the derivative of Eq. 5.47 for lines 2, 3 and 4 as done in Eqs. 5.48, 5.49 and 5.50 respectively

$$\begin{cases} \dfrac{\partial d_N}{\partial N} = \dfrac{M_x^2 + M_y^2}{N_{pl}^2 M_{pl}^2} \left[\dfrac{4}{\left(1 - \left(\frac{N}{N_{pl}}\right)^2\right)^3} + 4N \dfrac{-3}{\left(1 - \left(\frac{N}{N_{pl}}\right)^2\right)^4} \dfrac{-2N}{N_{pl}^2} \right] t - 1 \\ \dfrac{\partial d_N}{\partial M_x} = \dfrac{4N}{N_{pl}^2 \left(1 - \left(\frac{N}{N_{pl}}\right)^2\right)^3} \dfrac{2M_x}{M_{pl}^2} t \\ \dfrac{\partial d_N}{\partial M_y} = \dfrac{4N}{N_{pl}^2 \left(1 - \left(\frac{N}{N_{pl}}\right)^2\right)^3} \dfrac{2M_y}{M_{pl}^2} t \\ \dfrac{\partial d_N}{\partial t} = \dfrac{\partial F}{\partial N} \end{cases} \tag{5.48}$$

$$\begin{cases} \dfrac{\partial d_{Mx}}{\partial N} = \left(\dfrac{2M_x}{M_{pl}^2} \dfrac{-2}{\left(1 - \left(\frac{N}{N_{pl}}\right)^2\right)^3} \dfrac{-2N}{N_{pl}^2} \right) t \\ \dfrac{\partial d_{Mx}}{\partial M_x} = \dfrac{2}{\left[M_{pl} \left(1 - \left(\frac{N}{N_{pl}}\right)^2\right) \right]^2} t - 1 \\ \dfrac{\partial d_{Mx}}{\partial M_y} = 0 \\ \dfrac{\partial d_{Mx}}{\partial t} = \dfrac{\partial F}{\partial M_x} \end{cases} \tag{5.49}$$

$$\begin{cases} \dfrac{\partial d_{My}}{\partial N} = \left(\dfrac{2M_y}{M_{pl}^2} \dfrac{-2}{\left(1 - \left(\frac{N}{N_{pl}}\right)^2\right)^3} \dfrac{-2N}{N_{pl}^2} \right) t \\ \dfrac{\partial d_{My}}{\partial M_x} = 0 \\ \dfrac{\partial d_{Mx}}{\partial M_y} = \dfrac{2}{\left[M_{pl}\left(1 - \left(\frac{N}{N_{pl}}\right)^2\right)\right]^2} t - 1 \\ \dfrac{\partial d_{Mx}}{\partial t} = \dfrac{\partial F}{\partial M_y} \end{cases} \tag{5.50}$$

After convergence of the resolution, the distance between the stress state σ and the plastic surface is computed.

5.2.2.2 Plastic hinge at element midspan

In order to determine if a plastic hinge occurs at midspan, the internal forces at this specific location has to be computed and the stress state has to be compared with the plastic surface.

For small displacements (i.e. before the plastic hinge occurs), the bending moments around x and y at midspan are computed as

$$\begin{aligned} M_{x,mid} &= \frac{M_{x,A} + M_{x,B}}{2} + N u_{x,mid} \\ M_{y,mid} &= \frac{M_{y,A} + M_{y,B}}{2} + N u_{y,mid} \end{aligned} \tag{5.51}$$

where the subscripts A and B are related to both extremities and $u_{j,mid}$ is the midspan displacement of the element in the direction j ($j = x, y$) with regard to the straight line between the nodes A and B.

Before the occurrence of the plastic hinge at midspan, the beam can be represented in Fig. 5.4 in black at its initial position and in blue at its deformed one, the dotted line being the straight line between A and B. This displacement $u_{j,mid}$ is computed with the nodal displacement (see Fig. 5.5) through classical 2D-beam interpolation functions illustrated in Fig. 5.6 and described by Eq. 5.52. At midspan, w is taken equal to $l/2$.

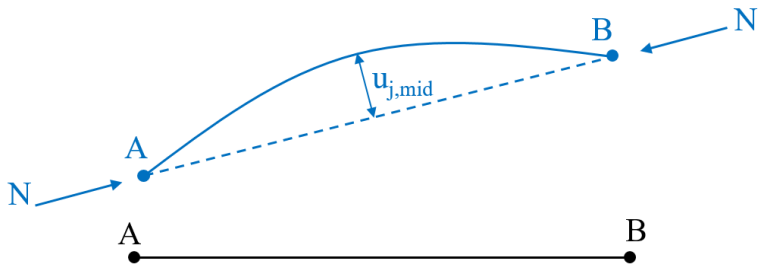

Figure 5.4: Midspan displacement

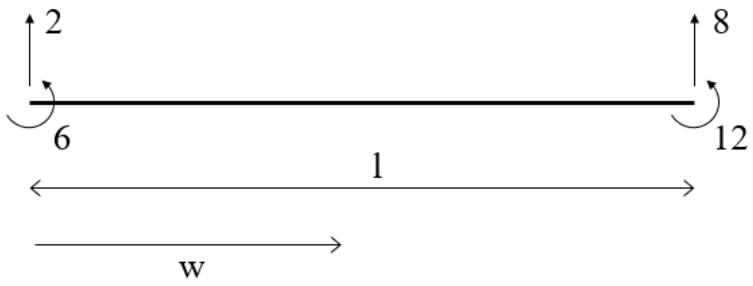

Figure 5.5: Nodal displacement on a 2D-beam element

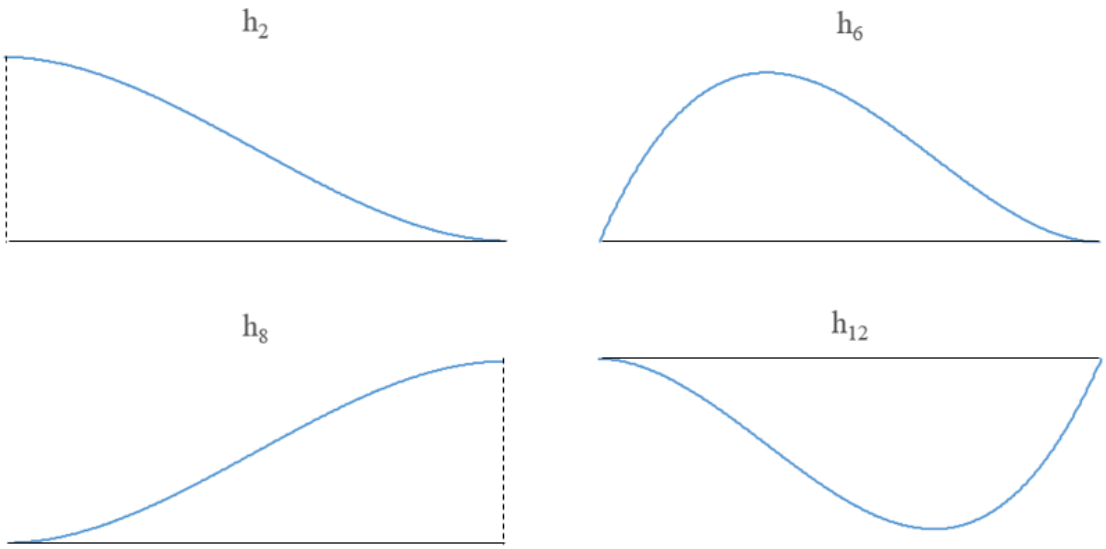

Figure 5.6: Interpolation functions for a 2D-beam (Eq. 5.52)

$$
\begin{aligned}
h_2(w) &= \frac{2w^3}{l^3} - \frac{3w^2}{l^2} + 1 \\
h_6(w) &= l\left(\frac{w^3}{l^3} - \frac{2w^2}{l^2} + \frac{w}{l}\right) \\
h_8(w) &= \frac{-2w^3}{l^3} + \frac{3w^2}{l^2} \\
h_{12}(w) &= l\left(\frac{w^3}{l^3} - \frac{w^2}{l^2}\right)
\end{aligned}
\tag{5.52}
$$

If we denote u_2 and u_8 the displacements associated to degrees of freedom 2 and 8 and θ_6 and θ_{12} the rotations associated to degrees of freedom 6 and 12 respectively (see Fig. 5.5) and if we assume that the displacements are small, then, the displacement $u_{j,mid}$ is given in Eq. 5.53.

$$
u_{j,mid} = u_2 h_2(l/2) + \theta_6 h_6(l/2) + u_8 h_8(l/2) + \theta_{12} h_{12}(l/2) - \frac{u_2 + u_8}{2} \tag{5.53}
$$

Then, using the axial force and Eq. 5.51 into Eq. 5.28 allows to check if a plastic hinge occurs at midspan. In this case, the element is divided into two elements with a plastic hinge between them.

The formulations used are then identical to the ones developed in Section 5.2.2.1.

5.2.3 Assembly

Each element has its own local axes system (x, y, z), in red in Fig. 5.7, and all the formulations developed in Sections 5.2.1 and 5.2.2 are expressed in this local frame.

However, all the elements have to be expressed in a common frame (X, Y, Z), in green in Fig. 5.7. The origin of this frame has an elevation equal to the jacket foundation level and is located at equal distance of all four leg foundations. The axes X and Y are horizontal and aligned with jacket planes and Z axis is vertical. The elementary stiffness matrices and loads have to be modified to fit with the global frame. This is achieved through rotation matrices $\underline{\underline{R}}$.

For an element with a local unitary frame (x, y, z) that is expressed in the global unitary frame (X, Y, Z), the rotation matrix $\underline{\underline{R}}$ is written in Eq. 5.54 where "$\cdot$" denotes a scalar product.

$$
\underline{\underline{R}} = \begin{bmatrix} \underline{\underline{\Phi}} & \underline{\underline{0}} & \underline{\underline{0}} & \underline{\underline{0}} \\ \underline{\underline{0}} & \underline{\underline{\Phi}} & \underline{\underline{0}} & \underline{\underline{0}} \\ \underline{\underline{0}} & \underline{\underline{0}} & \underline{\underline{\Phi}} & \underline{\underline{0}} \\ \underline{\underline{0}} & \underline{\underline{0}} & \underline{\underline{0}} & \underline{\underline{\Phi}} \end{bmatrix} \quad ; \quad \underline{\underline{\Phi}} = \begin{bmatrix} \underline{X} \cdot \underline{x} & \underline{Y} \cdot \underline{x} & \underline{Z} \cdot \underline{x} \\ \underline{X} \cdot \underline{y} & \underline{Y} \cdot \underline{y} & \underline{Z} \cdot \underline{y} \\ \underline{X} \cdot \underline{z} & \underline{Y} \cdot \underline{z} & \underline{Z} \cdot \underline{z} \end{bmatrix} \tag{5.54}
$$

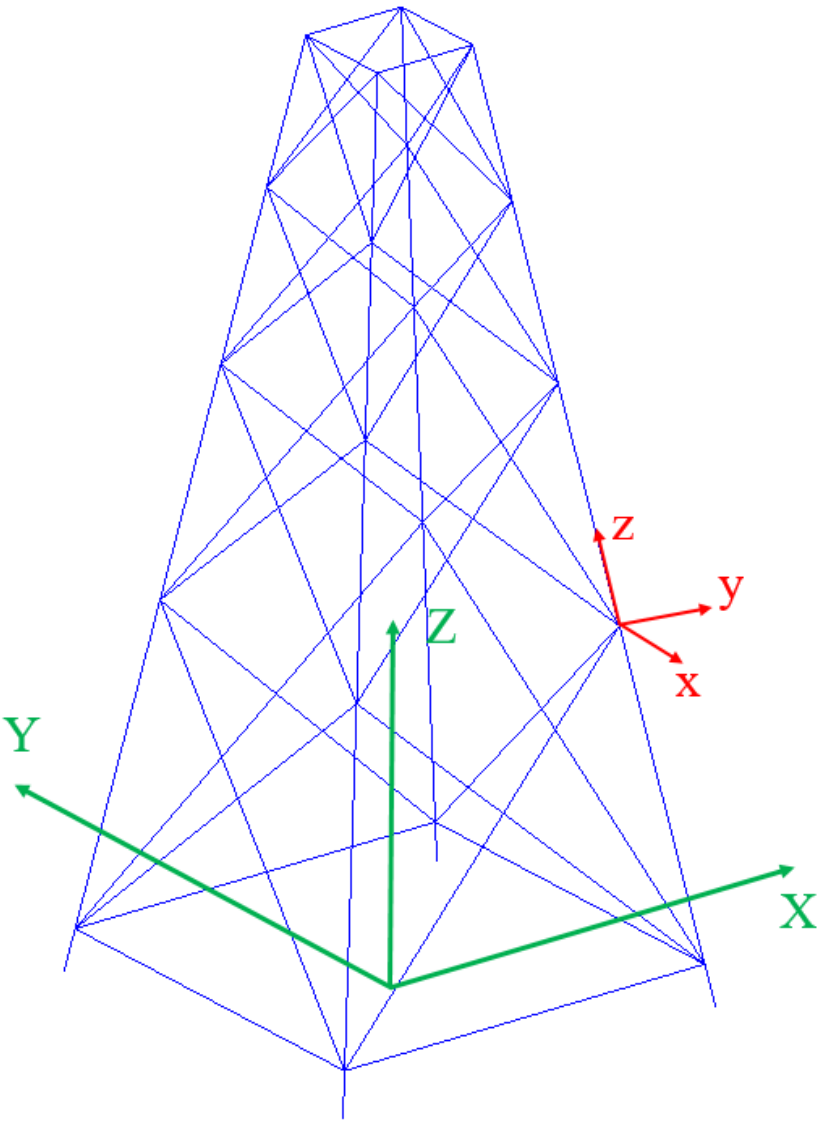

Figure 5.7: Global and local system of axes

Then, using a classical assembly method, the global stiffness matrix $\underline{\underline{K}}$ can be obtained from the elementary stiffness matrices $\underline{\underline{k}}$, as done in Eq. 5.55.

$$\underline{\underline{K}} = \sum_{assembly} \underline{\underline{R}}^T \, \underline{\underline{k}} \, \underline{\underline{R}} \tag{5.55}$$

Similarly for the local forces f that are expressed in the global system as F, as done in Eq. 5.56.

$$\underline{F} = \sum_{assembly} \underline{\underline{R}}^T \underline{f} \tag{5.56}$$

5.2.4 Displacement control

Typically, for a structure with n degrees of freedom submitted to a given nodal load vector F, the incremental matrices system can be solved as in Eq. 5.57.

$$\begin{bmatrix} K_{1,1} & K_{1,2} & K_{1,3} & \cdots & K_{1,n} \\ K_{2,1} & K_{2,2} & K_{2,3} & \cdots & K_{2,n} \\ K_{3,1} & K_{1,2} & K_{3,3} & \cdots & K_{3,n} \\ \vdots & \vdots & \vdots & \ddots & \vdots \\ K_{n,1} & K_{n,2} & K_{n,3} & \cdots & K_{n,n} \end{bmatrix} \begin{Bmatrix} \Delta u_1 \\ \Delta u_2 \\ \Delta u_3 \\ \vdots \\ \Delta u_n \end{Bmatrix} = \begin{Bmatrix} \Delta F_1 \\ \Delta F_2 \\ \Delta F_3 \\ \vdots \\ \Delta F_n \end{Bmatrix} \tag{5.57}$$

The formulation described in Eq. 5.57 is modified in order to impose nodal displacements [12]. If we denote $\Delta\bar{u}_2$ the imposed displacement increment on node 2, Eq. 5.57 becomes:

$$\begin{bmatrix} K_{1,1} & 0 & K_{1,3} & \cdots & K_{1,n} \\ 0 & 1 & 0 & \cdots & 0 \\ K_{3,1} & 0 & K_{3,3} & \cdots & K_{3,n} \\ \vdots & \vdots & \vdots & \ddots & \vdots \\ K_{n,1} & 0 & K_{n,3} & \cdots & K_{n,n} \end{bmatrix} \begin{Bmatrix} \Delta u_1 \\ \Delta\bar{u}_2 \\ \Delta u_3 \\ \vdots \\ \Delta u_n \end{Bmatrix} = \begin{Bmatrix} \Delta\hat{F}_1 \\ \Delta u_2 \\ \Delta\hat{F}_3 \\ \vdots \\ \Delta\hat{F}_n \end{Bmatrix} \tag{5.58}$$

with

$$\Delta\hat{F}_i = \Delta F_i - K_{i,2}\Delta\bar{u}_i \tag{5.59}$$

In general, for an imposed displacement increment $\Delta\bar{u}_j$ at node j, one has for $i = 1, 2, \cdots, n$ and $i \neq j$

$$K_{j,j} = 1 \quad ; \quad K_{i,j} = K_{j,i} = 0 \quad ; \quad \Delta F_j = \Delta\bar{u}_j \quad ; \quad \Delta\hat{F}_i = \Delta F_i - K_{i,j}\Delta\bar{u}_j \tag{5.60}$$

The same procedure can be applied for all the nodes where an imposed displacement is applied.

5.2.5 Matrices system resolution

Eq. 5.58 can be simply written under the form presented in Eq. 5.61 and this corresponds to the system equations to solve for the unknowns $\Delta\underline{u}$.

$$\underline{\underline{K}}\Delta\underline{u} = \Delta\underline{\hat{F}} \tag{5.61}$$

As this is solved by *Matlab*, the software uses more efficient algorithms depending on the matrix structure. In our case, the matrix is sparse and its structure is not triangular, not diagonal and not hermitian. *Matlab* chooses therefore a *LU* solver [6].

$$\Delta\underline{u} = \underline{\underline{K}}^{-1}\Delta\underline{\hat{F}} \tag{5.62}$$

This resolution is iterative as plasticity and nonlinear effects may occur. Eq. 5.61 is solved until convergence is reached, which can be expressed by $\omega \leq \varepsilon$ with ε the convergence criteria, taken equal to 10^{-3}, in Eq. 5.63.

$$\omega_{dof,sum} = \sum_{j=1}^{n} \left| \frac{\Delta F^{i}_{elem,j} - \Delta F^{i-1}_{elem,j}}{\Delta F^{i}_{elem,j}} \right| \quad ; \quad \omega = \frac{\varepsilon_{dof,sum}}{n} \tag{5.63}$$

5.2.6 Internal forces

The internal forces in all the elements is computed with Eq. 5.64

$$\Delta\underline{s}_{elem} = \underline{\underline{k}}_{elem}\ \underline{\underline{R}}_{elem}\ \Delta\underline{u}_{elem} \tag{5.64}$$

where $\underline{u}_{elem}$ corresponds to the displacement at the considered element nodes.

5.3 Implementation

The equations detailed in the previous Section 5.2 are implemented in a *MATLAB* code to compute the resistance of the collided jacket.

The first step of the algorithm is to provide the geometrical (dimensions, number of tubular elements, location of the connections, ...) and mechanical (flow stress σ_0, Young modulus E, ...) properties of the jacket as well as the collisions parameters (location of the impact point, direction of the striking ship, ...). In case of a collision point located on a tubular element

between two connections, this element is divided into two adjacent ones, in order to apply the impact point displacement on a node.

With these data, the model, such as the one presented in Fig. 5.7, can be built.

The whole collision time is divided into several time steps Δt defined by the user. Knowing the striking ship velocity v_{ship} and the chosen time step, the penetration Δu during that time step can be computed easily as $\Delta u = v_{ship}\Delta t$.

The elementary stiffness matrices $\underline{\underline{k}}$ and the elementary equivalent nodal loads vectors $\underline{f}$ can be computed with the equations described in Sections 5.2.1 and 5.2.2.

The assembly process is described by Eqs. 5.55 and 5.56. The displacement control is achieved using Eqs. 5.58 to 5.60.

After solving the matrix system, the internal effort $\Delta\underline{s}_{elem}$ in each tubular member can be computed with Eq. 5.64. The properties (displacement, crushing force, internal efforts) can be updated and the plasticity can be checked using the plasticity surface described in Eq. 5.28. This plasticity criteria can be easily computed with the nodal internal forces for tubular element ends, and requires the use of interpolation functions for the midspan of the element, as detailed in Section 5.2.2.2.

For each time step, several iterations may be required until convergence criteria is met. Then, the same procedure is performed for the next time steps.

The crushing force of the striking ship on the structure is computed at each time step. Assuming that the ship is perfectly rigid, its acceleration is also computed using the crushing force, and its velocity is updated. The methodology here described is then used as long as the ship velocity reaches zero.

The algorithm is represented graphically in Fig. 5.8.

5.4 Buckling of compressed tubular members

As discussed in Section 3.2.2, the collided jacket investigated in the present thesis corresponds to a real jacket. With this structure, the ratio D_e/t for the braces is equal to 13, where D_e is the external diameter of the tubular member and t its thickness. From other published papers, such as Travanca et al. [10] or Jin et al. [4], this ratio could go up to 50.

In our case, the ratio D_e/t is low compared to other installed structures, which makes the braces of the studied jacket stiffer. The deformation during the collision is therefore more likely to occur at the braces connections, which corresponds to punching that will be investigated in Chapter 6, than by buckling of the compressed braces.

However, the purpose of this thesis is to provide an algorithm able to assess the resistance of any collided jacket and buckling of compressed tubular members has to be modelled.

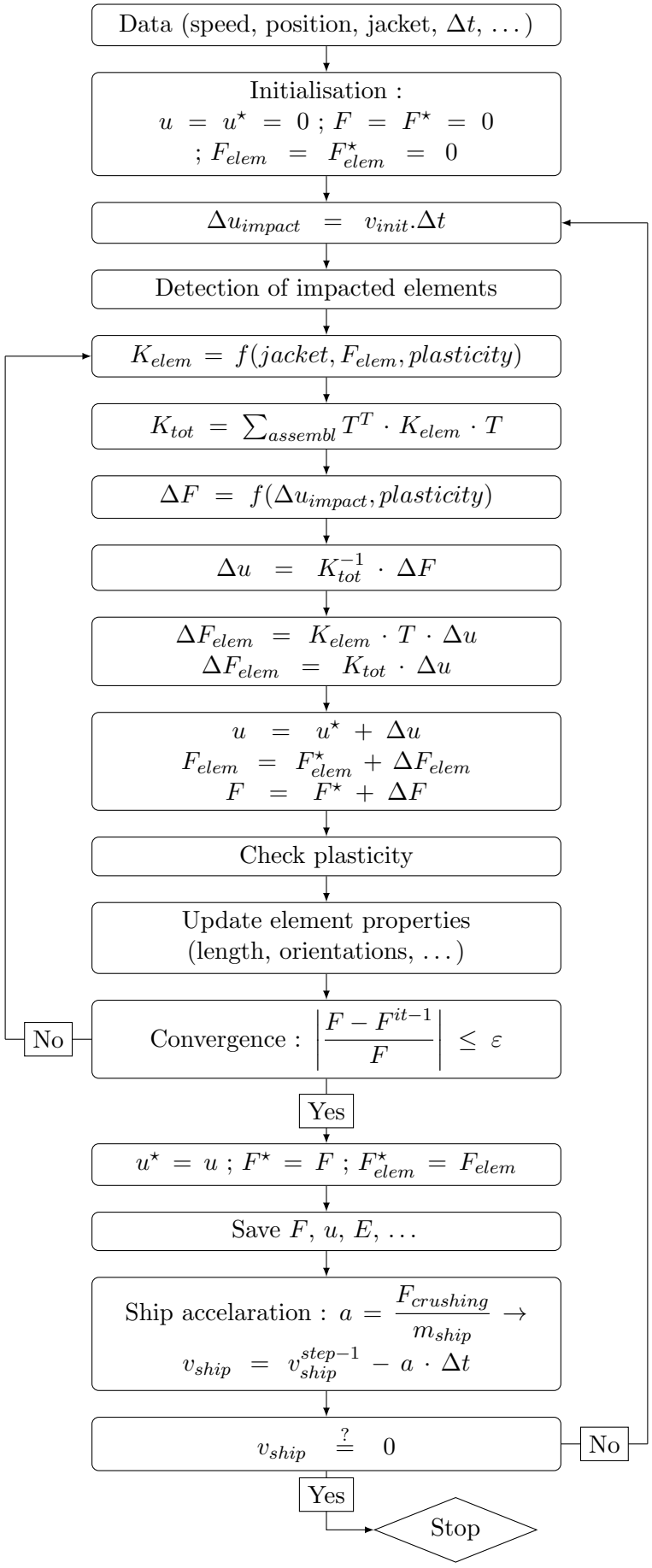

Figure 5.8: Algorithm to compute the jacket overall motion

Buckling consists in a sideways displacement of a compressed structural element, and is described amongst others by Massonet and Cescotto [5]. Let us consider the beam, initially perfectly straight, depicted in Fig. 5.9 and assumed to be part of the collided jacket. It is compressed with an axial force N and bent with bending moments M_A and M_B at nodes A and B respectively. If we assume that the beam is in the elastic regime, one has:

- At the first order of deformation, the lateral deflection u is due to the bending moments. At the studied cross-section, the bending moment is equal to $M = M_A\,(1 - w/l) + M_B w/l$.
- At the second order, the compressive forces N also creates a bending moment at the studied cross-section equal to Nu. The loading case could be stable for low values of compressive forces N but becomes unstable for large values. The value of N leading to instability depends on the beam geometry and material properties, the loading case and the boundary conditions.

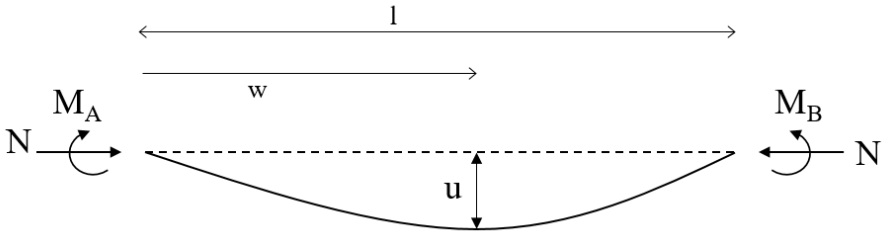

Figure 5.9: Lateral displacement of a compressed beam

As the lateral deformation increases, partial cross-section yielding occurs and leads to plastic hinges in the buckled beam. The cross-section the most likely to yield are located at the beam extremities (if they are clamped) and within the span of the beam, where the internal efforts are the largest.

In the previous example, the beam is initially perfectly straight. In practice however, some initial deformation exists and contributes to the lateral deformation u.

Buckling is accounted for in the presented algorithm. However, some assumptions are performed in order to keep the computation time short.

- All the jacket tubular members are assumed to be initially perfectly straight, no initial deformation are added in the model. At first order, the lateral deformation is therefore due to bending moments only.
- The second order effects are taken into account in the elementary elastic stiffness matrices described in Section. 5.2.1. Indeed, Timoshenko stability functions [9] are used to derive the formulations.
- Theoretically, buckling could occur by bifurcation for a perfectly straight member submitted to a compressive force but not bending moment. However, for all investigated collision

scenarios, bending moments appear in all tubular members of the jacket, and buckling occurs by divergence and includes second-order effects.

- As discussed in Section 5.2.2, it is considered that the cross-section is either in elastic regime or fully yielded, becoming a plastic hinge. The transition between both states, for which the extreme fibres are yielded and the other are still in elastic domain is not modelled. The formulation developed however allow to compute the energy dissipated through the plastic hinges.

- In the presented algorithm, plastic hinges may appear at beam extremities and at midspan. In reality, the third plastic hinge may occur at another cross-section than midspan. However, some numerical simulations demonstrated that assuming the third plastic hinge at midspan is close from its real location.

5.5 Numerical validation

The developed algorithm was validated by comparing the results with FE simulations performed on a full-scale jacket with *LS-DYNA*. As this Chapter covers only overall global deformations, it is compared with numerical model in which the jacket is modelled with beam finite elements that do not include cross-section deformation, such as crushing or punching, for example.

Several collision scenarios are investigated and modelled by imposing a constant velocity displacement on a node for a maximum node displacement of 0.24 m.

The investigated OWT jacket is introduced in Section 3.2.2 and is modelled in *LS-DYNA* with 9664 beam elements having an average length of 0.10 m.

For both the semi-analytical method and the numerical one, the material law is elastic - perfectly plastic, as described in Section 3.2.2. Here, the flow stress is equal to the yielding stress, i.e. $\sigma_0 = 255\ MPa$.

Please note that this deformation mode is the only one for which an elastic part is taken into account in the material model. Indeed, the analytical formulations developed in other Chapters would become too complex with an elastic part accounted for. The developed equations allow also to consider hardening, but it is not included here.

Several ship impact points are considered, as can be seen in Fig. 5.10, including two impacts on connections (in green) and two between connections (in red). For all the simulations, the impact point moves along the X axis on a distance of 0.24 m. For each of them, the deformed jacket computed with the algorithm presented in this Chapter is plotted in Figs. 5.11, 5.13, 5.15 and 5.17, with a displacement scale factor of 40. In those Figures, the solid lines correspond to the tubular members in compression and the dotted ones to members in tension, while the red spheres represent the plastic hinges occurring during the jacket deformation. The evolution of

the dissipated energy and of the crushing force is computed for all four scenarios and plotted in Figs. 5.12, 5.14, 5.16 and 5.18.

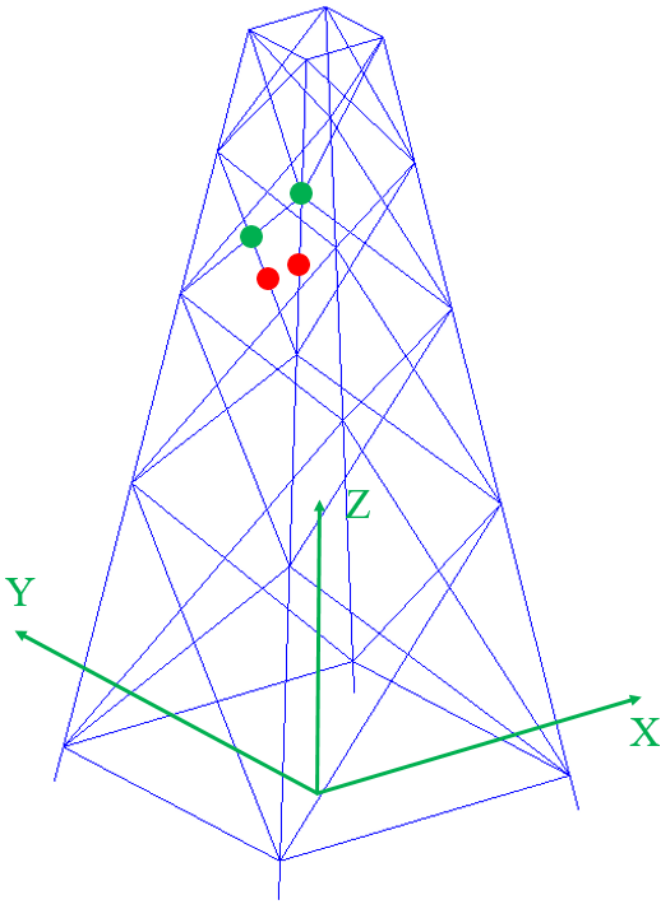

Figure 5.10: Impact points considered for the global deformation mode algorithm validation

Impact on the leg between connections

The elevation H of the impact point is 41 m. For a ship penetration of 0.24 m, the displacements, with a scale factor of 40, are given in Fig. 5.11. Internal energy and resistant force are plotted in Fig. 5.12. For a penetration larger than 0.1 m, the force becomes nearly constant due to the development of a three plastic hinges mechanism on the impacted tubular member.

At the end of the deformation, the difference of dissipated energy is equal to 0.1%.

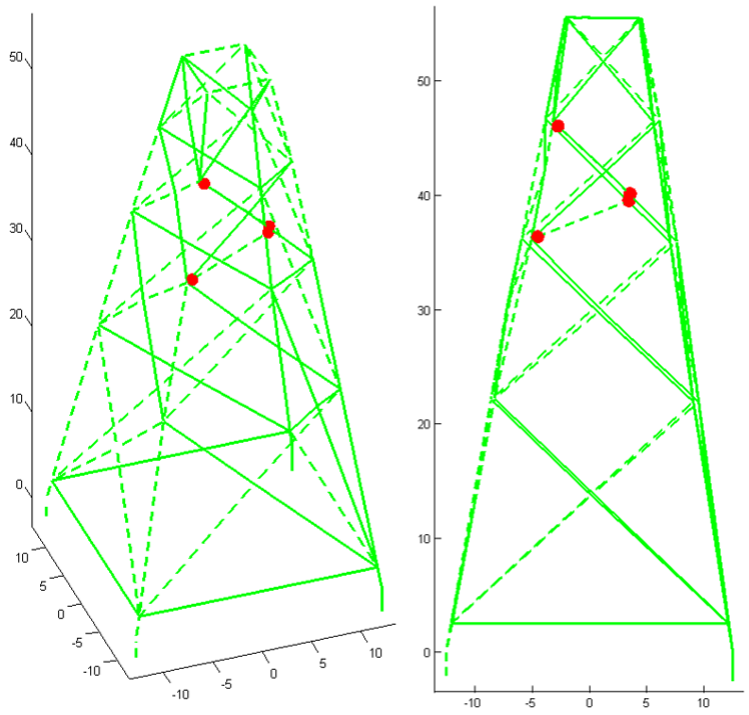

Figure 5.11: Displacement for a collision on a leg between connections (oblique and side view)

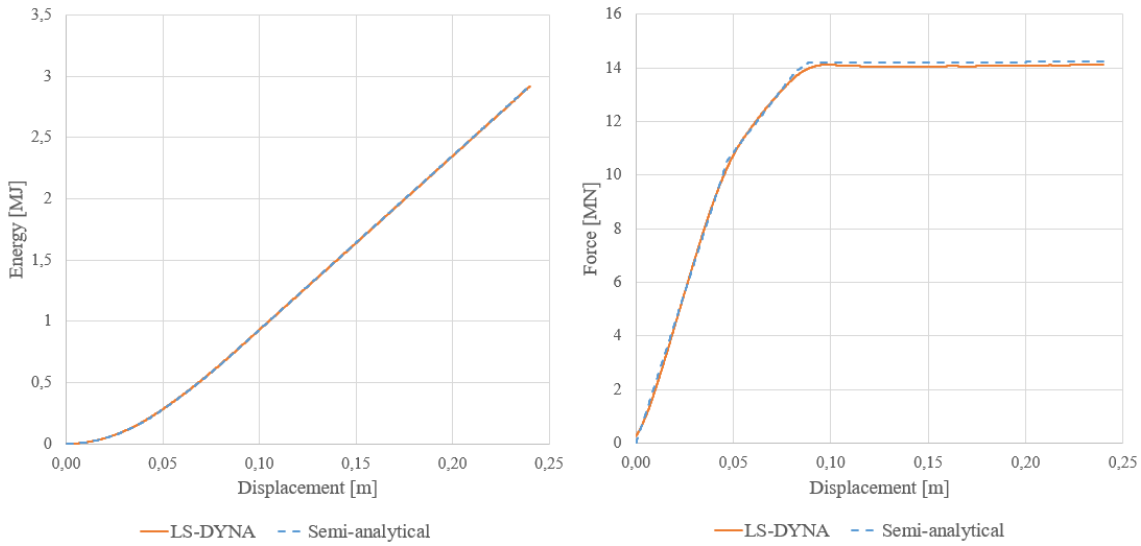

Figure 5.12: Comparison of the internal energy and total resistant force obtained semi-analytically and numerically for a collision on a leg between connections

Impact on the brace between connections

The elevation of the impact point is 39 m. The jacket deformation is presented in Fig. 5.13 and the internal energy and resistant force are plotted in Fig. 5.14.

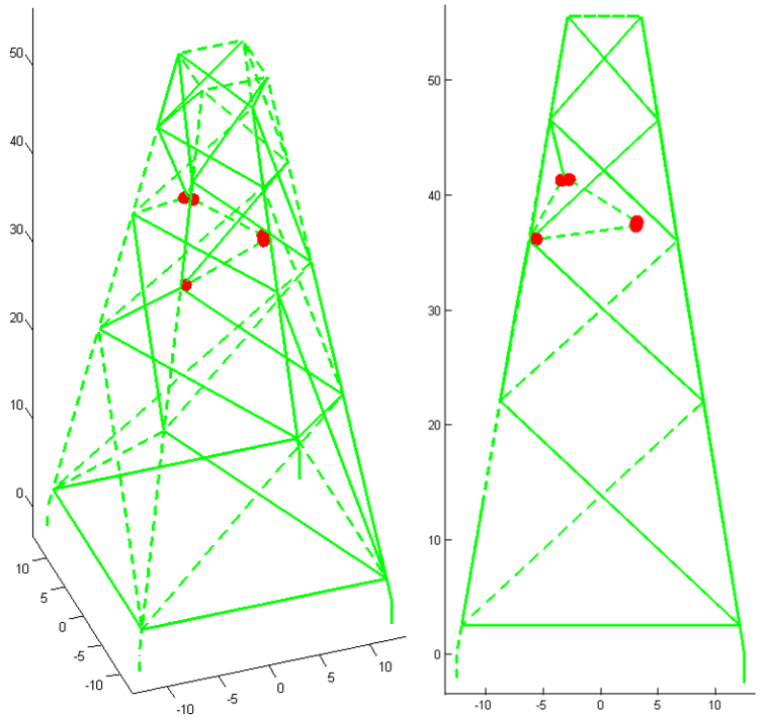

Figure 5.13: Displacement for a collision on a brace between connections (oblique and side view)

In this case, the discrepancy in terms of dissipation of energy between the semi-analytical and the numerical models is equal to 1%.

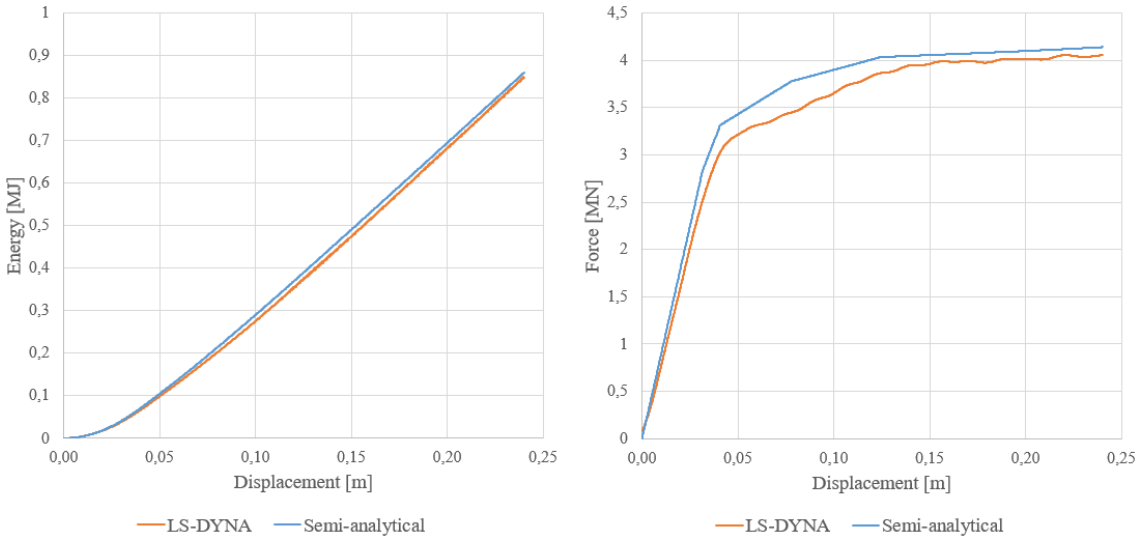

Figure 5.14: Comparison of the internal energy and total resistant force obtained semi-analytically and numerically for a collision on a brace between connections

Impact on the leg on a connection

The displacements are shown in Fig. 5.15 while the internal energy and resistant force are presented in Fig. 5.16.

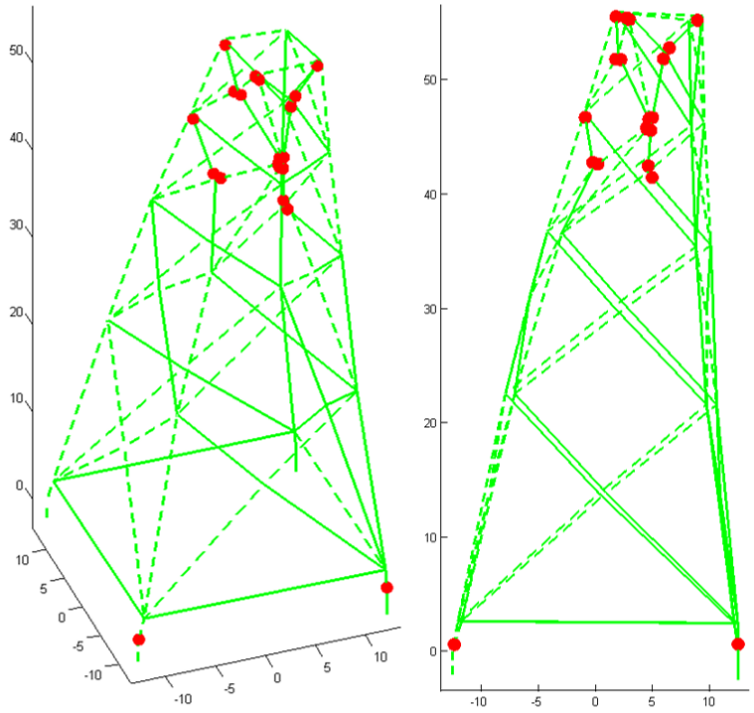

Figure 5.15: Displacement for a collision on a leg on a connection (oblique and side view)

Here, the discrepancy in terms of dissipated energy is equal to 10%. By analysing the results, this difference is due to fact that buckling of compressed braces cannot be modelled as accurately as with fine mesh in numerical model because plastic hinges may appear only in the middle of the element, which is not identical to what is observed in *LS-DYNA* results.

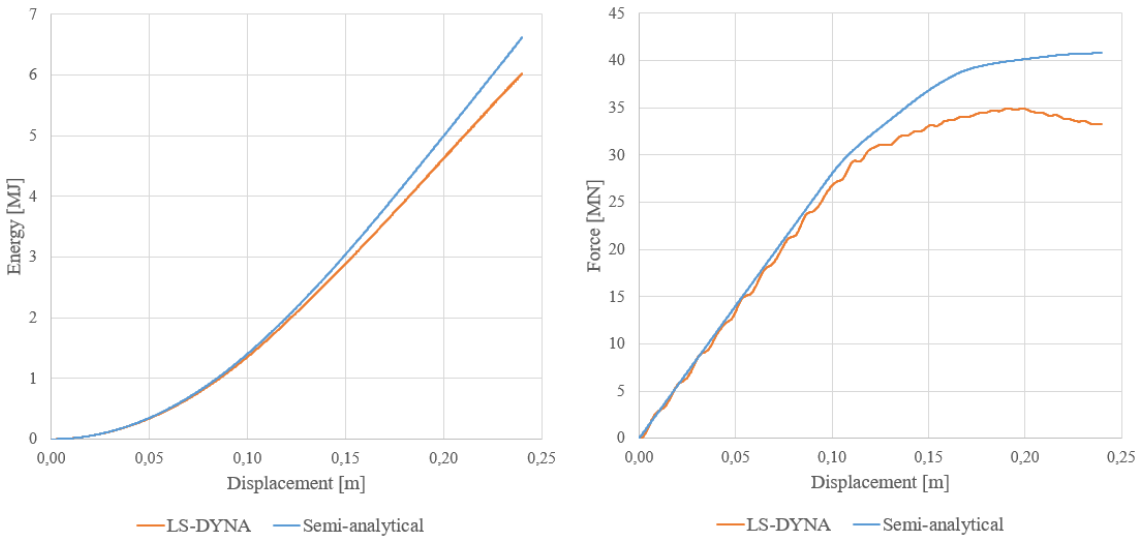

Figure 5.16: Comparison of the internal energy and total resistant force obtained semi-analytically and numerically for a collision on a leg on a connection

Impact on the crossing of braces

The displacements are given in Fig. 5.17 and the internal energy and resistant force are plotted in Fig. 5.18.

Regarding this final investigated scenario, the discrepancy is equal to 2%.

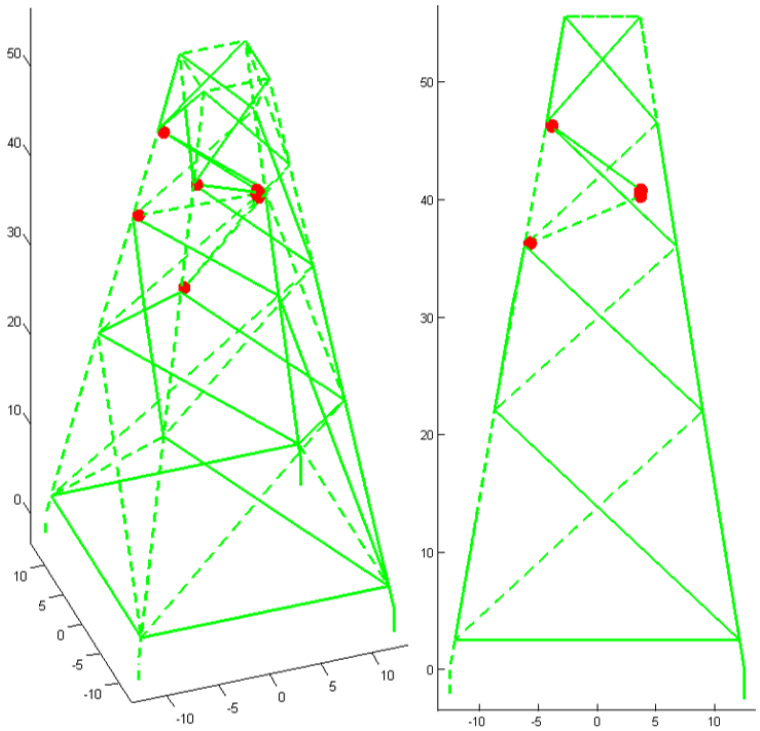

Figure 5.17: Displacement for a collision on the crossing of braces (oblique and side view)

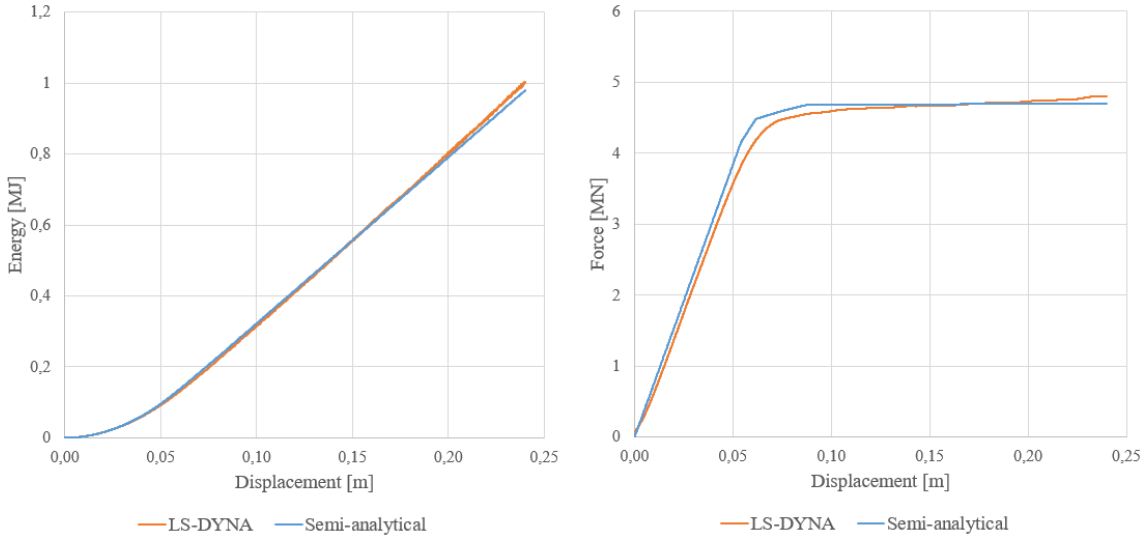

Figure 5.18: Comparison of the internal energy and total resistant force obtained semi-analytically and numerically for a collision on the crossing of braces

5.6 Conclusions

In this Chapter, a complete algorithm to compute the overall displacement of an OWT jacket impacted by a ship is described. The formulations cover the global jacket movement without any local tubular member cross-section deformations, these phenomena being included in other deformation modes listed in Chapter 3 and described in Chapters 4, 6 and 7.

The methodology described here is similar to the one used in FE approach, the main specificity here being that the size of the elements as each tubular member of the jacket corresponds to one single element in the model. We consider in the model that each element is a beam element with 6 degrees of freedom at each extremity (3 displacements and 3 rotations).

First, the elastic elementary stiffness is derived for a tubular beam element, including geometrical second order effects using Timoshenko stability functions and semi-rigid connections going from perfectly hinged to perfectly clamped.

Plastic hinges may appear if the stress state reaches the plastic surface, as it is defined in the Eurocode. Elementary stiffness matrix formulations are then modified at nodes where a plastic hinge occur. Considering the modified expressions, the stress state moves tangentially to the plastic surface, and external forces are considered to remain on the plastic surface at every node.

In the algorithm, it is assumed that only three plastic hinge locations are possible on an element, namely each extremity and the midspan. In case of a plastic hinge at midspan, the considered element is split into two adjacent elements with a plastic hinge between them.

The whole jacket model is built by assembling all the elementary stiffness matrices and load vectors. In order to consider a displacement control, some additional modifications on the global stiffness matrix and load vectors are performed. Finally, after solving the matrix system, the internal forces can be computed.

All the equations are implemented in an incremental algorithm in *MATLAB*. The crushing process is divided into several time steps, and the evolution of the resistance force, nodes displacements and internal forces is computed at each of them.

Finally, four collision scenarios are investigated to validate the formulations. The results computed with the methodology described in this Chapter are compared to the results provided by the *LS-DYNA* FE software. It appears from the validation that the developed model provides results in good accordance with the FE results, with discrepancies lower than 10%. Only situations where buckling of compressed braces occurs lead to an overestimation of the crushing force and dissipated energy, due to the fact that plastic hinges is assumed to appear only at the middle of the element and not at its real location. However, regarding the jacket considered in our study, such large global displacements do not occur for collisions energies investigated in the model, as will be computed in Section 8.5 dedicated to the validation of the complete algorithm.

Bibliography

[1] JD Aristizabal-Ochoa. First- and second-order stiffness matrices and load vector of beam-column with semi rigid connections. *Journal of Structural Engineering*, (123):669–678, 1997.

[2] SG Ekhande, M Selvappalam, and MKS Madugula. Stability functions for three-dimensional beam columns. *Journal of Structural Engineering*, (115(2)):467–479, 1989.

[3] Eurocode 3: Design of steel structures - part 1-1: General rules and rules for buildings. Standard, European Committee for Standardization, Brussels, 2005.

[4] WL Jin, J Song, SF Gong, and Y Lu. Evaluation of damage to offshore platform structures due to collision of large barge. *Engineering Structures*, (27):1317–1326, 2005.

[5] C Massonet and S Cescotto. *Mécanique des Matériaux*. de Boeck, 1994.

[6] Mathworks. *mldivide,* \. `https://nl.mathworks.com/help/matlab/ref/mldivide.html`, seen on October, 25 2017.

[7] CG Salmon and JE Johnson. *Steel structures: design and behavior*. Harper & Row, Inc., New York, 2nd edition edition, 1980. chapter 14.

[8] TH Soreide, J Amdahl, E Eberg, T Holmas, and O Hellan. USFOS - A Computer Program for Progressive Collapse Analysis of Steel Offshore Structures. Theory Manual. Technical Report STF71 F88038, SINTEF, 1988.

[9] S Timoshenko and J Gere. *Theory of elastic stability*. McGraw-Hill Book Co., Inc., New York, 2nd edition edition, 1961. Chapter II.

[10] J Travanca and H Hao. Energy dissipation in high-energy ship-offshore jacket platform collisions. *Marine Structures*, (40):1–37, 2015.

[11] CK Wang. *Intermediate structural analysis*. McGraw-Hill Book Co., Inc., New York, 1983. Chapter 20.

[12] B Wu, Z Xu, and Z Li. A note an imposing displacement boundary conditions in finite element analysis. *Communications in Numerical Methods in Engineering*, (24):777–784, 2008.

Chapter 6

Punching of legs by compressed braces

Abstract:

This Chapter presents a semi-analytical method developed to compute the energy dissipated by plastic deformation of punched offshore jacket legs during a ship collision event. Punching may occur on both impacted and rear legs at the connection with compressed braces.

Using the upper-bound theorem associated with plastic limit analysis, analytical expressions are derived to assess the resistant force and the deformation energy of a tubular member clamped at both extremities and crushed by an indenter. Those expressions are then enriched with some empirical parameters determined to assess the resistance of a leg punched by one or two connected braces, with several diameter ratios, angles between involved cylindrical members, different tubular member spans and gaps between connected braces.

These developments are successfully validated by comparison with both *NORSOK* standard-design formulas and nonlinear FE simulations performed on two and three tubular members models.

A general methodology is finally established in order to take into account punching on the whole height of the impacted OWT jacket.

6.1 Introduction

In Chapter 3, four deformation modes for a collided OWT jacket were identified, namely:

- local crushing of impacted tubular members (Chapter 4);
- global deformation of the whole jacket (Chapter 5);
- punching of legs by compressed braces (present Chapter);
- deformation at the base of the jacket (Chapter 7).

The purpose of this Chapter is to present semi-analytical developments performed to consider the *punching of a leg by compressed braces* deformation mode. A typical example of punching can be seen in Fig. 6.1 where the effective plastic strain distribution is plotted. The fringe levels are set in order to highlight in red the elements for which the effective plastic strain is larger than 1%.

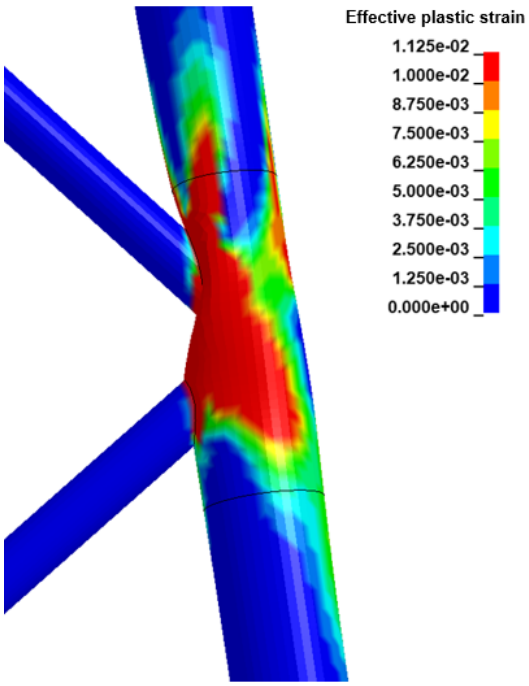

Figure 6.1: Effective plastic strain on a punched area

First, the formulations proposed by Buldgen, Le Sourne and Pire [2] (Chapter 4), developed for impacted tubular members, are extended to calculate analytically the resistance of a leg that is punched by one or two braces, as already investigated by Hsieh [6]. The deformation pattern description is modified to take into account the interface between the leg and the brace. However, the description of this pattern is not performed fully analytically and some empirical parameters are included to consider the ratio between leg and brace diameters. Resulting expressions are then validated by comparison with numerical simulations, in a range of geometrical parameters corresponding to typical wind turbine jackets.

As punching may occur on several braces - leg connections, a methodology used to predict the punching process on the whole jacket is developed and presented. The validation is performed by comparing resulting deformation energies and resistant forces with numerical simulation results for several ship collision scenarios.

6.2 General description of the punching deformation process

At the beginning of this study, some FE simulations were performed in order to identify the main parameters that govern the punching behaviour of an offshore wind turbine jacket impacted by a ship.

As an illustration, the collision scenario depicted in Fig. 6.2 was considered, involving aforementioned jacket and a non-bulbous OSV. The striking ship, considered as rigid for this study, has a mass of $6,000$ tons (added mass included) and an initial velocity of 5 m/s in the surge direction, its sway and heave movements being restrained. The initial kinetic energy is therefore 75 MJ.

As already discussed in Section 3.6, rupture has a negligible influence on the punching deformation mode and is thus not considered in this FE simulation.

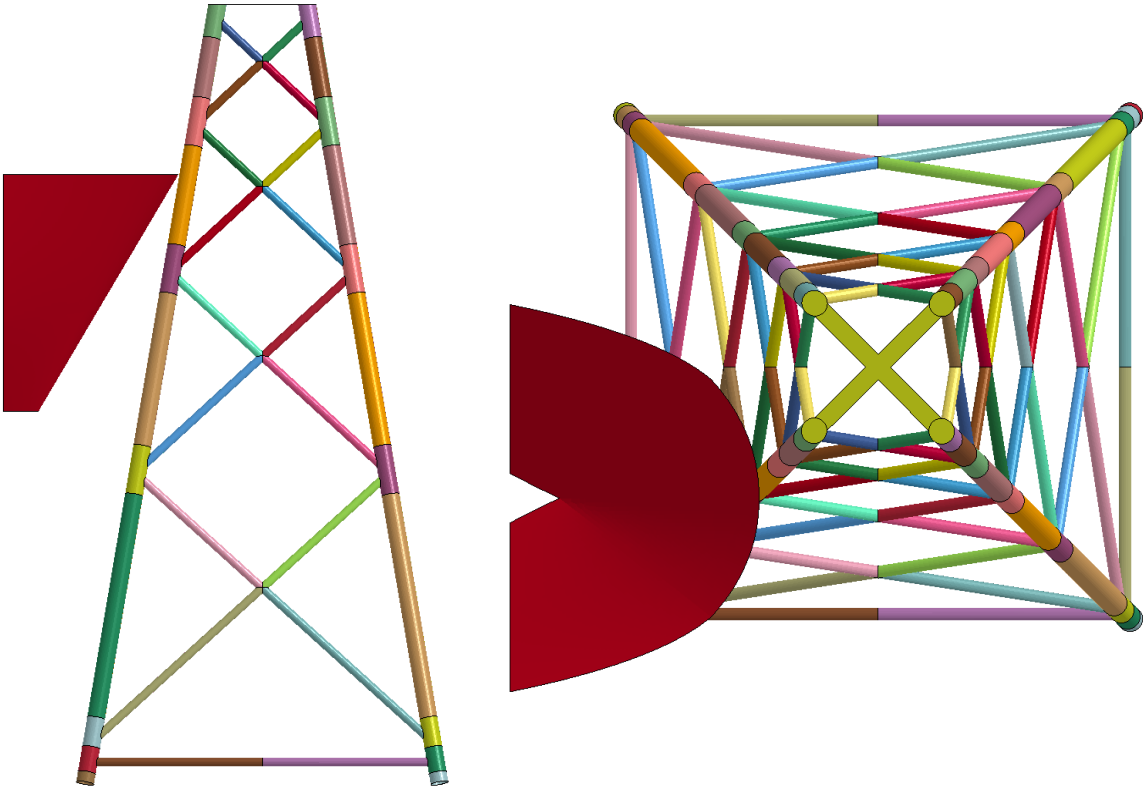

Figure 6.2: Collision scenario considered to illustrate the punching of legs by compressed braces

The deformation of the impacted jacket as well as the effective plastic strain distributed in the impacted plane are presented at 0.25, 0.45, 0.65 and 1 second after the collision in Figs. 6.3,

6.4, 6.5 and 6.6 respectively. The connections between braces and legs where punching occurs are highlighted by red circles. The elements submitted to effective plastic strains larger than 1% are depicted in red colour.

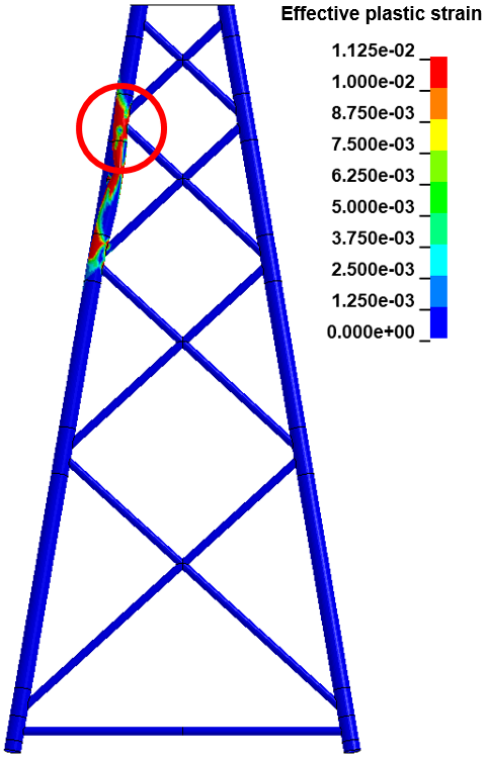

Figure 6.3: Effective plastic strain at 0.25 s

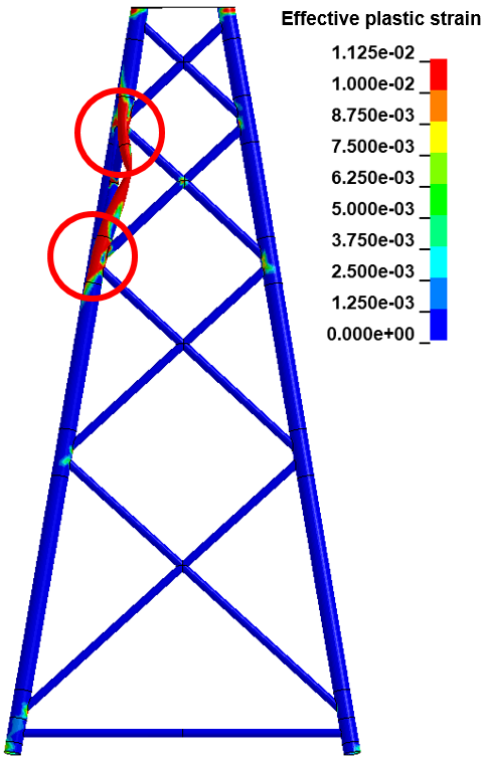

Figure 6.4: Effective plastic strain at 0.45 s

In those Figures, the effective plastic strain does not exceed 20% in the punched areas.

Numerical simulations showed that some tubular members are solicited in compression and others in tension, as shown in Fig. 6.7 where the axial internal forces of the cylindrical members located in the impacted plane are plotted. In this Figure, compressed tubular members are represented in full line and tensioned ones in dotted line. The span of the connection circled in green is also defined.

From these numerical results, it has been concluded that:

- For each connection, the punching process depends on several parameters, amongst others:
  - The number of involved braces (1 or 2) in the punching process
  - The type of solicitation of braces: tension or compression
  - The angle between the leg and the connected braces
  - The ratio between leg and brace diameters
  - The mechanical properties
  - ...
- The punching process on each connection is activated only when the ship penetration reaches a given value.

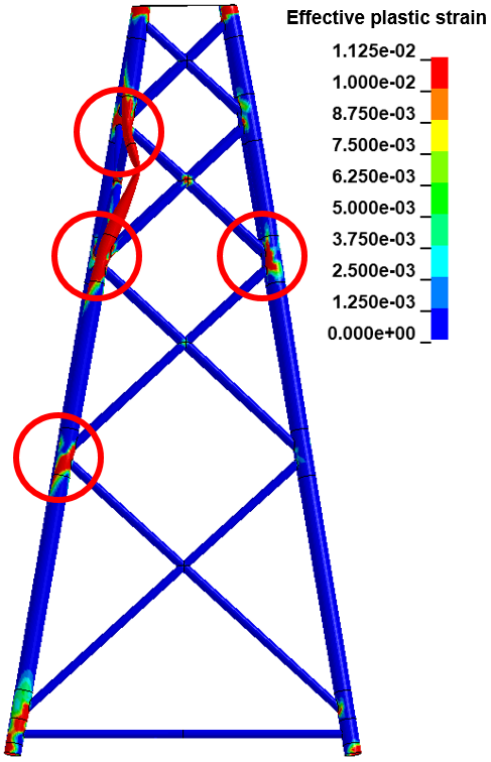

Figure 6.5: Effective plastic strain at 0.65 s

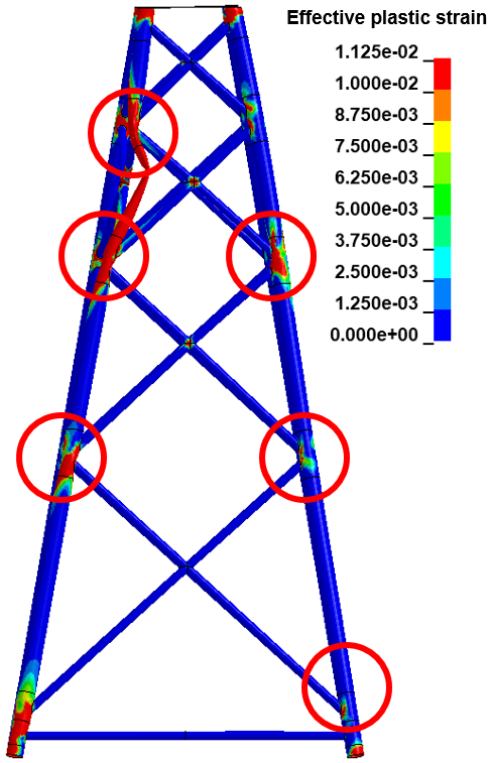

Figure 6.6: Effective plastic strain at 1 s

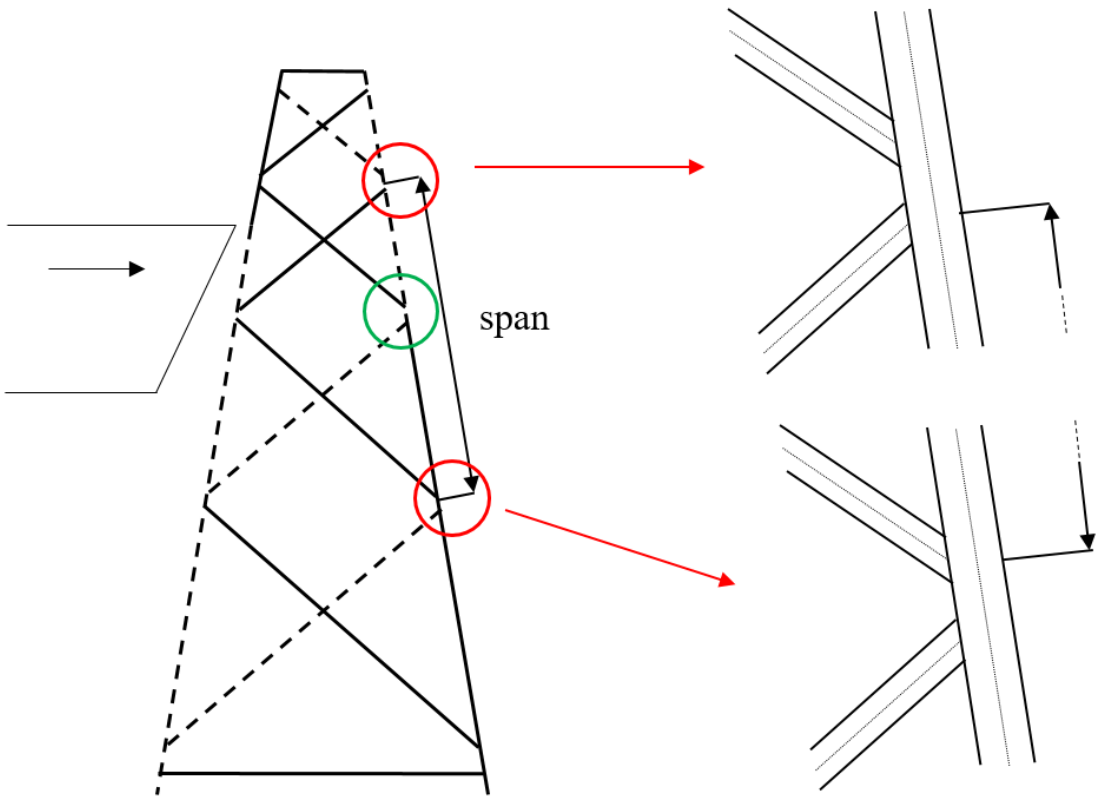

Figure 6.7: Compression and tension in the tubular elements of the collided jacket

- The punched connections are first located at level of the impact point and then spread as the ship penetration increases.

The equations developed to compute the resistance of a leg punched by compressed braces are described in the next Section. Then, the methodology that is used to take into account all the connections where punching may occur is presented.

6.3 Semi-analytical developments to assess the punching behaviour on one connection

Hsieh [6] developed formulations to assess the punching behaviour of tubular members in her Master's thesis as an extension of the work performed by Buldgen, Le Sourne and Pire [2] and under the supervision of those researchers. The results presented in this Section are developed based on her work.

6.3.1 Deformation mechanism

As mentioned in the introduction, four deformation modes were identified from numerical simulations on an offshore wind turbine jacket impacted by ship. The purpose of this section is to develop closed-form formulations dedicated to the *punching* deformation mode in order to compute rapidly the resistance of a leg punched by a compressed brace at one single connection.

The presented method is qualified as "semi-analytical" because it is mainly based on analytical developments (upper-bound theorem). However, the developed equations are not able to explicitly capture the intersection surface between the leg and the brace and to accurately model the cross-section local deformation. Therefore, the analytical expressions are enriched with two empirical parameters β and Q_β that allow to account for the ratio between leg and brace diameters (Eq. 6.1), as will be detailed later on.

$$\beta = \frac{D_{leg}}{D_{brace}} \tag{6.1}$$

The deformation patterns of the cross-section and along a punched leg, obtained from numerical simulations, are presented respectively in Figs. 6.8 and 6.9, while the displacement fields considered for semi-analytical derivations are plotted in Fig. 6.10 and 6.11 respectively. Although the interface between a leg and a brace is oval, as depicted in Fig. 6.12, an inscribed rectangular one is considered to simplify the derivations while being conservative. Moreover, this interface is assumed to displace without deforming all along the deformation process.

As the leg cross-section deformation is concerned, the described displacement field is similar to the one proposed by Buldgen et al. [2], who developed analytical formulations to assess the resistance of a fully clamped tubular member impacted by a ship bow (Chapter 4). However, the

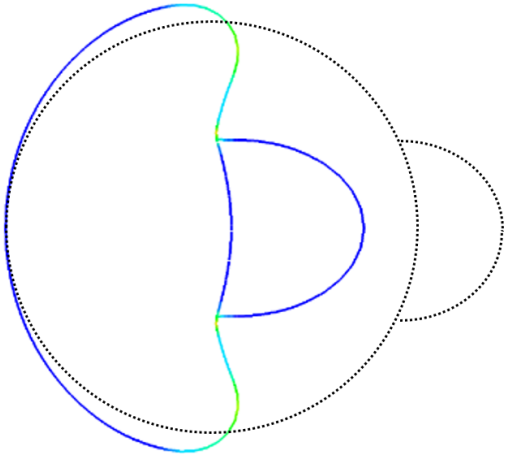

Figure 6.8: Initial and deformed leg cross-section (computed numerically)

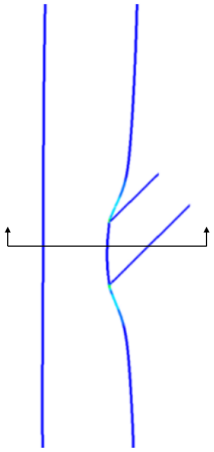

Figure 6.9: Deformation along the leg generators (computed numerically)

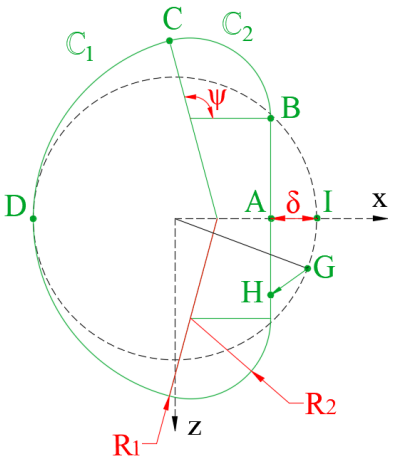

Figure 6.10: Assumption on the cross-section deformation

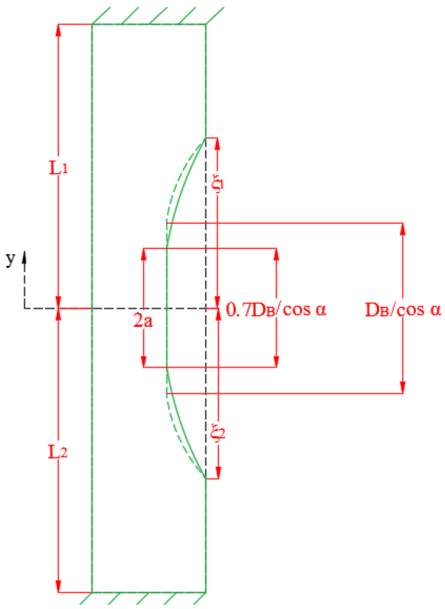

Figure 6.11: Assumption on the deformation along the leg generators

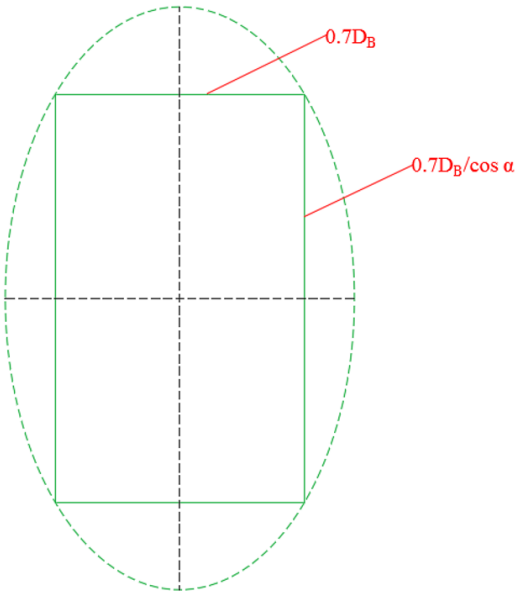

Figure 6.12: Interface area between the leg and the brace

choice of the displacement field along the generators is driven by the fact that the intersection area is rectangular and not elliptic.

During the whole deformation, the braces are assumed to remain rigid so all the energy is dissipated by the punched leg deformation. This latter is considered to be composed of independent rings able to slide without shearing along independent generators.

The deformation mechanism depicted in Fig. 6.10 was initially suggested by Wierzbicki and Suh [11]. It is composed of two arcs with a radius of R_1 and R_2 respectively and a straight line AB. At the junction of those areas are two plastic hinges B and C. The aforementioned authors described it by the following set of equations. The radius of the undeformed ring being denoted by R, the indentation δ may be expressed as :

$$\delta = 2R - [R_1 (1 + \cos\psi) + R_2 (1 - \cos\psi)] \tag{6.2}$$

where the angle ϕ is depicted in Fig. 6.10. A second expression comes from the assumption that the ring is inextensible during the whole deformation process. As the deformed cross-section remains symmetric with regard to x-axis, the mathematical expression in Eq. 6.3 stands for half the ring.

$$R_1 (\pi - \psi) + R_2\psi + \overline{AB} = \pi R \tag{6.3}$$

Using Eqs. 6.2 and 6.3, R_1 and R_2 can be expressed as functions of R and ψ.

$$R_1 = R + \frac{\delta (\psi - \sin\psi)}{\pi (1 - \cos\psi) - 2 (\psi - \sin\psi)} \tag{6.4}$$

$$R_2 = R - \frac{\delta\left(\pi - \psi + \sin\psi\right)}{\pi\left(1 - \cos\psi\right) - 2\left(\psi - \sin\psi\right)} \tag{6.5}$$

$$\overline{AB} = \left(R_1 - R_2\right)\sin\psi \tag{6.6}$$

The value of ψ was suggested by Wierzbicki and Suh [11] as a power dependence given by Eq. 6.7. The angle φ describes the position of the plastic hinges and is linked to ψ with Eq. 6.8.

$$\frac{R_2}{R} = \left(\frac{\varphi}{\varphi_0}\right)^n \tag{6.7}$$

$$\psi = \pi - \varphi \tag{6.8}$$

Zeinoddini et al. [12] proposed a linear relationship to express the value of φ (Eq. 6.9)

$$\frac{\delta}{2R} = 1 - \frac{\varphi}{\varphi_0} \tag{6.9}$$

which can be expressed with regard to ψ (Eq. 6.10)

$$\psi = \psi_0 + \left(\pi - \psi_0\right)\frac{\delta}{2R} \tag{6.10}$$

From this expression, it can be seen that the cross-section is completely crushed when $\psi = \pi$.

Both Wierzbicki and Suh [11] (Eq. 6.7) and Zeinoddini et al. [12] (Eq. 6.10) investigated the effect of the parameter ψ_0. They proposed some graphs giving the evolution of the non-dimensional resistant force (F is the resistant force, M_0 is the plate fully plastic bending moment and R is the tubular member radius) as a function of the non-dimensional penetration (Figs. 6.13 and 6.14). Here, $\psi_0 = \pi - \theta_0$. It appears that for a given penetration, the force increases with the reduction of ψ_0.

Buldgen et al. [2] used Eq. 6.10 to assess analytically the resistance of a dented tubular member. From this work, it was demonstrated that the crushing behaviour is well-predicted for a value of $\psi_0 = 3\pi/4$.

From results obtained by Lee et al. [8] and numerical simulations performed in the framework of this PhD thesis, it appears that expressions given here above is not well suited for the punching mode. Fig. 6.15 shows that the β ratio influences substantially the resistant force vs indentation curve.

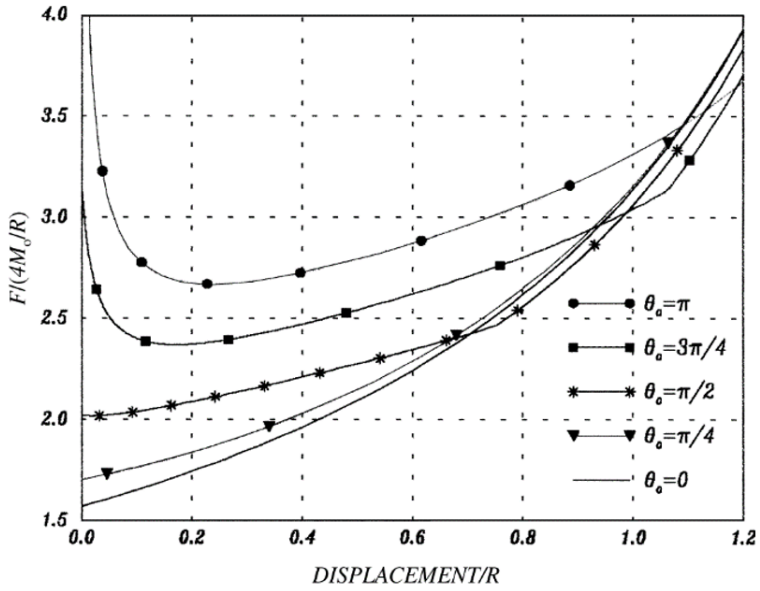

Figure 6.13: Non-dimensional force-penetration curve for laterally damaged tubular members according to [11]

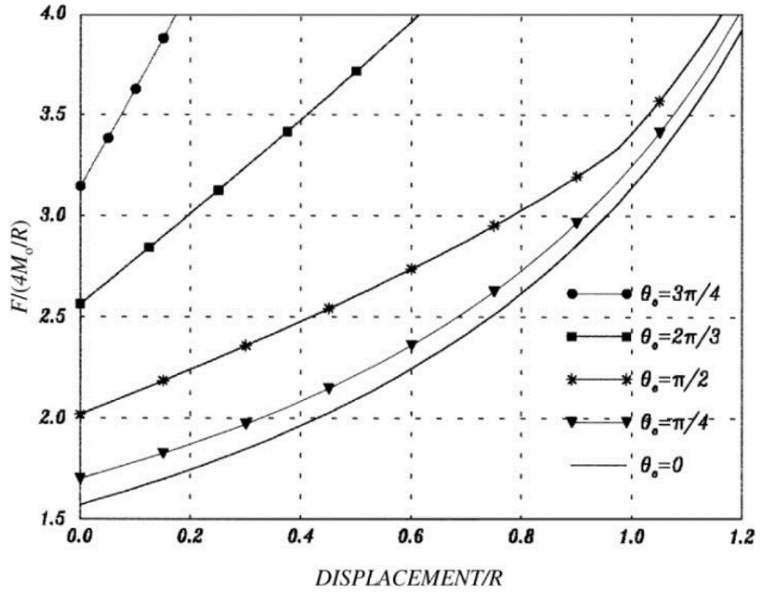

Figure 6.14: Non-dimensional force-penetration curve for laterally damaged tubular members according to [12]

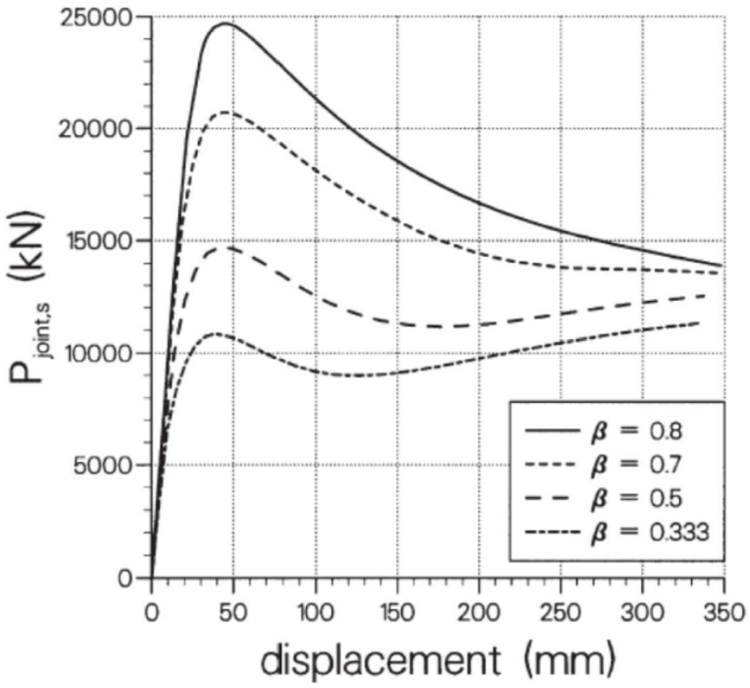

Figure 6.15: Force-penetration curves for several β ratios [8]

It also appears that the punching resistance cannot be represented by the equations described here above and used in Chapter 4. A value a ψ_0 leading to a higher resistant force has to be selected, and a value of $\psi_0 = \pi/3$ is suggested and checked later on. In addition, as the cross-section is completely crushed at $\psi = \pi/2$, a new expression of ψ is proposed:

$$\psi = \psi_0 + \left(\frac{1}{2}\pi - \psi_0\right)\frac{\delta}{2R} \tag{6.11}$$

with $\psi_0 = \pi/3$.

As mentioned above, the deformed cross-section remains symmetric with regard to x-axis during the whole deformation and the ring is assumed to be inextensible. Therefore, the distance $\overline{GI}$ and $\overline{AH}$ are the same. The displacement of a point G moving to point H may be written as:

$$w(\theta, \delta) = \sqrt{(x_H - x_G)^2 + (z_H - z_G)^2} \tag{6.12}$$

The deformed cross-section is then divided into three different areas, each being defined by the angle θ according to Eq. 6.13, respectively for the flat region, for the arc C_2 and for the arc C_1.

$$\begin{array}{ll} 0 \leq \theta \leq \frac{(R_1 - R_2)\sin\psi}{R} & \text{for } AB \\ \frac{(R_1 - R_2)\sin\psi}{R} \leq \theta \leq \frac{(R_1 - R_2)\sin\psi}{R} + \frac{R_2\psi}{R} & \text{for } C_2 \\ \frac{(R_1 - R_2)\sin\psi}{R} + \frac{R_2\psi}{R} \leq \theta \leq \pi & \text{for } C_1 \end{array} \tag{6.13}$$

The deformation varies also along the dented tubular member axis. The velocity field is supposed to vary linearly when $-\xi_2 \leq y \leq -a$ and $a \leq y \leq \xi_1$ and to be constant when $-a \leq y \leq a$, as suggested by Wierzbicki [11]. When $y < -\xi_2$ and $y > \xi_1$, the generators remain undeformed. Resulting expressions of the displacements are as follows:

$$\begin{array}{ll} W(\theta,\delta,y) = 0 & \text{if } y \in [\xi_1; L_1] \\ W(\theta,\delta,y) = w(\theta,\delta)\left(1 - \frac{y-a}{\xi_1(\delta)-a}\right) & \text{if } y \in [a; \xi_1(\delta)] \\ W(\theta,\delta,y) = w(\theta,\delta) & \text{if } y \in [-a; a] \\ W(\theta,\delta,y) = w(\theta,\delta)\left(1 + \frac{y+a}{\xi_2(\delta)-a}\right) & \text{if } y \in [-\xi_2(\delta); 0] \\ W(\theta,\delta,y) = 0 & \text{if } y \in [-L_2; -\xi_2(\delta)] \end{array} \tag{6.14}$$

The velocity field $\dot{W}(\theta,\delta)$ is then computed by deriving above expressions with respect to time.

$$\begin{array}{ll} \dot{W}(\theta,\delta,y) = 0 & \text{if } y \in [\xi_1; L_1] \\ \dot{W}(\theta,\delta,y) = \dot{w}(\theta,\delta)\left(1 - \frac{y-a}{\xi_1(\delta)-a}\right) & \text{if } y \in [a; \xi_1(\delta)] \\ \dot{W}(\theta,\delta,y) = \dot{w}(\theta,\delta) & \text{if } y \in [-a; a] \\ \dot{W}(\theta,\delta,y) = \dot{w}(\theta,\delta)\left(1 + \frac{y+a}{\xi_2(\delta)-a}\right) & \text{if } y \in [-\xi_2(\delta); 0] \\ \dot{W}(\theta,\delta,y) = 0 & \text{if } y \in [-L_2; -\xi_2(\delta)] \end{array} \tag{6.15}$$

FE simulations show that leg local deformation is followed by a global bending mode of the punched tubular member. At the beginning of the deformation, local punching is activated then global bending mode gradually develops. In reality, both mechanisms overlap during a certain period. However, for analytical developments, a threshold is defined as the minimal load that can activate the global bending mode. The evolution of the resistant force of a punched tubular member is plotted in Fig. 6.16, where the local resistance of a leg punched by a brace is depicted in red and the global resistance of this tubular member in green. The total resistance is the minimum of both of them, and is represented with thick lines. As long as $\delta < \delta_t$, the punching local mode is activated. When $\delta = \delta_t$, the deformation mode switches to the global one. δ_t is therefore the transition point (threshold) between local and global modes.

The global mode can be seen as a plastic bending of clamped beam, considering four plastic hinges, one at each beam extremity and two bounding the connection between the brace and the leg, as depicted in Fig. 6.17. As the tubular member is locally dented of a value δ_t, the global deflection is equal to $\delta - \delta_t$.

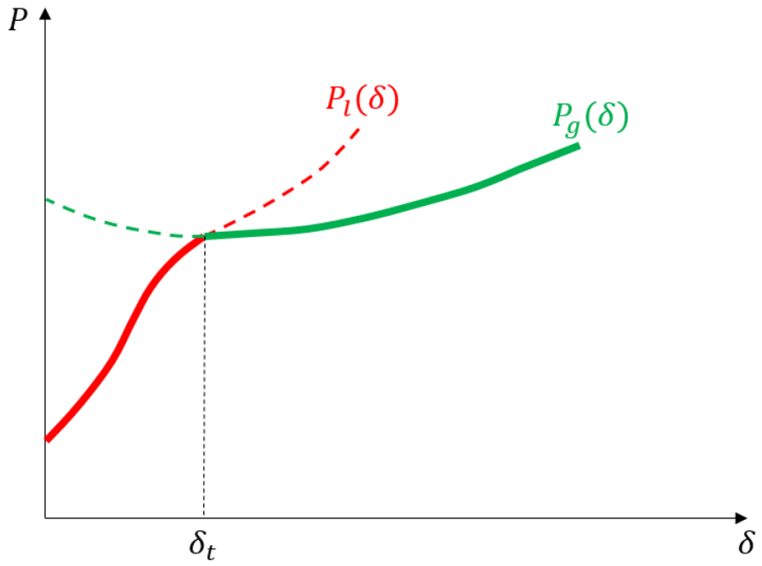

Figure 6.16: Evolution of the punching force with the local P_l and global P_g mode

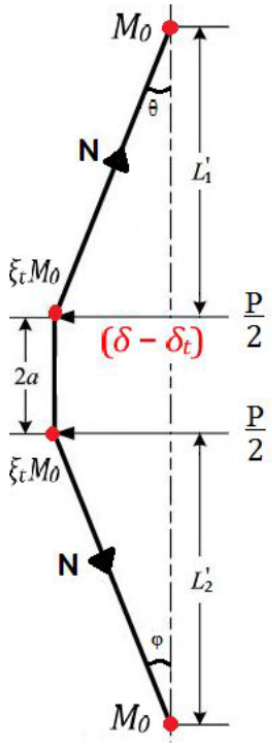

Figure 6.17: Punching global deformation mode mechanism [6]

6.3.2 Semi-analytical developments

The derivation of analytical expressions is based on the so-called upper-bound theorem (Jones [7] for more details), which states that the external power equals the internal energy rate, as expressed in Eq. 6.16.

$$P\dot{\delta} = \dot{E}_{int} \tag{6.16}$$

where P is the contact force between the leg and the brace, $\dot{\delta}$ is the velocity of the contact point and $\dot{E}_{int}$ is the rate of energy dissipated by the plastic deformation of the punched area.

6.3.2.1 Local punching resistance

During local section deformation, energy is dissipated through axial, flexural and shear effects. As suggested by Wierzbicki [11], shear effects can be neglected so a punched tubular member can be assumed to be composed of inextensible rings that can slide without friction along generators. The total energy rate is therefore the rate of energy dissipated by the rings $\dot{E}_r$ plus the rate of energy dissipated by the generators $\dot{E}_g$, as expressed in Eq. 6.17.

$$\dot{E} = \dot{E}_r + \dot{E}_g \tag{6.17}$$

The total internal energy rate is thus the sum of the contributions of the continuous velocity field (first integral in Eq. 6.18, with respectively the contribution of bending moments and membrane forces) and the discontinuous one at stationary or moving plastic hinges (summation):

$$\dot{E}_{int} = \int_S \left(M\dot{\kappa} + N\dot{\varepsilon}\right) dS + \sum_i \int_{\Gamma_{(i)}} M_0^{(i)} \left[\Omega\right]^{(i)} d\Gamma \tag{6.18}$$

where

- M is the bending moment and $\dot{\kappa}$ is the curvature rate
- N is the membrane force and $\dot{\varepsilon}$ is the extension rate
- M_0 is the fully plastic bending moment
- Ω is the relative rotation rate on both side of the hinge
- dS and $d\Gamma$ are the current deformed surface element and the hinge line respectively

Rate of energy dissipated by rings plastic deformation

As the rings are assumed to be inextensible, their deformation includes plastic circumferential bending of C_1 and C_2 and rotation of moving plastic hinges (Figs. 6.8 and 6.10). Here, the

circumferential bending moment is supposed to be independent of the axial force and is therefore considered as the fully plastic bending moment M_0. For the rings, Eq. 6.18 becomes:

$$\dot{E}_b = \int_L M\dot{\kappa} ds + \sum_i M_0^{(i)} [\Omega]^{(i)} \tag{6.19}$$

where L is the length of the circumference and i the number of plastic hinges. The curvature and curvature rate related to C_1 and C_2 are respectively given by:

$$\kappa_1 = \frac{1}{R_1} \quad ; \quad \dot{\kappa}_1 = \frac{\dot{R}_1}{R_1^2} \tag{6.20}$$

$$\kappa_2 = \frac{1}{R_2} \quad ; \quad \dot{\kappa}_2 = \frac{\dot{R}_2}{R_2^2} \tag{6.21}$$

The deformed cross-section being symmetric with regard to x-axis, mathematical derivations will be detailed for half a cross-section. Integration of the first term of Eq. 6.19 along C_1 is given by Eq. 6.22 and along C_2 by Eq. 6.23.

$$\int_C^D \dot{\kappa}_1 dS = R_1 (\pi - \psi) \frac{\dot{R}_1}{R_1^2} = \frac{\pi - \psi}{R_1} \frac{\partial R_1}{\partial \delta} \dot{\delta} \tag{6.22}$$

$$\int_B^C \dot{\kappa}_2 dS = R_2 \psi \frac{\dot{R}_2}{R_2^2} = \frac{\psi}{R_1} \frac{\partial R_2}{\partial \delta} \dot{\delta} \tag{6.23}$$

The plastic hinges are located at points B and C. The rate of rotation, denoted respectively Ω_B and Ω_C are related to the change of curvature $[\kappa]$ at both sides of the plastic hinges moving at a velocity V (Eq. 6.24).

$$[\Omega] = V[\kappa] \tag{6.24}$$

The plastic hinges rotation rates may then be written as:

$$\Omega_C = V_C \left(\frac{1}{R_2} - \frac{1}{R_1} \right) \quad ; \quad \Omega_B = V_B \frac{1}{R_2} \tag{6.25}$$

where V_B and V_C are the tangential velocities in the current deformed configurations of plastic hinges B and C respectively. They are defined as:

$$\begin{aligned} V_B &= -\frac{d(C_1 + C_2)}{dt} = \frac{d(R_1(\pi - \psi) + R_2\psi)}{dt} \\ &= (R_1 - R_2)\dot{\psi} - (\pi - \psi)\dot{R}_1 - \psi \dot{R}_2 \\ &= \left[(R_1 - R_2) \frac{\partial \psi}{\partial \delta} - (\pi - \psi) \frac{\partial R_1}{\partial \delta} - \psi \frac{\partial R_2}{\partial \delta} \right] \dot{\delta} \end{aligned} \tag{6.26}$$

$$\begin{aligned} V_C &= -\frac{dC_1}{dt} = \frac{d\left(R_1\left(\pi-\psi\right)+R_2\psi\right)}{dt} \\ &= R_1\dot{\psi} - \left(\pi-\psi\right)\dot{R}_1 \\ &= \left[R_1\frac{\partial\psi}{\partial\delta} - \left(\pi-\psi\right)\frac{\partial R_1}{\partial\delta}\right]\dot{\delta} \end{aligned} \tag{6.27}$$

Substituting Eqs. 6.22, 6.23 and 6.24 into Eq. 6.19 allows to obtain the energy rate of one ring (Eq. 6.28).

$$\dot{E}_b = 2M_0\left[\frac{V_B}{R_2} + \left(\frac{1}{R_2}-\frac{1}{R_1}\right)V_C + \int_C^D \dot{\kappa}_1 dl + \int_B^C \dot{\kappa}_2 dl\right] \tag{6.28}$$

where the fully plastic bending moment is equal to $M_0 = \sigma_0 t_p^2/4$.

In order to get the rate of energy dissipated by all the rings, $\dot{E}_b$ is integrated along the length of the dented tubular member. Using the velocity field expressed in Eq. 6.15 and using Eq. 6.28, one obtain:

$$\dot{E}_r = \int_{-\xi_2}^{-a}\dot{E}_b\left(1+\frac{y+a}{\xi_2-a}\right)dy + \int_{-a}^{a}\dot{E}_b dy + \int_a^{\xi_1}\dot{E}_b\left(1-\frac{y-a}{\xi_1-a}\right)dy \quad = \dot{E}_b\left(a+\frac{\xi_1+\xi_2}{2}\right) \tag{6.29}$$

Rate of energy dissipated by generators plastic deformation

With regard to generators, both length and curvature change during their deformation, so that bending and membrane effects are involved in energy dissipation. However, the circumferential curvature change is much larger than the longitudinal one. This later is therefore neglected so only the membrane effect is considered. This assumption is similar to the one proposed in Chapter 4 and Eq. 6.18 becomes for the generators:

$$\dot{E}_{gen} = \int_S N\dot{\varepsilon}dS = \int_C\int_{-\xi_2}^{\xi_1}\dot{\varepsilon}_m dy dl \tag{6.30}$$

where the extension rate $\dot{\varepsilon}_m$ is defined by Eq. 6.31

$$\dot{\varepsilon}_m(\theta,\delta,y) = \frac{\partial W}{\partial y}\frac{\partial\dot{W}}{\partial y} \tag{6.31}$$

and

$$\begin{array}{ll} \frac{\partial\dot{W}}{\partial y} = \frac{\partial W}{\partial y} = \dot{w}(\theta,\delta)\left(\frac{1}{\xi_1-a}\right) & \text{for } y\in[a;\xi_1] \\ \frac{\partial\dot{W}}{\partial y} = \frac{\partial W}{\partial y} = 0 & \text{for } y\in[-a;a] \\ \frac{\partial\dot{W}}{\partial y} = \frac{\partial W}{\partial y} = \dot{w}(\theta,\delta)\left(\frac{1}{\xi_2-a}\right) & \text{for } y\in[-\xi_2;-a] \end{array} \tag{6.32}$$

The energy rate for one single generator at a specific position θ is computed using following expression:

$$\dot{E}_m(\theta,\delta) = n_0 \int_{-\xi_2}^{\xi_1} \dot{\varepsilon}_m(\theta,\delta,y)dy = n_0 w(\theta,\delta)\frac{\partial w}{\partial \delta}\dot{\delta}\left[\frac{1}{\xi_1 - a} + \frac{1}{\xi_2 - a}\right] \tag{6.33}$$

where $n_0 = \sigma_0 t$ is the fully plastic membrane force of the generator per unit of width.

The rate of energy dissipated by all the generators is finally derived by integrating $\dot{E}_m$ along the tubular member circumference:

$$\begin{aligned}\dot{E}_g &= \int_C \dot{E}_m dl = 2Rn_0\dot{\delta}\left[\frac{1}{\xi_1 - a} + \frac{1}{\xi_2 - a}\right]\int_0^{\pi} w(\theta,\delta)\frac{\partial w}{\partial \delta}d\theta \\ &= \left[\frac{1}{\xi_1 - a} + \frac{1}{\xi_2 - a}\right]\dot{E}'_m\end{aligned} \tag{6.34}$$

Total energy rate

As explained above, the total energy rate is the sum of rings and generators contributions. So, using Eqs. 6.29 and 6.34, it comes:

$$\dot{E} = \dot{E}_r + \dot{E}_g = \dot{E}_b\left(a + \frac{\xi_1 + \xi_2}{2}\right) + \dot{E}'_m\left(\frac{1}{\xi_1 - a} + \frac{1}{\xi_2 - a}\right) \tag{6.35}$$

Evaluation of ξ_1 and ξ_2

The extend of the dented zone is $-\xi_2 \leq y \leq \xi_1$, where ξ_1 and ξ_2 are finite values. The damaged area increases during the loading process, so that ξ_1 and ξ_2 depend on the displacement δ.

The upper-bound theorem may be expressed as:

$$P_l(\delta)\dot{\delta} = \dot{E}_b\left(a + \frac{\xi_1 + \xi_2}{2}\right) + \dot{E}'_m\left(\frac{1}{\xi_1 - a} + \frac{1}{\xi_2 - a}\right) \tag{6.36}$$

The punching local resistance can then be computed as:

$$P_l(\delta) = \left[E_b\left(a + \frac{\xi_1 + \xi_2}{2}\right) + E'_m\left(\frac{1}{\xi_1 - a} + \frac{1}{\xi_2 - a}\right)\right]/\delta \tag{6.37}$$

The values of ξ_1 and ξ_2 are assessed by minimising the local resistant force given by Eq. 6.37. This minimisation is performed by using the first derivative of $P_l(\delta)$ with regard to ξ_1 and ξ_2.

$$\frac{\partial P_l}{\partial \xi_1} = 0 \quad \Rightarrow \quad \xi_1 = \min\left(a + \sqrt{\frac{2E'_m}{E_b}}; L_1\right) \tag{6.38}$$

$$\frac{\partial P_l}{\partial \xi_2} = 0 \quad \Rightarrow \quad \xi_2 = \min\left(a + \sqrt{\frac{2E'_m}{E_b}}; L_2\right) \tag{6.39}$$

6.3.2.2 Global punching resistance

The global punching mode is previously described in Fig. 6.17. The energy dissipated plastically in the plastic hinges and the work done by the external loads are respectively given by Eqs. 6.40 and 6.41.

$$W_{hinge} = M_0\theta + M_0\varphi + \xi_t M_0\theta + \xi_t M_0\varphi \tag{6.40}$$

$$W_p = \frac{P(\delta_t)}{2} L'_1\theta + \frac{P(\delta_t)}{2} L'_2\varphi \tag{6.41}$$

where $L'_1 = L_1 - a$ and $L'_2 = L_2 - a$.

The fully plastic bending moment of a circular cross-section beam can be expressed as $M_0 = 4R^2\sigma_0 t$. However, in the dented area, the beam section is no longer circular, and the plastic bending moment is reduced by a factor $\xi(\delta)$. The reduced plastic bending moment $\xi(\delta)M_0$ is therefore used in Eq. 6.40 in the dented area. This reduction factor is similar to the one proposed in Chapter 4 following a suggestion of De Oliveira et al. [3], who proposed to consider a simplified deformed cross-section, as depicted in Fig. 6.18. The reduction factor can then be expressed as:

$$\xi(\delta) = \frac{1}{2}\left(\left(\frac{\delta}{2R}\right)^2 - 1\right)\left(\frac{\delta}{2R} - 2\right) \tag{6.42}$$

Once global deformation mode is activated, i.e. when $\delta \geq \delta_t$, the energy dissipated by rotation of plastic hinges is equal to the external loads work. At this point, no axial forces develop in the dented tubular member, and therefore no energy is dissipated through axial elongation. Equating Eqs. 6.40 and 6.41 allows to write:

$$M_0\theta + M_0\varphi + \xi_t M_0\theta + \xi_t M_0\varphi = \frac{P(\delta_t)}{2} L'_1\theta + \frac{P(\delta_t)}{2} L'_2\varphi \tag{6.43}$$

The global indentation can be expressed as:

$$L'_1\theta = \delta - \delta_t = L'_2\varphi \tag{6.44}$$

When the beam plastic bending deformation mode is activated, the corresponding resistant force $P_g(\delta_t)$ (represented by the green curve in Fig. 6.16) may be calculated by substituting

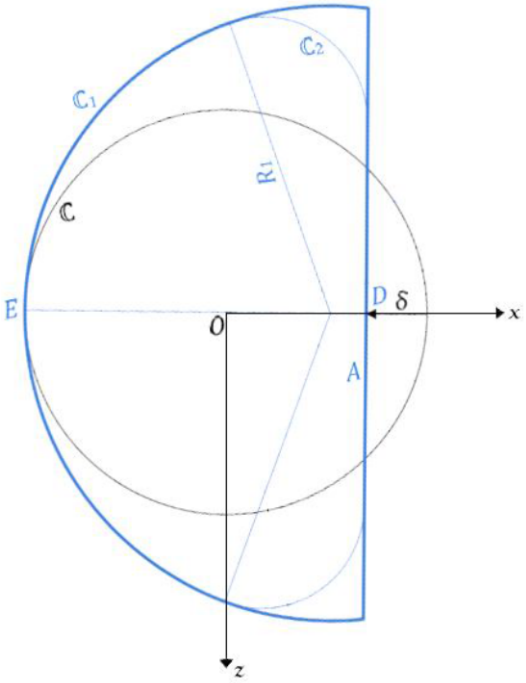

Figure 6.18: Damaged cross-section proposed by De Oliveira [3]

Eq. 6.44 into Eq. 6.43:

$$P_g(\delta_t) = \frac{L_1' + L_2'}{L_1' L_2'} \left(1 + \xi(\delta_t)\right) M_0 \tag{6.45}$$

At transition between local and global modes, corresponding resistant forces are equal, which may be written as:

$$P_l(\delta_t) = P_g(\delta_t) = \frac{L_1' + L_2'}{L_1' L_2'} \left(1 + \xi(\delta_t)\right) M_0 \tag{6.46}$$

In the case of punching, Eq. 6.45 has to be corrected by introducing the ratio β between leg and brace diameters, as defined in Eq. 6.1. Indeed, Eq. 6.45 is able to represent a curve plotted in Fig. 6.16. In the case of punching, a peak occurs at the threshold indentation δ_t, as can be seen in Fig. 6.19. Here, the green curve corresponds to the set of equations in which β parameter has not been introduced. It is shown that for large values of β, the force is underestimated (blue curve) and overestimated for low values of β (red curve).

It can be found in several references, such as Department of Energy [4], Moffat et al. [9] or Standards Norway [10] that the peak level is governed by the ratio β (first order) and by the geometry factor Q_β, function of β. Experiments were conducted by the Department of Energy on more than 50 T/Y joints and regression curves, such as the one depicted in Fig. 6.20, were extracted from experimental results. The relationship is approximately linear for $\beta < 0.6$ and increases faster for $\beta > 0.6$. The strength being non-dimensional, the parameter $\sqrt{Q_\beta}$ is introduced to represent the linear relationship, as depicted in Fig. 6.21.

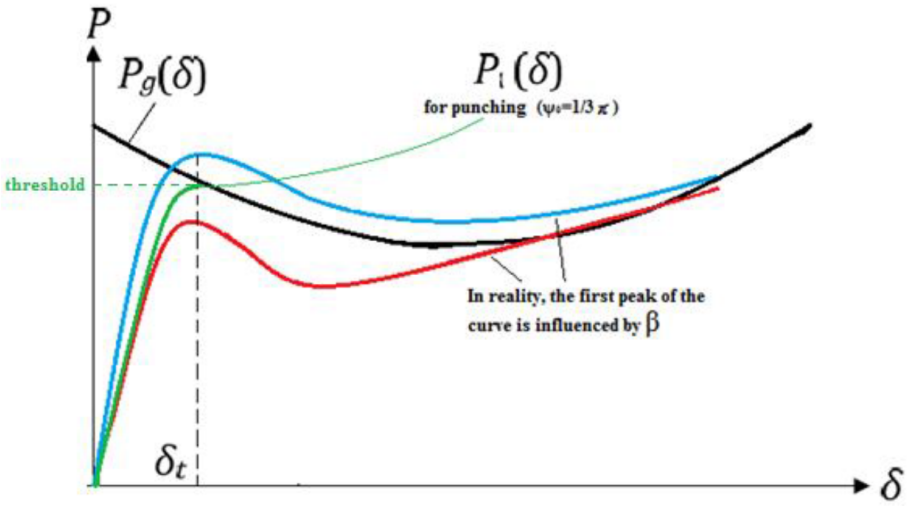

Figure 6.19: Punching force evolution - comparison between semi-analytical formulation and reality [6]

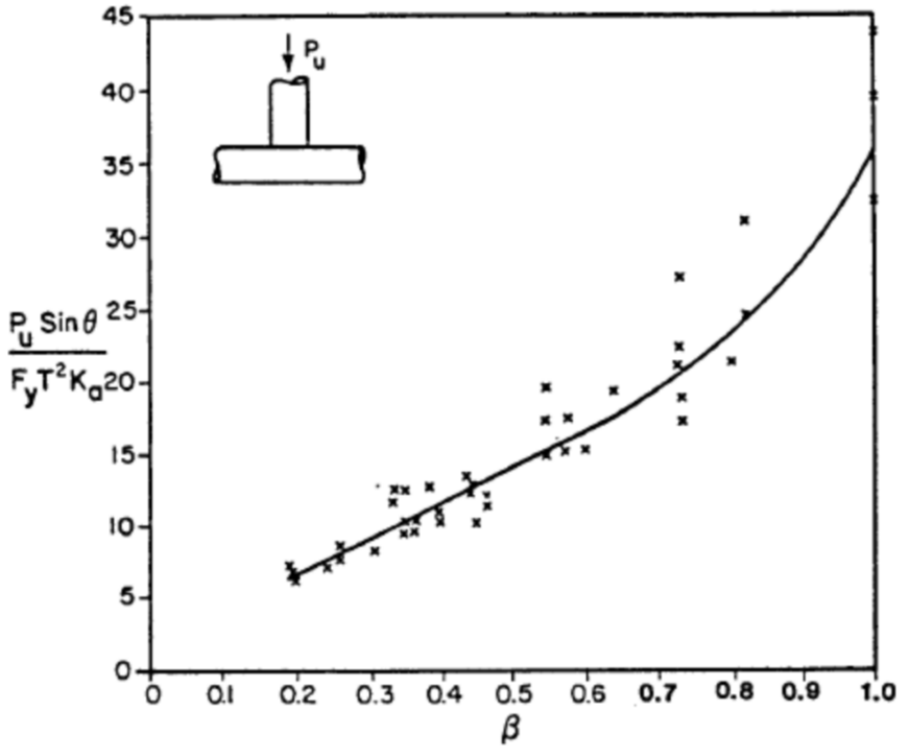

Figure 6.20: T/Y joints - non-dimensional strength with regard to β ratio (1) [10]

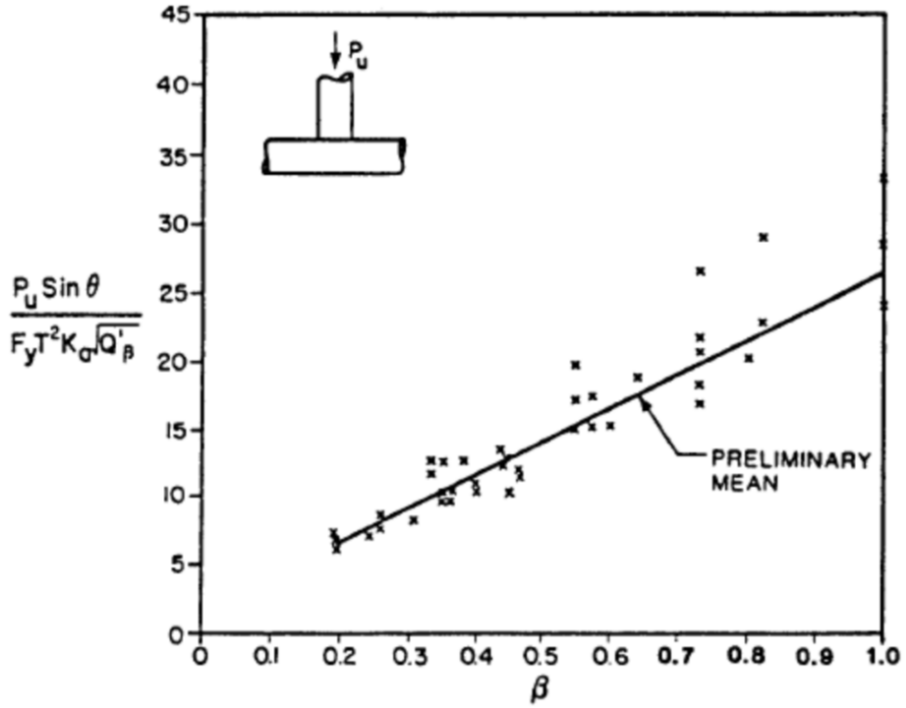

Figure 6.21: T/Y joints - non-dimensional strength with regard to β ratio (2) [10]

Considering empirical parameters β and Q_β, Eq. 6.46 is modified into Eq. 6.47. The extremities of the punched tubular member are not affected by parameters β and Q_β as they are not influenced by the brace diameter. The first term of Eq. 6.47 is therefore not affected by these parameters.

$$P_l(\delta_t) = P_g(\delta_t) = \frac{L'_1 + L'_2}{L'_1 L'_2} \left(1 + \beta\sqrt{Q_\beta}\xi(\delta_t)\right) M_0 \tag{6.47}$$

where

$$\begin{aligned} Q_\beta &= 1 && \text{for } \beta \leq 0.6 \\ Q_\beta &= \tfrac{0.3}{\beta(1-0.833\beta)} && \text{for } \beta > 0.6 \end{aligned} \tag{6.48}$$

When the punched tubular member indentation increases, the local indentation stops as soon as $\delta \geq \delta_t$ and the tubular member bends globally. The dissipated energy is then the sum of both bending moment and membrane force contributions. The plastic bending moment is influenced by the axial force and is expressed in Eq. 6.49 for the case of a tubular cross-section.

$$M = M_0 \cos\left(\frac{\pi}{2}\frac{N}{N_0}\right) \tag{6.49}$$

where $N_0 = 2\pi R\sigma_0 t$ is the plastic tensile capacity of the tubular member.

This expression cannot be used to get a closed-form solution for the global resistance. As suggested by De Oliveira [3], a simplified interaction equation given in Eq. 6.50 can be used and provides results similar to Eq. 6.49 for a non-dented cross-section. For a punched cross-section,

the plastic tensile capacity remains unchanged and the plastic bending capacity is reduced according to Eq. 6.42. The interaction function is also modified. However, in order to keep an expression that can be used later, the reduction factor and the β factor simply affect the bending moment resistance, as given in Eq. 6.51.

$$M = M_0 \left(1 - \frac{N^2}{N_0^2}\right) \tag{6.50}$$

$$M = \beta\sqrt{Q_\beta}\xi_t M_0 \left(1 - \frac{N^2}{N_0^2}\right) \tag{6.51}$$

From the beam analysis, and following the same methodology than Buldgen, Le Sourne and Pire [2] (Chapter 4), the global resistance can be expressed as:

$$P_g(\delta) = \frac{L_1' + L_2'}{L_1' L_2'} \left[\left(1 + \beta\sqrt{Q_\beta}\xi_t\right) M_0 \left(1 - \frac{N(\delta)^2}{N_0^2}\right) + N(\delta)(\delta - \delta_t)\right] \tag{6.52}$$

with

$$N(\delta) = \min\left(\frac{N_0^2(\delta - \delta_t)}{2\left(1 + \beta\sqrt{Q_\beta}\xi_t M_0\right)}; N_0\right) \tag{6.53}$$

6.3.3 Validation for punching on one connection

The above developments are validated by comparison with FE simulations, for a range of geometrical parameters covering the main tubular joints used by industries. As defined in the *NORSOK* Standard-Design of steel structures [10], the validity of the equations given in that document is restricted to the following geometrical parameters ranges:

$$\begin{aligned} &0.2 \leq \beta \leq 1.0 \\ &10 \leq \gamma \leq 50 \\ &30^\circ \leq \alpha \leq 90^\circ \\ &g/D \geq -0.6 \end{aligned} \tag{6.54}$$

where β, γ, α, g and D are defined in Fig. 6.22.

Using the nonlinear FE solver *LS-DYNA*, several numerical simulations were performed based on the jacket previously described in Section 3.2.2. As a benchmark, the impacted tubular member data are given in Table 6.1 and the effect of several parameters is investigated within a range of possible values.

The jacket elastic plastic material behaviour law is described in Section 3.2.2.

The punching process is simulated by imposing a given displacement at the interface between the leg and the brace. In order to obtain comparable results with semi-analytical ones, the effects

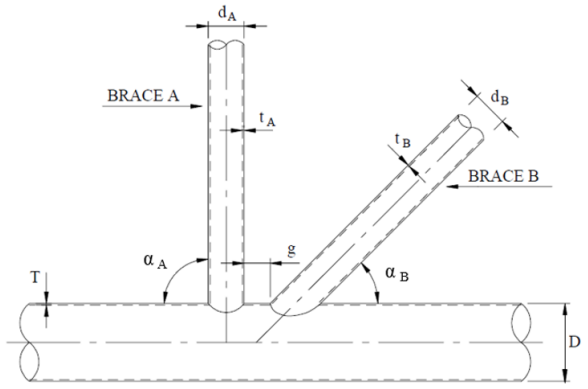

$$\beta_A = \frac{d_A}{D} \qquad \beta_B = \frac{d_B}{D}$$

$$\tau_A = \frac{t_A}{T} \qquad \tau_B = \frac{t_B}{T}$$

$$\gamma = \frac{D}{2T} \qquad \zeta = \frac{g}{D}$$

Figure 6.22: Definition of geometrical parameters of K-joint [10]

Table 6.1: Dimensions of the benchmark jacket

Property	Unit	Value
D_L	m	1.25
D_B	m	0.6
L	m	17
L_1	m	10.5
L_2	m	6.5
t_p	mm	40
α	$^\circ$	45
$B.C.$	–	*clamped*
β	–	0.48

of inertia forces are reduced as much as possible by choosing an indenting brace displacement, depicted in Fig. 6.23, such as the corresponding acceleration remains small. Such displacement is imposed on the set of nodes located at the interface between the punched leg and the brace.

The punched leg is assumed to be perfectly clamped at both extremities.

Both the leg and the brace are meshed with under-integrated Belytchko-Tsay shell elements [1, 5]. In order to represent correctly the punching process of the leg, the average length of finite elements used in this study is 25 mm.

For each set of parameters, the joint design axial force computed with the formulas proposed by *NORSOK N-004* regulation is also provided. As no further information is given in *NORSOK* recommendations [10], the resistant force is assumed to remain constant during the whole punching process. This basic assumption will be used later on to compute the resulting plastic deformation energy.

The comparisons between *NORSOK*, semi-analytical and numerical models in terms of punching force and dissipated energy are plotted in Figs. 6.24 and 6.25 respectively. It is worth noting that the semi-analytical force vs indentation curve starts from a non-zero value. This is due to the fact that the leg elastic deformation is neglected in the developed model, as the material behaviour is assumed to be rigid plastic, and that the initial contact area is non-zero. A certain load is therefore required to initiate the deformation.

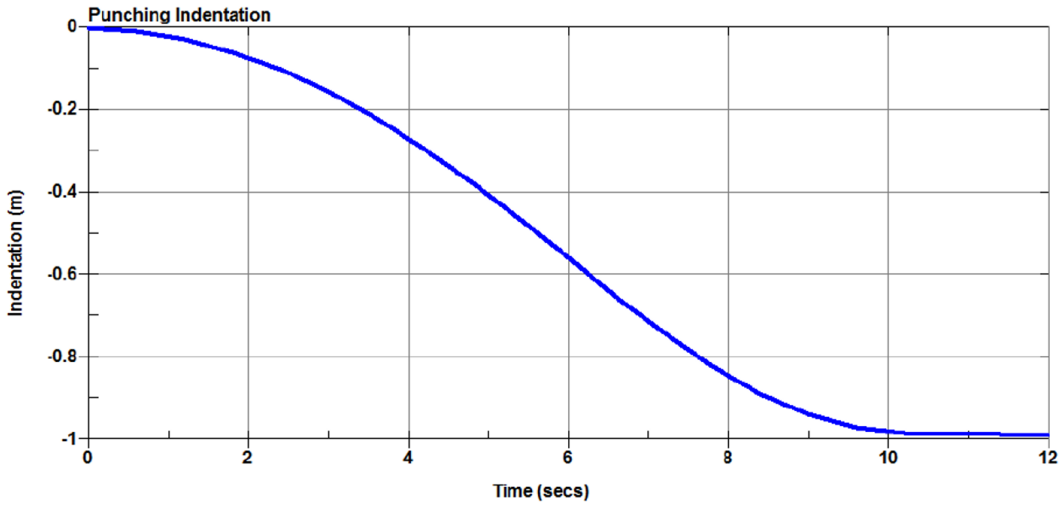

Figure 6.23: Displacement curve considered for the numerical simulations [6]

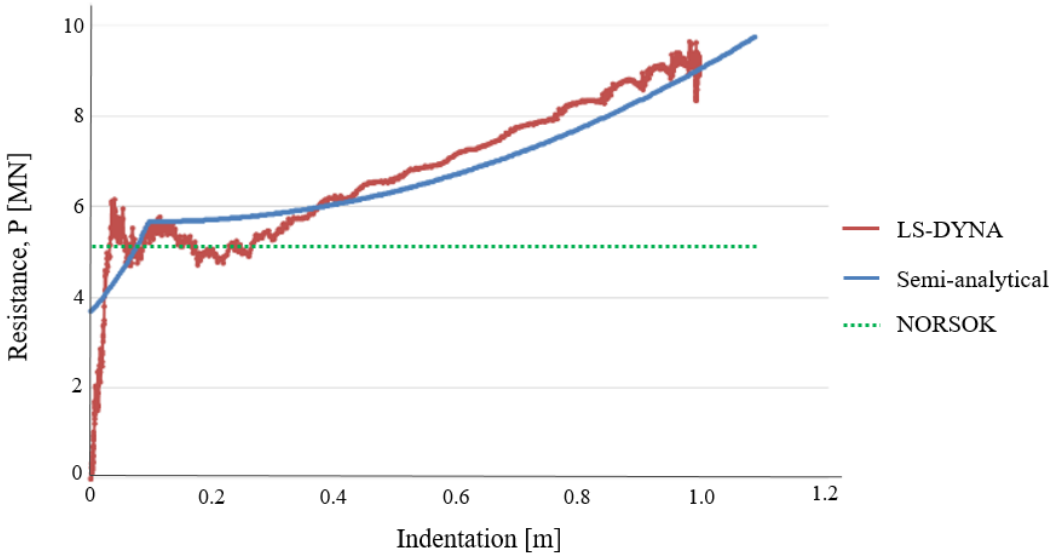

Figure 6.24: Punching force for the benchmark model for NORSOK, semi-analytical and numerical method

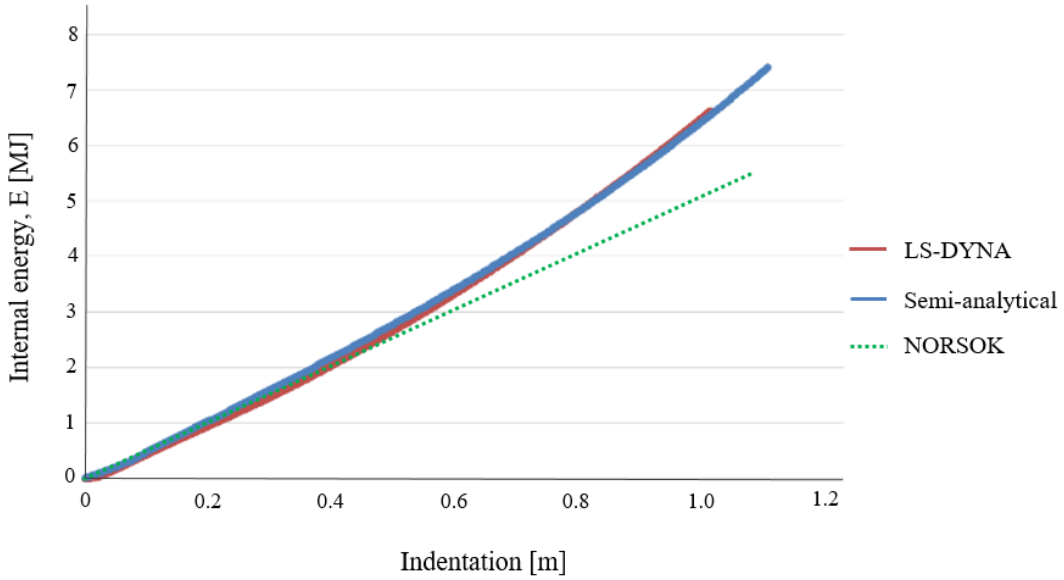

Figure 6.25: Dissipated energy for the benchmark model for NORSOK, semi-analytical and numerical method

The semi-analytical model is in good accordance with the numerical one, as the maximum discrepancy in terms of dissipated energy is lower than 8%. The results obtained from *NORSOK* formulas are also in quite good accordance with numerical ones when the indentation is small, i.e. as long as only local punching mode is involved. However, as the global deformation mode is not included in *NORSOK*, resulting force and deformation energy are not correctly calculated when the punched member global bending deformation becomes preponderant.

6.3.3.1 Sensitivity analysis of β ratio

Let us recall that the value of β ratio corresponds to the ratio between brace and leg diameters. The joint dimensions listed in Table 6.1 are considered for this sensitivity analysis and the brace diameter is varied such as to get several values of β, namely 0.32, 0.48, 0.64, 0.8 and 1. Crushing force and deformation energy evolutions with regard to leg indentation are plotted in Figs. 6.26 and 6.27 respectively.

For each value of β, the force reaches a peak for an indentation of about $\delta = 0.1\ m$, then a load shedding starts. Afterwards, the resistant force increases again, due to the change of deformation mechanism, switching between chord bending mode and chord tension mode. This mechanism was explained by Lee and Llewelyn-Parry [8].

Although the peak level is different for β equal to 0.32, 0.48 and 0.64, the curves tend towards a common value which corresponds to the maximum axial force without bending moment. However, the evolution of the crushing force is different for larger values of β. From numerical simulations, it can be seen that the cross-section deformation pattern of the punched leg differs for large values of β, as shown in Fig. 6.28.

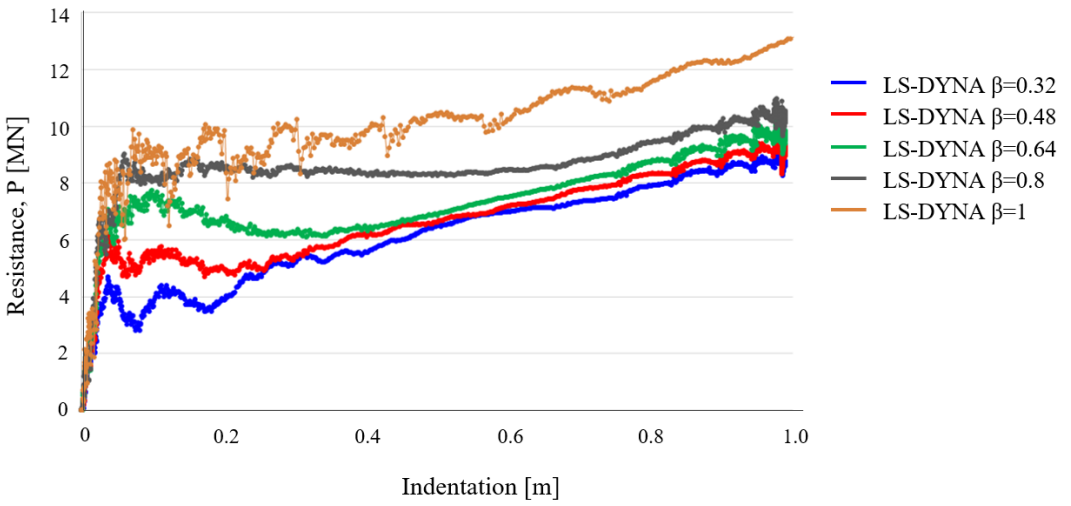

Figure 6.26: Punching force evolution for several values of β [6]

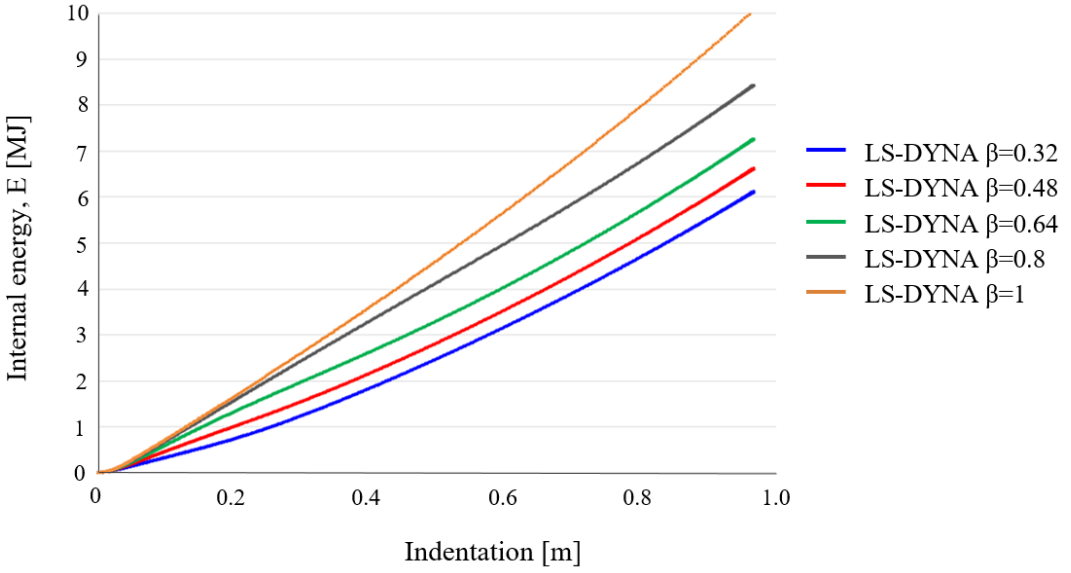

Figure 6.27: Dissipated energy evolution for several values of β [6]

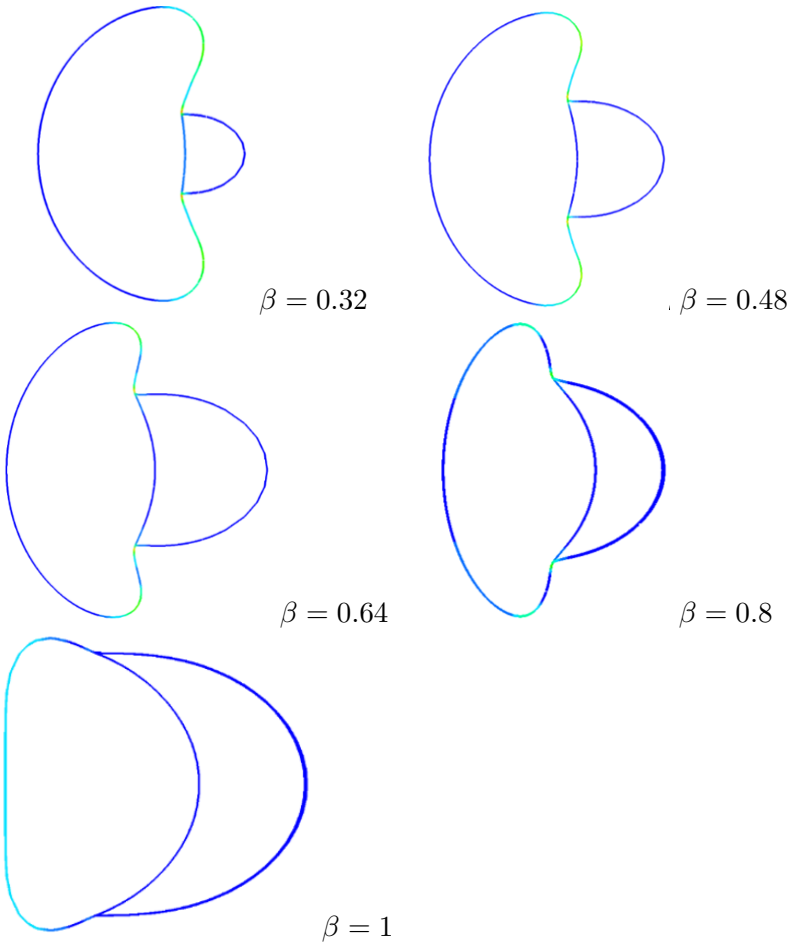

Figure 6.28: Comparison of crushed ring sections for different β ratios – Post-processed from *LS-DYNA* simulations

Semi-analytical and numerical resistant forces and dissipated energies are compared in Figs. 6.29, 6.30, 6.31 and 6.32 for $\beta = 0.32$, $\beta = 0.64$, $\beta = 0.8$ and $\beta = 1$ respectively.

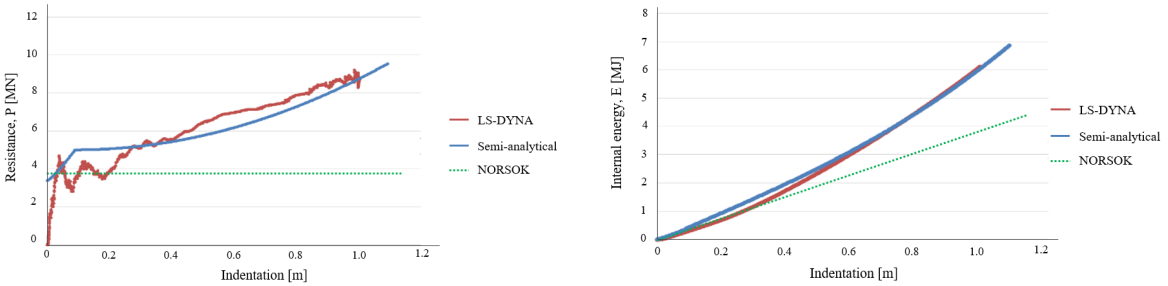

Figure 6.29: Comparison of punching forces and dissipated energies for $\beta = 0.32$

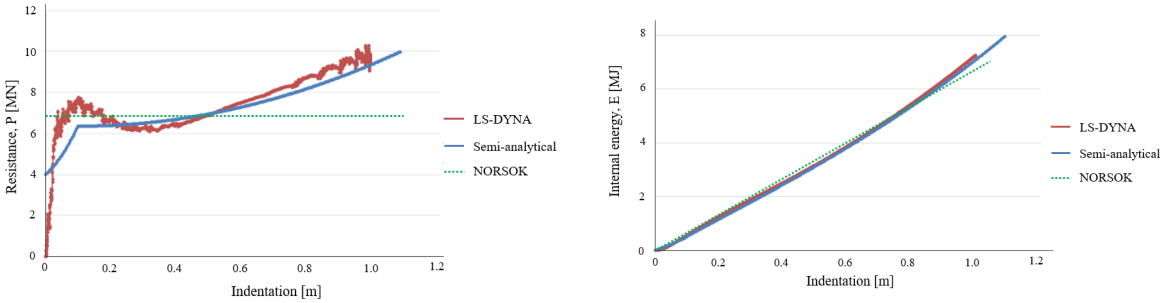

Figure 6.30: Comparison of punching forces and dissipated energies for $\beta = 0.64$

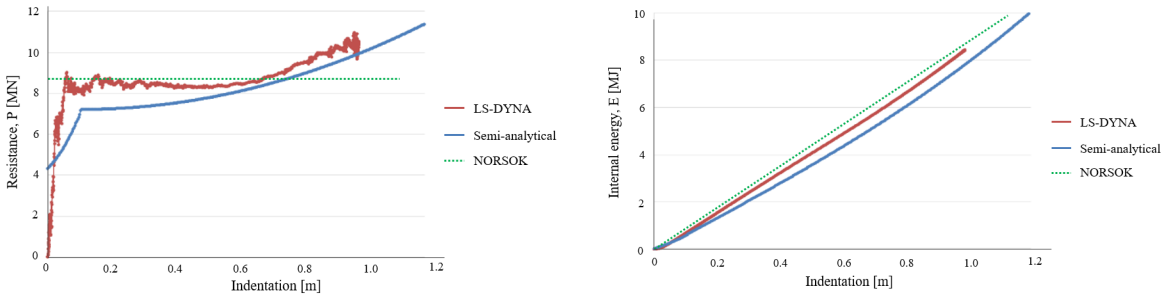

Figure 6.31: Comparison of punching forces and dissipated energies for $\beta = 0.8$

As can be seen from these Figures, the semi-analytical model is able to predict quite accurately the punching process as the maximum discrepancy in terms of dissipated energy remains lower than 20%. It also appears that except for $\beta = 0.32$, *NORSOK* formulas allow to obtain energy evolutions that correlate rather correctly with numerical ones.

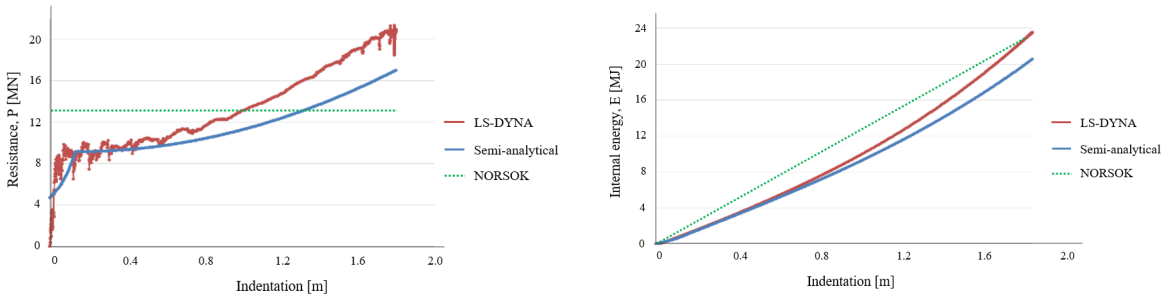

Figure 6.32: Comparison of punching forces and dissipated energies for $\beta = 1$

6.3.3.2 Sensitivity analysis of α angle

In the reference model, the angle between the leg and the brace axes, denoted α, was arbitrarily taken equal 45°. However, such angle may be completely different and the braces located at the base of the jacket are often connected perpendicularly to the legs. In that case, the shape of the intersection is no longer oval but circular.

As shown in Figs. 6.33 and 6.34, where the evolutions of the resistant forces and corresponding dissipated energies are compared for α equals 90°, semi-analytical results are in very good accordance with numerical ones.

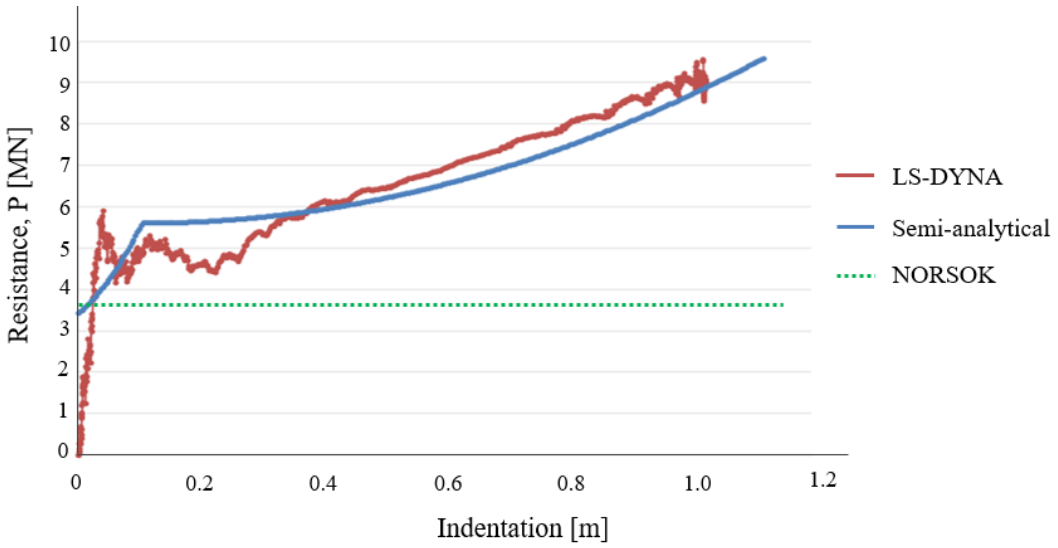

Figure 6.33: Comparison of the punching forces for $\alpha = 90°$

Here again, the discrepancy between semi-analytical and numerical energies remains low, with a maximum of 15% at $d = 0.22\ m$, while *NORSOK* formulas underestimate significantly the punching resistant force.

6.3.3.3 Effect of leg section span

The span, i.e. the distance between two braces - leg connections, decreases with the elevation on the jacket. As shown in Fig. 6.7, the span for one connection decreases for an increasing

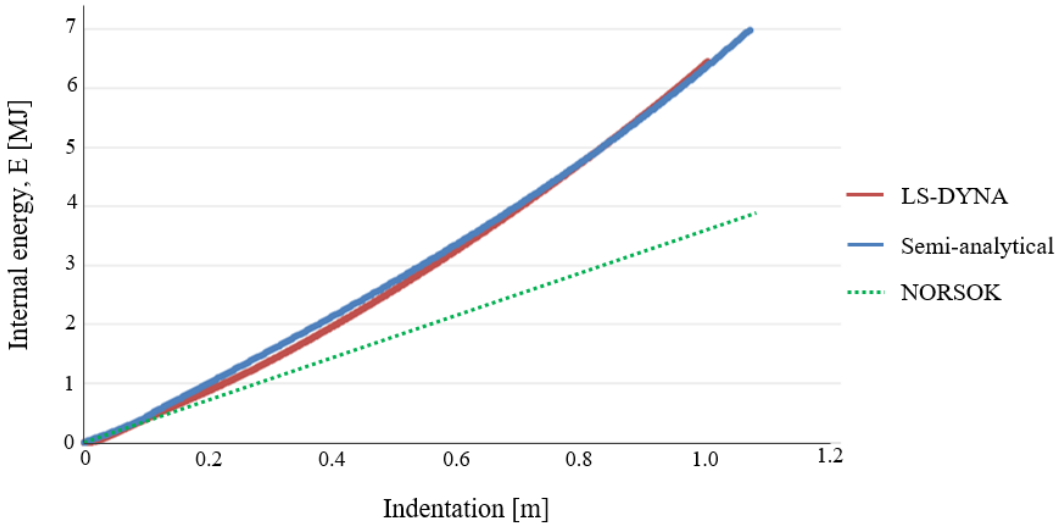

Figure 6.34: Comparison of the dissipated energy for $\alpha = 90°$

altitude on the jacket. The model has therefore to be able to represent the structural behaviour for several spans. Resistant forces and dissipated energies related to spans of 17 and 23.5 m are compared in Figs. 6.35 and 6.36 respectively.

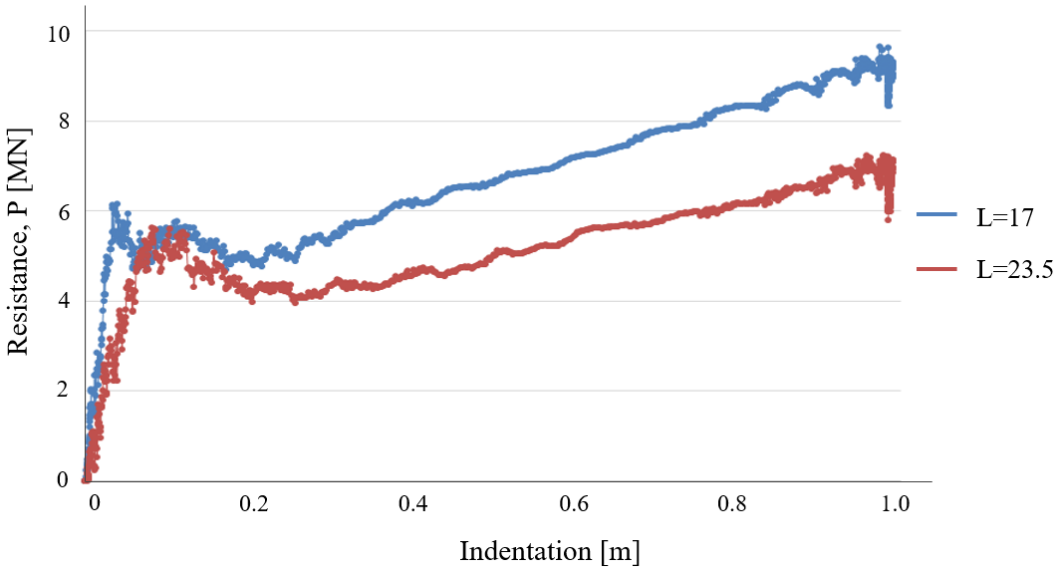

Figure 6.35: Punching forces for 17 m and 23.5 m spans [6]

The considered punched leg appears to be stiffer when the span is short. This is due to the axial flexibility at the supports and to the extension that occurs at the colliding point, as explained by De Oliveira et al. [3].

Comparisons between semi-analytical and numerical results are plotted in Figs. 6.37 and 6.38. The peak resistance is underestimated because the presented model does not take into account the axial stiffness of the punched tubular member. However, the correlation between semi-analytical and numerical dissipated energies remains good.

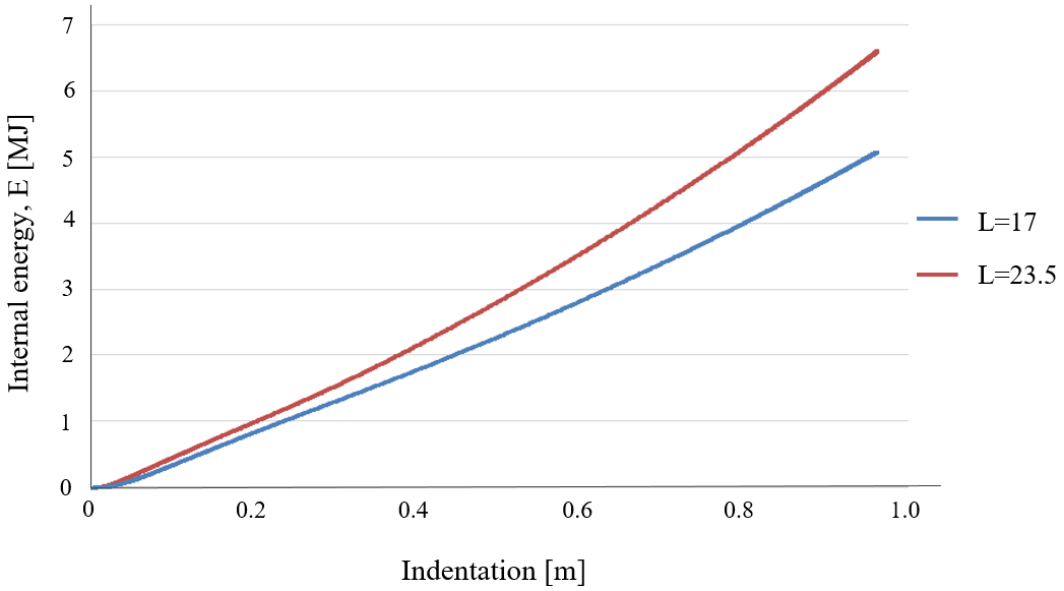

Figure 6.36: Dissipated energies for 17 m and 23.5 m spans [6]

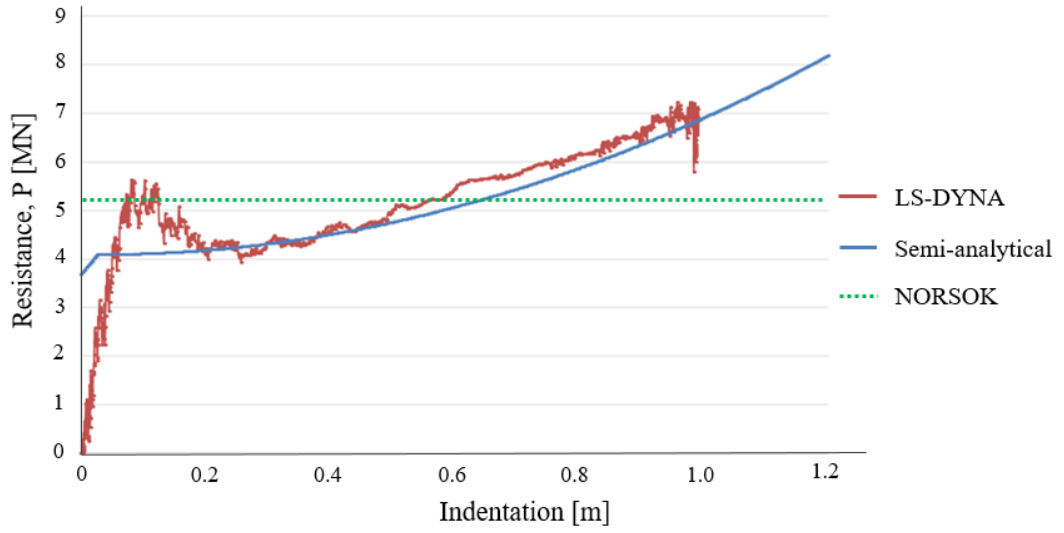

Figure 6.37: Comparison of the punching forces for a 23.5 m span

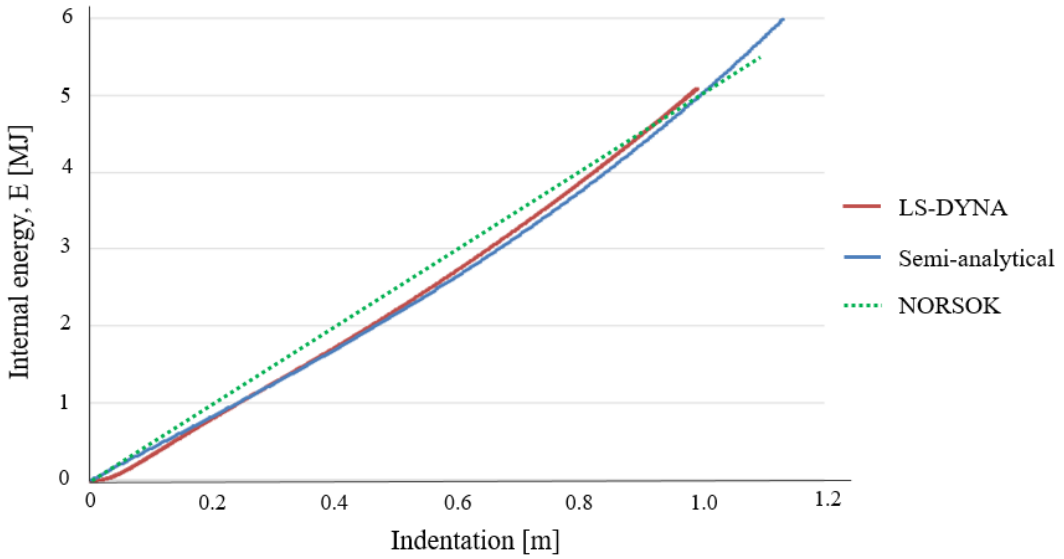

Figure 6.38: Comparison of the dissipated energies for a 23.5 m span

For this scenario, the discrepancy between semi-analytical and numerical energies does not exceed 15%. Note that the span is not considered by the formulas proposed in *NORSOK* design rules, because, as previously mentioned, only the cross-section deformation (local mode) is considered.

6.3.3.4 Effect of 2-braces punching

In Section 6.3.2, semi-analytical formulations have been derived to assess the resistant force as well as the energy dissipated by a leg that is punched by one brace. Sometimes, the leg is punched by two compressed braces that are connected at the same connection, with or without gap between them. The resulting deformation pattern is shown in Fig. 6.39. Similarly to the intersection surface of one brace on a leg assumed to be rectangular, as depicted in Figs. 6.11 and 6.12, it is assumed that the intersection surface is also rectangular for a two braces connection. The expression of dissipated energy rate is similar to the one derived for one brace (Eq. 6.35), with only minor differences due to the fact that the intersection between the leg and the braces has to be updated. The extension of the generator deflection is expressed in Eqs. 6.55 and 6.56 for one brace and two braces punching respectively. Dissipated energy rate is now as expressed in Eqs. 6.57, 6.58 and 6.59.

$$\xi_1 + 0.7\frac{D_B}{\cos\alpha} + \xi_2 = \xi_1 + 2a + \xi_2 \tag{6.55}$$

$$\xi_1 + 0.7\left(\frac{1}{2}\frac{D_B}{\cos\alpha} + gap + \frac{1}{2}\frac{D_B}{\cos\alpha}\right) + \xi_2 = \xi_1 + 2a + 0.7 \times gap + \xi_2 \tag{6.56}$$

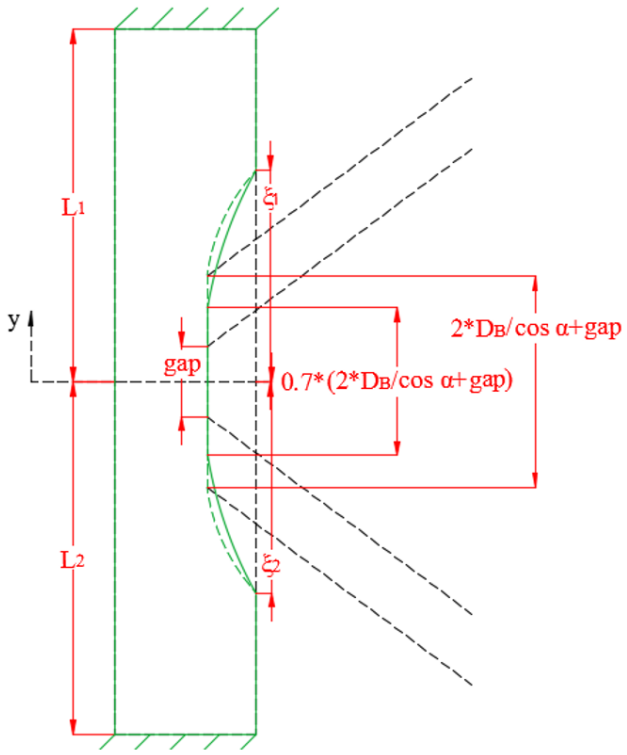

Figure 6.39: Deformation mechanism along the generators for 2-braces punching

$$\begin{aligned}\dot{E} &= \dot{E}_r + \dot{E}_g \\ &= \dot{E}_b \left(2a + 0.7 \times gap + \frac{\xi_1 + \xi_2}{2}\right) \\ &\quad + \dot{E}'_m \left(\frac{1}{\xi_1 - (2a + 0.7 \times gap)} + \frac{1}{\xi_2 - (2a + 0.7 \times gap)}\right)\end{aligned} \tag{6.57}$$

$$\xi_1 = \min\left(2a + 0.7 \times gap + \sqrt{\frac{2E'_m}{E_b}}; L_1\right) \tag{6.58}$$

$$\xi_2 = \min\left(2a + 0.7 \times gap + \sqrt{\frac{2E'_m}{E_b}}; L_2\right) \tag{6.59}$$

Without gap

First, a connection with two braces connected to one leg without any gap is considered. The β ratio is set to 0.48 and the α angle is equal to 45°. As expected, Figs. 6.40 and 6.41 show that resistant force and dissipated energy levels post-processed from numerical simulations are higher in case of double punching. The deviation at the first peak for the force is equal to 34%.

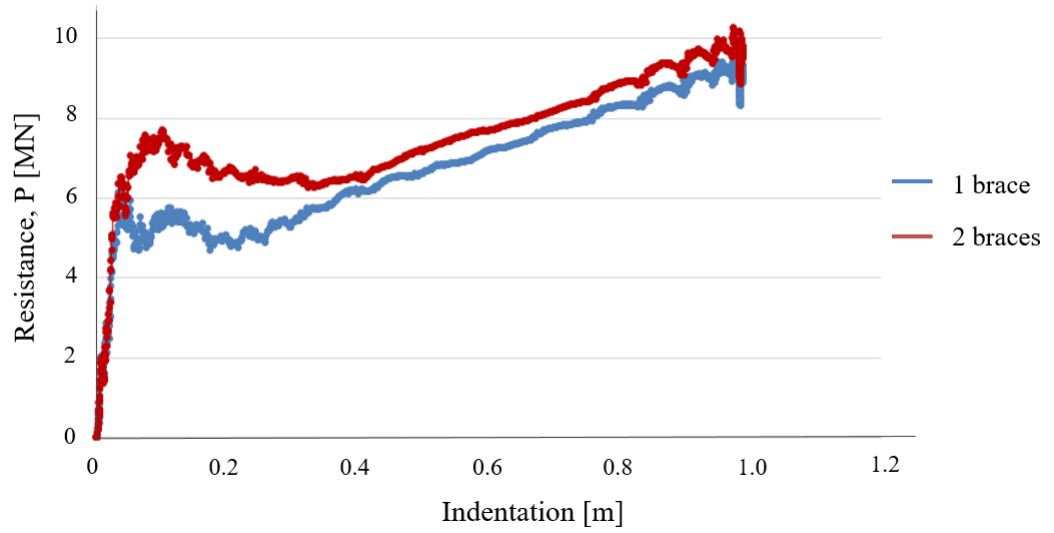

Figure 6.40: Punching forces for 1 and 2-braces punching without gap [6]

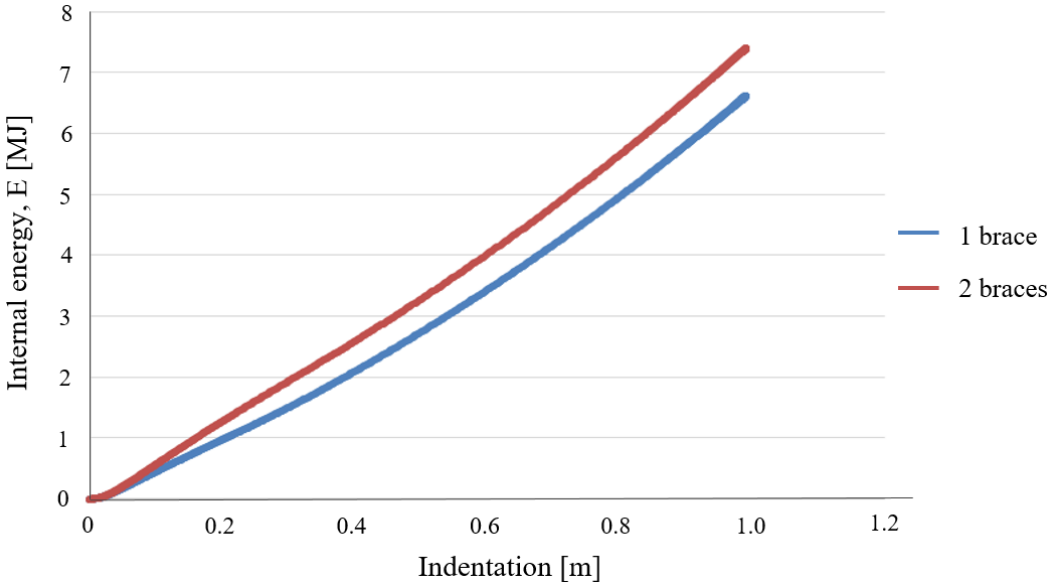

Figure 6.41: Dissipated energies for 1 and 2-braces punching without gap [6]

In the same way, as shown in Figs. 6.42 and 6.43 where semi-analytical results are compared with numerical ones, even if the discrepancy regarding the resistant force peak is around 19%, the proposed model predicts correctly the dissipated energy.

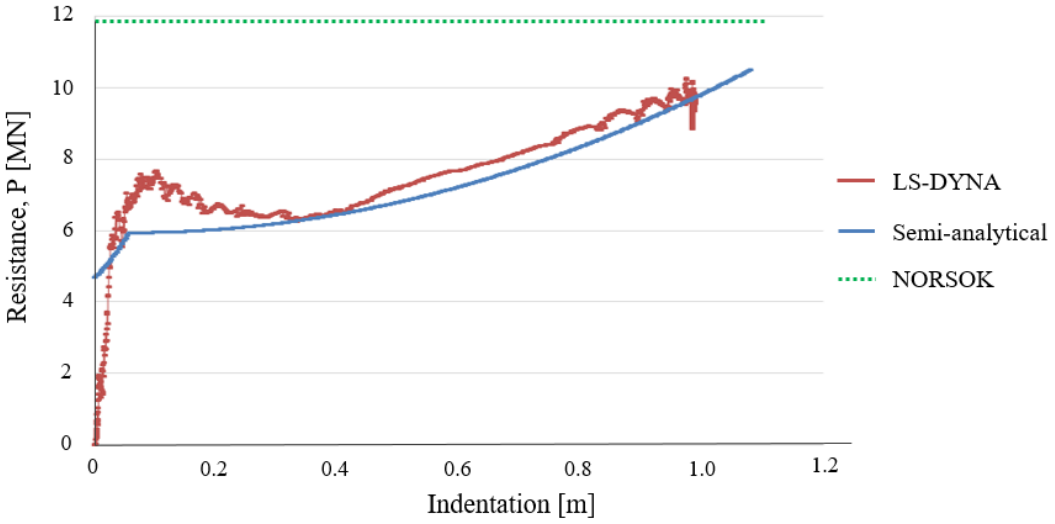

Figure 6.42: Comparison of the punching forces for a 2-braces punching without gap

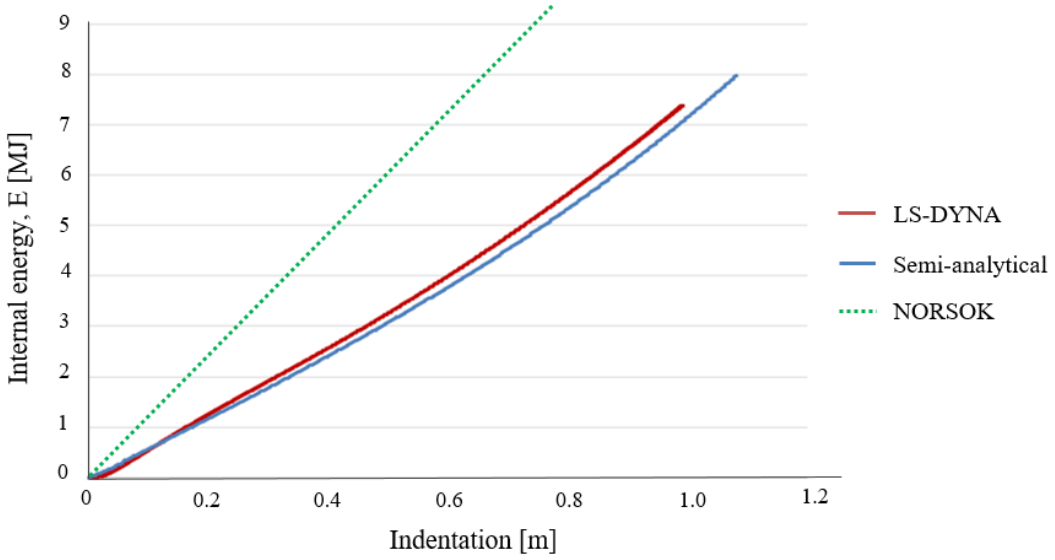

Figure 6.43: Comparison of the dissipated energies for a 2-braces punching without gap

In this case, the largest discrepancy between semi-analytical and numerical energies is around 6%. As can be seen from this scenario without gap between braces, *NORSOK* formulas overestimate considerably the punching resistant force, even at low penetration.

With gap

Then, the same structure is considered but this time a gap separates the connected braces. A gap $g = 0.82\ m$, corresponding to the investigated jacket, is selected.

Here again, resistant forces and dissipated energies are compared in Figs. 6.44 and 6.45 respectively. Although a discrepancy still occurs around the force peak, the dissipated energy calculated by the proposed semi-analytical model is in good accordance with the one post-processed from *LS-DYNA* simulation.

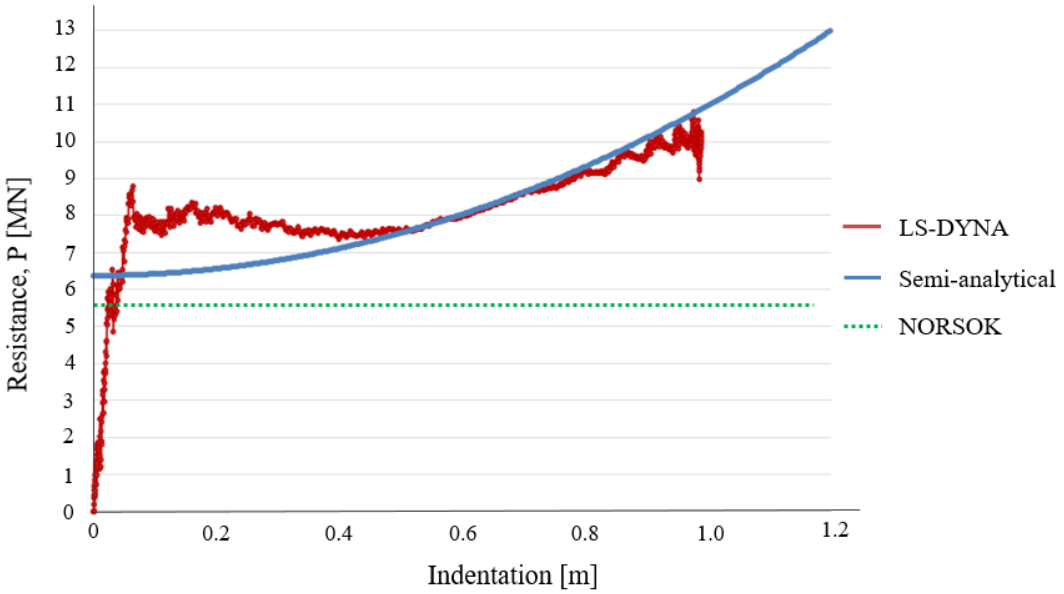

Figure 6.44: Comparison of the punching forces for a 2-braces punching with gap

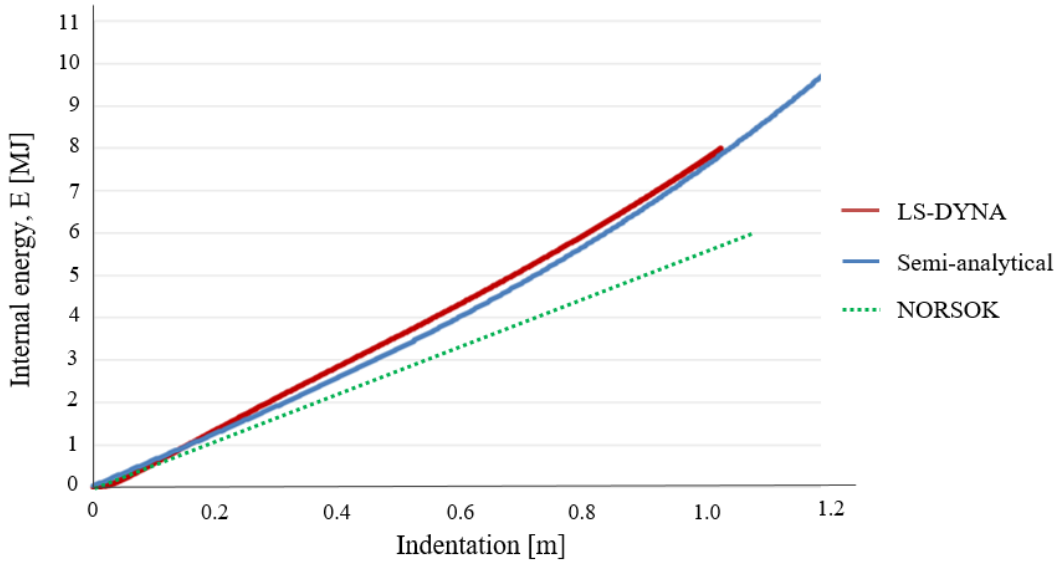

Figure 6.45: Comparison of the dissipated energies for a 2-braces punching with gap

For this last set of parameters, discrepancy between semi-analytical and numerical energies does not exceed 10%, which shows the accuracy of the semi-analytical model. As can be seen from the semi-analytical curve in Fig. 6.44, the global mode is activated since the beginning of the punching process, and no local deformation occurs. This can explain the difference with the *NORSOK* result.

6.3.3.5 Sensitivity analysis of ψ_0 value

As described in Section 6.3.1, it was assumed that the parameter ψ_0 has a value of $\psi_0 = \pi/3$ as long as punching of one tubular member by another is considered. This assumption still has to be verified. Therefore, the punching scenario described in Table 6.1 is considered and several values of ψ_0 are investigated in the simplified model. The resistant force – penetration curves for ψ_0 values of $\pi/4$, $\pi/3$, $\pi/2$ and $3\pi/4$ as well as the curve obtained numerically are compared in Fig. 6.46.

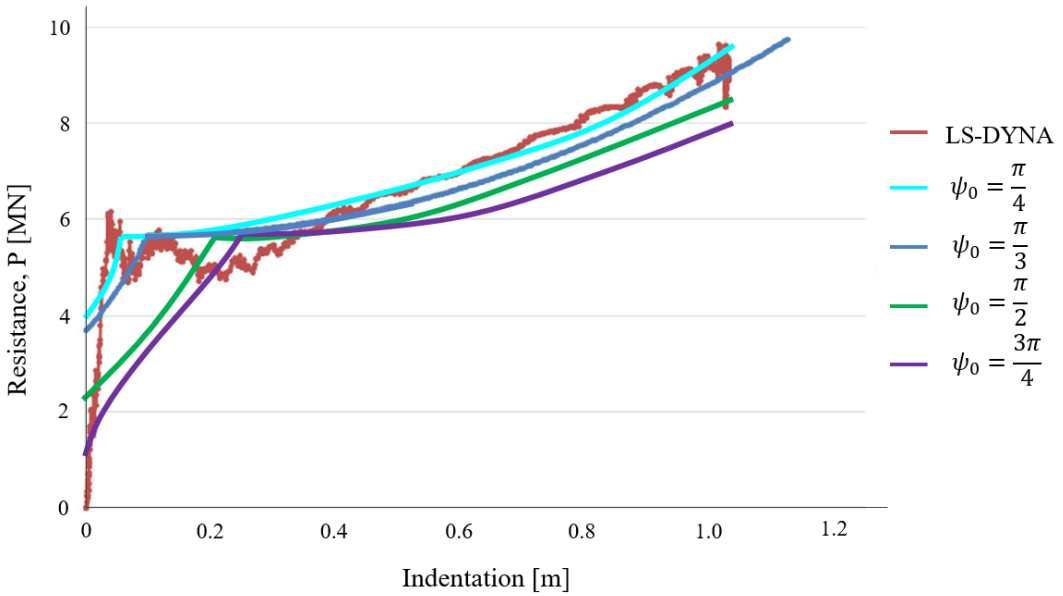

Figure 6.46: Force - penetration curve for several ψ_0 values

For a penetration of 1 m, the dissipated energy computed numerically is equal to 6.7 MJ. Table 6.2 presents the internal energy computed with the simplified method for several values of ψ_0 as well as the discrepancy with respect to the numerical result, this later being considered as the reference. It appears from this Table that the value $\psi_0 = \pi/3$ is the optimal value.

Table 6.2: Dissipated energy for several values of ψ_0 for the benchmark connection

ψ_0	E $[MJ]$	Disc. [%]
$\pi/4$	6.9	3
$\pi/3$	6.6	1
$\pi/2$	6.1	9
$3\pi/4$	5.7	15

The value of ψ_0 was also investigated for other connection properties previously studied. For each of them, the internal energy computed numerically is compared to the semi-analytical results with several values of ψ_0, as done in Tables 6.3 and 6.4. Several values of $\beta = 0.32; 0.64; 0.8; 1$ are considered (Section 6.3.3.1), as well as the effect of α (Section 6.3.3.2) and two braces punching (Section 6.3.3.4). As ψ_0 affects only the cross-section deformation, the span has no influence on the local deformation of the punched tubular member.

Table 6.3: Dissipated energies for several values of ψ_0 and β

	$\beta = 0.32$		$\beta = 0.64$		$\beta = 0.8$		$\beta = 1$	
	$E\ [MJ]$	Disc. [%]	$E\ [MJ]$	Disc. [%]	$E\ [MJ]$	Disc. [%]	$E\ [MJ]$	Disc. [%]
Num.	6.1	–	7.3	–	8.4	–	10.0	–
$\psi_0 = \pi/4$	6.3	3	7.6	4	8.4	0	10.3	3
$\psi_0 = \pi/3$	6.0	2	7.2	1	8.2	2	9.7	3
$\psi_0 = \pi/2$	5.5	10	6.7	8	7.4	12	8.9	11
$\psi_0 = 3\pi/4$	5.2	15	7.2	15	6.9	18	8.2	18

Table 6.4: Dissipated energies for several values of ψ_0, angle α and number of braces

	$\alpha = 90°$		2 braces without gap		2 braces with gap	
	$E\ [MJ]$	Disc. [%]	$E\ [MJ]$	Disc. [%]	$E\ [MJ]$	Disc. [%]
Num.	6.5	–	7.5	–	8.0	–
$\psi_0 = \pi/4$	6.6	2	7.6	1	8.3	4
$\psi_0 = \pi/3$	6.4	2	7.3	3	8.2	2
$\psi_0 = \pi/2$	5.7	12	6.8	9	8.0	0
$\psi_0 = 3\pi/4$	5.4	17	6.4	15	7.6	5

These additional results confirm the choice of $\psi_0 = \pi/3$.

6.3.3.6 Comparison with *NORSOK* results

In order to summarise above results, Tables 6.5 and 6.6 compare the punching forces calculated by the three methods for the Y-joints (one brace) and K-joints (two braces) respectively. The 3 semi-analytical forces (SA) correspond respectively to the initiation of the punching (local mode), the initiation of the global mode (change of curvature in the curve) and the mean between these values. The numerical force ($Num.$) corresponds to the peak resistant force occurring shortly after the beginning of the punching process.

The discrepancy of the *NORSOK* and the semi-analytical model with respect to the numerical one, considered as the reference one, is also given (the mean value is taken into consideration for the semi-analytical model).

Table 6.5: Comparison of punching force with *NORSOK*, semi-analytical and numerical methods for Y-joints

α	β	*NORSOK*	SA_{min}	SA_{max}	SA_{mean}	$Num.$	Disc. *NORSOK*-$Num.$	Disc. SA_{mean}-$Num.$
[°]	[–]	$[MN]$	$[MN]$	$[MN]$	$[MN]$	$[MN]$	[%]	[%]
45	0.48	5.2	3.6	5.7	4.7	6.1	15	23
45	0.32	3.8	3.3	5.0	3.7	4.8	21	23
45	0.64	6.7	4.0	6.4	5.2	7.8	14	33
45	0.8	8.6	4.3	7.2	5.8	9.1	12	36
45	1	13.2	4.6	9.2	6.9	9.8	−35	29
90	0.48	3.7	3.4	5.7	4.6	5.9	37	22

Table 6.6: Comparison of punching force with *NORSOK*, semi-analytical and numerical methods for K-joints

α	β	g	*NORSOK*	SA_{min}	SA_{max}	SA_{mean}	$Num.$	Disc. $_{NORSOK\text{-}Num.}$	Disc. $_{SA_{mean}\text{-}Num.}$
[°]	[−]	$[m]$	$[MN]$	$[MN]$	$[MN]$	$[MN]$	$[MN]$	[%]	[%]
45	0.48	0	11.9	4.7	6	5.4	7.8	−53	31
45	0.48	0.82	5.7	6.4	/	6.4	8.9	36	28

From these Tables, it appears that the force computed by all three methods are comparable, even if the discrepancies are large in some cases.

However, when dealing with crashworthiness, dissipation of energy is a much more relevant design criteria than crushing force. Considering the energy dissipated plastically, the proposed model provides clearly a significant improvement in comparison with *NORSOK N-004* regulation.

As mentioned before, the three hinges global mechanism is not included in *NORSOK*, and assuming the force provided by this recommendation as constant for the whole penetration process allows to understand the limitations of the model. The new semi-analytical model takes into account the span of the punched tubular member for a global deformation mode and provides a closed-form relation between the force and the penetration.

6.4 Punching process on a complete jacket

6.4.1 Methodology to assess punching on the whole jacket

The semi-analytical model presented here above was developed to compute the resistance and the dissipated energy of a leg punched by one or two compressed braces at one single connection. Comparisons with FE results demonstrated that derived expressions allow to represent correctly the response of a clamped tubular member punched by one or two tubes.

As the overall OWT jacket is concerned, punching can occur on both impacted and rear legs and at several connections, as shown in Fig. 6.6. The tool developed to assess the plastic energy dissipated by deformation of the overall jacket has to be able to predict the punching at all connections between legs and braces. Therefore, an algorithm for punching was developed and is presented here.

For the next developments, the deformation in one single plane of the jacket is considered. From Fig. 6.47, the total ship penetration is equal to δ_{tot}, while the penetration in planes 1 and 2 are equal to $\delta_1 = \delta_{tot} \times \cos\alpha$ and $\delta_2 = \delta_{tot} \times \sin\alpha$ respectively. As the strategy is identical for all the planes, only plane 1 is considered here and one denote $\delta_1 = \delta$.

For each connection on the impacted leg corresponds two connections on the rear leg, as can be seen in Fig. 6.48. Indeed, considering a connection between the impacted leg (left here) and

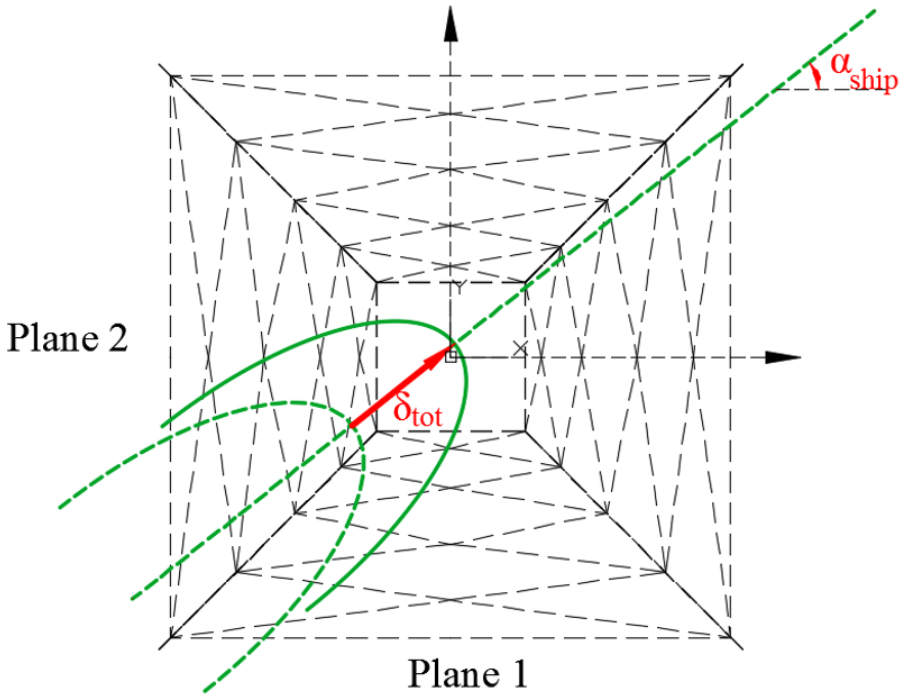

Figure 6.47: Top view of a jacket and striking ship

braces, punching can be due to both compressed braces welded to the considered connection. The compression in those braces is then transmitted to two different connections on the rear leg (right here). Scenarios where only one of the two braces is submitted to compression (Fig. 6.7) have also to be investigated.

In order to assess the punching scheme, the properties of each connection have to be determined, as they will allow to compute the initial value of the punching force. Indeed, the deformation due to punching starts for a non-zero value of the force, as already presented above, in Fig. 6.24 amongst others.

Punching can occur only if the brace connected to the leg is in compression. The first step is therefore to identify which are the braces in compression. We rely on the algorithm developed to take into account the overall motion of the whole jacket, presented by the authors in Chapter 5. After the first iteration, the algorithm provides the axial force sign (tension or compression) in all the members of the jackets, including the braces.

At each connection, it becomes possible to identify the number of compressed connected braces, namely none, one or two. Then, the intersection surface between the leg and the braces is defined as follows:

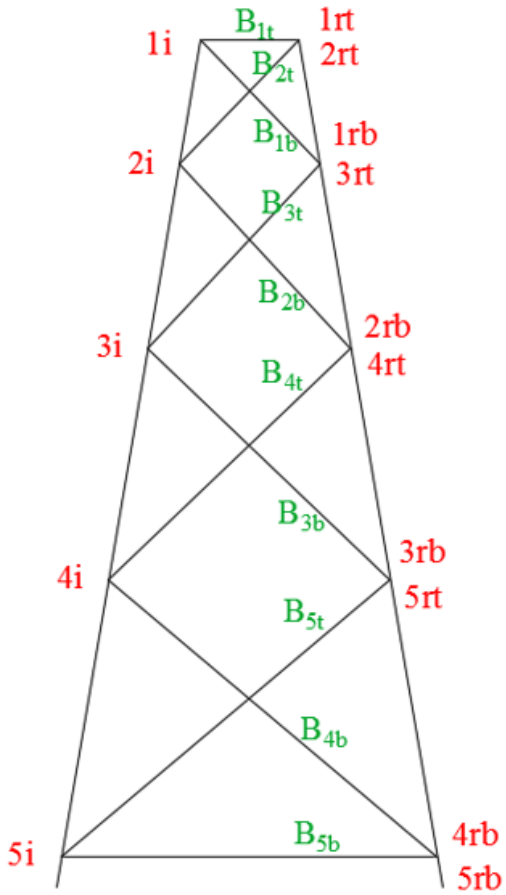

Figure 6.48: Names of connections and braces

- No compressed brace:
  Punching cannot occur at this connection.
- One compressed brace:
  One brace punching intersection surface (Section 6.3.2).
- Two compressed braces:
  Two braces punching intersection surface (Section 6.3.3.4).

Then, using mechanical and geometrical parameters of the connection (σ_0, β ratio, α angles, number of compressed braces, ...), the force required to initiate the punching is computed for each connection on both impacted and rear legs.

Punching can occur either on the impacted leg or on the rear leg. Similarly, the process can be initiated on one or both of them. The compression force in the brace has to be larger than the initial force of the connection to activate the punching on that connection. In addition, if both braces connected to the impacted leg are in compression, both connections on the rear leg that are related to the one on the impacted leg have to be activated. The algorithm related to the case of two compressed braces, with the top one or the bottom one compressed, is given in Figs. 6.49, 6.50 and 6.51 respectively. We denote B_{Nt} and B_{Nb} the axial force in the top and bottom brace related to the connection N, and F_{Ni}, F_{Nrt} and F_{Nrb} are the initial forces for punching at node Ni, Nrt and Nrb where N is the number of the connection and defined as a so-called *level*.

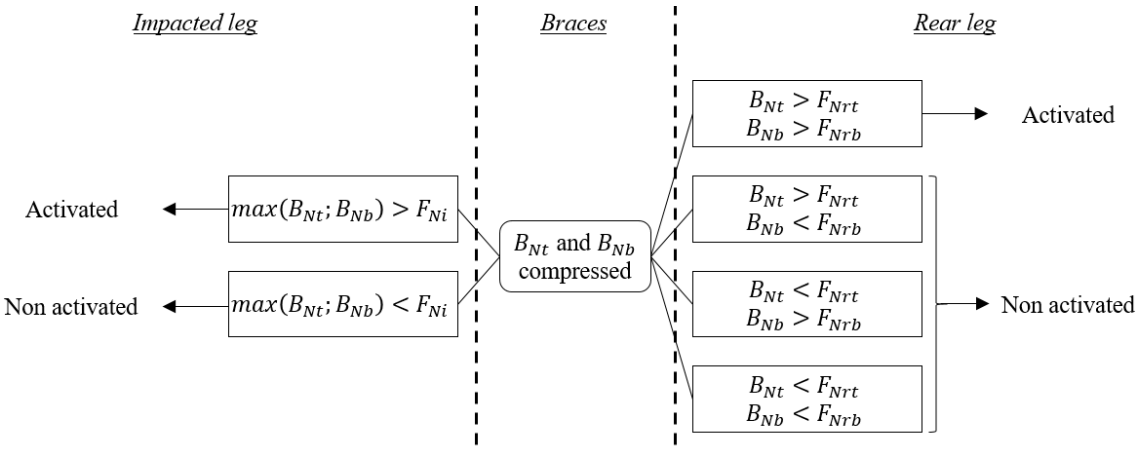

Figure 6.49: Activation of punching for both braces compressed

Once connections where punching is initiated are identified, the displacement due to punching at each connection has to be computed and linked to the penetration of the ship into the jacket.

We consider that a so-called *level* is activated if this level is activated on the impacted leg or on the rear leg. Then, the level located above the highest activated level and the one below the lowest activated level are supposed to remain fixed (the so-called *fixed points*). The activated levels displacements are then assumed to vary linearly, from the fixed points (zero displacement)

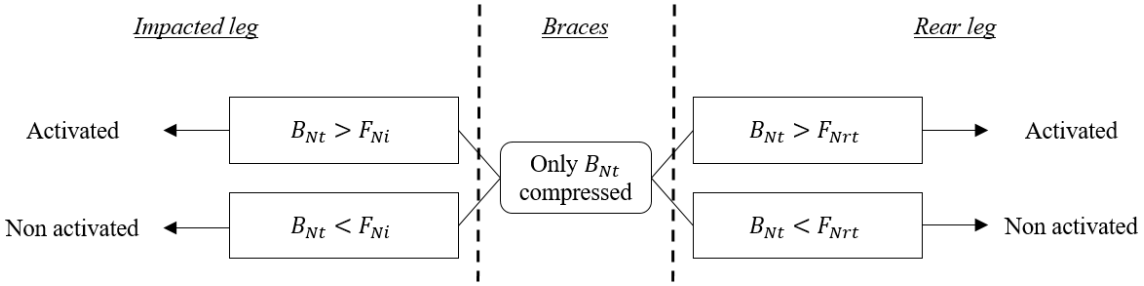

Figure 6.50: Activation of punching for top brace compressed

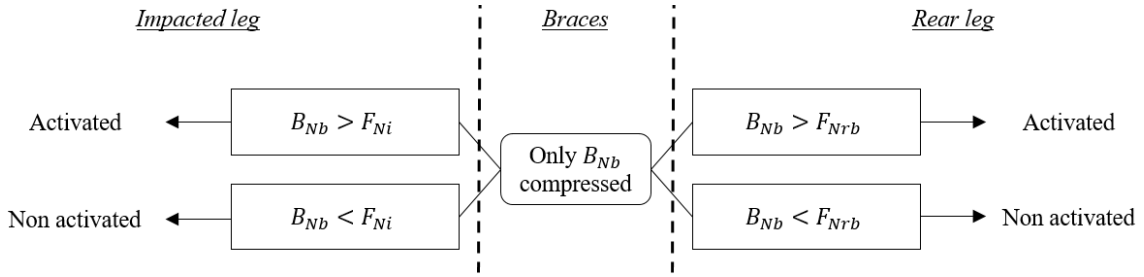

Figure 6.51: Activation of punching for bottom brace compressed

up to the ship penetration δ. Let us take an example, illustrated by Fig. 6.52, where levels 3 and 4 are activated. In this case, levels 2 and 5 are considered as fixed points and the displacement at levels 3 and 4 are computed with linear interpolation, as defined in Fig. 6.52. We denote the displacement at the level N as δ_N. The value of δ_N $(N = 3, 4)$ is computed with Eq. 6.60.

$$\delta_N = \left(1 - \frac{h_N}{H_b}\right)\delta \tag{6.60}$$

The braces are assumed to transmit rigidly the displacement from the impacted leg to the rear leg. The displacement computed for a level is balanced by the deformation on the impacted or on the rear leg by the same amount.

Knowing the displacement at each connections, the resistant force and the dissipated energy is computed using equations described in previous Sections.

In this Chapter, punching was divided into two successive phases: local denting and global bending. This latter is already taken into consideration in the *overall motion* deformation mode (Chapter 5) and is not modelled in the *punching* deformation mode.

The methodology used to compute the local punching force related to a given level N is illustrated in Figs. 6.53, 6.54 and 6.55.

As level N is concerned, the resistant force acting at the connection on the impacted leg is assumed to be the lowest value between the resistant force on the impacted and on the rear leg, i.e. $M_{tot,N} = \min\left(R_{tot,Ni}; R_{tot,Nr}\right)$.

The force computed acts at the elevation of the considered level on the impacted leg. However, the required force is the one acting on the ship. If we denote R_{ship} the force acting on the

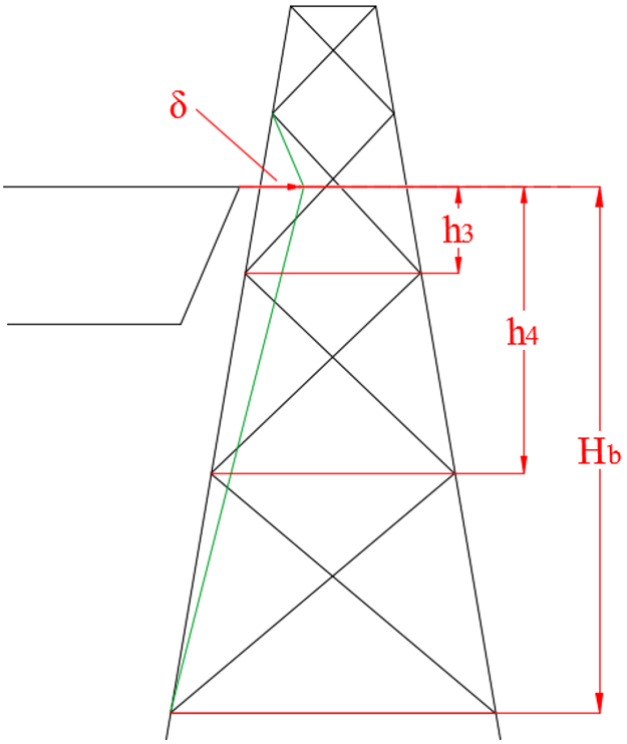

Figure 6.52: Punching displacement at each level

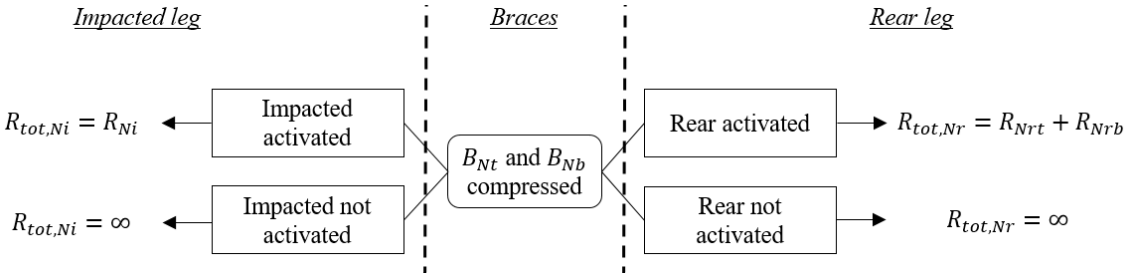

Figure 6.53: Computation of punching force at one level for both braces compressed

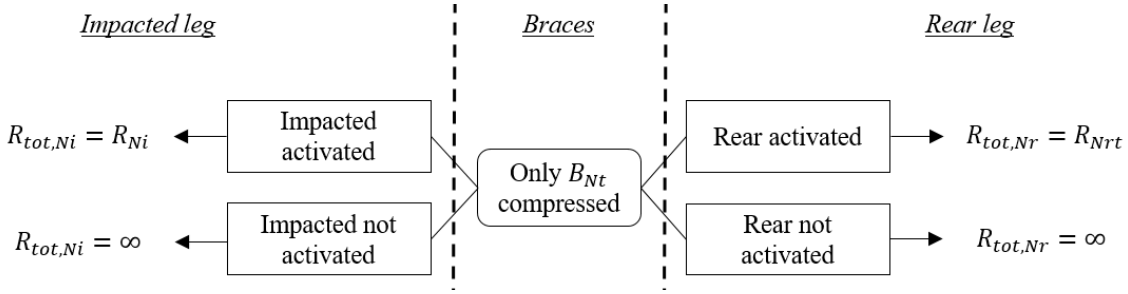

Figure 6.54: Computation of punching force at one level for top brace compressed

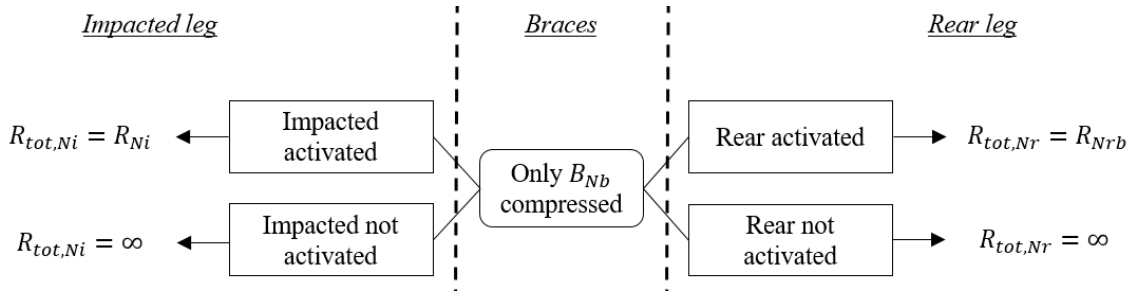

Figure 6.55: Computation of punching force at one level for bottom brace compressed

ship, one can write the virtual power theorem as:

$$R_{ship,N} \times \dot{\delta} = \dot{E}_{int,N} \tag{6.61}$$

The dissipated energy rate is expressed as a function of δ_N but can be derived with regard to δ using Eq. 6.60, as given in Eqs. 6.62 and 6.63, in order to derive the force which acts on the ship.

$$\dot{E}_{int,N} = f(\dot{\delta}_N) = f(\dot{\delta})\frac{\partial \delta_N}{\partial \delta} \tag{6.62}$$

$$\frac{\partial \delta_N}{\partial \delta} = 1 - \frac{h_N}{H_b} \tag{6.63}$$

Finally, the contribution of each level can be added, as expressed in Eq. 6.64 in order to get the total resistant force acting on the ship in that plane.

$$R_{ship,tot} = \sum R_{ship,N} \tag{6.64}$$

The same methodology can be used for the plane 2, taking $\delta = \delta_2$.

6.4.2 Validation on a full-scale jacket

The described methodology is validated with FE simulations of ship collisions on the aforementioned full OWT jacket. The jacket model is fully presented in Section 3.2.2.

The validation process will consist in comparing the evolution of the energy dissipated by punching with regard to the total ship penetration with both semi-analytical and numerical models. For the semi-analytical model, only punching deformation mode is accounted for. In the numerical model, the energy dissipation is computed by adding the internal energy related to the element sets located around the connections with the braces.

The first collision simulation is depicted in Fig. 6.2. The top part of the ship is located at an elevation of 43 m from the foundation level of the jacket. The ship is given a mass of 6,000 tons (added mass included) and an initial velocity of 5 m/s in the surge direction, corresponding to a kinetic energy of 75 MJ. The sway and the heave movements are restrained.

The maximum displacement obtained from simplified and numerical models are equal to 3.28 m and 3.16 m respectively, which is a discrepancy of 4%. The effective plastic strain distributed on the whole structure and around the impact point provided by *LS-DYNA* are presented in Figs. 6.56 and 6.57 respectively when the ship penetration is maximum. The elements with an effective plastic strain exceeding 1% are depicted in red.

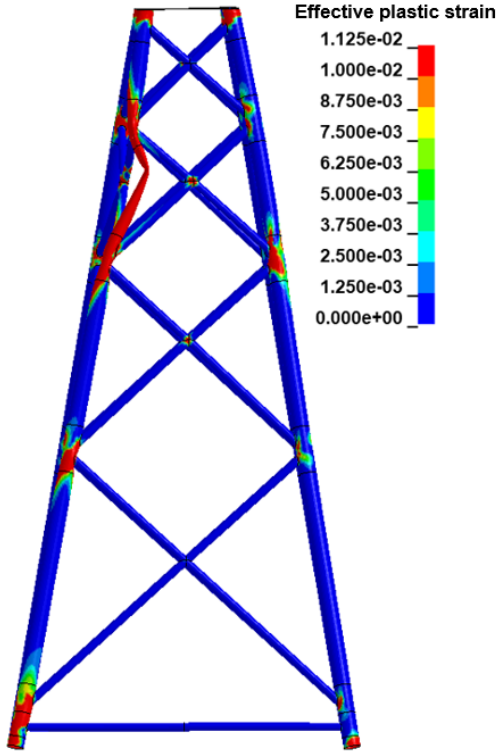

Figure 6.56: Jacket effective plastic strain for right angle collision at maximum ship penetration

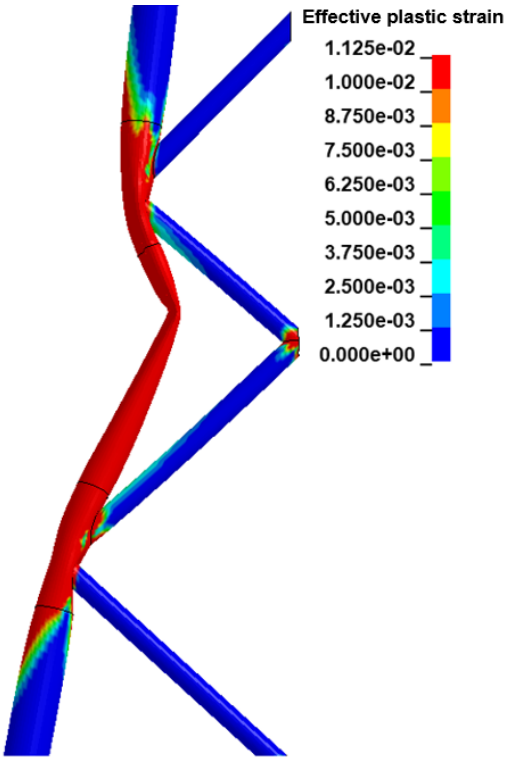

Figure 6.57: Jacket effective plastic strain around the impact point for right angle collision at maximum ship penetration

However, as can be seen in Fig. 6.57, the elements sets located on the impacted leg just above and below the impact point are highly deformed and the dissipation of energy is due to two deformation modes: the plastic bending of the impacted tubular member (Chapter 4) and the punching. It is difficult to identify clearly the contribution of each deformation mode in the energy dissipated plastically by this elements sets. It is assumed for those sets that half of the energy is dissipated by tubular member bending and half by punching. The evolution of internal energy due to punching for the considered collision scenario is plotted in Fig. 6.58 for both semi-analytical and numerical simulations.

As can be seen in Fig. 6.58, the semi-analytical results are in quite good accordance with the numerical ones, which validates the presented formulations for this collision scenario.

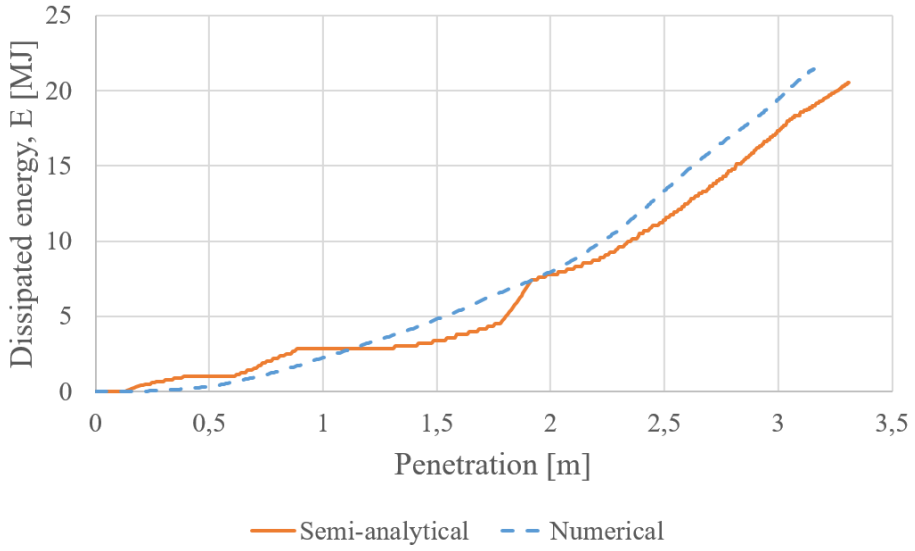

Figure 6.58: Evolution of the punching dissipated energy for semi-analytical and numerical models for right angle collision

Another collision scenario was investigated to validate the methodology, consisting in a 45 degrees angle collision, as depicted in Figs. 6.59 and 6.60, with the elevation of the impact point still at 43 meters. The striking ship initial kinetic energy is still equal to 75 MJ.

In this scenario, the maximum ship penetration computed with the presented method is 3.16 m, while the numerical simulation gives 2.98 m. The discrepancy between both is 6%.

The effective plastic strain distribution for the maximum penetration provided by *LS-DYNA* is presented in Figs. 6.61 and 6.62.

In Fig. 6.63, semi-analytical and numerical plastic energies dissipated by punching are compared.

As previously, the semi-analytical curve is in good accordance with the numerical one, which tends to validate the algorithm used to compute the punching dissipated energy.

6.5 Conclusions

This Chapter presents innovative developments to quickly assess the energy which is dissipated by plastic deformation when a clamped tubular member is punched by one or two tubular members. This kind of deformation occurs at some locations of an OWT jacket when it is impacted by a ship. Punching deformations are rather localised on both impacted and rear legs, at connections with compressed braces.

First, the punching mechanism is described, both locally, in the dented area, and globally on the total height of the structure. By performing nonlinear FE simulations of ship impacts against a full-scale OWT jacket, we can identify a kinematically admissible deformation pattern near the punched zone and understand the punching evolution at each brace-leg connection.

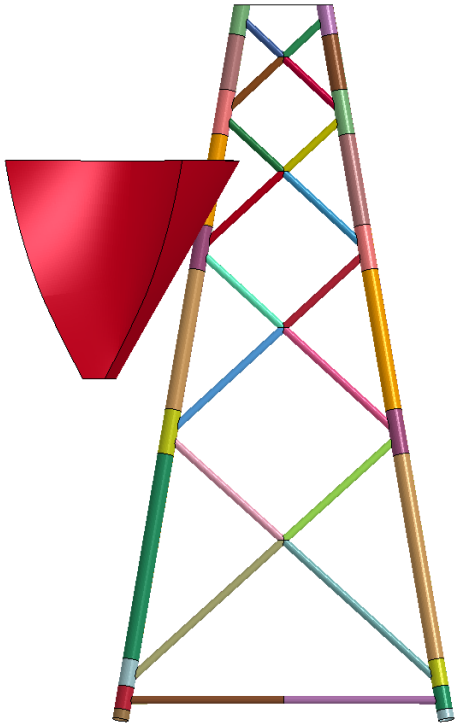

Figure 6.59: 45 degrees collision scenario (side view)

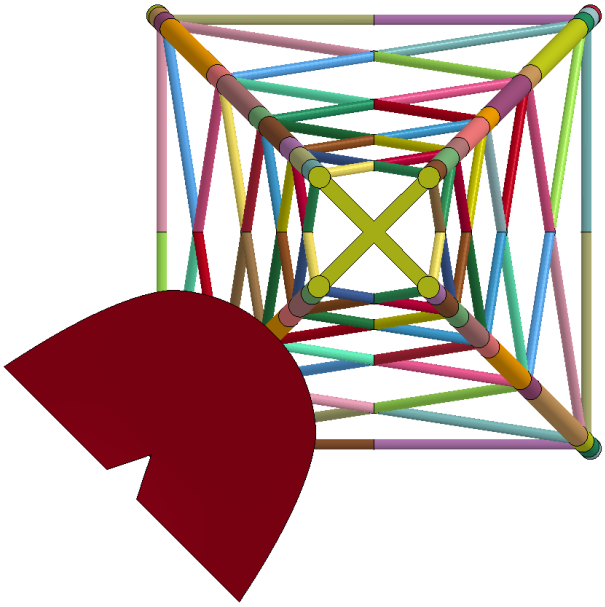

Figure 6.60: 45 degrees collision scenario (top view)

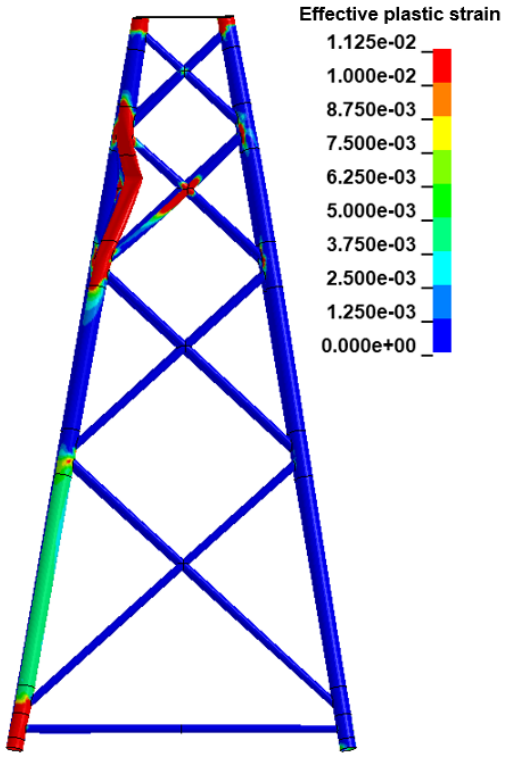

Figure 6.61: Jacket effective plastic strain for 45 degree collision at maximum ship penetration

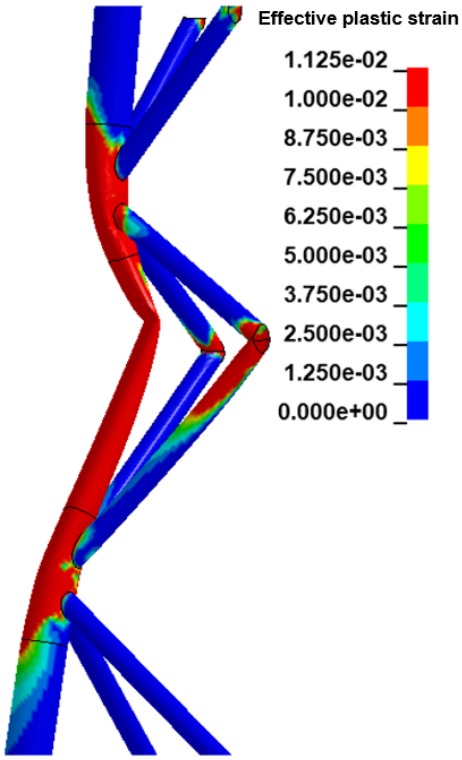

Figure 6.62: Jacket effective plastic strain around the impact point for 45 degree collision at maximum ship penetration

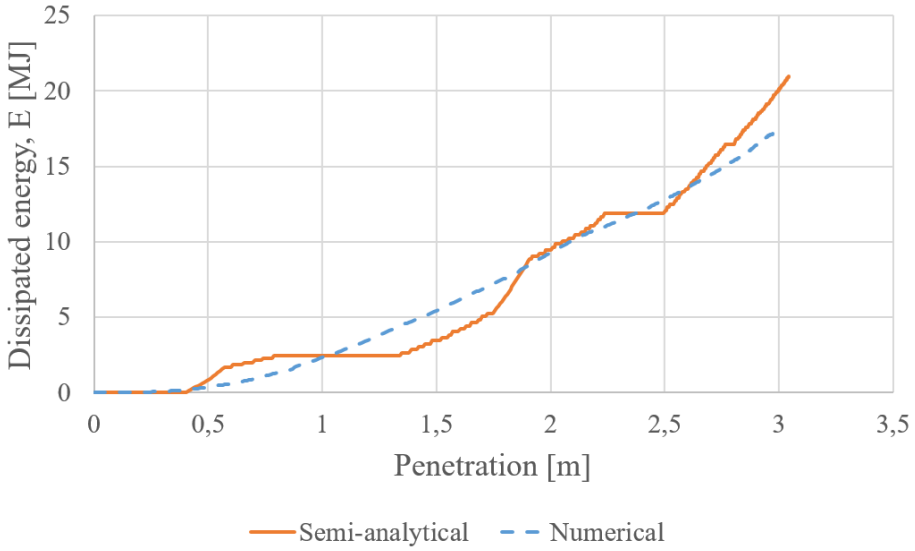

Figure 6.63: Evolution of the punching dissipated energy for semi-analytical and numerical models for 45 degrees collision

Using the upper-bound theorem associated with plastic limit analysis, analytical formulations are derived to assess the resistance and the dissipated energy of both local dent and global bending for a tubular member crushed by a linear indenter. Two empirical parameters are then integrated to the model to take into account the leg-brace diameter ratio. Several geometrical parameters are considered, such as the length of the punched tubular member, the gap between two connected braces and the angle between the tubular members involved. In order to make the model fully analytical, additional research is needed to derive analytically the resistant force of a leg section punched by a brace, whatever the leg and braces diameters.

Validation of the proposed semi-analytical expressions is achieved by comparison with both *NORSOK N-004* standard design values and numerical simulations. Post-processing and comparing resistant forces as well as dissipated energies, obtained numerically and with the proposed model, allow to show that this semi-analytical model is able to represent correctly the punching process. It also appears that in many situations, the proposed model constitutes a significant improvement in comparison with *NORSOK* design formulas.

Finally, a methodology is established to model the punching process on the whole height of the jacket. Based on semi-analytical developments, the required force to initiate punching on a connection is computed. It is compared to the compression force in the brace computed with an algorithm that describes the jacket behaviour in the overall motion mode. Then, the punching force can be computed at the connections where punching is activated and this force is transmitted to be applied on the striking ship.

This methodology is similarly validated against FE simulations performed on full-scale OWT jacket and is shown to be in good accordance with the numerical model.

Bibliography

[1] T Belytschko, I Lin, and CS Tsay. Explicit algorithms for the nonlinear dynamics of shells. *Computer Methods in Applied Mechanics and Engineering*, (42):225–251, 1984.

[2] L Buldgen, H Le Sourne, and T Pire. Extension of the super-elements method to the analysis of a jacket impacted by a ship. *Marine Structures*, (38):44–71, 2014.

[3] J de Oliveira, T Wiersbicki, and W Abramowicz. Plastic behavior of tubular members under lateral concentrated load. Technical Report n° 82-0708, DNV, 1982.

[4] Department of Energy (prepared by Wimpey Offshore), London. *Background to new static strength guidance for tubular joints in steel offshore structures*, Stationery Office Books edition, 1990.

[5] JO Hallquist. LS-DYNA theoretical manual. Technical report, Livermore Software Technology Corporation, 2006.

[6] JR Hsieh. Analytical formulations for ship offshore wind turbine collisions. Master's thesis, ICAM Nantes, 2015.

[7] N Jones. *Structural impact*. Cambridge: Cambridge University Press, 1997.

[8] MMK Lee and A Llewelyn-Parry. Strength of ring-stiffened tubular T-joints in offshore structures – a numerical parametric study. *Journal of Constructational Steel Research*, (51):239–264, 1999.

[9] DG Moffat, J Kruzelecki, and J Blachut. The effect of chord length and boundary condition on the static strength of a tubular T-joint under brace compression loading. *Marine Structure*, (9):935–947, 1996.

[10] Standards Norway. *NORSOK n-004: Design of steel structures*, 2004.

[11] T Wierzbicki and MS Suh. Indentation of tubes under combined loading. *International Journal of Mechanical Sciences*, 30:229–248, 1988.

[12] M Zeinoddini, JE Harding, and Parke GAR. Contribution of ring resistance in the behaviour of steel tubes subjected to a lateral impact. *International Journal of Mechanical Sciences*, (42):2303–2320, 2000.

Chapter 7

Deformation at the base of the jacket

Abstract:

This Chapter presents the analytical developments carried out to assess the energy dissipated plastically at the base of an OWT jacket impacted by a ship. The jacket components involved in this mechanism are both the impacted leg and the rear leg, considered as clamped at the foundation level, as well as the horizontal bottom brace considered as rigidly fixed on the legs. The foundation system is assumed to consist in piles inserted into sleeves with cement grout.

The base of the jacket is divided into four zones and a kinematically admissible displacement field is assumed for each of them. Based on plastic limit analysis, analytical formulations are derived to assess the resistance and the dissipated energy for each considered area and therefore of the whole jacket base.

To validate the method, full scale ship-jacket collisions are simulated both analytically and numerically. Plastic energy dissipated at the base of the jacket is compared successfully with nonlinear FE simulation results.

Reference paper:

T Pire, H Le Sourne, S Echeverry and P Rigo. Analytical formulations to assess the energy dissipated at the base of an offshore wind turbine jacket impacted by a ship. *Marine Structures*, (59):192-218, 2018.

7.1 Introduction

Four deformation modes of an OWT jacket impacted by a ship were identified in Chapter 3, namely:

- local crushing of impacted tubular members (Chapter 4);
- global deformation of the whole jacket (Chapter 5);
- punching of legs by compressed braces (Chapter 6);
- deformation at the base of the jacket (present Chapter).

The three firsts are studied in details in the previous Chapters 4 to 6.

In this Chapter, the deformation at the base of the jacket, as shown in Fig. 7.1 and zoomed in Fig. 7.2 and Fig. 7.3 for impacted and rear legs respectively, is investigated. Fringe levels are set in a way that the areas where the effective plastic strain is larger than a value of 1% is in red. This allows for an easy understanding of the most deformed zones of the impacted jacket. For a 75 MJ collision impact, the maximum effective plastic strain does not exceed 9% in the most stretched area (Fig. 7.2) while it reaches 16% near the fold (Fig. 7.3).

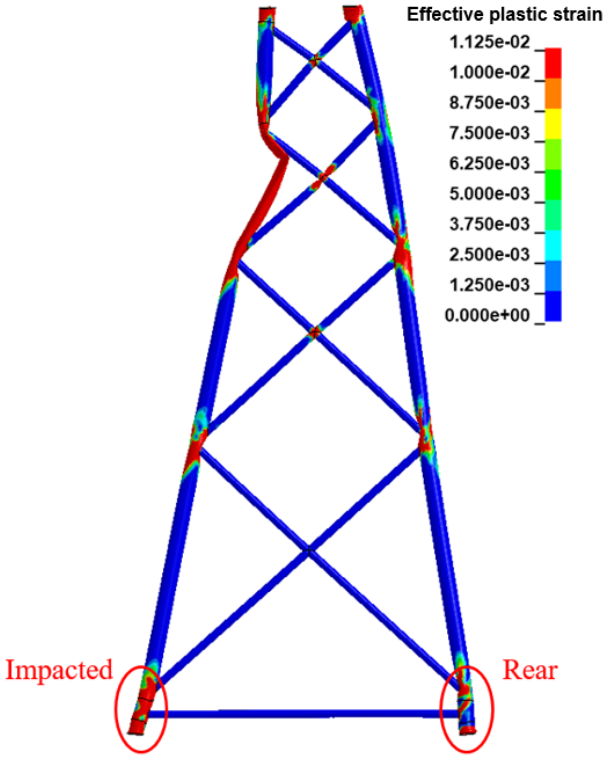

Figure 7.1: Plastic strain of one plane of an impacted jacket without considering rupture

As discussed in Section 3.6, rupture of elements is intentionally not included in the FE model, as it is demonstrated that its effect on the deformation at the base of the jacket is negligible. Similarly, rupture is not included in the analytical developments.

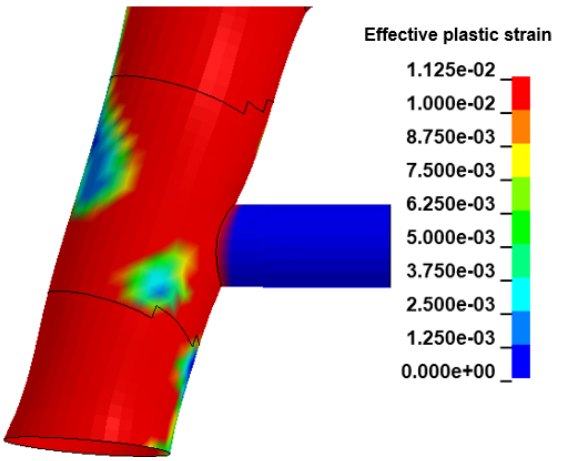

Figure 7.2: Plastic strain at the base of the impacted leg (zoom of "Impacted" area of Fig. 7.1)

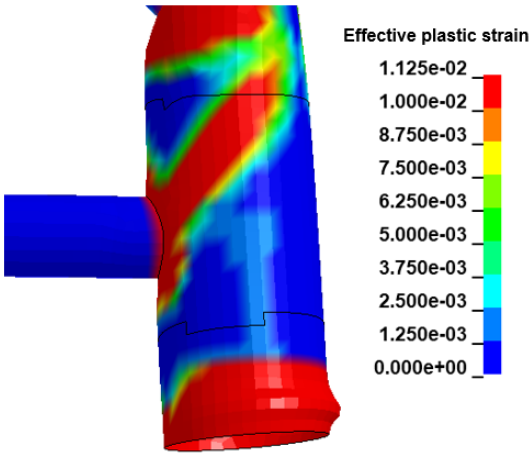

Figure 7.3: Plastic strain at the base of the rear leg (zoom of "Rear" area of Fig. 7.1)

Plastic limit analysis is performed in order to derive some explicit expression of the energy dissipated by plastic deformation of the lower part of the jacket. The purpose of this Chapter is thus to detail the performed analytical developments and to present some comparisons of the resulting deformation energies with numerical results.

The present work is based on the geometrical and mechanical properties of a real OWT jacket that was already presented in Section 3.2.2. The analytical developments presented in this Chapter are validated using this jacket dimensions. The investigated jacket is designed such as the braces are stronger than the joints. It can be assumed that most of the OWT jackets have similar structural arrangements and geometry. The developed expressions can therefore be assumed to assess properly the resistance of any jacket subjected to ship impact, as long as the braces resistance larger than the joint resistance assumption is met. It is worth noting that oil and gas platforms are not covered by the present research.

7.2 Description of the deformation mechanism

The deformation mechanism at the base of the jacket is supposed to occur only if the ship hits a leg. Indeed, braces are much more flexible than legs and brace rupture would occur near the impact point before the efforts at the base of the jacket become large enough to activate the mechanism.

Considering impacts on a leg, several collision scenarios were investigated to identify the striking ship minimum initial kinetic energy required to initiate the mechanism depicted in Fig. 7.1. Therefore, a $6,000$ tons (added mass included) ship with variable initial velocity colliding a jacket was studied, and it appeared from the results that the deformation pattern at the foundation level occurs for a striking velocity of 3 m/s, corresponding to a 27 MJ kinetic energy.

In our model, the trajectory of the striking ship is considered as arbitrary, which means that the deformation pattern can take place on the two faces of the jacket adjacent to the impacted leg. In the following, analytical formulations are developed in one single face and the displacement at the impact point is the projection of the total displacement of the ship along the horizontal vector of the plane, which is the projection of vector x on X and Y axes as shown in Fig. 7.4. The legs are assumed to be clamped at foundation level.

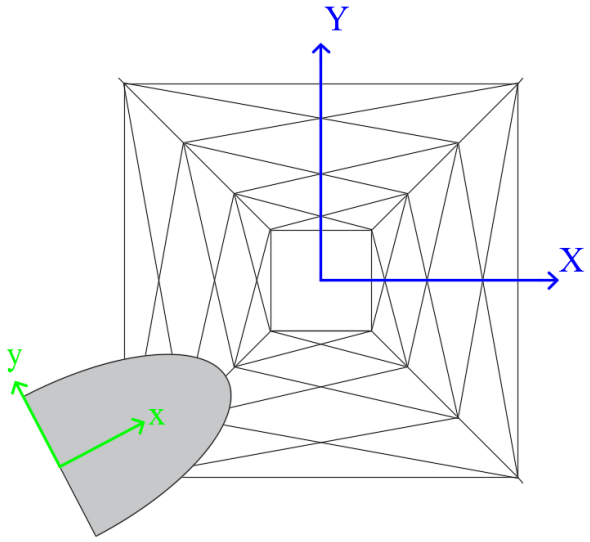

Figure 7.4: Ship collision references

A side view of a plane of a jacket is given in Fig. 7.5, where the initial structure is depicted in black dotted lines and the deformed structure in green solid lines. The impacted leg is isolated in Fig. 7.6 with a non-regular vertical scale. The horizontal bottom brace is assumed to remain horizontal, with a constant length and at the same altitude during the deformation process. The legs above this level are also considered as rigid.

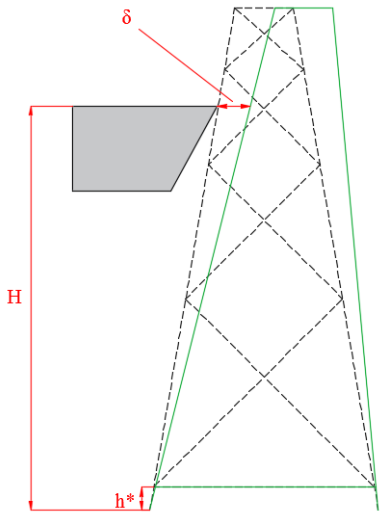

Figure 7.5: One plane of jacket displacement

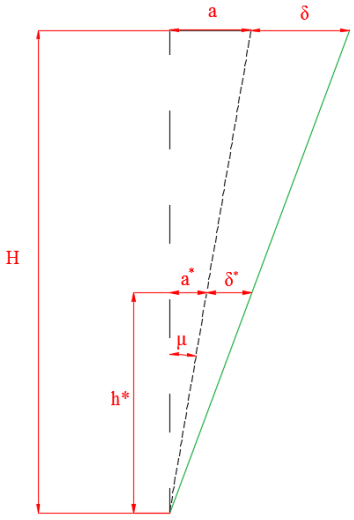

Figure 7.6: Impacted leg displacement

Angles and lengths of the deformed structure are depicted in Figs. 7.7 and 7.8 for impacted and rear leg respectively.

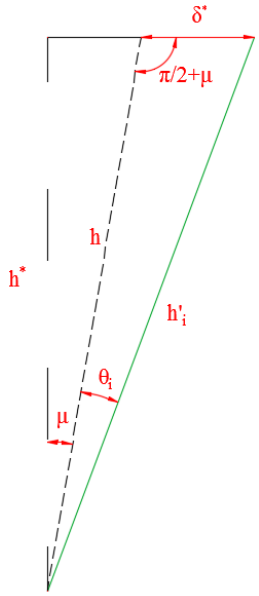

Figure 7.7: Angles and displacements of impacted leg at its base

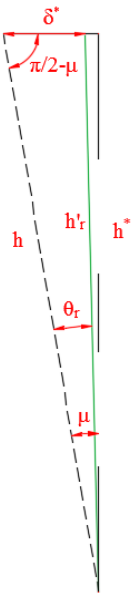

Figure 7.8: Angles and displacements of rear leg at its base

The following general geometrical relations can be extracted from above Figures:

$$\delta^\star = \frac{h^\star \delta}{H} \tag{7.1}$$

$$h = \frac{h^\star}{\cos\mu} \tag{7.2}$$

Then, considering the impacted leg, geometrical considerations allow to write:

$$h_i'^2 = h^2 + \delta^{\star 2} + 2h\delta^\star \sin\mu \tag{7.3}$$

$$\frac{\sin\theta_i}{\delta^\star} = \frac{\sin\left(\pi/2+\mu\right)}{h_i'} = \frac{\cos\mu}{h_i'} \tag{7.4}$$

Using Eqs. 7.3 and 7.4, the rotation angle of the impacted leg is given by:

$$\theta_i = \sin^{-1}\left(\frac{\delta^\star \cos\mu}{\sqrt{h^2 + \delta^{\star 2} + 2h\delta^\star \sin\mu}}\right) \tag{7.5}$$

Similarly, as the rear leg is concerned:

$$h_r'^2 = h^2 + \delta^{\star 2} - 2h\delta^\star \sin\mu \tag{7.6}$$

$$\frac{\sin\theta_r}{\delta^\star} = \frac{\sin\left(\pi/2 - \mu\right)}{h_r'} = \frac{\cos\mu}{h_r'} \tag{7.7}$$

Using Eqs. 7.6 and 7.7, the rotation angle of the rear leg writes:

$$\theta_r = \sin^{-1}\left(\frac{\delta^\star \cos\mu}{\sqrt{h^2 + \delta^{\star 2} - 2h\delta^\star \sin\mu}}\right) \tag{7.8}$$

In addition to these modifications of angles and lengths, the model also considers the deformation of some leg cross-sections. A cross-section view at mid-diameter of the tubular members is depicted in Fig. 7.9.

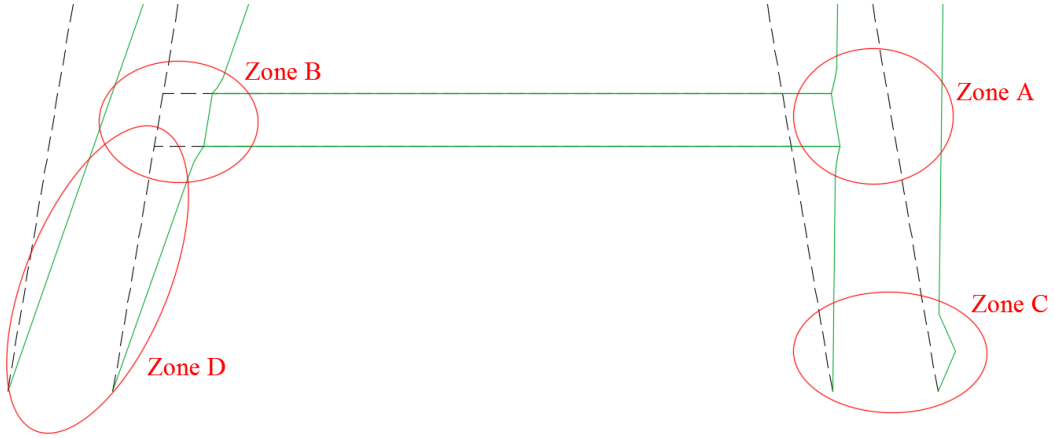

Figure 7.9: Modification of cross-sections at mid-diameter and definition of zones

As shown in the Figure above, the base of the jacket may be divided into 4 zones, named from A to D and for each of them, the energy rate expression will be derived individually.

7.3 Derivation of deformation energy rates for zones *A* to *D*

In this Section are given the detailed calculations for zones A to D, as described in Fig. 7.9.

As already done in Chapters 4 and 6, analytical formulations are derived using the so-called upper-bound theorem (Jones for more details [3]), which states that the external forces work rate equals the internal energy rate:

$$P\dot{\delta} = \sum \dot{E}_{int} \tag{7.9}$$

where P is the contact force between the ship bow and the structure, $\dot{\delta}$ is the velocity of the contact point and $\dot{E}_{int}$ is the dissipated energy rate for the considered deformed zone (the summation will involve the zones A to D, in our case).

The expressions of $\dot{E}_{int}$ will be expressed in terms of impacted and rear legs rotation velocities $\dot{\theta}_i$ and $\dot{\theta}_r$ while the external work rate will be expressed in terms of impact point translational velocity $\dot{\delta}$. These quantities are related by the following expressions:

$$\dot{\theta}_i = \frac{\partial \theta_i}{\partial \delta^\star} \frac{\partial \delta^\star}{\partial \delta} \dot{\delta} \tag{7.10}$$

$$\dot{\theta}_r = \frac{\partial \theta_r}{\partial \delta^\star} \frac{\partial \delta^\star}{\partial \delta} \dot{\delta} \tag{7.11}$$

Then, by using Eqs. 7.8, 7.8 and 7.1 successively, it comes:

$$\frac{\partial \theta_i}{\partial \delta^\star} = \frac{\cos\mu}{\sqrt{h^2 + \delta^{\star 2} + 2h\delta^\star \sin\mu - (\delta^\star \cos\mu)^2}} \left(1 - \delta^\star \frac{\delta^\star + h^\star \sin\mu}{h^2 + \delta^{\star 2} + 2h\delta^\star \sin\mu}\right) \tag{7.12}$$

$$\frac{\partial \theta_r}{\partial \delta^\star} = \frac{\cos\mu}{\sqrt{h^2 + \delta^{\star 2} - 2h\delta^\star \sin\mu - (\delta^\star \cos\mu)^2}} \left(1 - \delta^\star \frac{\delta^\star - h^\star \sin\mu}{h^2 + \delta^{\star 2} - 2h\delta^\star \sin\mu}\right) \tag{7.13}$$

$$\frac{\partial \delta^\star}{\partial \delta} = \frac{h^\star}{H} \tag{7.14}$$

Let us consider that the material is rigid – perfectly plastic, with a flow stress denoted σ_0.

The following subsections describe the mathematical developments performed to get the analytical formulations of the dissipated energy rate for each zone.

7.3.1 Zone *A*: rear leg at horizontal brace level

As the zone A is concerned (Fig. 7.9), typical effective plastic strain contours post-processed from nonlinear FE simulations are plotted in Fig. 7.10. A pattern of deformation, such as the one represented by a continuous line in Figs. 7.11 and 7.12, is then postulated. As shown in Fig. 7.8, the rear leg is assumed to rotate at foundation level with an angle θ_r. Moreover, the leg cross-section is supposed to deform over a length equal to $\xi_1(\lambda) + 2R_{bpd} + \xi_2(\lambda)$. In Fig. 7.12, the dotted line represents the position of the undeformed but rotated rear leg. While the leg is rotating, the brace is supposed to remain horizontal and at the same elevation. As the compression of the brace can be neglected, a deformation of the leg cross-section occurs. At mid-height of the brace section, the value of λ is equal to zero. The brace remaining undeformed,

the angle between its extremity and the vertical axis is equal to μ and the inclination of the extremity with respect to the vertical axis is $\mu - \theta_r$.

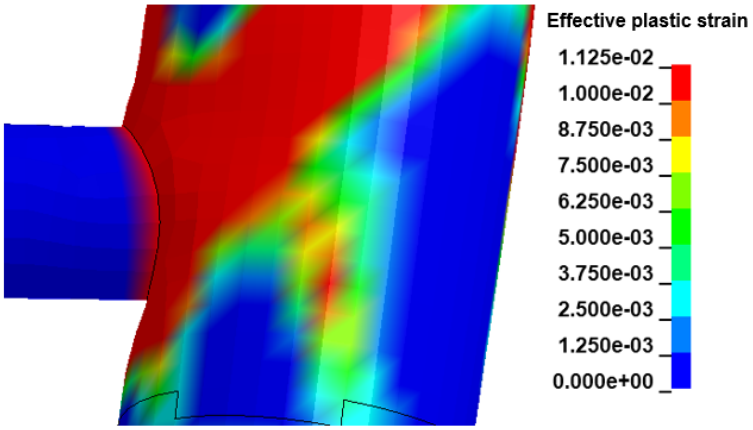

Figure 7.10: Effective plastic strain in zone A

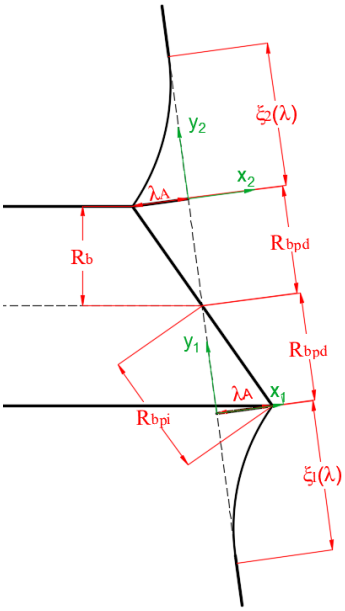

Figure 7.11: Deformation pattern at mid-diameter in zone A (displacements)

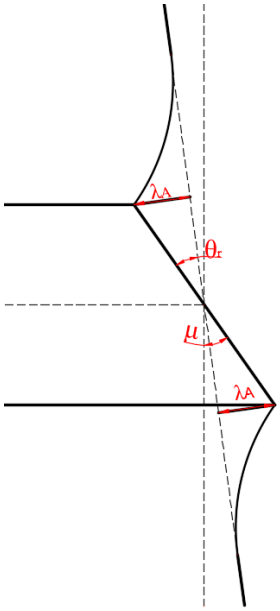

Figure 7.12: Deformation pattern at mid-diameter in zone A (angles)

At the upper part, the leg section tends to extend along the brace axis direction while it tends to be compressed at the lower part. At mid-height of the brace, the leg section is assumed to remain undeformed.

Geometrical considerations from Fig. 7.11 allow to write:

$$R_{bpi} = \frac{R_b}{\cos \mu} \tag{7.15}$$

$$R_{bpd} = R_{bpi} \cos \theta_r \tag{7.16}$$

$$\lambda_A = R_{bpi} \sin \theta_r \tag{7.17}$$

$$\frac{\partial \lambda_A}{\partial \theta_r} = R_{bpi} \cos \theta_r \tag{7.18}$$

As the cross-section deformation patterns for the upper (above mid brace level) and lower (below mid brace level) parts are different, analytical derivations of the corresponding internal energy rates have to be carried out separately.

7.3.1.1 Lower part

The developments presented here are based on the work presented in Chapter 4 to study the resistance of a vertical tubular member impacted by a ship bow.

In the following, the system of axes (x_1, y_1) depicted in Fig. 7.11 is considered.

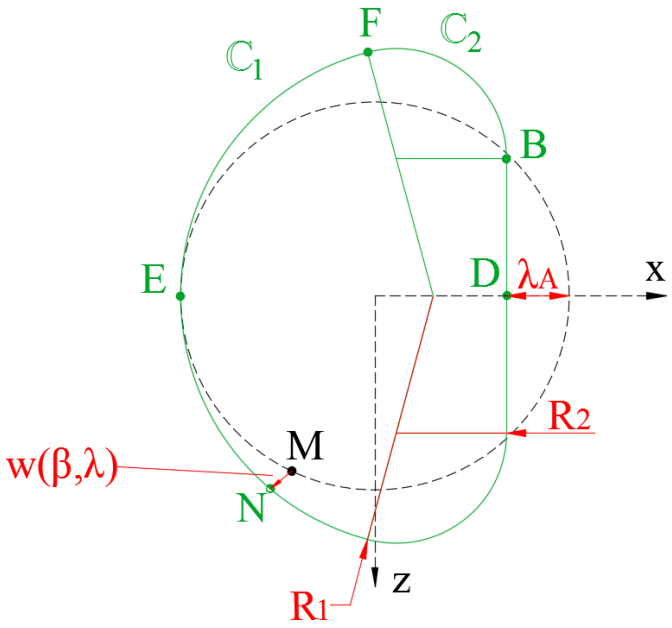

Figure 7.13: Cross-section deformation during crushing at the lower part of zone A

A displacement field proposed by Wierzbicki and Suh [8] and depicted in Fig. 7.13 is assumed. The black dotted line describes the initial cross-section of the leg and the green solid line is the deformed cross-section, supposed to be symmetric with respect to x-axis. Let us consider a point M of the initial cross-section with coordinates $(x_M, z_M) = (R\cos\beta, R\sin\beta)$. During the deformation process, the point M translates to point N (x_N, z_N) belonging to $\mathbb{C}'$. The

displacement $w(\beta, \lambda_A)$ of point M is equal to the distance $\overline{MN}$ that can be written as:

$$w_l(\beta, \lambda_A) = \sqrt{(x_N - x_M)^2 + (z_N - z_M)}^2 \tag{7.19}$$

The mathematical developments to get $w(\beta, \lambda_A)$ are detailed in Refs. [1, 7, 8].

The displacement field involves the cross-section deformation but also extends along the axis of the leg between $[-\xi_1(\lambda_A); R_{bpd}]$. As done by Wierzbicki and Suh [8], the velocity field $\dot{w}(\beta, \lambda_A)$ is supposed to vary linearly on the considered portion of the leg $-\xi_1(\lambda_A) < y < R_{bpd}$ and the leg is assumed to remain undamaged for $y < -\xi_1(\lambda_A)$.

$$\begin{array}{ll} \dot{W}_l(\beta, \lambda_A, y) = \dot{w}_l(\beta, \lambda_A)\left(1 + \frac{y}{\xi_1(\lambda_A)}\right) & \text{if } y \in [-\xi_1(\lambda_A); 0] \\ \dot{W}_l(\beta, \lambda_A, y) = \dot{w}_l(\beta, \lambda_A)\left(1 + \frac{y}{R_{bpd}}\right) & \text{if } y \in [0; R_{bpd}] \\ \dot{W}_l(\beta, \lambda_A, y) = 0 & \text{if } y < -\xi_1(\lambda_A) \end{array} \tag{7.20}$$

The axial extension of the deformed area $\xi_1(\lambda_A)$ will be determined later on.

As proposed by Wierzbicki and Suh [8] and similarly to Chapters 4 and 6, the tubular member is composed of independent rings, keeping a constant perimeter during the crushing process, which are free to slide along generators without shearing. As a consequence, the total energy rate of the crushing mechanism is given by the sum of the energy rates of the rings and the generators.

$$\dot{E}_A = \dot{E}_r + \dot{E}_g \tag{7.21}$$

Let us first consider the energy rate of the rings. The energy dissipation $\dot{E}_b$ is due to the rotation of moving plastic hinges and to the change of curvature of the tubular members:

$$\dot{E}_b = 2m_0\left(\frac{V_B}{R_2} + \left(\frac{1}{R_2} - \frac{1}{R_1}\right)V_F + \int_F^E \dot{\chi}_1 dl + \int_D^F \dot{\chi}_2 dl\right) \tag{7.22}$$

where $m_0 = \sigma_0 t^2/4$ is the tubular member bending capacity per unit of length, σ_0 and t are respectively the flow stress and the thickness of the tubular member, V_B and V_F are the velocities of plastic hinges B and F respectively and $\dot{\chi}_1$ and $\dot{\chi}_2$ are the changes of curvature of $\mathbb{C}_1$ and $\mathbb{C}_2$ respectively.

Integrating this expression along the generator leads to:

$$\dot{E}_r = \int_{-\xi_1}^{0} \dot{E}_b\left(1 + \frac{y}{\xi_1}\right)dy + \int_0^{R_{bpd}} \dot{E}_b\left(1 - \frac{y}{R_{bpd}}\right)dy = \dot{E}_b\frac{\xi_1 + R_{bpd}}{2} \tag{7.23}$$

As the generators are considered, both their length and curvature are supposed to vary during the crushing process. Considering conservatively that the energy dissipated by generators

bending can be neglected, the rate of membrane deformation can be written as:

$$\dot{\varepsilon}\left(\beta, \lambda_A, y\right) = \frac{\partial W_l}{\partial y}\frac{\partial \dot{W}_l}{\partial y} \tag{7.24}$$

For one single generator with a given value of β, integration along the deformed section writes:

$$\dot{E}_m\left(\beta, \lambda_A\right) = n_0 \int_{-\xi_1}^{R_{bpd}} \dot{\varepsilon}\left(\beta, \lambda_A, y\right) dy = n_0 \dot{\lambda}\left(\frac{1}{\xi_1} + \frac{1}{R_{bpd}}\right) w_l(\beta, \lambda_A)\frac{\partial w_l}{\partial \lambda_A} \tag{7.25}$$

where $n_0 = \sigma_0 t$ is the tubular member axial resistance per unit of length. By integrating over the whole section (β varying from 0 to 2π), we get the contribution of all the generators:

$$\dot{E}_g = 2Rn_0\dot{\lambda}_A\left(\frac{1}{\xi_1} + \frac{1}{R_{bpd}}\right)\int_0^{2\pi} w_l(\beta, \lambda_A)\frac{\partial w_l}{\partial \lambda_A}d\beta = \left(\frac{1}{\xi_1} + \frac{1}{R_{bpd}}\right)\dot{E}'_m \tag{7.26}$$

The total energy rate can then be computed using Eqs. 7.21, 7.23 and 7.26:

$$\dot{E} = \dot{E}_b\frac{\xi_1 + R_{bpd}}{2} + \left(\frac{1}{\xi_1} + \frac{1}{R_{bpd}}\right)\dot{E}'_m \tag{7.27}$$

Applying the upper-bound theorem (Eq. 7.9) and considering that the contact force between the leg and the brace $P(\lambda_A)$ is punctual and located at $y = -R_{bp}$, one can write:

$$\begin{aligned} P\left(\lambda_A\right)\dot{\lambda}_A &= \dot{E}_b\frac{\xi_1 + R_{bpd}}{2} + \left(\frac{1}{\xi_1} + \frac{1}{R_{bpd}}\right)\dot{E}'_m \\ \Leftrightarrow P\left(\lambda_A\right) &= \left(\dot{E}_b\frac{\xi_1 + R_{bpd}}{2} + \left(\frac{1}{\xi_1} + \frac{1}{R_{bpd}}\right)\dot{E}'_m\right)\dot{\lambda}_A^{-1} \end{aligned} \tag{7.28}$$

Finally, the unknown axial extension of the deformed area ξ_1 can be determined by minimising the crushing force $P(\lambda)$:

$$\frac{\partial P(\lambda_A)}{\partial \xi_1} = 0 \qquad \Rightarrow \qquad \xi_1(\lambda_A) = \min\left(\sqrt{\frac{2\dot{E}'_m}{\dot{E}_b}}\ ; h'_r\right) \tag{7.29}$$

7.3.1.2 Upper part

Deriving the rate of energy dissipated by deformation of the part located above the mid-brace level requires to consider the coordinate system (x_2, y_2) shown in Fig. 7.11.

In this case, the leg cross-section deforms by extending along the direction of the brace. As for the lower part, the impacted tubular member is assumed to be composed of generators supported by independent rings that are free to slide on each other without shearing. The rings, initially circular, are then assumed to become elliptic, as depicted in Fig. 7.14. Considering the

deformation along the generators (leg axis), the velocity fields defined for the lower part analysis (Eq. 7.20) are reused for the upper part study.

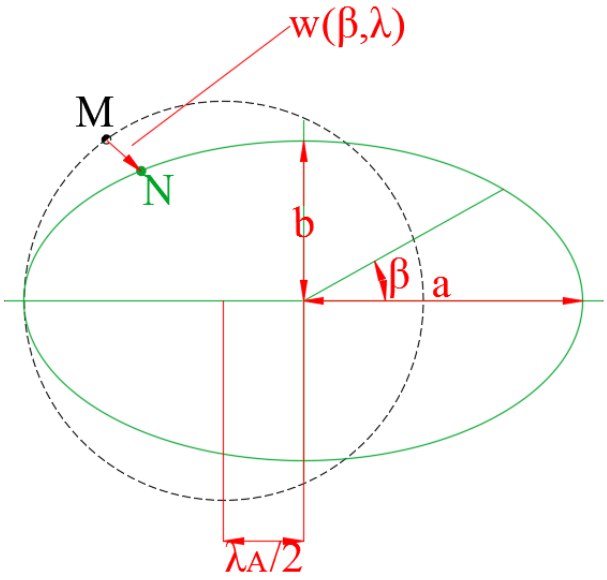

Figure 7.14: Cross-section deformation during crushing at the upper part of zone A

As done previously, let us assume that the perimeter of the rings remains constant during the deformation process. At level $y = 0$, we thus have:

$$2a = 2D + \lambda_A \qquad \Rightarrow \qquad a = R + \frac{\lambda_A}{2} \tag{7.30}$$

The perimeters of an ellipse before and after deformation are:

$$P_{before} = 2\pi R \qquad \text{and} \qquad P_{after} \cong 2\pi\sqrt{\frac{a^2+b^2}{2}} \tag{7.31}$$

By equating both expressions it comes:

$$b = \sqrt{R^2 - R\lambda_A - \frac{\lambda_A^2}{4}} \tag{7.32}$$

By definition of an ellipse, the eccentricity e, the radius of curvature $r(\beta)$ and the curvature $\chi(\beta)$ are equal to:

$$e = \frac{\sqrt{a^2-b^2}}{a} \tag{7.33}$$

$$r(\beta) = \frac{a^2}{b^2}\left(1 - e^2\cos^2\beta\right)^{3/2} \tag{7.34}$$

$$\chi(\beta) = \frac{1}{r(\beta)} = \frac{b^2}{a^2}\left(1 - e^2\cos^2\beta\right)^{-3/2} \tag{7.35}$$

Following the same methodology as for the lower part, the rates of energy dissipated by plastic deformation of rings $\dot{E}_r$ and generators $\dot{E}_g$ are derived as follows.

First, the rate of energy dissipated by plastic bending of one ring writes:

$$\dot{E}_b = m_0 \int_C \dot{\chi} dl = 2m_0 \int_0^{\pi} |\dot{\chi}(\beta)| \, \overline{ds}(\beta) \, d\beta \tag{7.36}$$

where

$$\overline{ds}(\beta) = \sqrt{a^2\cos^2\beta + b^2\sin^2\beta} \tag{7.37}$$

and

$$\dot{\chi}(\beta) = \frac{\partial\chi(\beta)}{\partial\lambda_A}\frac{\partial\lambda_A}{\partial\theta_r}\dot{\theta}_r \tag{7.38}$$

Eqs. 7.30, 7.32 and 7.35 allow to write:

$$\begin{aligned}\frac{\partial\chi(\beta)}{\partial\lambda_A} = {} & \frac{2bb'a^2 - 2aa'b^2}{a^4}\left(1 - e^2\cos^2\beta\right)^{-3/2} \\ & + \frac{b^2}{a^2}\frac{-3}{2}\left(1 - e^2\cos^2\beta\right)^{-5/2}\left(-2ee'\cos^2\beta\right)\end{aligned} \tag{7.39}$$

with

$$a' = \frac{\partial a}{\partial\lambda_A} = \frac{1}{2} \tag{7.40}$$

$$b' = \frac{\partial b}{\partial\lambda_A} = \frac{-\left(R - \lambda_A/2\right)}{2\sqrt{R^2 - R\lambda_A - \lambda_A^2/4}} \tag{7.41}$$

$$e' = \frac{\partial e}{\partial\lambda_A} = \frac{abb' - b^2a'}{a^2\sqrt{a^2b^2}} \tag{7.42}$$

Introducing Eqs. 7.40, 7.41 and 7.42 into Eq. 7.39 leads to:

$$\begin{aligned}\frac{\partial\chi(\beta)}{\partial\lambda_A} = {} & \frac{-a^2\left(R + \frac{\lambda_A}{2}\right) - ab^2}{a^4}\left(1 - e^2\cos^2\beta\right)^{-3/2} \\ & + \frac{b^2}{a^2}\frac{3}{2}\left(1 - e^2\cos^2\beta\right)^{-5/2} 2e\cos^2\beta\frac{\left(R + \lambda_A/2\right)a + b^2}{2a^2\sqrt{a^2 - b^2}}\end{aligned} \tag{7.43}$$

Integrating $\dot{E}_b$ for all the rings give the total flexural energy rate $\dot{E}_r$

$$\dot{E}_r = \int_{-R_{bpd}}^{0} \dot{E}_b \left(1 + \frac{y}{R_{bpd}}\right) dy + \int_{0}^{\xi_2} \dot{E}_b \left(1 - \frac{y}{\xi_2}\right) dy = \dot{E}_b \frac{R_{bpd} + \xi_2}{2} \tag{7.44}$$

As the generators are concerned, their flexural energy is neglected (as done for the lower part) so only membrane deformation is assumed to occur. Similarly to Eqs. 7.25 and 7.26, the corresponding energy rate writes:

$$\dot{E}_m\left(\beta, \lambda_A\right) = n_0 \int_{-R_{bpd}}^{\xi_2} \dot{\varepsilon}\left(\beta, \lambda_A, y\right) dy = n_0 \dot{\lambda} \left(\frac{1}{R_{bpd}} + \frac{1}{\xi_2}\right) w_u(\beta, \lambda_A) \frac{\partial w_u}{\partial \lambda_A} \tag{7.45}$$

$$\dot{E}_g = 2R n_0 \dot{\lambda}_A \left(\frac{1}{R_{bpd}} + \frac{1}{\xi_2}\right) \int_0^{2\pi} w_u(\beta, \lambda_A) \frac{\partial w_u}{\partial \lambda_A} d\beta = \left(\frac{1}{R_{bpd}} + \frac{1}{\xi_2}\right) \dot{E}'_m \tag{7.46}$$

To define the displacement field $w(\beta, \lambda)$, let us consider the point M from the initial cross-section moving to point N in the deformed cross-section (see Fig. 7.14). Their coordinates are respectively $(x_M, z_M) = (R\cos\beta, R\sin\beta)$ and $(x_N, z_N) = (\lambda_B/2 + a\cos\beta, b\sin\beta)$ and the displacement is:

$$w_u\left(\beta, \lambda_A\right) = \sqrt{\left(x_N - x_M\right)^2 + \left(z_N - z_M\right)^2} \tag{7.47}$$

$$\frac{\partial w_u\left(\beta, \lambda_A\right)}{\partial \lambda_A} = \frac{1}{2 w_u} \left(\left(x_N - x_M\right)\left(1 + \cos\beta\right) - \left(z_N - z_M\right) \frac{R - \lambda_A/2}{b} \sin\beta\right) \tag{7.48}$$

As done previously for the lower part, the unknown axial extension of the deformed area ξ_2 is determined by minimising the corresponding resistant force to obtain:

$$\xi_2\left(\lambda_A\right) = \sqrt{\frac{2\dot{E}'_m}{\dot{E}_b}} \tag{7.49}$$

7.3.2 Zone *B*: impacted leg at horizontal brace level

The deformation pattern at mid-diameter of the leg is depicted in Figs. 7.15 and 7.16.

Geometrical relations associated to zone B are the following ones:

$$R_{bpi} = \frac{R_b}{\cos\mu} \tag{7.50}$$

$$R_{bpd} = R_{bpi}\cos\theta_i \tag{7.51}$$

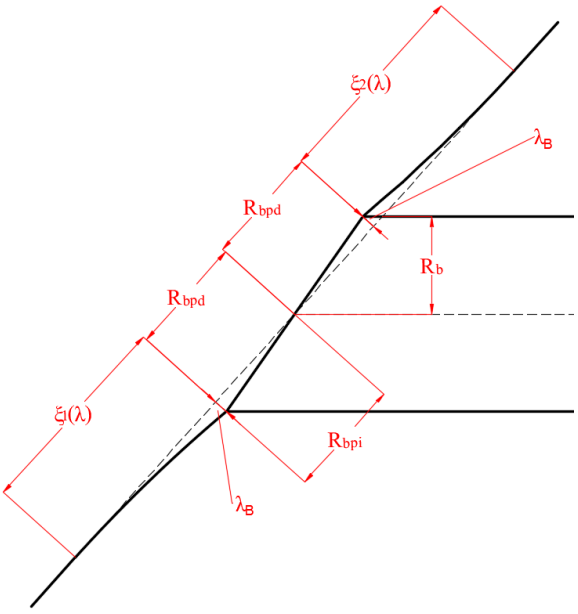

Figure 7.15: Deformation pattern at mid-diameter in zone B (displacements)

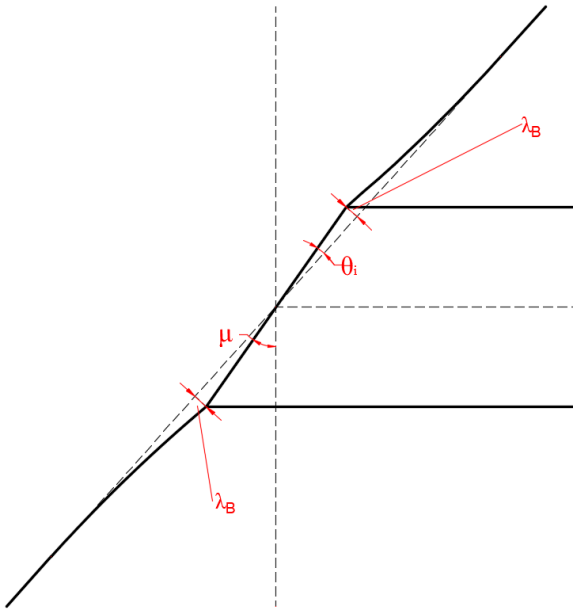

Figure 7.16: Deformation pattern at mid-diameter in zone B (angles)

$$\lambda_B = R_{bpi} \sin \theta_i \tag{7.52}$$

$$\frac{\partial \lambda_B}{\partial \theta_i} = R_{bpi} \cos \theta_i \tag{7.53}$$

Analytical derivations to determine the rate of energy dissipated plastically in zone B are similar to the one performed for zone A (see Section 7.3.1), except that λ_A has to be replaced by λ_B. Moreover, the cross-section deformation (see Fig. 7.13) related to the lower part of zone A is now related to the upper part for zone B, and vice-versa (see Fig. 7.14).

7.3.3 Zone C: rear leg near foundation level

As can be seen in Fig. 7.3, the rear leg may feature a local asymmetric buckling at foundation level leading to a so-called "elephant foot" deformation pattern. In addition, the leg rotates with an angle θ_r, as depicted in Fig. 7.8.

Let us consider first the leg cross-section deformation. As done in previous subsections, a displacement field such as the one depicted in Figs. 7.17 and 7.18 is postulated, where black dotted lines represent the initial position of the leg and green continuous lines the deformed configuration. It is assumed that the length at mid-diameter remains constant during the deformation.

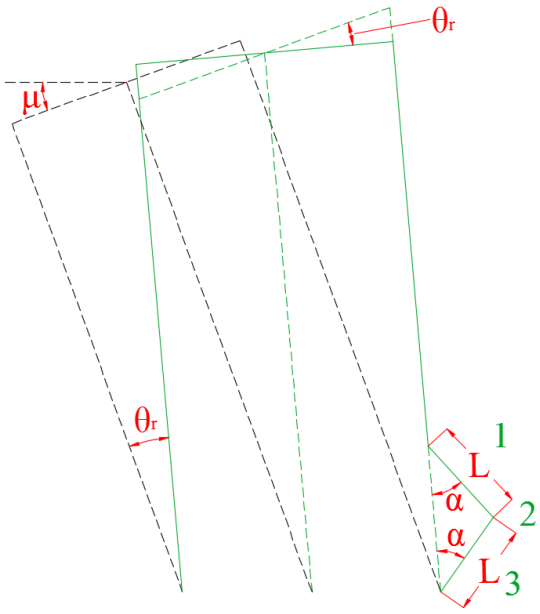

Figure 7.17: Deformation pattern of the rear leg at foundation level

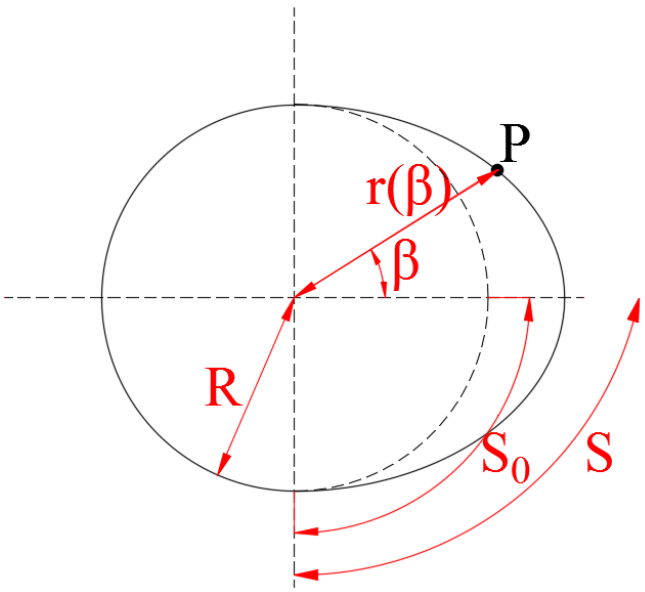

Figure 7.18: Rear leg cross-section deformation at ring 2 near foundation level

The leg is supposed to be clamped on its whole bottom cross-section at foundation level. For $\beta \in [-\pi/2; \pi/2]$, the generator displacement field is drawn in Fig. 7.17. For the other values of β, no bending of the generators occur, and their elongation remains small and is therefore neglected in the total dissipated energy in this zone C.

As done previously, the tubular member is represented by rings that can slide freely along generators without shearing, but in this case, the generators length is supposed to remain constant during the deformation while the rings can extend.

For $\beta = 0$, the assumption of non-elongation of generators allows to write that:

$$\begin{aligned} &2L\cos\alpha + R\tan\theta_r = 2L \\ &\alpha = \cos^{-1}\left(1 - \frac{R}{2L}\tan\theta_r\right) \end{aligned} \tag{7.54}$$

For other values of β, the distance between corresponding point and rotation axis is considered and Eq. 7.54 writes:

$$\alpha(\beta) = \cos^{-1}\left(1 - \frac{R\cos\beta}{2L}\tan\theta_r\right) \tag{7.55}$$

The value of folding length L will be discussed later on.

In this deformation mode, the energy is supposed to dissipate plastically both by rotation around 3 plastic hinges, located at levels 1, 2 and 3 (see Fig. 7.17) and by elongation of the rings.

In the following developments, the angle β and the vector $\underline{s}(\beta) = [r(\beta)\cos\beta; r(\beta)\sin\beta]$ define the position of a point P belonging the leg cross-section, as shown in Fig. 7.18. The notation $\underline{s}'(\beta)$ stands for $\partial\underline{s}(\beta)/\partial\beta$ while $\|\underline{s}'(\beta)\|$ is the norm of the vector.

7.3.3.1 Rotation of plastic hinges

Let us first derive the rate of energy dissipated by the 3 plastic hinges which take place at levels 1, 2 and 3 over a circumferential distance limited by $\beta \in [-\pi/2; \pi/2]$.

The contribution of plastic hinge 1 to deformation energy rate can be computed as:

$$\dot{E}_{H,1} = 2m_0 \int_0^{\pi/2} \dot{\alpha}(\beta) R d\beta = 2m_0 \int_0^{\pi/2} \frac{\partial\alpha(\beta)}{\partial\theta_r} R d\beta \dot{\theta}_r \tag{7.56}$$

with

$$\frac{\partial\alpha(\beta)}{\partial\theta_r} = \frac{1}{\sqrt{1 - \left(1 - \frac{R\cos\beta}{2L}\tan\theta_r\right)^2}} \frac{R\cos\beta}{2L\cos^2\theta_r} \tag{7.57}$$

As the plastic hinge 2 is concerned, the expression is similar, except that the integration domain changes and the hinge rotation angle is twice as compared to hinge 1.

$$\dot{E}_{H,2} = 4m_0 \int_0^{\pi/2} \dot{\alpha}(\beta) \overline{ds} d\beta = 4m_0 \int_0^{\pi/2} \frac{\partial\alpha(\beta)}{\partial\theta_r} \overline{ds} d\beta \dot{\theta}_r \tag{7.58}$$

with $\overline{ds} = \|\underline{s}'(\beta)\|$.

One can write:

$$\underline{s}\,(\beta) = [r\,(\beta)\cos\beta; r(\beta)\sin\beta] \tag{7.59}$$

$$\underline{s}'\,(\beta) = \left[\frac{\partial r(\beta)}{\partial\beta}\cos\beta - r\,(\beta)\sin\beta; \frac{\partial r\,(\beta)}{\partial\beta}\sin\beta + r\,(\beta)\cos\beta\right] \tag{7.60}$$

Then, one has:

$$r\,(\beta) = R + L\sin\alpha \tag{7.61}$$

where α is a function of β. So,

$$\begin{aligned}\frac{\partial r\,(\beta)}{\partial\beta} &= L\cos\alpha\frac{\partial\alpha}{\partial\beta} \\ &= L\cos\alpha\frac{-1}{\sqrt{1 - \left(1 - \frac{R\cos\beta}{2L}\tan\theta_r\right)^2}}\frac{R\sin\beta}{2L}\tan\theta_r\end{aligned} \tag{7.62}$$

Eq. 7.60 can be rewritten as:

$$\underline{s}'(\beta) = \begin{bmatrix} L\cos\alpha\frac{\partial\alpha}{\partial\beta}\cos\beta - (R + L\sin\alpha)\sin\beta; \\ L\cos\alpha\frac{\partial\alpha}{\partial\beta}\sin\beta + (R + L\sin\alpha)\cos\beta \end{bmatrix} \tag{7.63}$$

After calculation we obtain:

$$\overline{ds} = \left\|\underline{s}'(\beta)\right\| = \sqrt{\left(L\cos\alpha\frac{\partial\alpha}{\partial\beta}\right)^2 + (R + L\sin\alpha)^2} \tag{7.64}$$

Finally, the contribution of the third plastic hinge is very similar to the one of hinge 1 and writes:

$$\dot{E}_{H,3} = 2m_0\int_0^{\pi/2}\left(\dot{\alpha}(\beta) + \dot{\theta}_r(\beta)\right)Rd\beta = 2m_0\int_0^{\pi/2}\left(\frac{\partial\alpha(\beta)}{\partial\theta_r} + \frac{\partial\theta_r(\beta)}{\partial\theta_r}\right)Rd\beta\dot{\theta}_r \tag{7.65}$$

where $\theta_r(\beta) = \theta_r\cos\beta$ and $\partial\theta_r(\beta)/\partial\theta_r = \cos\beta$.

It is worth noting that the whole rear leg bottom cross-sections rotates. The contribution of this rotation for $\beta \in [-\pi/2; \pi/2]$ is already taken into account in Eq. 7.65 but still has to be evaluated for the remaining part of the section, i.e for $\beta \in [\pi/2; 3\pi/2]$.

The plastic bending moment of the section can be computed as:

$$M_{pl} = 2\int_0^{\pi} d\beta\int_{R_1}^{R_2}\sigma_0 r\sin\beta r dr = 2\sigma_0\left(-\cos\beta\right)|_0^{\pi}\left.\frac{r^3}{3}\right|_{R_1}^{R_2} = 4\sigma_0\frac{R_2^3 - R_1^3}{3} \tag{7.66}$$

where σ_0 is the yielding stress of the material which constitutes the jacket and where R_1 and R_2 are respectively the internal et external radii of the leg.

As we do consider only the remaining part of the section ($\beta \in [\pi/2; 3\pi/2]$), only half of the contribution of the rotation of the whole cross-section is considered that is:

$$\dot{E}_{H,4} = \frac{1}{2}M_{pl}\dot{\theta}_r \tag{7.67}$$

7.3.3.2 Elongation of the rings

The energy dissipated by elongation of the rings located between plastic hinges 1 and 3 can be written as:

$$\dot{E}_m = 4n_0\int_0^L\int_0^{\pi/2}\dot{\varepsilon}\overline{ds}d\beta dz \tag{7.68}$$

Note that the coefficient 4 is due to the fact that the integrations are performed only on a quarter section ($\beta \in [0; \pi/2]$) and on a segment of length L ($z \in [0; L]$).

The strain rate of those rings $\dot{\varepsilon}$ can be expressed as:

$$\dot{\varepsilon} = \frac{\dot{S}}{S_0} = \frac{\partial S}{\partial \theta_r}\frac{\dot{\theta}_r}{S_0} \tag{7.69}$$

where $S_0 = \pi/2R$ and S are the initial and final lengths of this segment (see Fig. 7.18).

Similarly to Eqs. 7.59 and 7.60, one has:

$$\underline{s}\,(\beta, z) = [r\,(\beta, z)\cos\beta; r(\beta, z)\sin\beta] \tag{7.70}$$

$$\underline{s}'\,(\beta) = \left[\frac{\partial r(\beta, z)}{\partial \beta}\cos\beta - r\,(\beta, z)\sin\beta;\ \frac{\partial r\,(\beta, z)}{\partial \beta}\sin\beta + r\,(\beta, z)\cos\beta\right] \tag{7.71}$$

where the radius of the deformed ring $r(\beta, z)$ is equal to $R + z\sin\alpha(\beta)$.

Performing the same developments as before, an expression similar to Eq. 7.64 is obtained for $\overline{ds}$:

$$\overline{ds} = \left\|\underline{s}'(\beta, z)\right\| = \sqrt{\left(z\cos\alpha\frac{\partial\alpha}{\partial\beta}\right)^2 + (R + z\sin\alpha)^2} \tag{7.72}$$

By introducing Eqs. 7.69 and 7.72 into Eq. 7.68, the membrane deformation energy rate becomes:

$$\begin{aligned}\dot{E}_m &= 4n_0\frac{\dot{\theta}_r}{S_0}\int_0^L\int_0^{\pi/2}\frac{\partial S}{\partial\theta_r}\overline{ds}d\beta dz = 4n_0\frac{\dot{\theta}_r}{S_0}\int_0^L\frac{\partial S}{\partial\theta_r}\int_0^{\pi/2}\overline{ds}d\beta dz \\ &= 4n_0\frac{\dot{\theta}_r}{\pi R}\frac{\partial}{\partial\theta_r}\int_0^L S_\beta\,(z)\,dz\end{aligned} \tag{7.73}$$

In this last expression, $S_\beta\,(z) = \int_0^{\pi/2}\overline{ds}d\beta$ is the length the deformed portion (defined by $\beta \in [0; \pi/2]$) of a ring located at position z.

7.3.3.3 Total deformation energy rate

The rate of total deformation energy dissipated in zone C is obtained by summing the energy rates related to plastic hinges rotations and rings membrane deformation.

$$\dot{E}_C = \dot{E}_{H,1} + \dot{E}_{H,2} + \dot{E}_{H,3} + \dot{E}_{H,4} + \dot{E}_m \tag{7.74}$$

Integrals in Eqs. 7.56, 7.58, 7.65 and 7.73 cannot be solved analytically and are therefore solved numerically using a trapeze method.

The value of the folding length L still has to be discussed. Some authors studied the problem of axial crushing of cylindrical members, such as Singace et al. [5], Singace [4], Sugimoto and Chen [6] and Alexander [2] amongst others. Alexander found out that, for tubular members subjected to pure compression, the value of L was equal to $\sqrt{Dt}$ where D is the diameter of the tubular member and t its thickness.

However, in the case of a ship collision on a jacket, the loading is more complex that pure compression. By post-processing FE simulations carried out for several ship-jacket collisions, it appears that a value of $L = \sqrt{Dt}/1.5$ gives more accurate results for diameters and thicknesses considered in offshore jacket design.

7.3.4 Zone *D*: impacted leg between foundation and horizontal brace level

The impacted leg deforms in zone D by rotating at foundation level and by extending. These two deformation modes are studied independently in the next paragraphs.

7.3.4.1 Rotation of the impacted leg

The deformation of the impacted leg due to the rotation is depicted in Figs. 7.19 and 7.20, where black dotted lines represent its initial position while continuous green lines represent the deformed structure.

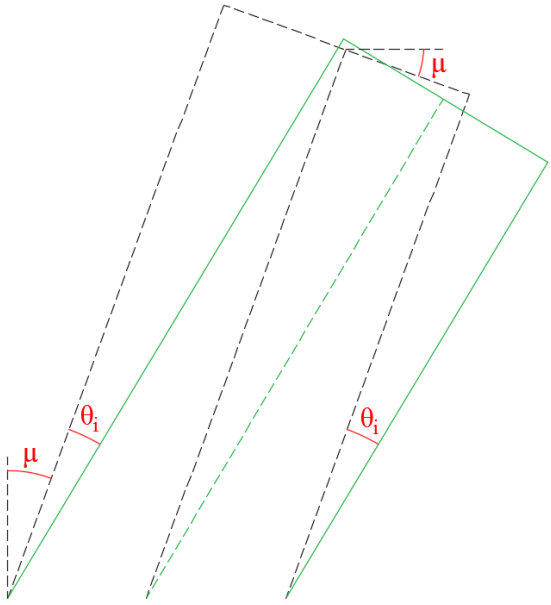

Figure 7.19: Deformation pattern of the impacted leg

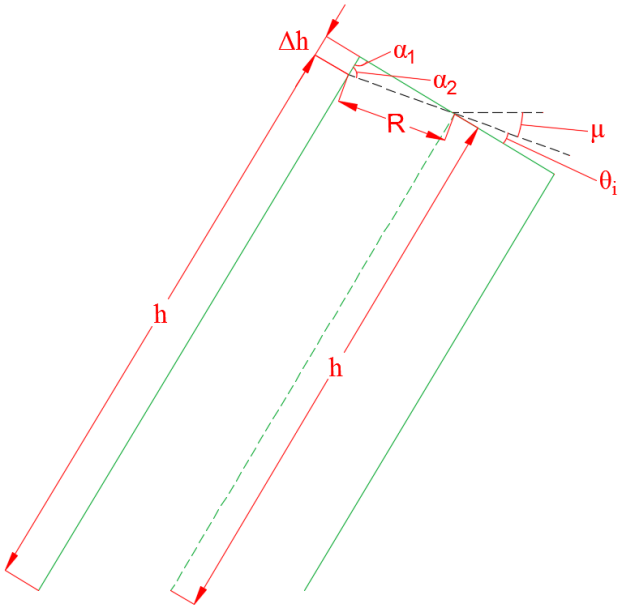

Figure 7.20: Dimensions of the deformed impacted leg

The leg is considered as clamped at foundation level. As we consider an elastic – perfectly plastic material law for the jacket, a plastic hinge appears at foundation level when the leg

rotates and the corresponding deformation energy rate writes:

$$\dot{E}_{D,1} = M_{pl}\dot{\theta}_i \tag{7.75}$$

where M_{pl} is the plastic resistant moment of the leg tubular cross-section (see Eq. 7.66).

Finally, Eq. 7.10 allows to write the deformation energy rate as a function of the striking ship velocity:

$$\dot{E}_{D,1} = M_{pl}\dot{\theta}_i = M_{pl}\frac{\partial\theta_i}{\partial\delta^\star}\frac{\partial\delta^\star}{\partial\delta}\dot{\delta} \tag{7.76}$$

As can be seen in Fig. 7.20, this rotation occurs with a change of length of the leg generators. The elongation at the neutral axis is assumed to be equal to zero, as for pure flexural deformation, and elsewhere extends from foundation level to the position of the vertical brace. The position angle β is still depicted in Fig. 7.18.

From Figs. 7.19 and 7.20, one has:

$$\alpha_1 = \frac{\pi}{2} + \mu \tag{7.77}$$

$$\alpha_2 = \frac{\pi}{2} - (\mu + \theta_i) \tag{7.78}$$

$$\Delta h = \frac{R\sin\theta_i}{\cos\mu}\cos\beta \tag{7.79}$$

The tensile strain of a single generator can be written as:

$$\varepsilon = \frac{\Delta h}{h} = \frac{R\sin\theta_i\cos\beta}{h\cos\mu} \tag{7.80}$$

and its derivative with respect to θ_i as:

$$\frac{\partial\varepsilon}{\partial\theta_i} = \frac{R\cos\theta_i\cos\beta}{h\cos\mu} \tag{7.81}$$

Then, by integrating the dissipation of energy for all the generators, it comes:

$$\dot{E}_{D,2} = n_0\int_0^{2\pi}\dot{\varepsilon}Rd\beta = n_0\int_0^{2\pi}\frac{\partial\varepsilon}{\partial\theta_i}Rd\beta\dot{\theta}_i \tag{7.82}$$

Finally, from Eqs. 7.81 and 7.82, the energy rate related to generators elongation due to rotation writes:

$$\dot{E}_{D,2} = 4n_0 \frac{R^2 \cos\theta_i}{h \cos\mu} \dot{\theta}_i \tag{7.83}$$

7.3.4.2 Elongation of the impacted leg

In addition to the elongation of the generators due to the rotation, an elongation of the impacted leg occurs from a length h to a length h'_i for all the generators (see Fig. 7.7).

The corresponding rate of energy is:

$$\dot{E}_{D,3} = N_{pl} \frac{\partial \left(h'_i - h\right)}{\partial \delta^\star} \frac{\partial \delta^\star}{\partial \delta} \ \dot{\delta} \tag{7.84}$$

where $N_{pl} = \sigma_0 \pi \left(R_2^2 - R_1^2\right)$ is the plastic resistance of the leg tubular cross-section, and where the second term of right hand side can be calculated from Eq. 7.3:

$$\frac{\partial \left(h'_i - h\right)}{\partial \delta^\star} = \frac{\delta^\star + h \sin\mu}{h'_i} \tag{7.85}$$

7.4 Numerical validation

In order to validate the analytical developments presented in the previous section, numerical simulations have been carried out using the nonlinear FE solver *LS-DYNA*.

The internal forces distribution at the base of the jacket during the collision process is very complex due to the high level of redundant constraints in the jacket, the non-symmetrical loading and the material nonlinear behaviour. It is thus uneasy to limit the FE model to the lower part of the jacket and to find a realistic loading. To overcome this difficulty, both the full jacket and the colliding ship bow are modelled and the jacket mesh is divided into several parts (represented by the different colours in Fig. 7.21), for which the internal energy can be post-processed individually.

In order to validate the formulations developed in previous sections for zones A to D, the ship is supposed to collide the jacket on a leg, following a trajectory parallel to one of its plane, as can be seen in Fig. 7.22. Considering such scenario, most of the deformation at the base of the jacket is expected to occur in the same direction than the ship trajectory.

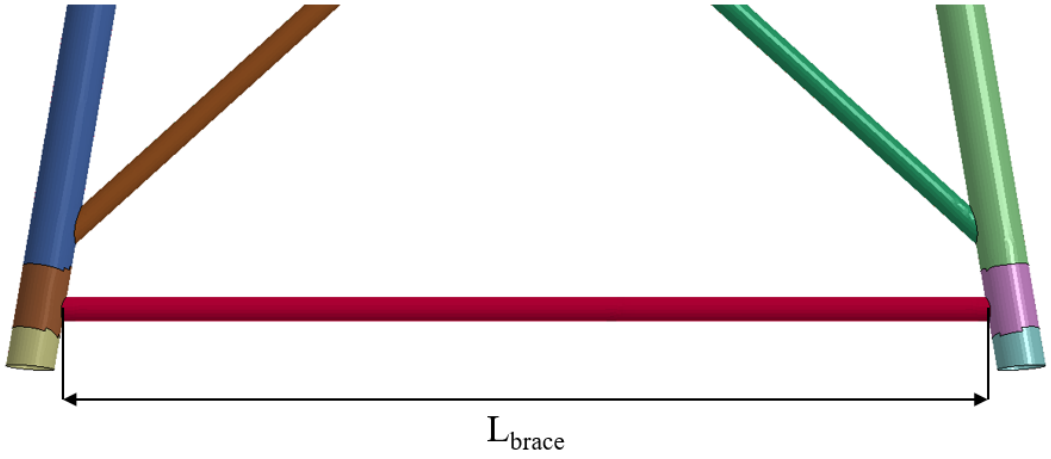

Figure 7.21: Definition of parts in the numerical simulations

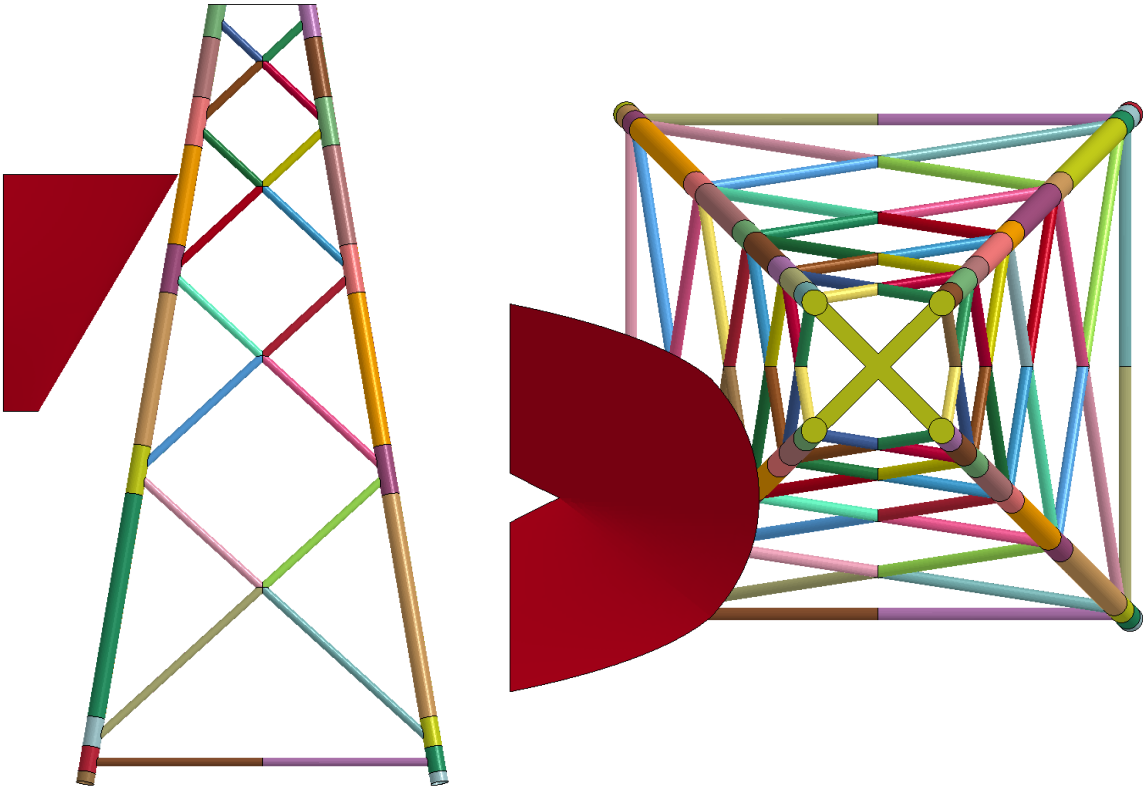

Figure 7.22: Collision scenario considered to validate the analytical formulations for the base of the OWT jacket

The ship moves forward at a constant velocity of 5 m/s and the simulation is stopped when the bow displacement δ exceeds 7.5 m, which corresponds to a value of $\delta^{\star} = 0.5$ m.

First, the hypothesis which states that the horizontal bottom brace length L_{brace}, as represented in Fig. 7.21, remains constant during the crushing process is checked. As shown by Fig. 7.23 which presents the brace length evolution, its axial deformation does not exceed 0.2% and can therefore be neglected.

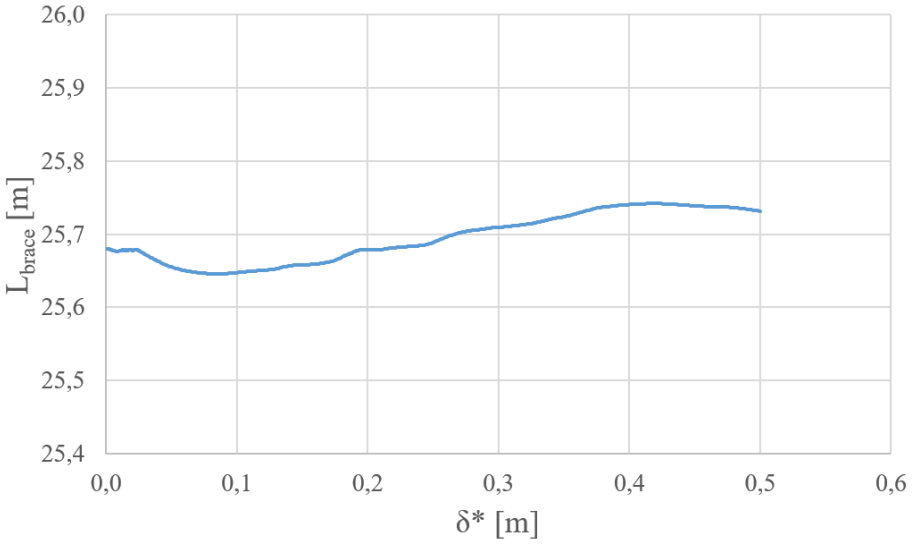

Figure 7.23: Evolution of the bottom brace length during the considered collision

Splitting the jacket base FE model into several part allows to post-process the internal energy for each part, corresponding more or less to each zone. It is however worth noting that in our analytical developments, the elongation of the impacted leg is modelled only for zone D while corresponding elongation in the numerical model extends also to the part associated to zone B. Therefore, the dissipation $\dot{E}_{D,3}$ is arbitrary divided into two parts and distributed into zones B and D for 20% and 80% respectively. In Figs. 7.24 to 7.27, the evolution of internal energies obtained analytically and numerically are compared.

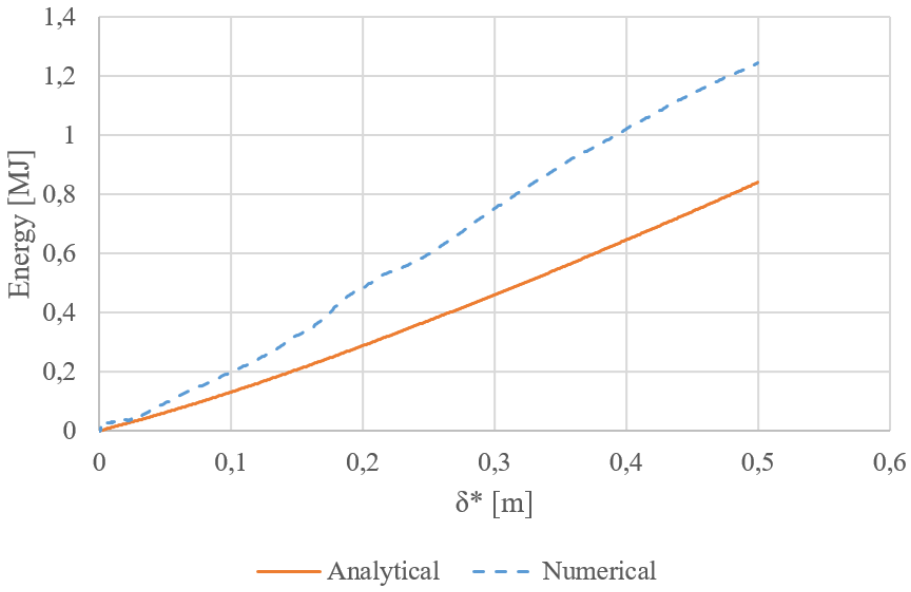

Figure 7.24: Comparison between analytical and numerical approaches for the energy dissipated in zone A

Table 7.1 below gives the values of dissipated energies computed with the analytical and the numerical methods, as well as the discrepancy, considering the numerical solution as the reference.

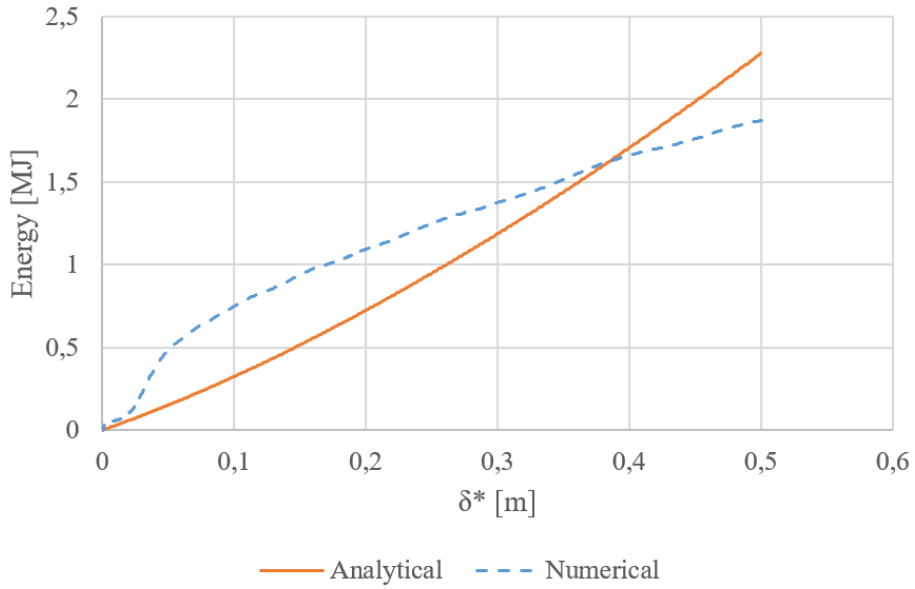

Figure 7.25: Comparison between analytical and numerical approaches for the energy dissipated in zone B

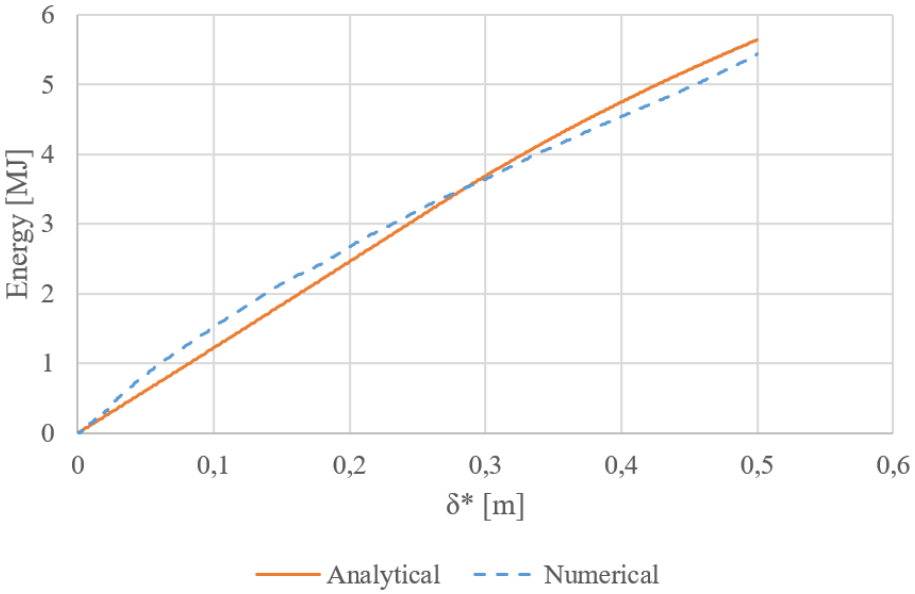

Figure 7.26: Comparison between analytical and numerical approaches for the energy dissipated in zone C

Table 7.1: Energies computed by numerical and analytical methods and discrepancy for 0 degree collision

Zone	Energy for $\delta^\star = 0.5\ m$ (numerical) $[MJ]$	Energy for $\delta^\star = 0.5\ m$ (analytical) $[MJ]$	Disc. [%]
A	1.24	0.84	32
B	1.87	2.28	22
C	5.44	5.64	4
D	15.73	15.18	3
Total	24.28	23.94	2

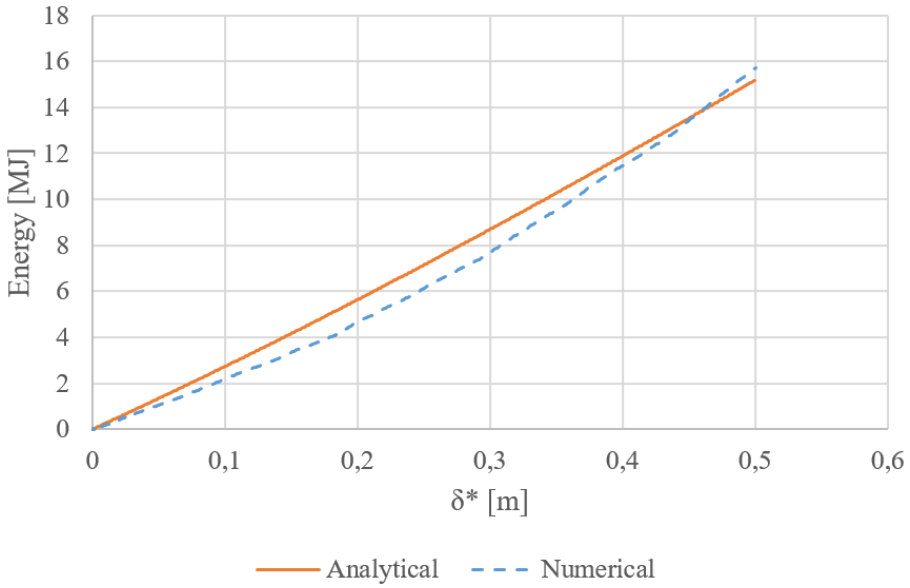

Figure 7.27: Comparison between analytical and numerical approaches for the energy dissipated in zone D

Except for zones A and B, which dissipated the less energy, the discrepancy is lower than 15%, which proves the accuracy of the model. The difference between numerical and analytical results for zones A and B can be explained by the fact that the deformation of the leg is influenced by the displacement of the inclined brace located above. The deformation patterns of both punching and zone A overlap, as can be seen in Fig. 7.3. A part of energy dissipated in zone A is actually due to punching, which is not taken into account in the model presented in this Chapter. Nevertheless, it has to be mentioned that the part of energy dissipated in zone A is small with regard to the total energy dissipated at the base of the jacket. As a consequence, such discrepancy has low influence on the final overall result.

An additional simulation was performed with another collision angle α of 30 degrees (Fig. 3.14) considering the same impact point with the same ship and jacket.

Considering this scenario, the deformation at the base of the jacket is much reduced with regard to a collision angle of 0 degree because much more energy is dissipated through the global motion of the whole structure. Therefore, the displacement $\delta^\star$ is equal to 0.06 m according to axis X and the corresponding displacement with regard to axis Y is 0.035 m. For this scenario, zones A and C are subjected only to the displacement according to axis X while the efforts in zones B and D are the resultant of the resistance in both axes, the total resistance being computed as $R_{tot} = \sqrt{R_X^2 + R_Y^2}$.

The results in term of dissipated energy for this scenario are given in Table 7.2.

The discrepancy zone by zone is higher than for the 0 degree scenario, due to a complex overall displacement of the jacket that is not included in the model. However, the discrepancy for the total deformation mode is lower than 15%, which tends to validate the analytical formulations.

Table 7.2: Energies computed by numerical and analytical methods and discrepancy for 30 degree collision

Zone	Energy for $\delta^\star = 0.5\ m$ (numerical) $[MJ]$	Energy for $\delta^\star = 0.5\ m$ (analytical) $[MJ]$	Disc. [%]
A	0.16	0.12	25
B	0.69	0.63	9
C	0.78	0.98	26
D	1.43	1.468	2
Total	3.06	3.19	4

Finally, the deformation at the base of the jacket represents a small part of energy dissipation in the case of collisions with large collision angle.

The analytical formulations are also validated for other values of external diameter – thickness ratios. Therefore, the structure, the striking ship as well as the impact point and ship trajectory depicted in Fig. 7.22 are considered. All geometrical properties are identical except the legs thickness that varies from 30 mm to 70 mm, corresponding to ratios D_e/t varying from 18.6 to 43.3. Those thicknesses range corresponds to actual industrial limits. The ship is given a mass of $6,000$ tons (added mass included) and an initial kinetic energy of 5 m/s, corresponding to an initial kinetic energy of 75 MJ. It appears that the deformation pattern described in this paper appears for all the thicknesses investigated.

For each ratio considered, the main results are given in Table 7.3. The maximum displacement $\delta^\star$ for the 75 MJ impact is computed numerically. For this displacement, the dissipated energy is computed with both analytical and numerical models and the resulting discrepancy is given.

Table 7.3: Energies computed by numerical and analytical methods and discrepancy for several leg thicknesses

Thickness $[mm]$	D_e/t $[-]$	$\delta^\star_{max}$ $[m]$	Energy (num.) $[MJ]$	Energy (anal.) $[MJ]$	Disc. [%]
30	43.3	0.09	3.08	3.01	3
40	32.5	0.06	2.69	2.71	1
60	21.7	0.03	2.03	1.97	3
70	18.6	0.02	1.21	1.24	3

As can be seen and similarly to the previous investigated collision scenarios, the discrepancy between analytical and the numerical results remains very low, showing the accuracy of the method for external diameter – thickness ratio varying from 18.6 to 43.3.

7.5 Conclusion

In this Chapter, analytical formulations are developed to compute the resistance and the dissipated energy at the base of any OWT jacket, with the structural arrangement described in the present work and the assumption of braces stronger than joints, when it is impacted by a ship on one of its legs. The analytical developments are performed for a displacement in one plane of the jacket, but can be extended to an oblique ship-jacket collision leading to displacements in two main planes.

First, numerical simulations are performed in order to understand the deformation process at the base of the jacket and to choose realistic deformation patterns for the analytical developments. It appears that, for the jacket considered in this study, a collision energy of about 27 MJ is required to initiate the deformation at the foundation level. This first step consists in splitting the base of the jacket into 4 zones for which the dissipated energies are computed individually.

On both impacted and rear legs, a plastic deformation occurs at the connection with the bottom brace, due to the fact that the brace is assumed to remain constantly horizontal while the legs are rotating around the clamping at the foundation level. Once realistic displacement fields have been chosen, applying the upper-bound theorem allows to derive analytically the corresponding dissipated energy.

For the impacted leg, a plastic hinge appears at foundation level. As the rear leg is concerned, a partial local buckling of the section as well as a rotation at the base occur. The plastic elongation of the impacted leg is also taken into account.

Validation of the analytical developments is achieved by performing FE simulations. Two collision scenarios are investigated and various external diameter – thickness ratio varying from 18.6 to 43.3 are studied. For all of them, comparison of both analytical and numerical dissipated energies show that the analytical model is in good accordance with the numerical one.

Bibliography

[1] Plastic behavior of tubular members under lateral concentrated load. Technical Report n 82-0708, Det Norske Veritas, 1982.

[2] JM Alexander. An approximate analysis of the collapse of thin cylindrical shells under axial loading. *Quarterly Journal of Mechanics and Applied Mathematics*, (13):10–15, 1960.

[3] N Jones. *Structural impact*. Cambridge: Cambridge University Press, 1997.

[4] AA Singace. On the eccentricity factor in the progressive crushing of tubes. *International Journal of Solids Structures*, (32(24)):3589–3602, 1995.

[5] AA Singace, H Elsobky, and TY Reddy. Axial crushing analysis of tubes deforming in the multi-lobe mode. *International Journal of Mechanical Sciences*, (41):865–890, 1999.

[6] H Sugimoto and WF Chen. Inelastic post-buckling behavior of tubular members. *Journal of Structural Engineering*, (111):1965–1978, 1985.

[7] MS Suh. *Plastic analysis of dented tubes subjected to combined loading*. PhD thesis, Cambridge: Massachusetts Institute of Technology, Department of Ocean Engineering, 1987.

[8] T Wierzbicki and MS Suh. Indentation of tubes under combined loading. *International Journal of Mechanical Sciences*, (30):229–248, 1988.

Chapter 8

General algorithm to assess the crashworthiness of an offshore wind turbine jacket

Abstract:

In the previous Chapters, the semi-analytical formulations derived to compute the resistant force corresponding to the four deformation modes are presented. The general algorithm developed to combine each of them and compute the total resistance of an OWT jacket impacted by a ship is presented in this Chapter.

As a user, the data required to describe the striking ship, the collided jacket and the collision scenario have to be provided.

During a collision, several contact points between the ship and the jacket may appear. Therefore, a methodology is established to identify all the potential impacted tubular members and connections and also their distances with regard to the striking ship.

Then, the general algorithm is described, as well as the interactions between all four deformation modes.

Finally, the semi-analytical model is validated by comparing the results with FE simulations. The developed method is shown to be in good accordance with FE for most cases, and further researches are suggested to improve the model for some specific collision scenarios.

8.1 Introduction

In Chapter 3, the main parameters governing the OWT jacket behaviour when collided by a ship are discussed. Based on numerical simulations, four deformation modes were identified, namely:

- local crushing of impacted tubular members (Chapter 4);
- global deformation of the whole jacket (Chapter 5);
- punching of legs by compressed braces (Chapter 6);
- deformation at the base of the jacket (Chapter 7).

For each of them, simplified formulations, either analytical or semi-analytical, were developed and are fully described in the previous Chapters 4 to 7. From those developments, the evolution of the resistance with regard to the ship penetration may be computed for each mode independently.

During a ship - jacket collision, all four deformation modes may occur simultaneously. An algorithm is therefore developed to take into account all of them and to compute the total energy dissipated by local crushing, global deformation, punching and deformation near the foundation level. The deformation in one mode may also have an influence on the other ones. As the deformation modes interact and are not independent, the developed method is denoted as a so-called "continuous element method".

Some authors described methods to take into account several deformation modes in the framework of ship collisions. Based on analytical formulations that describe the deformation of plates transversally loaded (Yu [11], Zhang [12] or Jones [5] amongst others), girders (Zhang [12], Wierzbicki et al. [9] or Hong et al. [4]), T or X sections (Amdahl [1], Wierzbicki et al. [9] or Yang et al. [10]), the resistant force in a collision event was investigated by Liu [7], Lützen [8], Le Sourne et al. [6] or Haris and Amdahl [3] for ship-ship collisions or by Buldgen [2] for ship - lock gate collision.

In the present Chapter, the implementation of the simplified method to assess the crashworthiness of an OWT jacket in *Matlab* is described. First, the methodology used to built the models of both the striking ship and the collided OWT jacket is introduced. For such collisions, the resistant force between the ship and the jacket may be transmitted through several contact points that have to be identified. Then, an algorithm is developed to consider the four deformation modes and assess the total resistant force. The interactions between the deformation modes is also discussed.

The validation of the algorithm presented in this Chapter will be the aim of Section 8.5.

8.2 Ship - jacket collision models

In order to fully define a ship collision on an OWT jacket, several data are required, namely:

- The striking ship geometry, as detailed in Section 3.2.1;
- The OWT jacket geometrical and mechanical properties, as detailed in Section 3.2.2;
- The collision scenario, as detailed in Section 3.2.3.

8.3 Collision points

During a ship collision event, several tubular members of the jacket may be impacted either by the stem or by the bulb. All the potential impacted tubular members have therefore to be identified and their initial distances with regard to the striking ship has also to be computed.

8.3.1 Detection of potential impacted tubular members

First, all the tubular members that could be directly impacted by the ship have to be identified. As described in Section 3.2.1, the geometrical descriptions of the stem and the bulb are different (Figs. 3.2 and 3.3), which has also an influence on the computation of the local crushing (investigated in Chapter 4). Therefore, the search for potential impacted elements should be performed for the stem and the bulb separately.

A bulbous bow ship cross-section is presented in Fig. 8.1. The stem is boxed with a green rectangle. Its height is equal to h_b (Fig. 3.4) and its width corresponds to the width of the ship upper deck. Similar box is drawn for the bulb, as represented with the blue rectangle.

Those boxes are then extended along the ship trajectory, which is defined in Fig. 3.14, as represented in Figs. 8.2 and 8.3 for side and top views respectively.

Using the coordinates of each connections and the extremities of each tubular member that are known from the jacket data, the connections and tubular members that are totally or partially located inside the boxes can be listed, creating four lists:

- Tubular members inside the stem box;
- Tubular members inside the bulb box;
- Connections inside the stem box;
- Connections inside the bulb box;

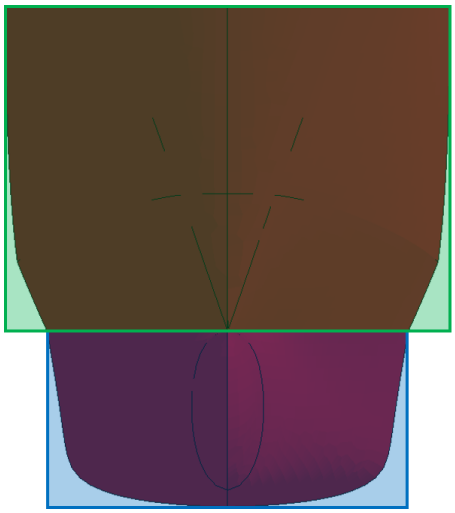

Figure 8.1: Front view of the volume of potential contacts (bow only)

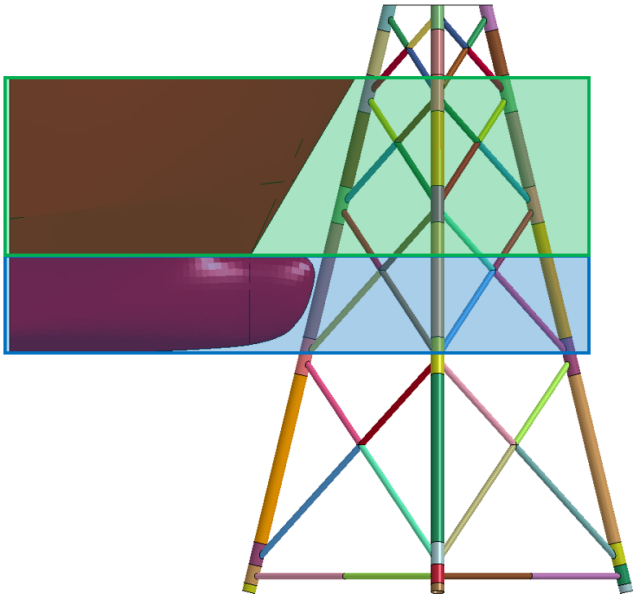

Figure 8.2: Side view of the volume of potential contacts

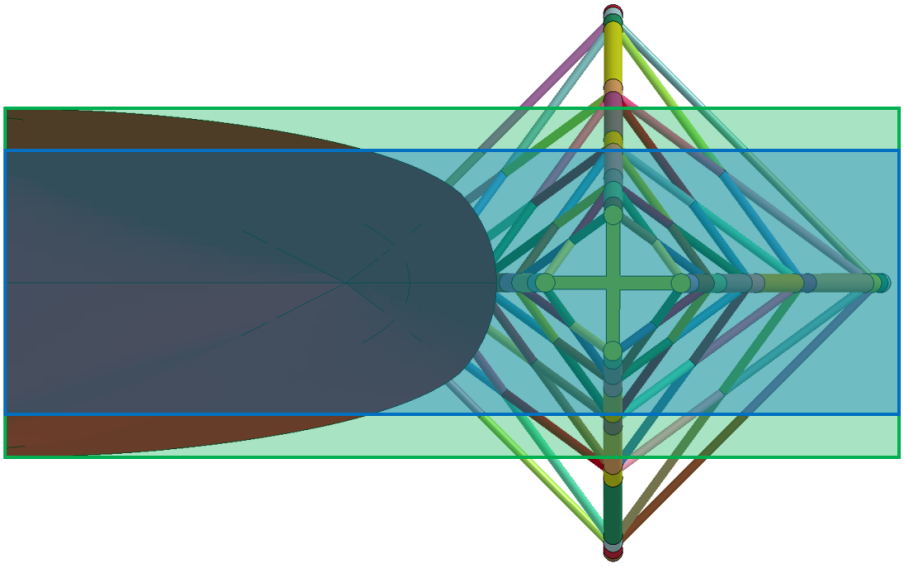

Figure 8.3: Top view of the volume of potential contacts

8.3.2 Distance from the striking ship to the jacket members

The initial distance between all the potential impacted connections or tubular members with regard to the striking ship has to be computed. This will allow us to further identify the tubular members impacted during the collision scenario investigated.

8.3.2.1 Check of contact of the striking ship on one tubular member

For potential contact on a cylindrical member, the check is performed for several elevations, while it is performed at the elevation of the node for a connection impact.

Both the stem and the bulb are divided by several horizontal planes, as represented in Fig. 8.4. The mathematical expressions that define the geometry of the striking ship are detailed in Section 3.2.1 in Eqs. 3.1 and 3.2 for the stem and the bulb respectively.

The 2D expression of the intersection between the stem or the bulb and a horizontal plane, highlighted with the red curves in Fig. 8.4, is obtained by setting the vertical variable z to the elevation of the given plane in Eqs. 3.1 or 3.2. It has to be mentioned that this intersection is an ellipse, that is further denoted $\mathbb{S}$.

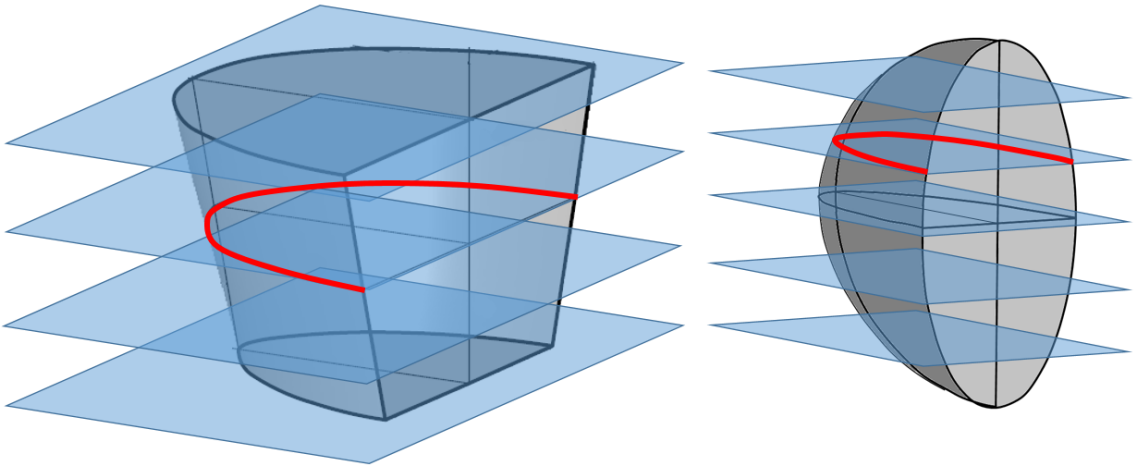

Figure 8.4: Stem and bulb divided by horizontal planes

The mathematical expression of a cylinder in a global frame was also described in Chapter 4 in Eq. 4.44. The 2D expression in the horizontal plane is similarly computed and also corresponds to an ellipse denoted $\mathbb{C}$.

Let us consider α_1 the angle between the axis X and the projection of the impacted tubular member on a horizontal plane, α_2 the ship trajectory (Fig. 3.14), (a_1, b_1) and (a_2, b_2) the long and short radii of $\mathbb{C}$ and $\mathbb{S}$ respectively.

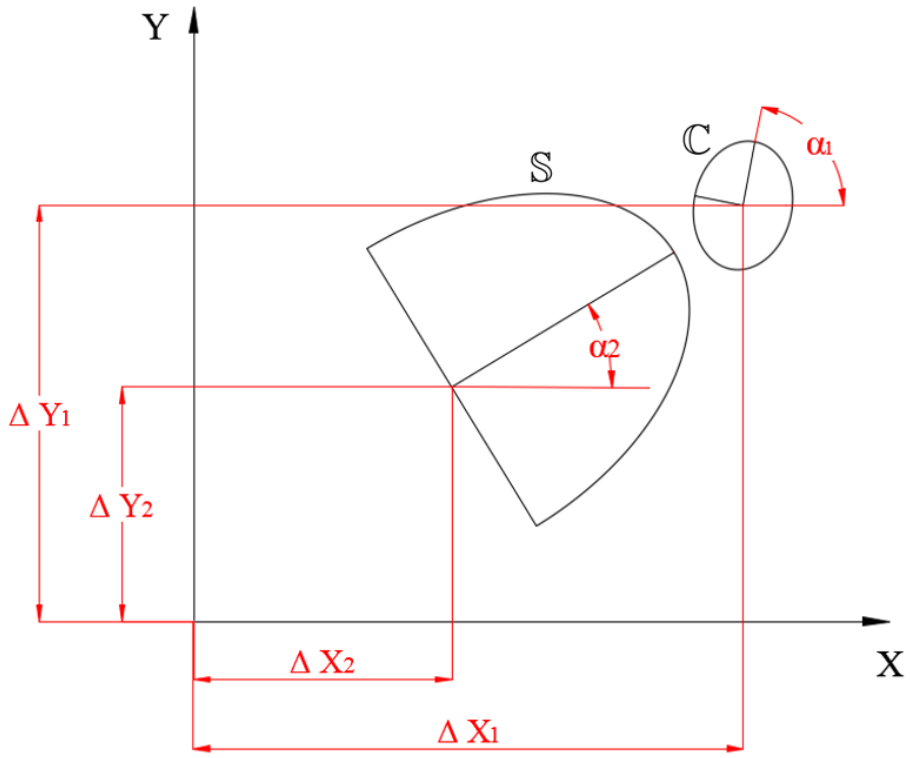

Figure 8.5: Angles and position of both ellipses with regard to the global frame

Then, the expressions of $\mathbb{C}$ and $\mathbb{S}$ are given in Eqs. 8.1 and 8.2 respectively.

$$\begin{aligned}\mathbb{C} \equiv & \left(\frac{(X-\Delta X_1)\cos\alpha_1 + (Y-\Delta Y_1)\sin\alpha_1}{a_1}\right)^2 \\ & + \left(\frac{-(X-\Delta X_1)\sin\alpha_1 + (Y-\Delta Y_1)\cos\alpha_1}{b_1}\right)^2 - 1 = 0\end{aligned} \tag{8.1}$$

$$\begin{aligned}\mathbb{S} \equiv & \left(\frac{(X-\Delta X_2)\cos\alpha_2 + (Y-\Delta Y_2)\sin\alpha_2}{a_2}\right)^2 \\ & + \left(\frac{-(X-\Delta X_2)\sin\alpha_2 + (Y-\Delta Y_2)\cos\alpha_2}{b_2}\right)^2 - 1 = 0\end{aligned} \tag{8.2}$$

Contact occurs between the ship and the tubular member at the investigated elevation if both expressions in Eqs. 8.1 and 8.2 are fulfilled for at least one point, denoted A in Fig. 8.6.

This is achieved using a Newton-Raphson method, given in Eq. 8.3.

$$\begin{Bmatrix} X_{i+1} \\ Y_{i+1} \end{Bmatrix} = \begin{Bmatrix} X_i \\ Y_i \end{Bmatrix} - \begin{bmatrix} \frac{\partial \mathbb{C}}{\partial X} & \frac{\partial \mathbb{C}}{\partial Y} \\ \frac{\partial \mathbb{S}}{\partial X} & \frac{\partial \mathbb{S}}{\partial Y} \end{bmatrix}^{-1} \begin{Bmatrix} \mathbb{C} \\ \mathbb{S} \end{Bmatrix} \tag{8.3}$$

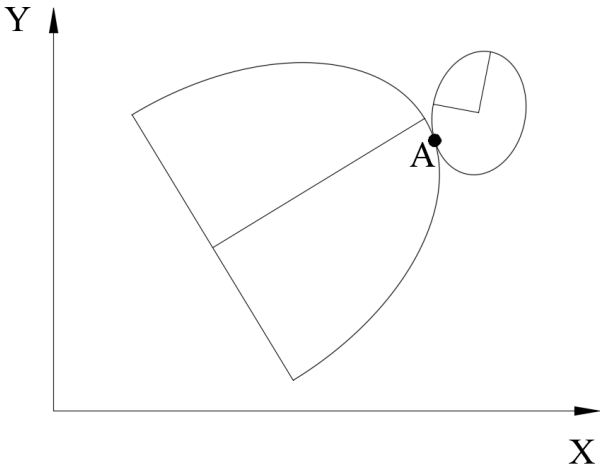

Figure 8.6: Contact point between ellipses $\mathbb{C}$ and $\mathbb{S}$

with

$$\begin{aligned}\frac{\partial \mathbb{C}}{\partial X} &= 2\frac{(X-\Delta X_1)\cos\alpha_1 + (Y-\Delta Y_1)\sin\alpha_1}{a_1}\frac{\cos\alpha_1}{a_1} \\ &- 2\frac{-(X-\Delta X_1)\sin\alpha_1 + (Y-\Delta Y_1)\cos\alpha_1}{b_1}\frac{\sin\alpha_1}{b_1}\end{aligned} \tag{8.4}$$

$$\begin{aligned}\frac{\partial \mathbb{S}}{\partial X} &= 2\frac{(X-\Delta X_2)\cos\alpha_2 + (Y-\Delta Y_2)\sin\alpha_2}{a_2}\frac{\cos\alpha_2}{a_2} \\ &- 2\frac{-(X-\Delta X_2)\sin\alpha_2 + (Y-\Delta Y_2)\cos\alpha_2}{b_2}\frac{\sin\alpha_2}{b_2}\end{aligned} \tag{8.5}$$

$$\begin{aligned}\frac{\partial \mathbb{C}}{\partial Y} &= 2\frac{(X-\Delta X_1)\cos\alpha_1 + (Y-\Delta Y_1)\sin\alpha_1}{a_1}\frac{\sin\alpha_1}{a_1} \\ &+ 2\frac{-(X-\Delta X_1)\sin\alpha_1 + (Y-\Delta Y_1)\cos\alpha_1}{b_1}\frac{\cos\alpha_1}{b_1}\end{aligned} \tag{8.6}$$

$$\begin{aligned}\frac{\partial \mathbb{S}}{\partial Y} &= 2\frac{(X-\Delta X_2)\cos\alpha_2 + (Y-\Delta Y_2)\sin\alpha_2}{a_2}\frac{\sin\alpha_2}{a_2} \\ &+ 2\frac{-(X-\Delta X_2)\sin\alpha_2 + (Y-\Delta Y_2)\cos\alpha_2}{b_2}\frac{\cos\alpha_2}{b_2}\end{aligned} \tag{8.7}$$

8.3.2.2 Methodology to compute the distance between the striking ship and all potential impacted tubular members

Let us consider the collision scenario depicted in Figs. 8.2 and 8.3. All the potential impacted tubular members and connections are fully located in the red box represented in Fig. 8.7.

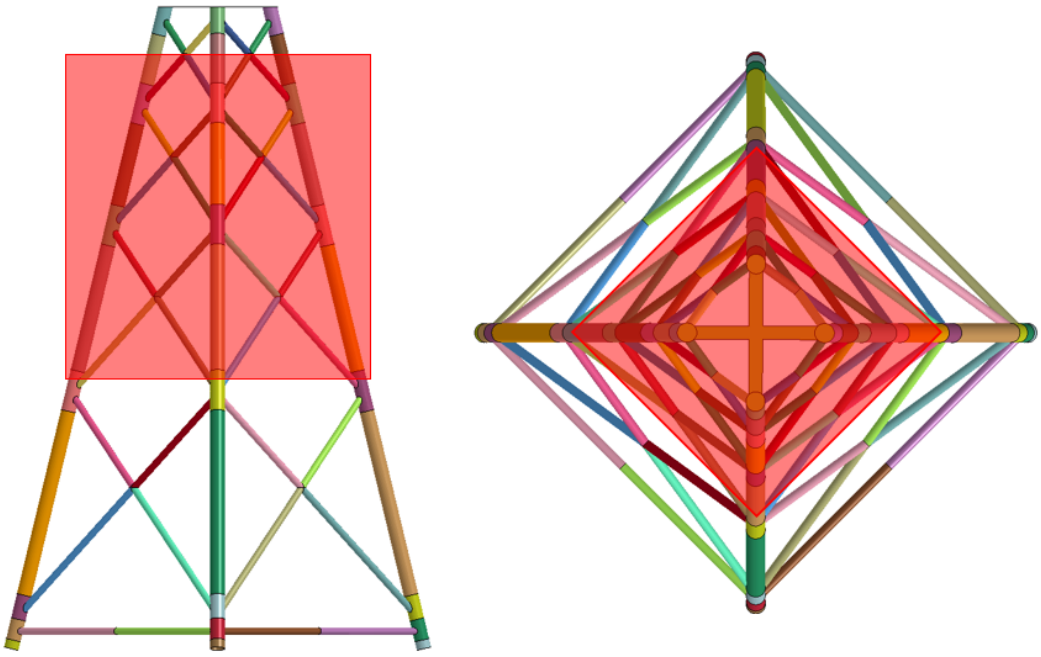

Figure 8.7: Box containing all the potential impacted tubular members and connections

Initially, the striking ship is located on its trajectory line, such as it is fully out of the red box. Then, the ship is moved along its trajectory to detect impacts on each of the potential impacted tubular members using the following methodology:

- For each potential impacted tubular member
  - For each horizontal plane
    - The ship moves forwards with space steps equal to the potential impacted tubular member radius until contact occurs.
    - The ship moves backwards with space steps equal to 0.1 m until contact disappears.
    - The ship moves forwards with space steps equal to 0.01 m until contact occurs.
  - The displacement of the ship and the coordinates (X, Y, Z) of the first contact point are saved.
- For each potential connection
  - The elevation of the connection is known
    - The ship moves forwards with space steps equal to the potential impacted tubular member radius until contact occurs.

    - The ship moves backwards with space steps equal to 0.1 m until contact disappears.
    - The ship moves forwards with space steps equal to 0.01 m until contact occurs.
  - The displacement of the ship and the coordinates (X, Y, Z) of the first contact point are saved.

The methodology developed to move the striking ship until contact occurs with the collided jacket tubular members or connections is represented in Fig. 8.8, where the evolution of the striking ship position is plotted with blue points and the red line corresponds to the real initial distance.

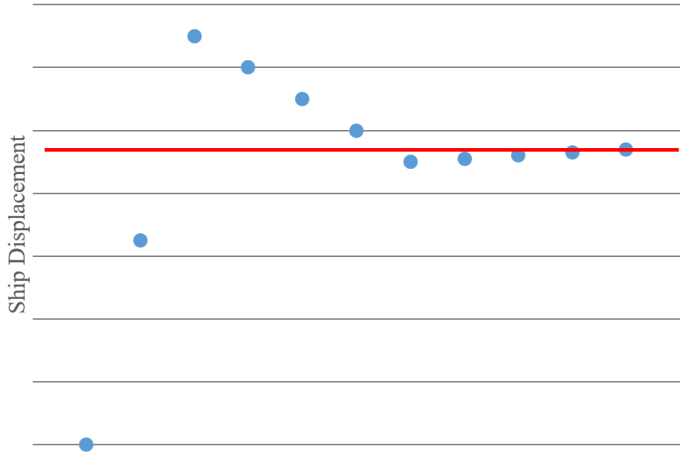

Figure 8.8: Graphical representation of the striking ship displacement to detect contacts

8.4 Computation of the total resistant force

In Chapters 4 to 7, formulations describing the resistant force with regard to the ship penetration were described for the four deformation modes independently.

During a collision, all four modes may occur simultaneously, and an algorithm has to be implemented to take all of them into account and compute the total resistant force of the collided jacket. It is described in Section 8.4.1. Some details of implementation as well as the influences of one deformation mode over another ones are detailed in Section 8.4.2.

8.4.1 Deformation mode involved for each time step

The methodology used to compute the total resistant force of an OWT collided by a ship is described below.

1. **Include the collision scenario data:**

   The data required to describe the striking ship, the collided jacket and the collision scenario models are fully described in Section 8.2.

2. **Choose the resolution time step interval Δt:**

   The total resistant force of the collided jacket is computed at several times during the collision. A time step interval has then to be defined by the user. A short time step interval will provide a more accurate result and smoother force-penetration curve, but will also require a larger computation time.

   Several time step intervals Δt were investigated to determine the optimal value. The resistant force for the collision scenario depicted in Fig. 8.13 was computed for Δt equal to 0.001 s, 0.002 s, 0.005 s and 0.01 s and the results at the beginning of the collision is depicted in Fig. 8.9. It appears from the results that no significant variation between 0.001 s and 0.002 s time step interval can be observed. Therefore, a time step interval of 0.002 s is considered in the framework of this PhD thesis.

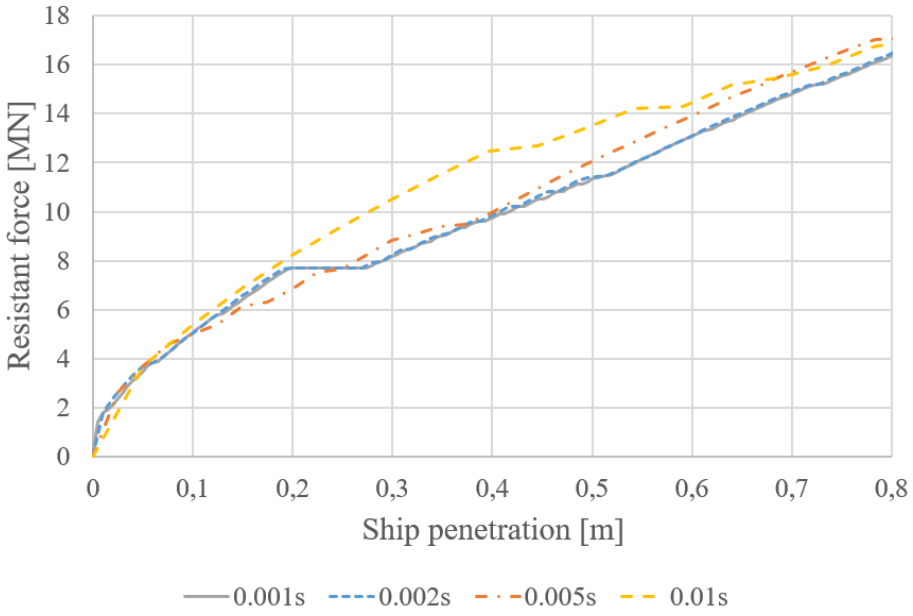

Figure 8.9: Resistant force computed with several time step intervals

   Usually, the total collision time for a 75 MJ energy collision event is between 0.8 and 1.2 s, corresponding to 400 to 600 time steps.

3. **Initialisation of variables:**

   Some variables are initialised to a zero value before starting the computation.

   - The displacement $(u_i^\star; i = 1, 4)$ for each deformation mode i. Note that for the *local crushing* deformation mode, the displacement has to be initialised for each potential impacted tubular member or connection. For the *punching* mode, initial value has to be given to each connection. Finally, the initial position of each connection has to be known in the *overall motion* deformation mode.
   - The total force and dissipated energy.
   - The internal forces in each tubular members, which are used for the *overall motion* deformation mode.

4. **Computation:**

The next points detailed in this item are performed at each time step and allow to compute the total resistance of the collided jacket. We denote by Δx the variation of the variable x during one time step.

(a) The ship penetration increment $\Delta\delta$ during the current time step is equal to $\Delta\delta = v_{ship} \cdot \Delta t$, where v_{ship} is the ship velocity at the current time step. Computing this increment allows also to compute the total ship penetration δ since the first contact with the jacket.

(b) Following the methodology described in Section 8.3, the initial distance between the ship the potential impacted tubular members is computed. At each time step, the detection of impacted elements is achieved using those results as well as the total ship penetration δ and the jacket displacements (computed with the *global motion* deformation mode algorithm). The cases of contact on a connection or on a tubular member are considered:

- Impact on a connection:
  Let us consider the connection k. The initial distance from the striking ship is denoted as d_k and its displacement in the ship trajectory direction computed with the *global motion* deformation mode algorithm is u_k. Contact occurs if $\delta \geq d_k + u_k$.
- Impact on a tubular member:
  We consider the tubular member l whose extremities are the connections m and n. The initial distance between the first contact point and the ship is d_l and the displacements of connections m and n along the ship trajectory direction are u_m and u_n respectively. Using the nodal displacements and the interpolation functions (described in Chapter 5), the displacement of the first contact point of element l u_l can be computed with the nodal displacements of nodes m and n. Then, contact occurs if $\delta \geq d_l + u_l$

The detection of impacted connections or tubular members is represented in Fig. 8.10 for a small part of the collided jacket, with the undeformed jacket in solid line and the deformed one in dotted line.

(c) The resistant force F_i is computed for each deformation mode i, using the formulation described in Chapters 4 to 7, and taking into account the effect of one deformation mode on the others (this will be investigated in Section 8.4.2).

If we consider the time t, the displacement at that particular time for the deformation mode i is equal to $u_i^t = u_i^{\star,t-1} + \Delta\delta$.

(d) For the current time step, the total jacket resistant force F_{tot} is assumed to be equal to the minimum of the four forces F_i computed.

The total energy dissipated is equal to $E^t = E^{t-1} + (F_{tot}^t + F_{tot}^{t-1})/2 \cdot \Delta\delta$.

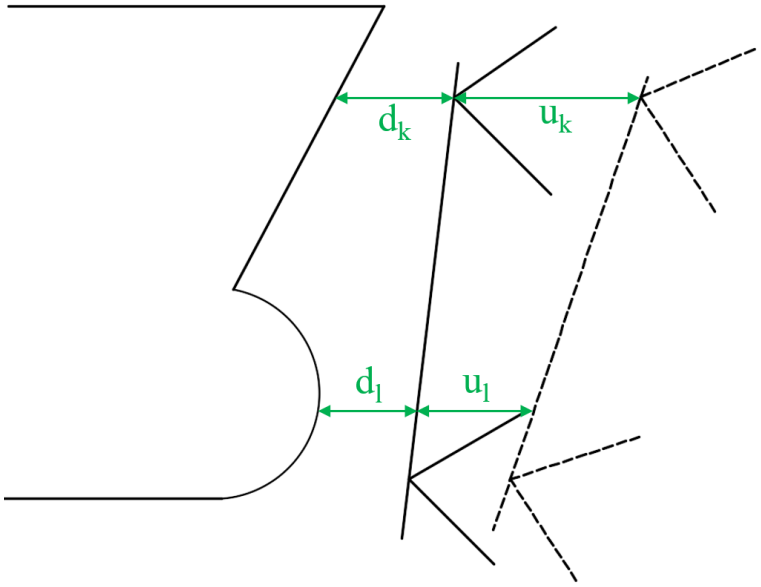

Figure 8.10: Detection of contacts between the striking ship and jacket connections or tubular members

The properties are updated only for that mode. For example, the updated deformation at time t for mode i is equal to $u_i^{\star,t} = u_i^{\star,t-1} + \Delta\delta$ for the activated deformation mode and $u_j^{\star,t} = u_j^{\star,t-1}$ for the others.

(e) The acceleration of the striking ship is computed as $a = F_{tot}/m_{ship}$ where m_{ship} is the mass of the striking ship.

(f) The velocity of the ship is updated as $v_{ship}^t = v_{ship}^{t-1} - a \cdot \Delta t$.

(g) A loop following the process starting at stage (a) is performed until the velocity of the striking ship reaches 0.

5. **Results:**

The most interesting results from the simulation are the evolutions of both the dissipated energy E and the resistant force F_{tot} with the total ship penetration.

All the steps described here above are graphically represented in the algorithm presented in Fig. 8.11.

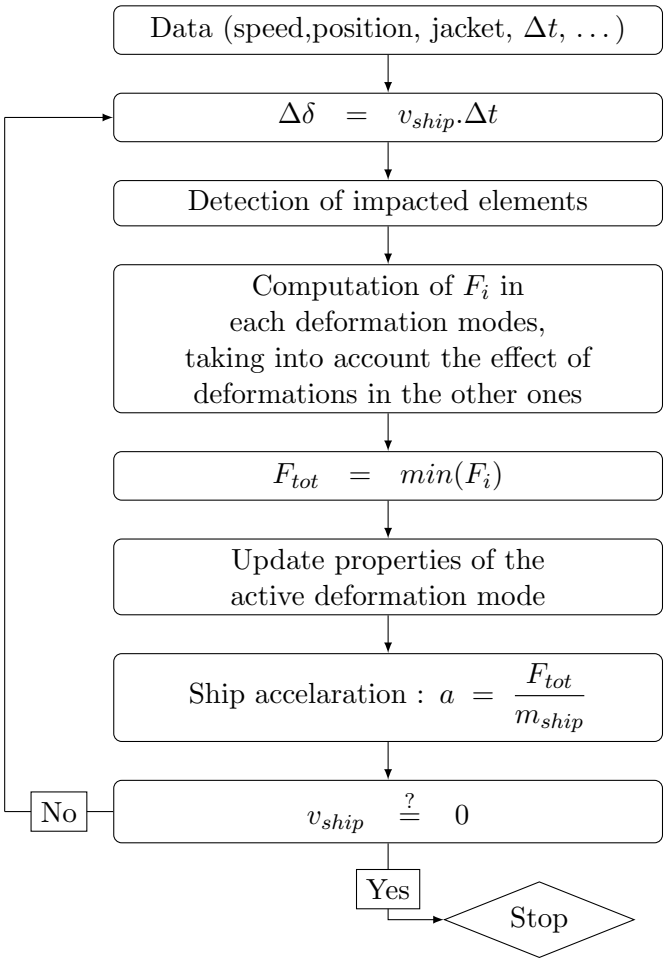

Figure 8.11: General algorithm including all deformation modes

8.4.2 Implementation and interactions of the four deformation modes

In the so-called "continuous element method", interactions between the deformation modes exist. Those interactions implemented in the algorithm are detailed here after. Some particular cases are also investigated in the next Sections.

8.4.2.1 Additional comments on the local crushing deformation mode

Impact on a tubular member or a connection

Chapter 4 is dedicated to the *local crushing of impacted tubular members*. As described, the tubular member is first locally dented and becomes then a three-hinge mechanism. However, this three-hinge mechanism cannot be activated for an impact on a connection, as the connected braces prevent any displacement due to this mechanism.

Several contact points

If contact occurs at more than one point, the resistant force for the local crushing mode consists in the sum of the resistant force at all the contact points.

8.4.2.2 Additional comments on the global motion deformation mode

Implementation for the impacted tubular members

The structural behaviour of a tubular member impacted by an indenter is investigated in Chapter 4. At first, the tubular member is locally dented, and then a three-hinges mechanism is activated.

If the local denting is included only in the *local crushing* deformation mode, the plastic mechanism can be captured by both the *local crushing* mode (Fig. 4.10) and the *global motion* deformation mode (Fig. 5.11). In the complete algorithm, the mechanism should not be taken into account twice and it should be therefore prevented to occur in one of the two deformation modes.

In the *local crushing* deformation mode, the three-hinges mechanism computation takes into account the reduction of the resistant plastic bending moment at the impact point, while this reduction is not included in the *global motion* deformation mode. Therefore, the mechanism is implemented in the *local crushing* deformation mode and is prevented to occur in the *global motion* mode.

Therefore, the flow stress σ_0 of the impacted tubular member is artificially increased by a factor $1,000$ in the *global motion* deformation mode. Plastic hinges cannot thus develop, but the elastic deformation of the cylindrical member is still taken into account.

The number of impacted cylindrical members during the collision event is unknown before running the simulation. For members impacted after the first contact with the jacket, the mechanical properties of the tubular members before they are impacted are equal to the regular values and are increased by the factor $1,000$, as described above, after they are hit to prevent computing the three-hinges mechanism twice.

Implementation for the jacket base

As for the deformation of impacted tubular members, the deformation at the base of the jacket in taken into account in both *base jacket* and *global motion* deformation modes.

It is similarly assumed that plastic hinges may not occur at the jacket base in the *global motion* deformation mode, and the flow stress σ_0 is increased by a factor $1,000$ for the corresponding elements.

Contact points

As detailed in Chapter 5, the displacement control is applied on a node. In the initial jacket model, the nodes correspond to the intersection of tubular elements, as each tubular member is modelled as one single 3D beam element. If the contact occurs on a connection, the displacement control is applied directly to the node corresponding to that connection. In case of an impact on a tubular member, a node has to be created at the impact point, on which the displacement control is applied. Therefore, the impacted tubular member is divided into two tubular members with a node between them.

During the simulation, contacts may occur on a tubular member after the first impact. The impacted tubular member is similarly divided into two elements during the simulation itself. The displacements and internal forces at the new node are computed using the interpolation functions, as described in Section 5.2.2.2.

8.4.2.3 Additional comments on the punching deformation mode

Effect of overall motion on punching

As described in Chapter 6 dedicated to *punching*, the force - penetration curve starts from an initial non-zero value (Fig. 6.24) due to the material behaviour used in the model (rigid - perfectly plastic) and to the intersection surface between the compressed brace and the punched leg. Punching is therefore activated once a given compression force is reached in the brace.

The *global motion* deformation mode is able to capture the internal forces in all the jacket tubular members. Punching in a connection is therefore activated if the compressive force, computed with the global motion algorithm detailed in Section 5.3, reaches the values required to initiate the deformation.

Contact points

As described in Section 6.4, the punching force is computed at each punched connection. The corresponding resistant force due to punching acting on the striking ship is computed considering the elevations of both the considered punched level N, as defined in Fig. 6.48, and the ship impact point (Fig. 6.52 and Eq. 6.60).

In case of several impact points (Fig. 8.12), the punching force at each connection is transmitted to the striking ship through all the contact points. It is however assumed that this punching force at the considered elevation of level N is transmitted to the ship through the impact point with the closest elevation.

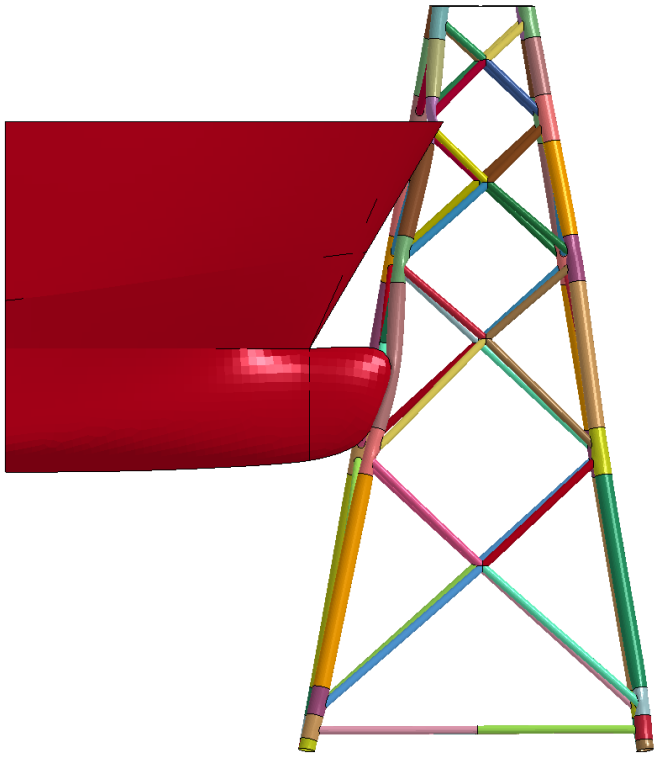

Figure 8.12: Collision scenario with several contact points

8.4.2.4 Crushing and punching of a connection

An impacted leg connection could be crushed from one side and punched from the other side. If we denote δ_{cruch} and δ_{punch} the cross-section denting due to crushing and punching respectively, the sum of both of them should not exceed the leg diameter. In order to take into account the thickness, the deformation is limited to $\delta_{cruch} + \delta_{punch} \leq 0.9D_e$.

If the limit of deformation is reached, it is assumed that no deformation could occur in the local crushing deformation mode. For punching, the value of the resistant force at the considered connection is artificially increased, such as the punching deformation takes place on the rear leg instead of the impacted leg.

8.5 Numerical validation for ship-jacket collisions

This algorithm has to be validated. Therefore, the results provided by the developed code (semi-analytical) are compared with FE simulation (numerical) results for several collision scenarios.

All the data required for the analytical model are listed in Section 8.2 are are given a value here.

The non-bulbous and bulbous striking ship bows, both considered as rigid, and the impacted OWT jacket are described in Section 3.2.

8.5.1 Comparison of numerical and semi-analytical results

Several collision scenarios are investigated, considering both non-bulbous and bulbous striking ships. For each of them, a side view and a top view of the collision is presented. Then, the results consist in:

- The evolutions of resistant force and dissipated energy with regard to the striking ship penetration;
- The penetration computed with both numerical and developed semi-analytical methods for dissipated energies equal to 27, 48 and 75 MJ (corresponding to ship mass of $6,000$ tons and initial velocity of 3, 4 and 5 m/s respectively), and the discrepancy between those two values considering the numerical model as the reference;
- The maximum and mean discrepancies on the ship penetration with regard to the dissipated energy;
- The distribution of dissipated energy between the four deformation modes, computed with the semi-analytical model.

8.5.1.1 Non-bulbous striking ship collisions

A0: Collision on a leg between two connections and $\alpha = 0°$:

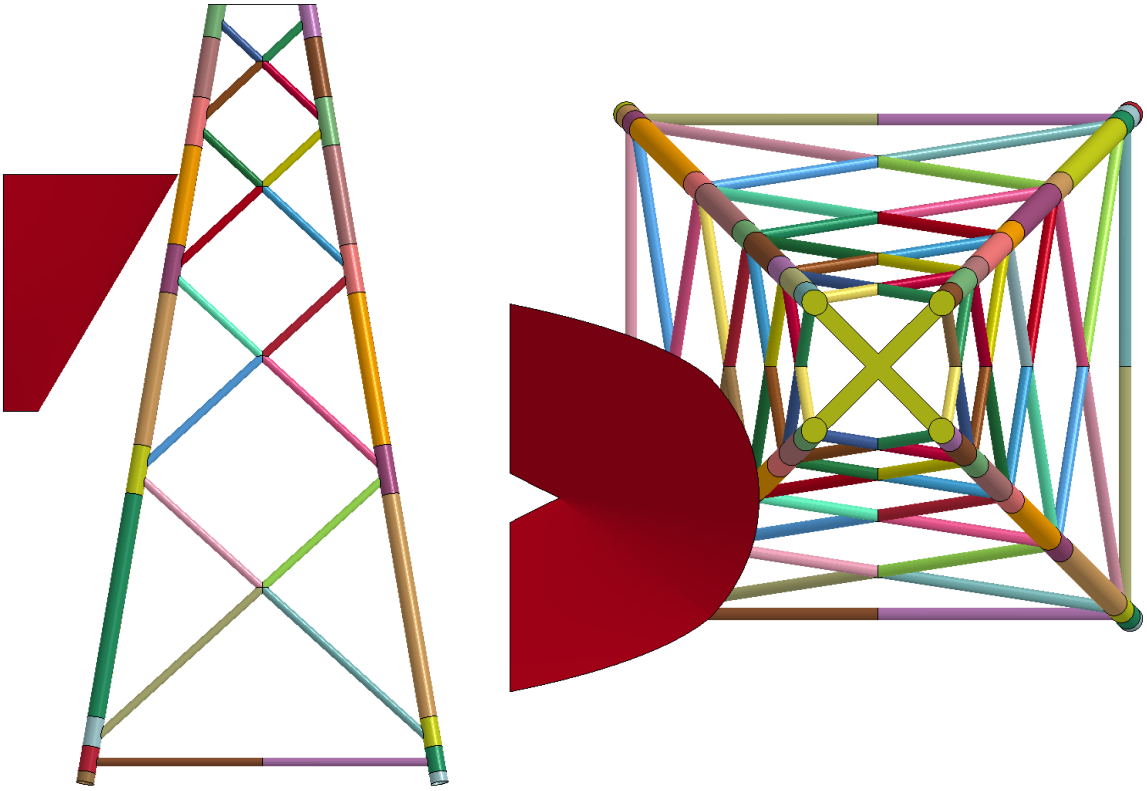

Figure 8.13: Collision scenario on a leg between two connections and $\alpha = 0°$

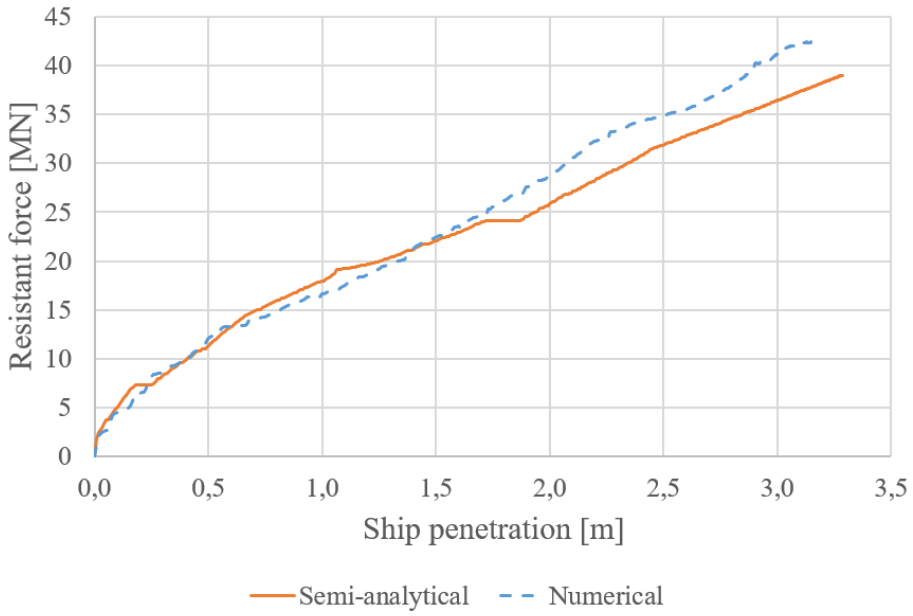

Figure 8.14: Resistant force for a collision on a leg between two connections and $\alpha = 0°$

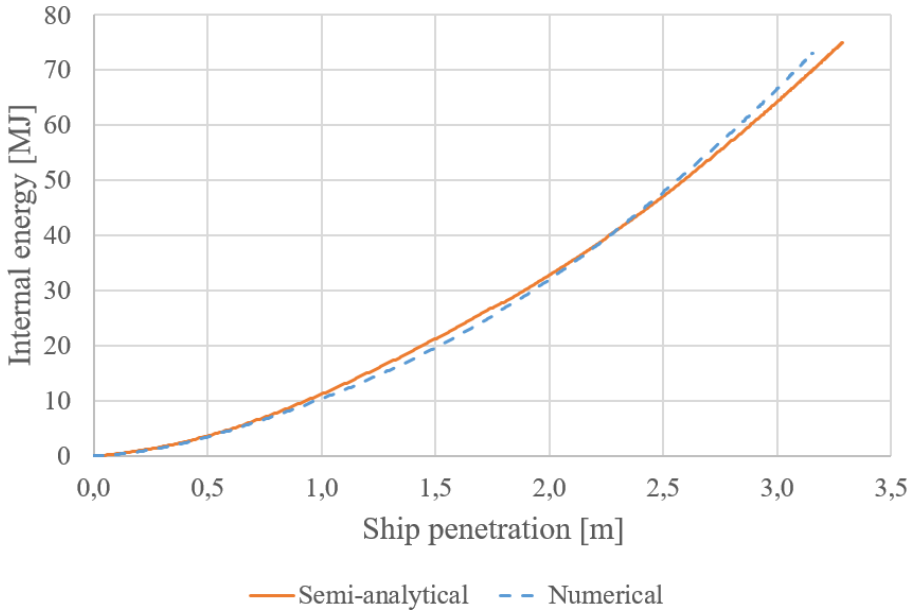

Figure 8.15: Dissipated energy for a collision on a leg between two connections and $\alpha = 0°$

Table 8.1: Discrepancy on the ship penetration for a collision on a leg between two connections and $\alpha = 0°$

$E\ [MJ]$	Pen. num. $[m]$	Pen. semi-anal. $[m]$	Discrepancy [%]
27	1.81	1.76	3
48	2.51	2.53	1
75	3.16	3.28	4

On the whole energy-penetration curves (Fig. 8.15):

- Maximum discrepancy: 6%
- Mean discrepancy: 2%

Table 8.2: Distribution of energy dissipation into the four deformation modes for a collision on a leg between two connections and $\alpha = 0°$

	Local crushing	Overall motion	Punching	Base
Energy $[MJ]$	39.66	2.21	22.39	10.74
Distribution [%]	53	3	30	14

A30: Collision on a leg between two connections and $\alpha = 30°$:

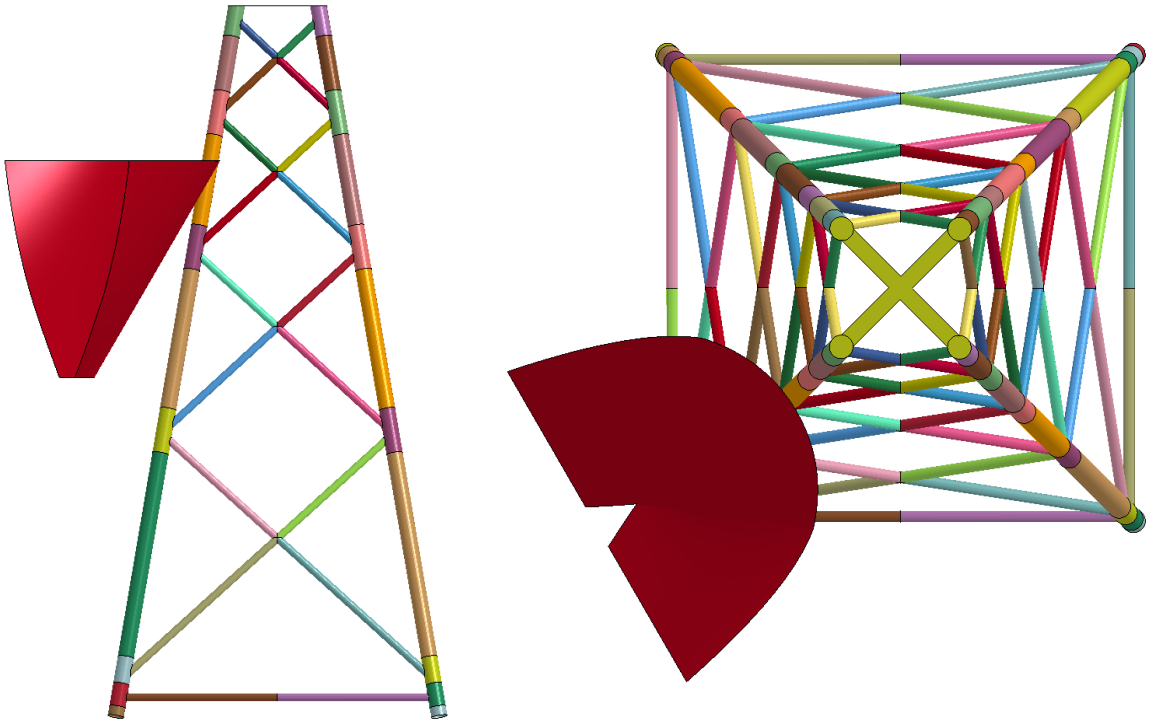

Figure 8.16: Collision scenario on a leg between two connections and $\alpha = 30°$

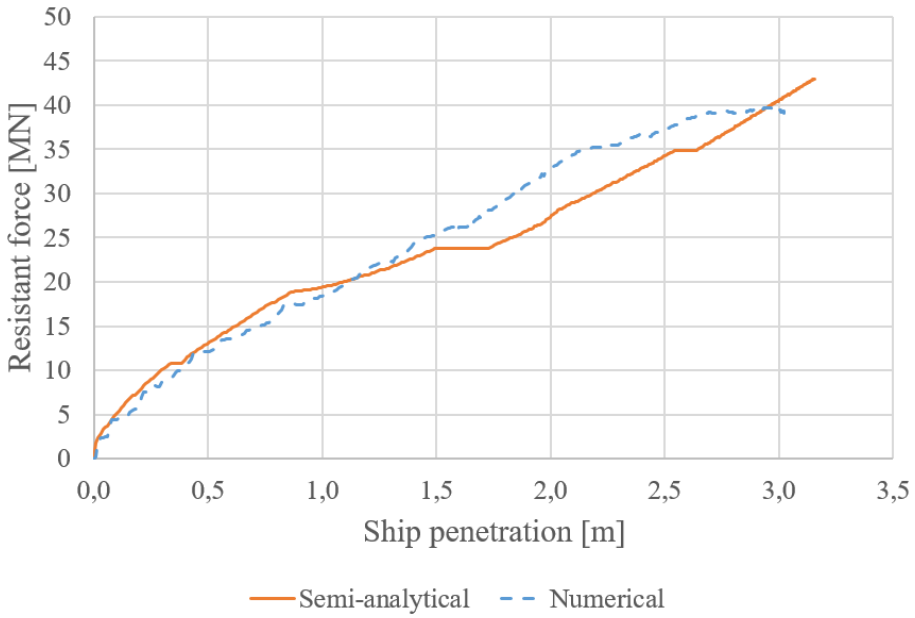

Figure 8.17: Resistant force for a collision on a leg between two connections and $\alpha = 30°$

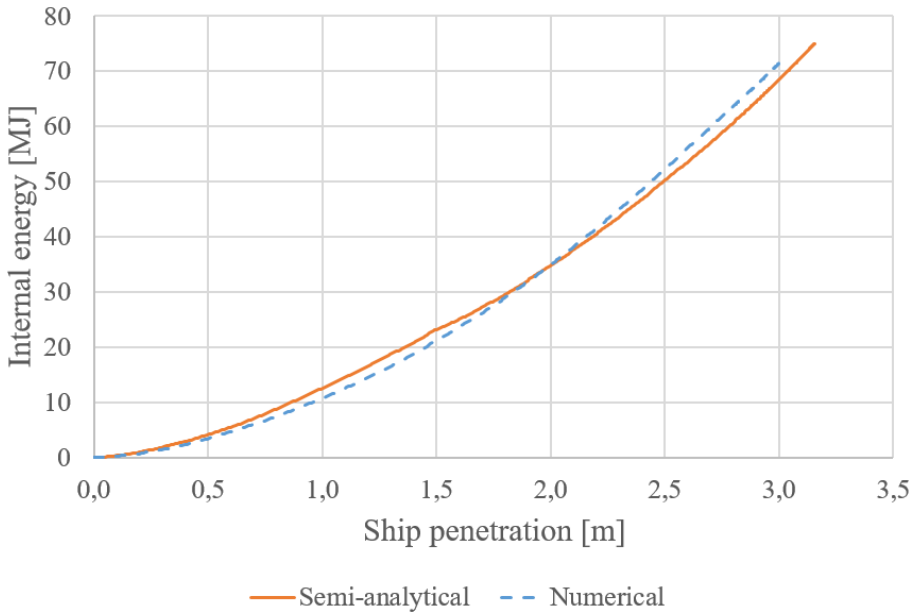

Figure 8.18: Dissipated energy for a collision on a leg between two connections and $\alpha = 30°$

Table 8.3: Discrepancy on the ship penetration for a collision on a leg between two connections and $\alpha = 30°$

$E\ [MJ]$	Pen. num. $[m]$	Pen. semi-anal. $[m]$	Discrepancy [%]
27	1.73	1.69	2
48	2.39	2.43	2
75	3.03	3.15	4

On the whole energy-penetration curves (Fig. 8.18):

- Maximum discrepancy: 10%
- Mean discrepancy: 4%

Table 8.4: Distribution of energy dissipation into the four deformation modes for a collision on a leg between two connections and $\alpha = 30°$

	Local crushing	Overall motion	Punching	Base
Energy $[MJ]$	43.49	3.05	28.46	0
Distribution [%]	58	4	38	0

A45: Collision on a leg between two connections and $\alpha = 45°$:

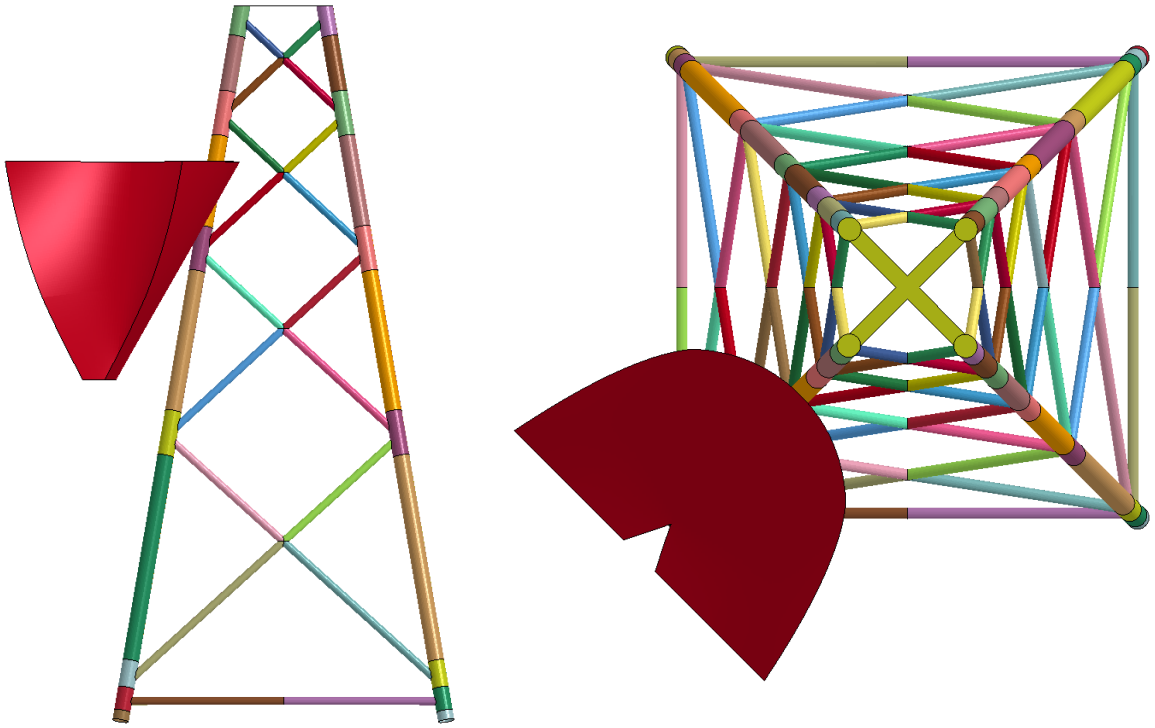

Figure 8.19: Collision scenario on a leg between two connections and $\alpha = 45°$

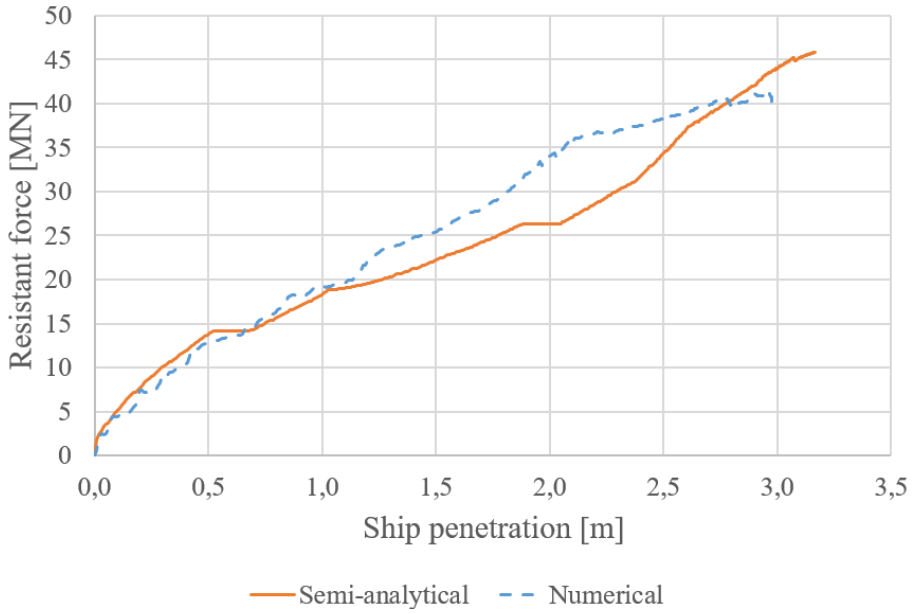

Figure 8.20: Resistant force for a collision on a leg between two connections and $\alpha = 45°$

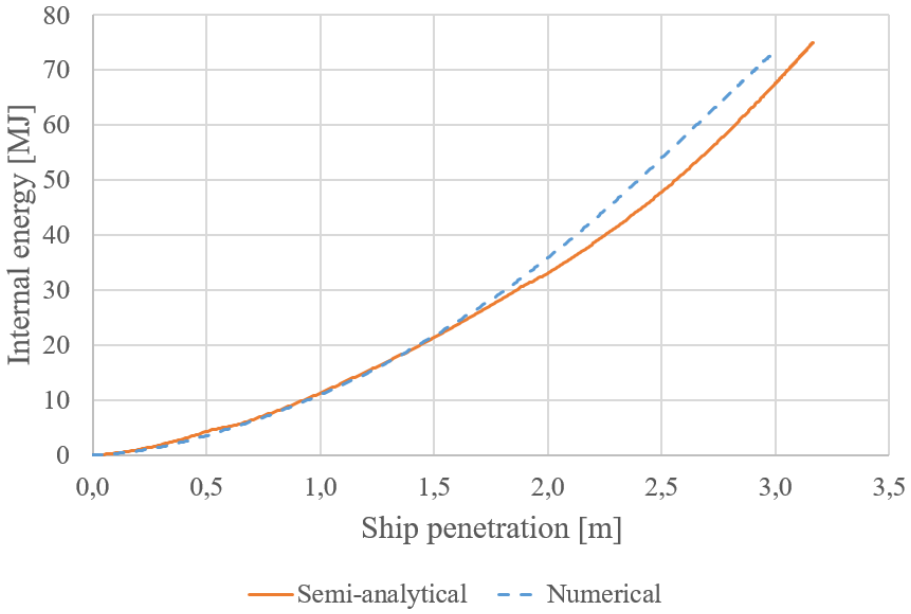

Figure 8.21: Dissipated energy for a collision on a leg between two connections and $\alpha = 45°$

Table 8.5: Discrepancy on the ship penetration for a collision on a leg between two connections and $\alpha = 45°$

E $[MJ]$	Pen. num. $[m]$	Pen. semi-anal. $[m]$	Discrepancy [%]
27	1.70	1.74	2
48	2.35	2.50	6
75	2.98	3.16	6

On the whole energy-penetration curves (Fig. 8.21):

- Maximum discrepancy: 10%
- Mean discrepancy: 4%

Table 8.6: Distribution of energy dissipation into the four deformation modes for a collision on a leg between two connections and $\alpha = 45°$

	Local crushing	Overall motion	Punching	Base
Energy $[MJ]$	48.93	4.00	19.73	2.34
Distribution [%]	65	5	26	4

B0: Collision on a leg on a connection and $\alpha = 0°$:

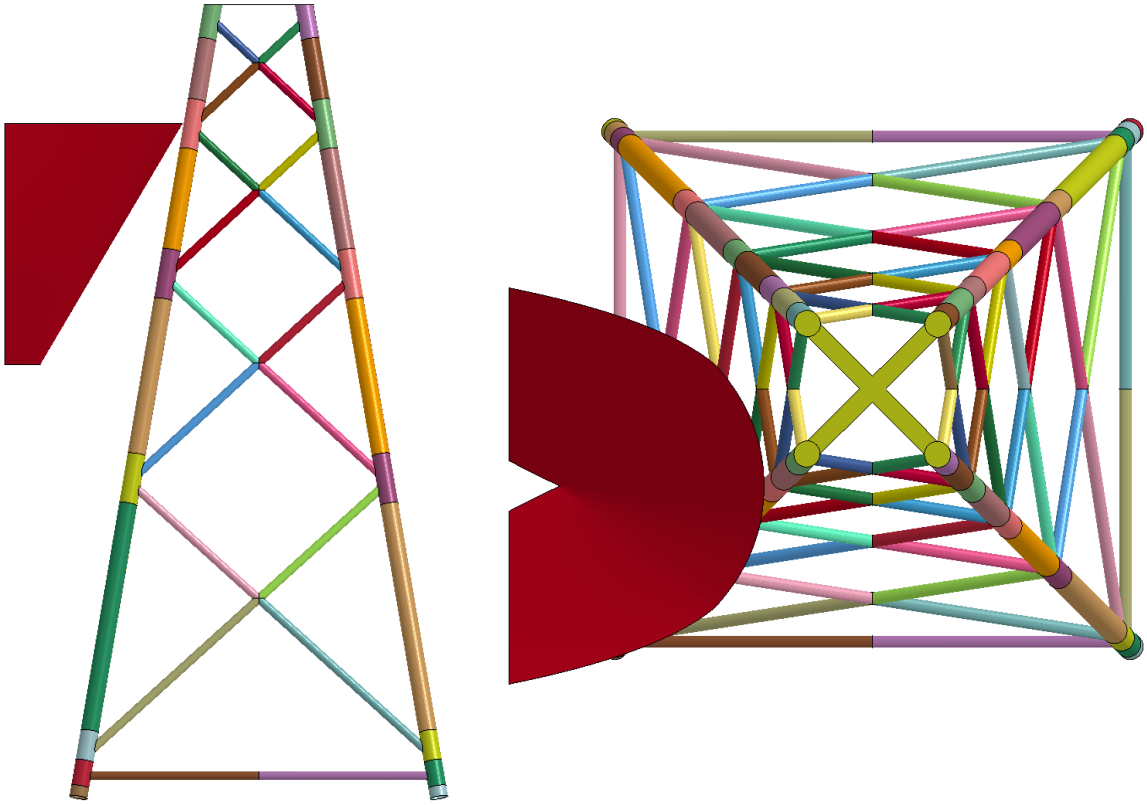

Figure 8.22: Collision scenario on a leg on a connection and $\alpha = 0°$

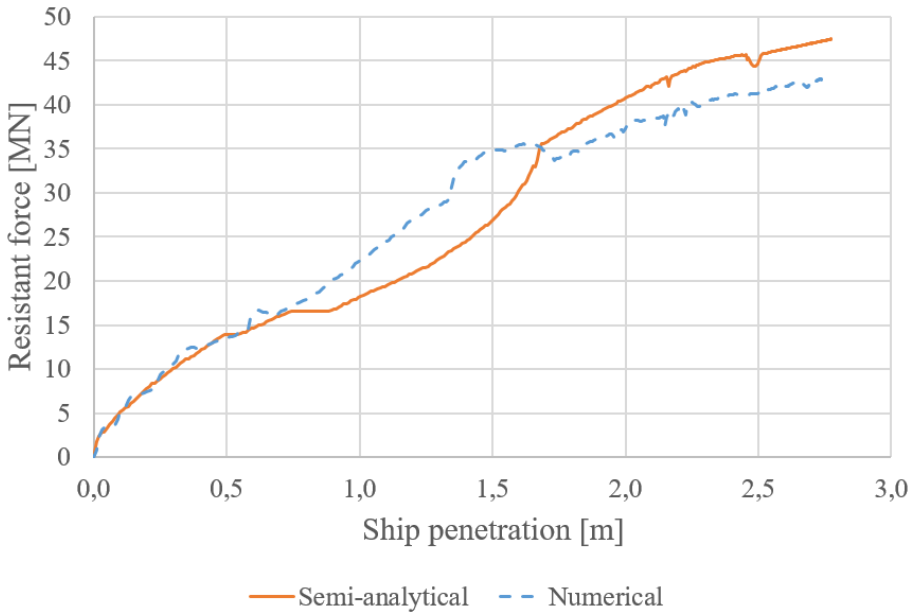

Figure 8.23: Resistant force for a collision on a leg on a connection and $\alpha = 0°$

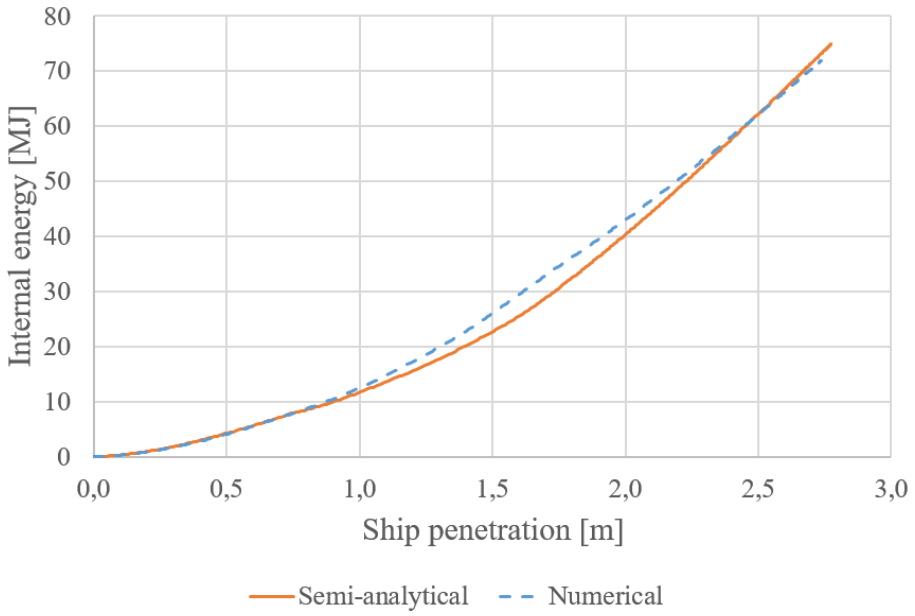

Figure 8.24: Dissipated energy for a collision on a leg on a connection and $\alpha = 0°$

Table 8.7: Discrepancy on the ship penetration for a collision on a leg on a connection and $\alpha = 0°$

$E\ [MJ]$	Pen. num. $[m]$	Pen. semi-anal. $[m]$	Discrepancy [%]
27	1.53	1.65	8
48	2.14	2.18	2
75	2.74	2.77	1

On the whole energy-penetration curves (Fig. 8.24):

- Maximum discrepancy: 8%
- Mean discrepancy: 3%

Table 8.8: Distribution of energy dissipation into the four deformation modes for a collision on a leg on a connection and $\alpha = 0°$

	Local crushing	Overall motion	Punching	Base
Energy $[MJ]$	20.58	10.18	12.52	31.72
Distribution [%]	27	14	17	42

B30: Collision on a leg on a connection and $\alpha = 30°$:

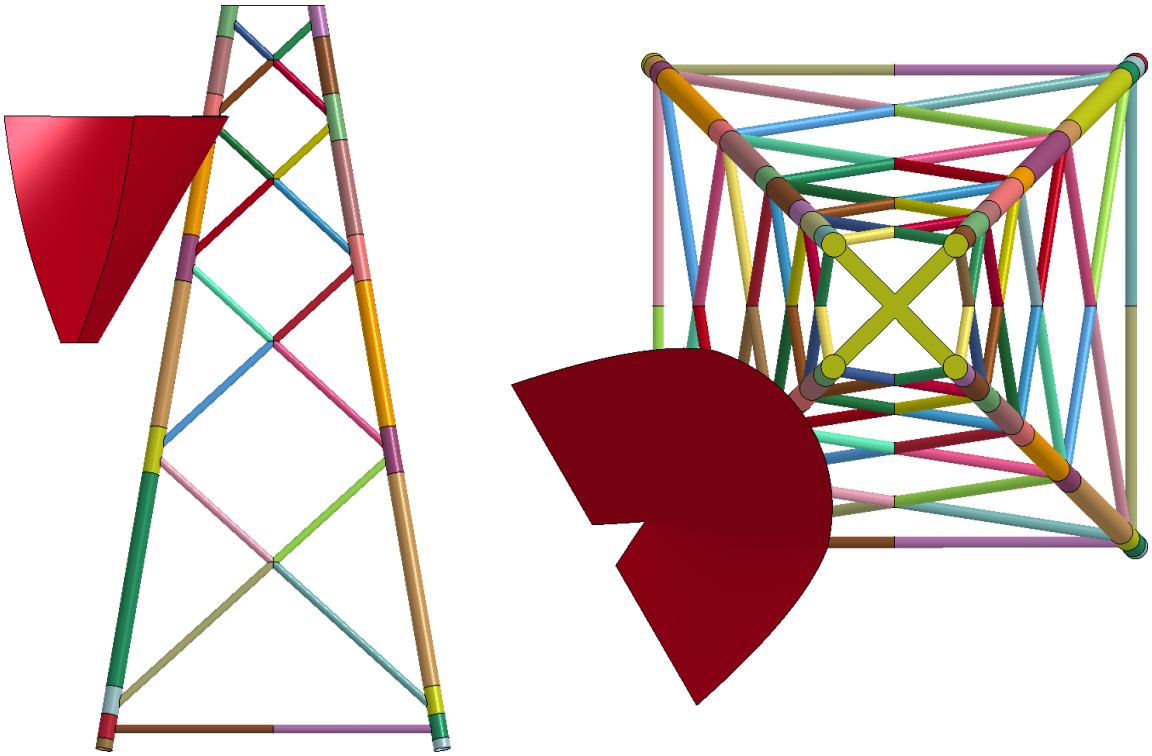

Figure 8.25: Collision scenario on a leg on a connection and $\alpha = 30°$

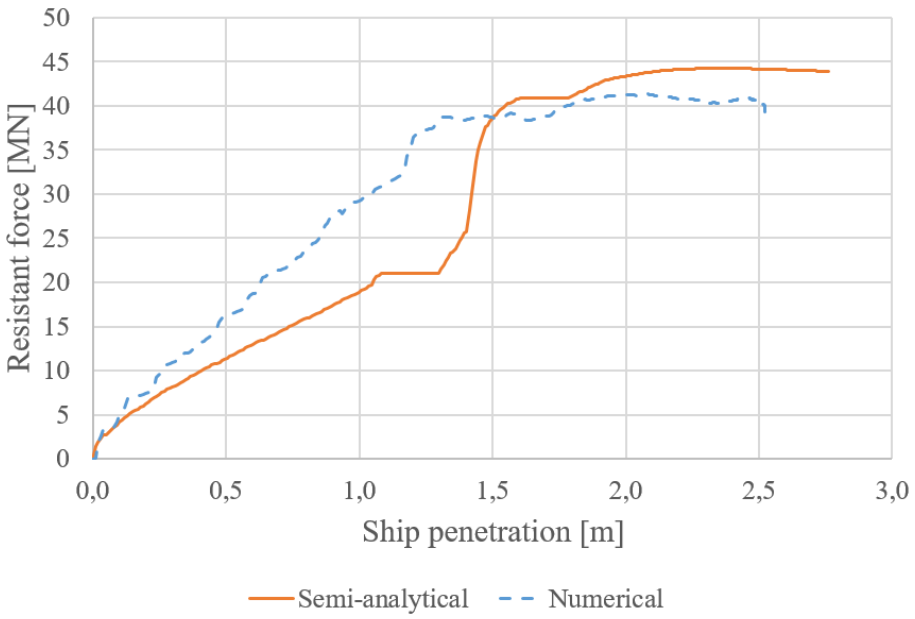

Figure 8.26: Resistant force for a collision on a leg on a connection and $\alpha = 30°$

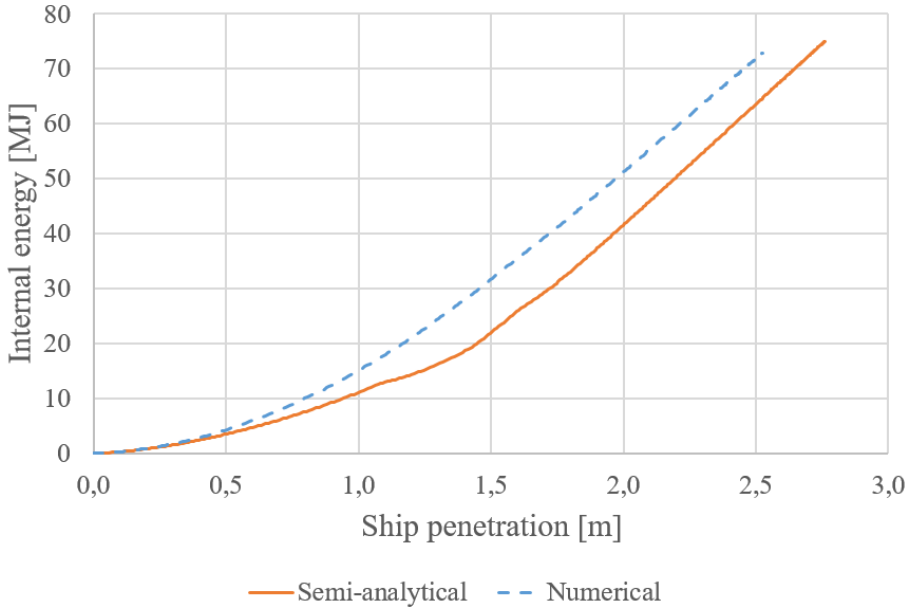

Figure 8.27: Dissipated energy for a collision on a leg on a connection and $\alpha = 30°$

Table 8.9: Discrepancy on the ship penetration for a collision on a leg on a connection and $\alpha = 30°$

$E\ [MJ]$	Pen. num. $[m]$	Pen. semi-anal. $[m]$	Discrepancy [%]
27	1.37	1.63	19
48	1.92	2.15	12
75	2.53	2.76	9

On the whole energy-penetration curves (Fig. 8.27):

- Maximum discrepancy: 25%
- Mean discrepancy: 15%

Table 8.10: Distribution of energy dissipation into the four deformation modes for a collision on a leg on a connection and $\alpha = 30°$

	Local crushing	Overall motion	Punching	Base
Energy $[MJ]$	11.23	46.76	17.01	0
Distribution [%]	15	62	23	0

B45: Collision on a leg on a connection and $\alpha = 45°$:

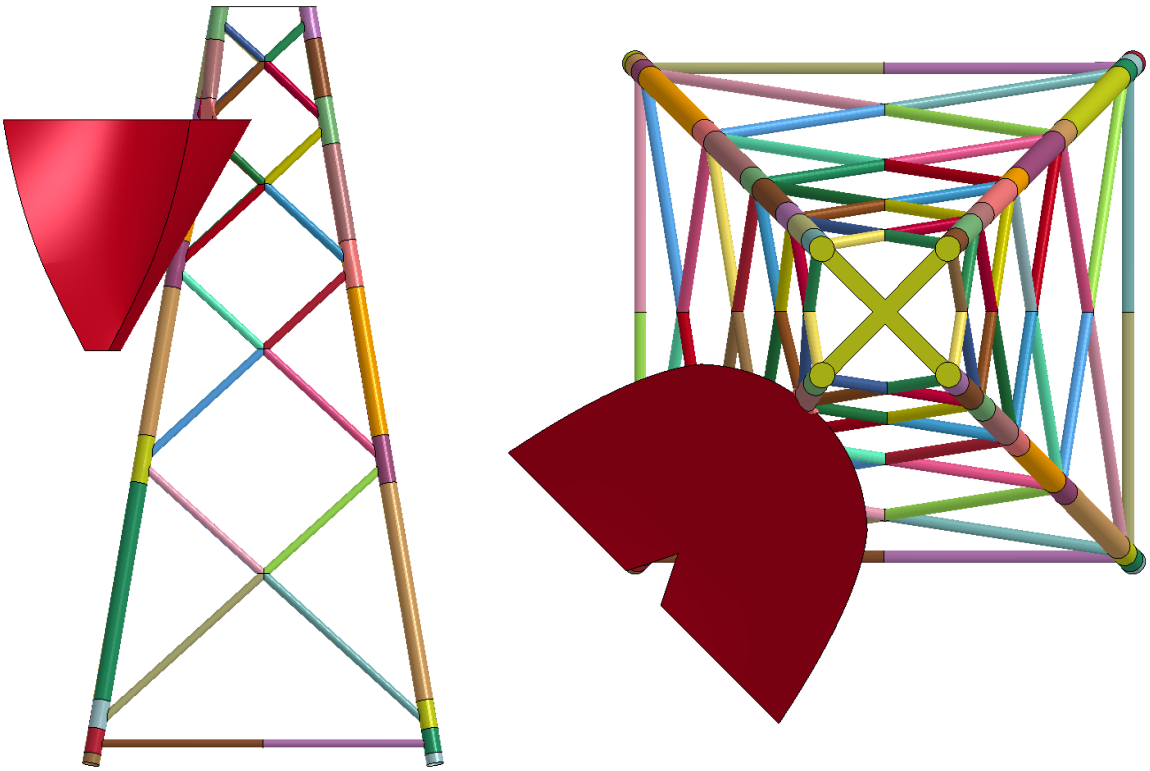

Figure 8.28: Collision scenario on a leg on a connection and $\alpha = 45°$

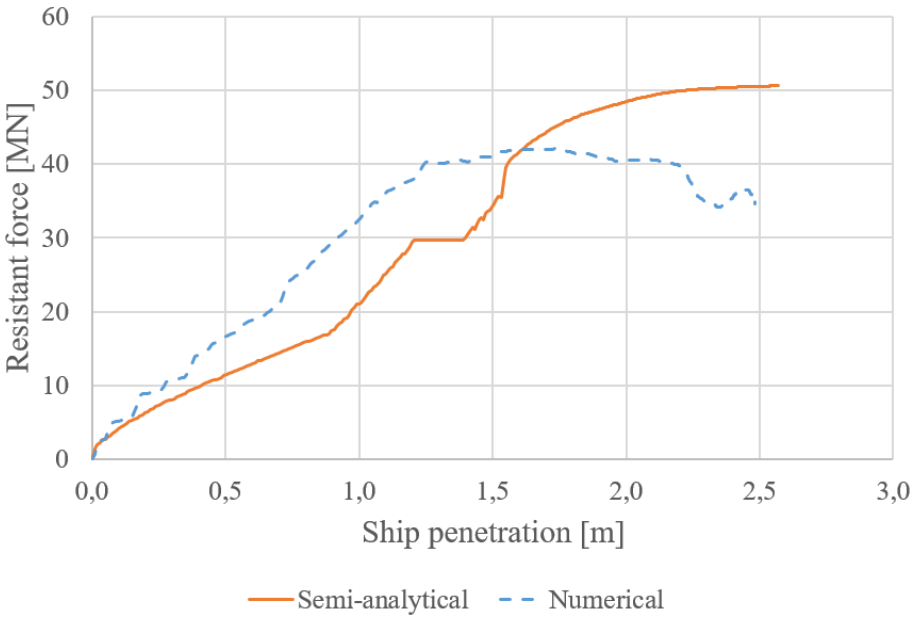

Figure 8.29: Resistant force for a collision on a leg on a connection and $\alpha = 45°$

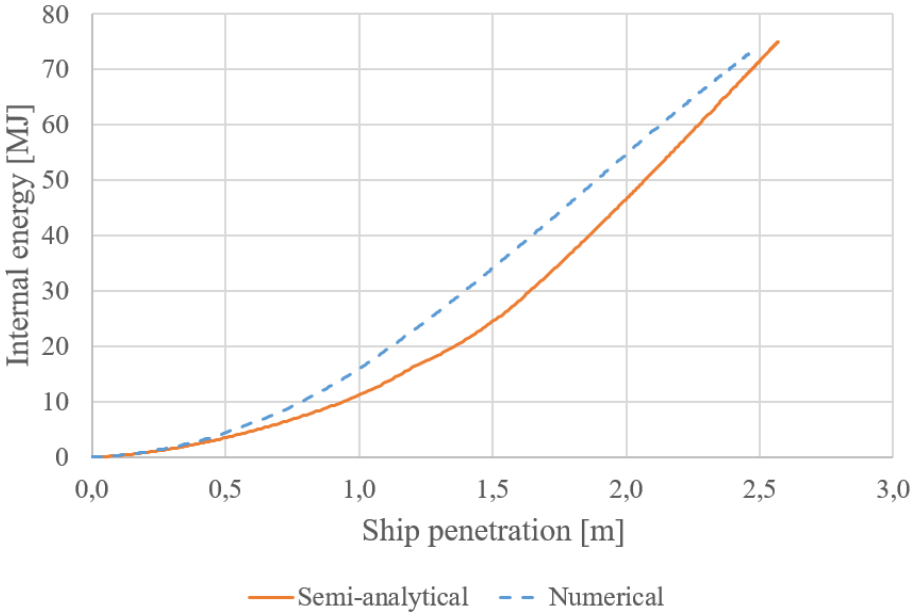

Figure 8.30: Dissipated energy for a collision on a leg on a connection and $\alpha = 45°$

Table 8.11: Discrepancy on the ship penetration for a collision on a leg on a connection and $\alpha = 45°$

$E\ [MJ]$	Pen. num. $[m]$	Pen. semi-anal. $[m]$	Discrepancy [%]
27	1.32	1.57	19
48	1.84	2.03	10
75	2.48	2.57	4

On the whole energy-penetration curves (Fig. 8.30):

- Maximum discrepancy: 21%
- Mean discrepancy: 13%

Table 8.12: Distribution of energy dissipation into the four deformation modes for a collision on a leg on a connection and $\alpha = 45°$

	Local crushing	Overall motion	Punching	Base
Energy $[MJ]$	8.39	52.41	14.26	0
Distribution [%]	11	70	19	0

C0: Collision on a brace and $\alpha = 0°$:

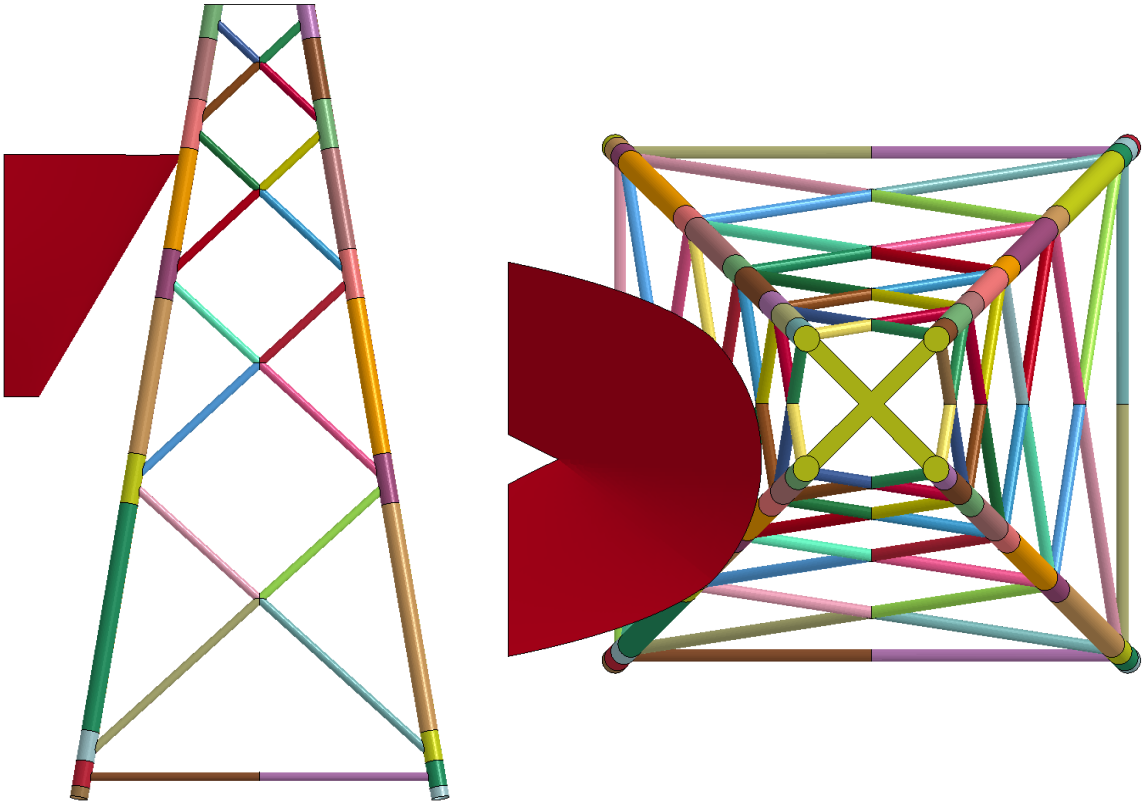

Figure 8.31: Collision scenario on a brace and $\alpha = 0°$

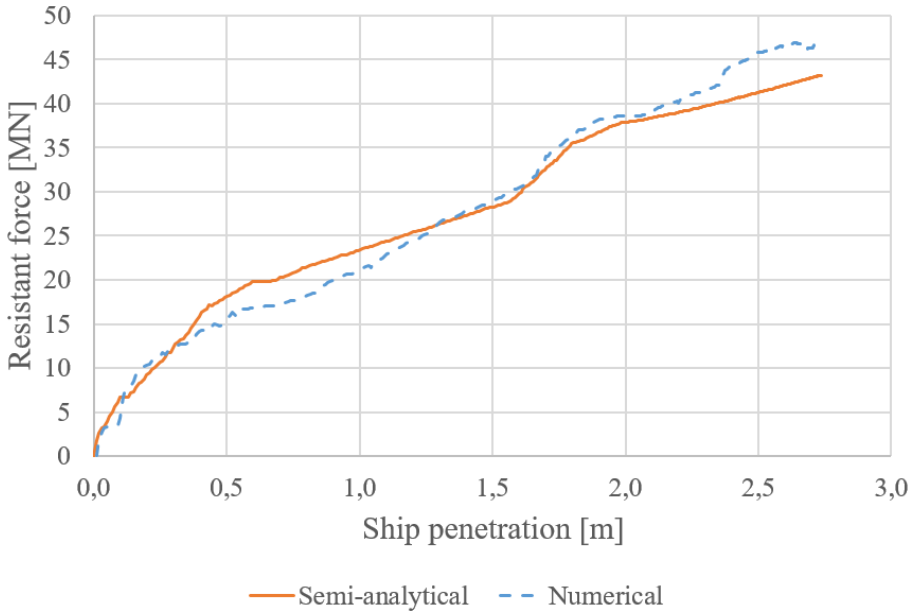

Figure 8.32: Resistant force for a collision on a brace and $\alpha = 0°$

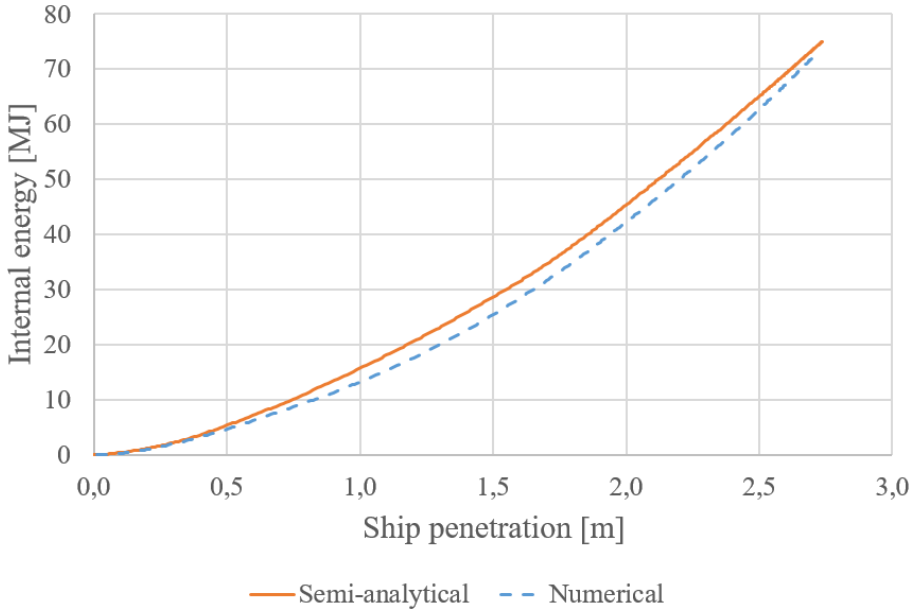

Figure 8.33: Dissipated energy for a collision on a brace and $\alpha = 0°$

Table 8.13: Discrepancy on the ship penetration for a collision on a brace and $\alpha = 0°$

$E\ [MJ]$	Pen. num. $[m]$	Pen. semi-anal. $[m]$	Discrepancy [%]
27	1.56	1.44	8
48	2.15	2.07	4
75	2.72	2.74	1

On the whole energy-penetration curves (Fig. 8.33):

- Maximum discrepancy: 10%
- Mean discrepancy: 6%

Table 8.14: Distribution of energy dissipation into the four deformation modes for a collision on a brace and $\alpha = 0°$

	Local crushing	Overall motion	Punching	Base
Energy $[MJ]$	33.26	3.01	25.58	13.15
Distribution [%]	44	4	34	18

8.5.1.2 Bulbous striking ship collisions

D0: Bulbous ship collision on a leg and $\alpha = 0°$

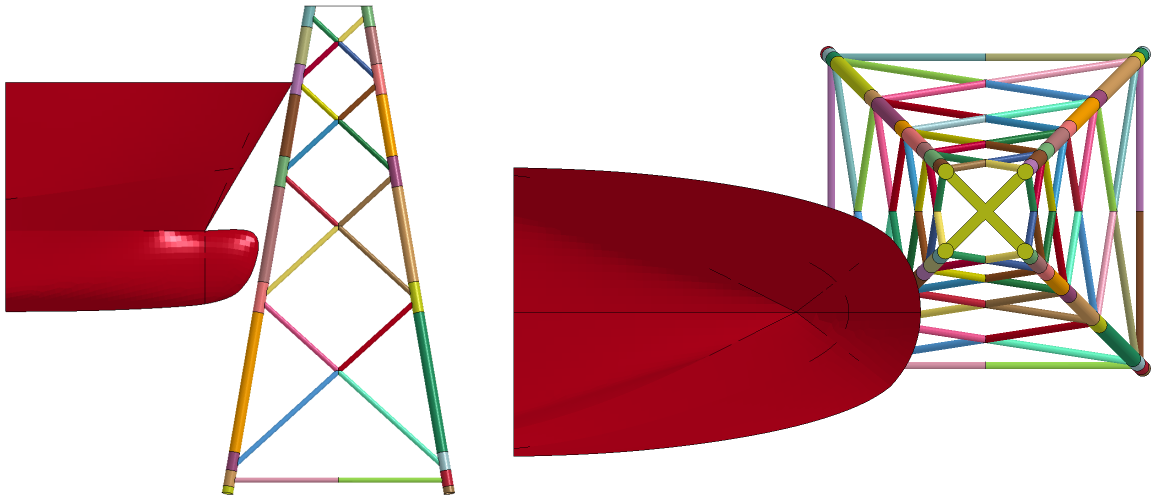

Figure 8.34: Bulbous ship collision scenario on a leg and $\alpha = 0°$

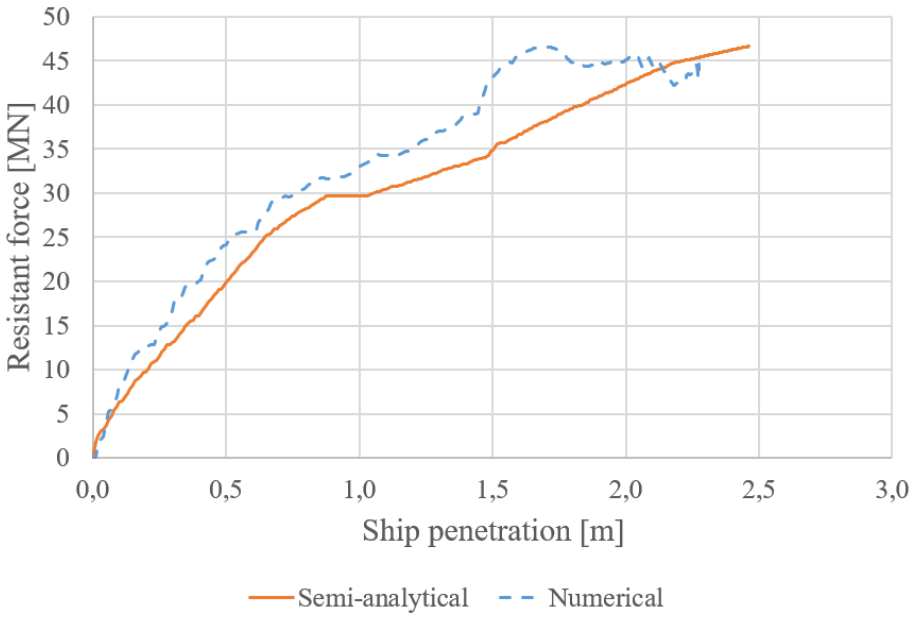

Figure 8.35: Resistant force for a bulbous ship collision on a leg and $\alpha = 0°$

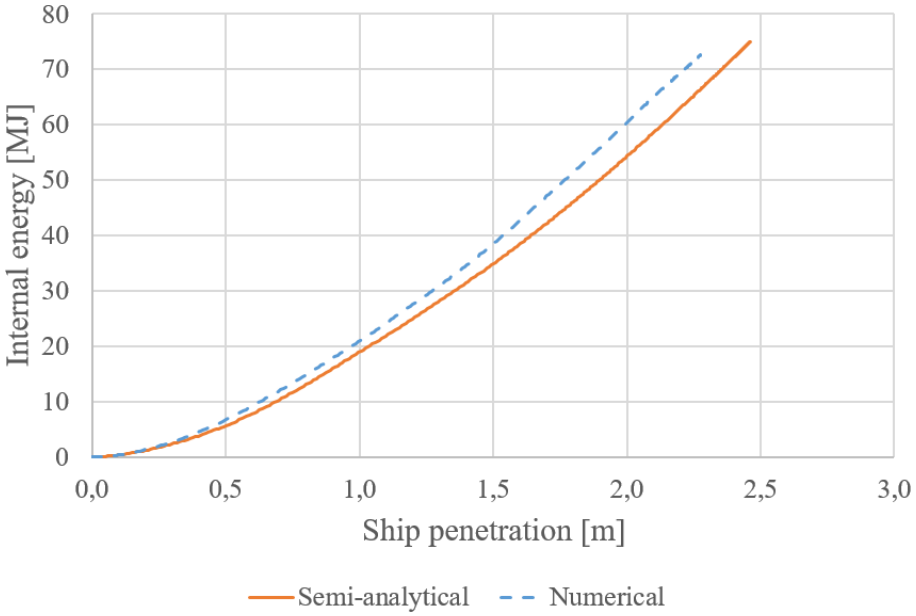

Figure 8.36: Dissipated energy for a bulbous ship collision on a leg and $\alpha = 0°$

Table 8.15: Discrepancy on the ship penetration for a bulbous ship collision on a leg and $\alpha = 0°$

$E\ [MJ]$	Pen. num. $[m]$	Pen. semi-anal. $[m]$	Discrepancy [%]
27	1.18	1.26	7
48	1.72	1.84	7
75	2.28	2.46	8

On the whole energy-penetration curves (Fig. 8.36):

- Maximum discrepancy: 10%
- Mean discrepancy: 7%

Table 8.16: Distribution of energy dissipation into the four deformation modes for a collision on a leg between two connections and $\alpha = 0°$

	Local crushing	Overall motion	Punching	Base
Energy $[MJ]$	19.33	3.11	20.35	32.21
Distribution [%]	26	4	27	43

D30: Bulbous ship collision on a leg and $\alpha = 30°$

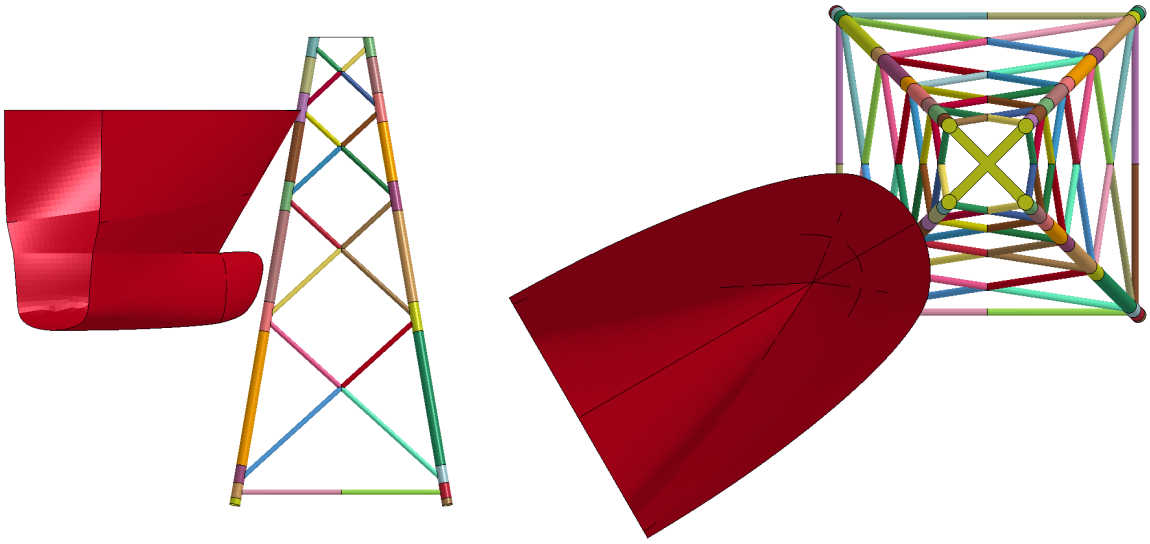

Figure 8.37: Bulbous ship collision scenario on a leg and $\alpha = 30°$

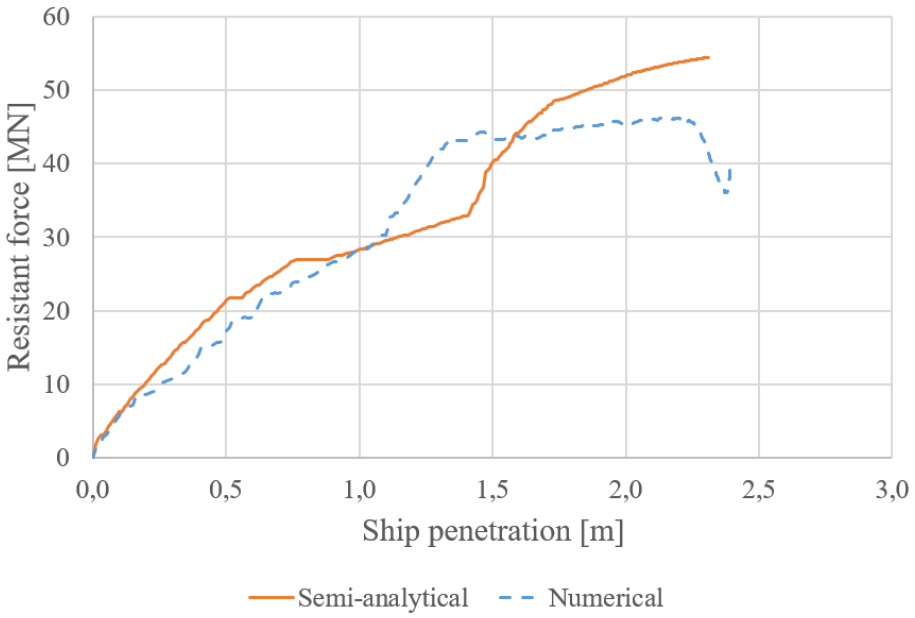

Figure 8.38: Resistant force for a bulbous ship collision on a leg and $\alpha = 30°$

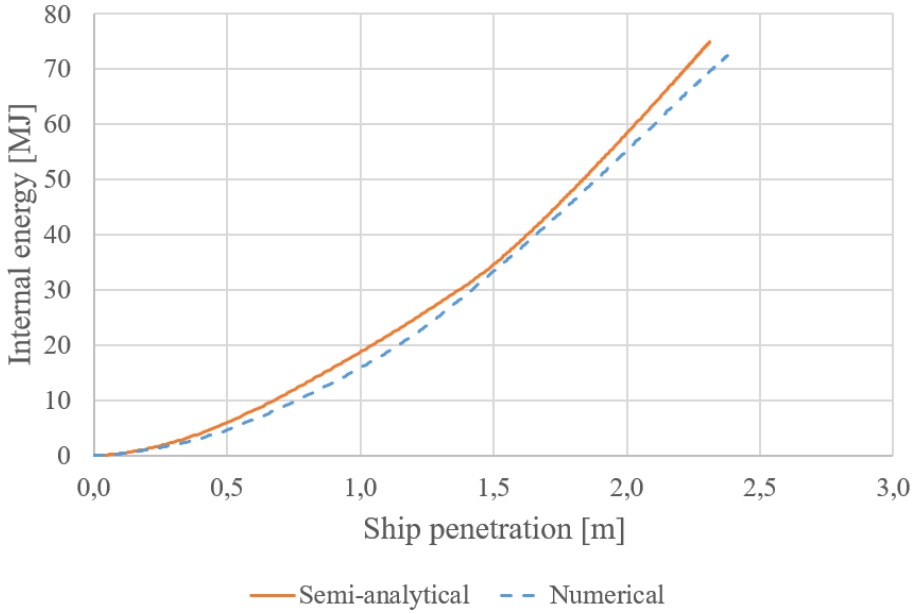

Figure 8.39: Dissipated energy for a bulbous ship collision on a leg and $\alpha = 30°$

Table 8.17: Discrepancy on the ship penetration for a bulbous ship collision on a leg and $\alpha = 30°$

E $[MJ]$	Pen. num. $[m]$	Pen. semi-anal. $[m]$	Discrepancy [%]
27	1.34	1.28	4
48	1.84	1.80	2
75	2.39	2.31	3

On the whole energy-penetration curves (Fig. 8.39):

- Maximum discrepancy: 10%
- Mean discrepancy: 4%

Table 8.18: Distribution of energy dissipation into the four deformation modes for a collision on a leg between two connections and $\alpha = 30°$

	Local crushing	Overall motion	Punching	Base
Energy $[MJ]$	44.13	4.16	25.78	0.93
Distribution [%]	59	6	34	1

D45: Bulbous ship collision on a leg and $\alpha = 45°$

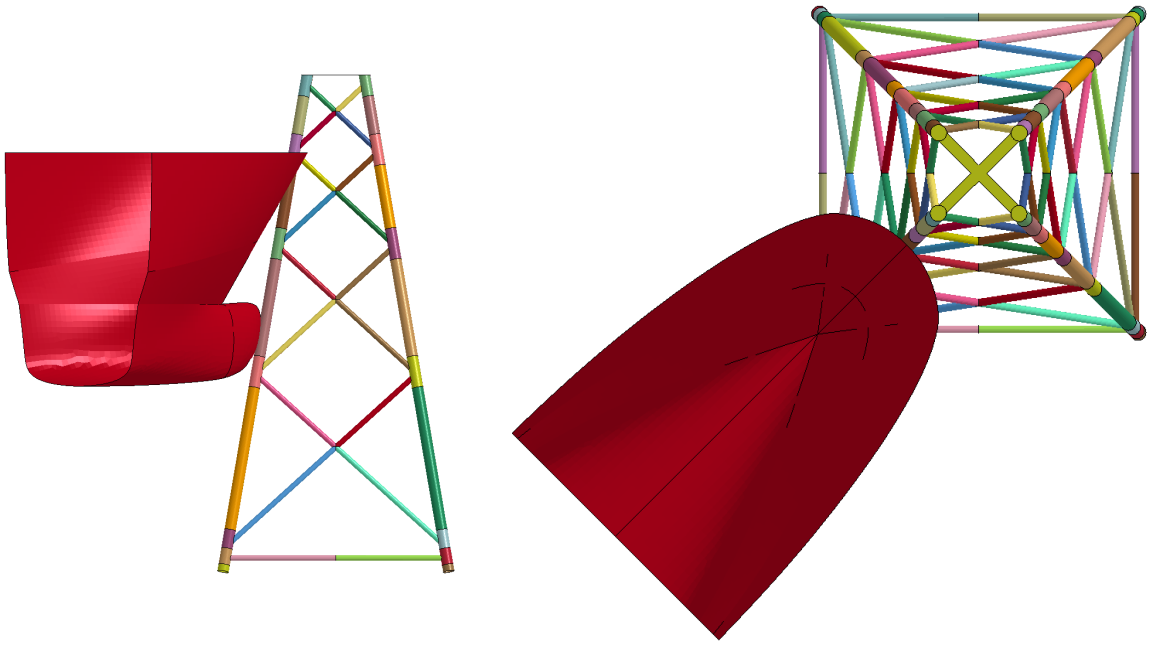

Figure 8.40: Bulbous ship collision scenario on a leg and $\alpha = 45°$

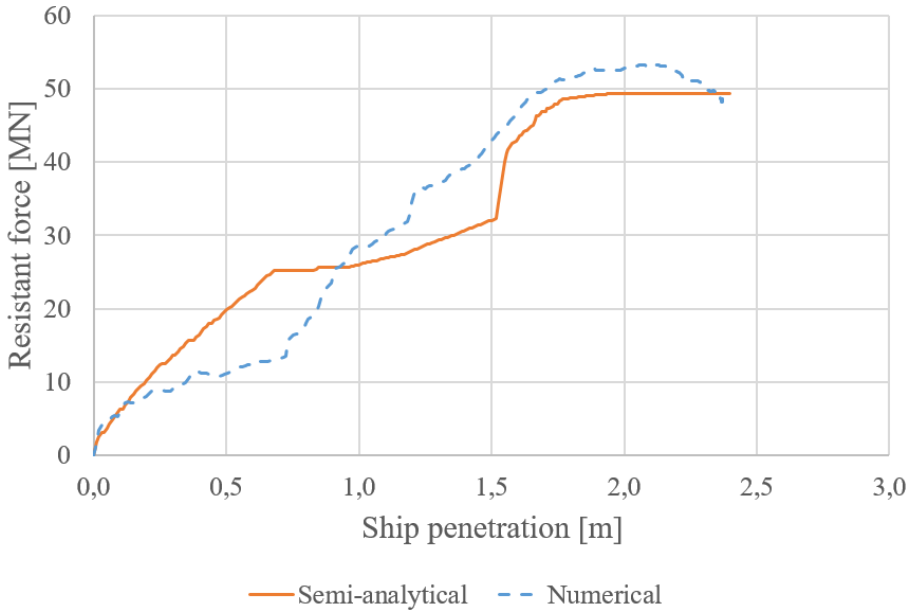

Figure 8.41: Resistant force for a bulbous ship collision on a leg and $\alpha = 45°$

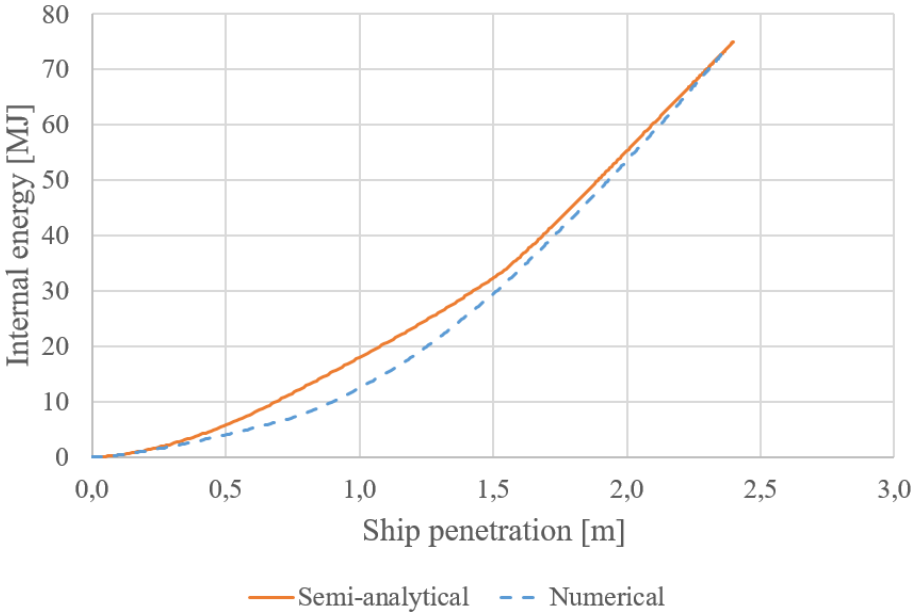

Figure 8.42: Dissipated energy for a bulbous ship collision on a leg and $\alpha = 45°$

Table 8.19: Discrepancy on the ship penetration for a bulbous ship collision on a leg and $\alpha = 45°$

$E\ [MJ]$	Pen. num. $[m]$	Pen. semi-anal. $[m]$	Discrepancy [%]
27	1.44	1.33	8
48	1.89	1.85	2
75	2.37	2.40	1

On the whole energy-penetration curves (Fig. 8.36):

- Maximum discrepancy: 20%
- Mean discrepancy: 6%

Table 8.20: Distribution of energy dissipation into the four deformation modes for a collision on a leg between two connections and $\alpha = 45°$

	Local crushing	Overall motion	Punching	Base
Energy $[MJ]$	54.85	3.86	16.29	0
Distribution [%]	73	5	22	0

8.5.2 Discussion of the results

The ship penetration computed with the FE and the semi-analytical models are denoted δ_{FE} and δ_{SA} respectively.

The discrepancies are computed for all investigated collision scenarios and for various energy levels of $1, 2, 3, \ldots, 75\ MJ$. The results for energies of 27, 48 and 75 MJ are summarised in Table 8.21, as well as the maximum and mean discrepancies and the coefficient of variation (CoV) associated to the non-dimensional ship penetration δ^{nd} (Eq. 8.8).

$$\delta^{nd} = \frac{\delta_{SA}}{\delta_{FE}} \tag{8.8}$$

The CoV is defined as the ration between the standard deviation σ of a variable x and the mean value μ, as given in Eq. 8.9. In this case, the ship penetration is made non-dimensional for each level of energy and the expression of the CoV becomes Eq. 8.10.

$$CoV = \frac{\sigma}{\mu} = \frac{\sqrt{\frac{1}{n}\sum_{1}^{n}(x-\mu)^2}}{\mu} \tag{8.9}$$

$$CoV = \frac{\sqrt{\frac{1}{75}\sum_{i=1}^{75}\left(\frac{\delta_{SA}}{\delta_{FE}} - \frac{\delta_{FE}}{\delta_{FE}}\right)^2}}{\frac{\delta_{FE}}{\delta_{FE}}} = \sqrt{\frac{1}{75}\sum_{i=1}^{75}\left(\delta^{nd} - 1\right)^2} \tag{8.10}$$

Table 8.21: Discrepancies [%] between numerical and semi-analytical models for all investigated collision scenarios

	Scenario	Fig.	27 MJ [%]	48 MJ [%]	75 MJ [%]	Max [%]	Mean [%]	CoV [%]
Non-bulbous	A0: Leg span, $\alpha = 0°$	8.15	3	1	4	6	2	3
	A30: Leg span, $\alpha = 30°$	8.18	0	2	4	10	4	4
	A45: Leg span, $\alpha = 45°$	8.21	2	6	6	10	4	5
	B0: Leg connection, $\alpha = 0°$	8.24	8	2	1	8	3	4
	B30: Leg connection, $\alpha = 30°$	8.27	19	12	9	25	15	16
	B45: Leg connection, $\alpha = 45°$	8.30	19	10	4	21	13	14
	C0: Brace span, $\alpha = 0°$	8.33	8	4	1	10	6	6
Bulbous	D0: Leg, $\alpha = 0°$	8.36	7	7	8	10	7	7
	D30: Leg, $\alpha = 30°$	8.39	4	2	3	10	4	6
	D45: Leg, $\alpha = 45°$	8.42	8	2	1	20	6	9
							6	8

First, it has to be reminded that the results are obtained by assuming that the striking ship is rigid and that rupture of elements is not included in the material law.

From the comparison performed in the previous Section 8.5.1 and summarised in Table 8.21, it appears that the developed semi-analytical model provides results in good accordance with FE simulations for most collision scenarios.

Based on those investigated scenarios, the mean discrepancy of the model on the ship penetration is equal to 6% with a CoV of 8%. For low collision angles α, the discrepancy on dissipated energy between both models is even lower than 10% during the whole collision, with an mean discrepancy of 5% and a CoV of 6%.

However, some improvements in the semi-analytical model have to be performed for scenarios with large collision angles α, and especially when the initial contact corresponds to a connection (for example collision scenarios $B30$ Fig. 8.26 and $B45$ Fig. 8.29). For those scenarios, it appears that the force computed with the semi-analytical model is much lower than the numerical one for ship penetration until about 1.5 m, which means that the model is too soft. Similar trends are observed for scenarios $D30$ (Fig. 8.38) and $D45$ (Fig. 8.41) for bulbous bow striking ship.

To solve this issue, the deformation of the connections submitted to punching in two perpendicular directions and to local crushing, as represented in Fig. 8.43, should be investigated and analytical formulations able to take into account simultaneously those three deformation modes (two of punching and one of crushing) should be developed.

For those collision events, the energy is underestimated (and thus the penetration overestimated) with the semi-analytical model, which is conservative with regard to the jacket deformation.

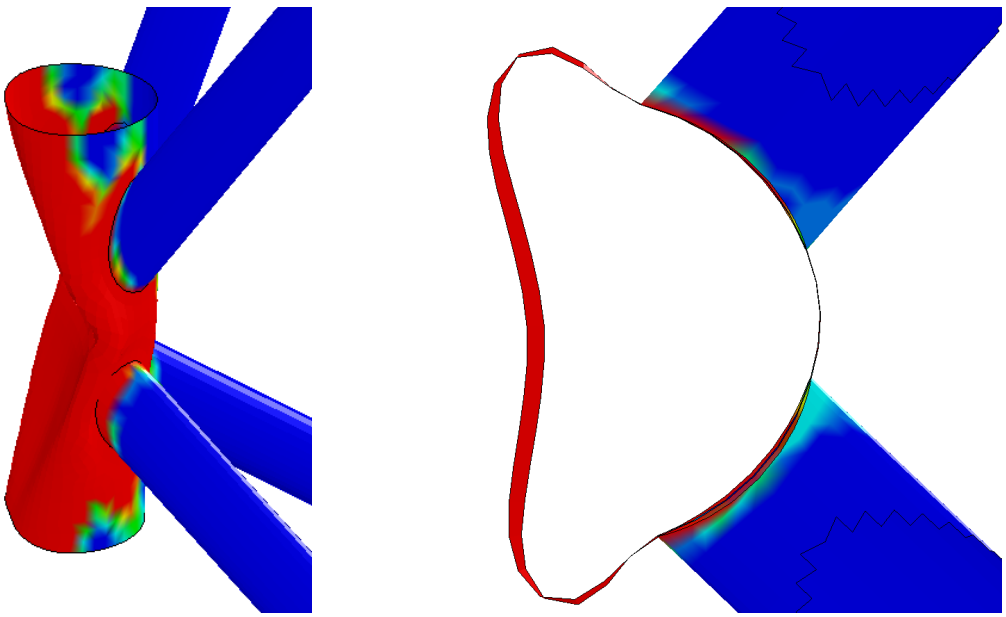

Figure 8.43: Connection subjected to two-sides punching and crushing (general view and cross-section deformation)

For a given initial kinetic energy, the collision scenarios with the largest ship penetrations correspond to scenarios for which the initial impact point is located on a leg between two leg - braces connections or on braces. For those scenarios and 75 MJ of impact energy, the ship penetration is about $3-3.50$ m, as long as rupture of tubular elements is not taken into account. For collisions on a connection, the ship penetration is about $2.50-2.80$ m.

Collisions between connections are therefore the most damaging scenarios during the collision process.

The damage caused by the considered collision however decreases the tubular members resistance and affects the OWT jacket stability, which could lead to the collapse of the tower and the nacelle. In the present thesis, the consequence of the collision event and the resulting deformation on the jacket stability is not investigated. To do so, models including the tower and the nacelle that take into account gravity loads have to be built.

The distribution of dissipated energy between the four deformation modes, summarised in Table 8.22 for all the investigated collision scenarios, is highly related to the collision scenario, and especially on the ship elevation.

Table 8.22: Distribution of energy dissipation into the for deformation modes for the investigated collision scenarios

	Scenario	Table	Local crushing [%]	Overall motion [%]	Punching [%]	Base [%]
Non-bulbous	A0: Leg span, $\alpha = 0°$	8.2	53	3	30	14
	A30: Leg span, $\alpha = 30°$	8.4	58	4	38	0
	A45: Leg span, $\alpha = 45°$	8.6	65	5	26	4
	B0: Leg connection, $\alpha = 0°$	8.8	27	14	17	42
	B30: Leg connection, $\alpha = 30°$	8.10	15	62	23	0
	B45: Leg connection, $\alpha = 45°$	8.12	11	70	19	0
	C0: Brace span, $\alpha = 0°$	8.14	44	4	34	18
Bulbous	D0: Leg, $\alpha = 0°$	8.16	26	4	27	43
	D30: Leg, $\alpha = 30°$	8.18	59	6	34	1
	D45: Leg, $\alpha = 45°$	8.20	73	5	22	0

For collisions between connections, most of the energy is dissipated through the *local crushing of impacted tubular members* mode. Indeed, the three-hinges mechanism may be activated and large displacements occur near the impact point, leading to a large amount of dissipated energy.

However, for collisions on a connection, this mechanism is not activated, and energy is dissipated at that connection through cross-section deformation until the cross-section is totally flat. Then, the three other modes dissipate a lot of energy. For collision angle $\alpha = 0°$ (collision scenarios B0), one plane of the jacket (Fig. 6.47) is deformed and all the deformation modes are activated. For large values of collision angle α (collision scenarios B30 and B45), the impacted point moves along the ship trajectory and only few deformation occurs in the two planes adjacent to the impacted leg. A large part of the energy is thus dissipated through the *overall motion* deformation mode.

As discussed in Chapter 3, the FE model is built using Belytschko-Tsay shell elements that are four-nodes shell elements with one single point of integration, as represented in Fig. 8.44, in comparison with fully integrated shell elements, as represented in Fig. 8.45. Those elements are thus under-integrated and hourglass modes may occur during the simulations. Hourglass modes correspond to non-physical zero energy modes for which the deformation cannot be captured by the unique integration point. For 2D shell elements, two hourglass modes are represented are represented in Fig. 8.46. In all the FE simulations presented in this Chapter, the hourglass energy is lower than 1 MJ, which corresponds to less than 2% of the total energy (75 MJ).

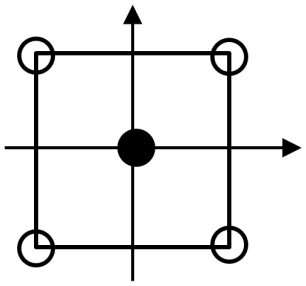

Figure 8.44: Four-nodes shell element under-integrated

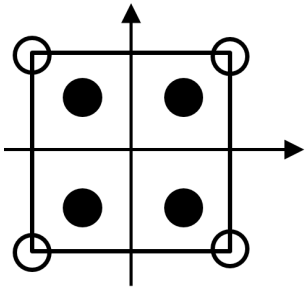

Figure 8.45: Four-nodes shell element fully integrated

Figure 8.46: Two hourglass modes for 2D shell elements

The aim of developed method is to compute the crashworthiness of an OWT jacket quickly. This goal is achieved, as the computation time is about 3 minutes[1], which is significantly shorter than with FE simulations, lasting about 10 hours[2].

[1] *MATLAB R2009a*, processor Intel®Core™i3-3217U, CPU 1.80 GHz, RAM 8 Go ($DDR3$, 800 MHz)
[2] *LS-DYNA R-611*, processor Intel®Xeon®, CPU E5-2630 v2 2.60 GHz (2 processors), RAM 64 Go ($DDR3$, 1600 MHz)

8.6 Conclusions

The general algorithm developed to compute the total resistance of an OWT jacket impacted by a ship is described in this Chapter. All the steps, starting from providing the collision data until getting the results, required to compute the jacket resistance are detailed.

At first, the user has to built the collision model, including the striking ship geometry, the jacket mechanical and geometrical properties as well as the collision scenario.

The contact force between the ship and the jacket may occur through several contact points that do not appear simultaneously. A methodology is developed to identify all the potential impacted tubular members and connections between legs and braces. For each of them, the distance with regard to the striking ship, initially located on its trajectory line and such as it is out of contact with the jacket, is computed.

An algorithm is then developed to compute the total resistance of the collided jacket, including the four deformation modes that are described individually in Chapters 4 to 7. The collision time is divided into several time steps for which the resistance is computed. The increment of penetration is computed based on the ship velocity, which allows to detect all the impacted elements. Then, the resistant force is computed for the four deformation modes, taking into account the interactions between them. For the considered time step, the total resistant force is assumed to be the minimum one. The ship acceleration is deduced from this force, and its velocity is updated. This procedure is followed until the striking ship stops.

This general algorithm is finally validated by comparing the results with FE simulations. Several collision scenarios are modelled with both methods including a non-bulbous and a bulbous bow, considered as rigid, and several ship elevations and collision angles. For each of them, the evolution of the resistant force and the dissipated energy is plotted and the discrepancy between the semi-analytical and the numerical methods is computed.

From the validation process, the developed semi-analytical model is shown to provide accurate results with a mean discrepancy of 6% with regard to the FE simulations. For the investigated collision events, maximum discrepancies are lower than 10%, except for collisions on leg - braces connections, where discrepancies are larger and the dissipated energy is shown to be underestimated. Analytical developments including the effect of crushing and punching in a common formulation is suggested as further research to improve the model. The results also demonstrate that collisions between connections lead to the largest ship penetration for a given initial kinetic energy. The distribution of dissipated energy between the four deformation modes according to the collision scenario is also discussed. Finally, the reduction of computation time with regard to FE simulations is shown to be significant.

Bibliography

[1] J Amdahl. *Energy absorption in ship-platform impact.* PhD thesis, Norwegian Institute of Technologies, Trondheim, 1982.

[2] L Buldgen. *Simplified analytical methods for the crashworthiness and the seismic design of lock gates.* PhD thesis, University of Liege, Belgium, 2014.

[3] S Haris and J Amdahl. Analysis of ship–ship collision damage accounting for bow and side deformation interaction. *Marine Structures*, (32):18–48, 2013.

[4] L Hong and J Amdahl. Plastic mechanism analysis of the resistance of ship longitudinal girders in grounding and collision. *International Journal of Ships and Offshore Structures*, (3):159–171, 2008.

[5] N Jones. *Structural impact.* Cambridge: Cambridge University Press, 1997.

[6] H Le Sourne, N Besnard, C Cheylan, and N Buannic. A ship collision analysis program based on upper bound solutions and coupled with a large rotational ship movement analysis tool. *Journal of Applied Mathematics*, (2012):1–28, 2012.

[7] B Liu. Analytical method to assess double-hull ship structures subjected to bulbous bow collision. *Ocean Engineering*, (142):27–38, 2017.

[8] M Lützen. *Ship collision damage.* PhD thesis, Technical University of Denmark, Copenhagen, 2001.

[9] T Wierzbicki and W Abramowicz. On the crushing mechanics of thin-walled structures. *Journal of Applied Mechanics*, (50):727–734, 1983.

[10] PDC Yang and JB Caldwell. Collision energy absorption of ship's bow structures. *International Journal of Impact Engineering*, (7):181–196, 1988.

[11] X Yu. *Structural analysis with large deformations until fracture and with dynamic failure.* PhD thesis, University of Hamburg, Germany, 1996.

[12] S Zhang. *The mechanics of ship collisions.* PhD thesis, Technical University of Denmark, Copenhagen, 1999.

Chapter 9

Conclusions and perspectives

Abstract:

In this concluding Chapter, the thesis is summarised and the main topics investigated in each Chapter are highlighted.

Then, the personal scientific contributions performed during the PhD are highlighted and detailed.

Finally, the applications of the developed methodology and associated algorithm are discussed and further research topics are suggested to extend the model.

9.1 Summary of the research

As discussed in **Chapter 1**, the number of offshore wind farms is expanding and represents a part of the development of renewable sources of energy. In addition the number of navigating ships is increasing. Therefore, the probability of a ship collision on an OWT raises. From the state of the art, it appears that such ship - OWT collisions are currently mainly investigated with FE simulations, which provides accurate results but is time-demanding and not suitable for a pre-design stage.

The development of a simplified tool able to compute quickly the resistance of an OWT jacket, including both local and global deformations, is thus required. This is the aim of this thesis.

The developed method is based on analytical developments derived using the upper-bound theorem associated with a plastic limit analysis, while the validation of the model is achieved by comparison with FE simulations performed with *LS-DYNA* nonlinear solver. The theoretical background of these two methods in the framework of ship collisions is detailed in **Chapter 2**.

Using FE simulations, the structural behaviour of an OWT jacket impacted by a ship is investigated in **Chapter 3**. First, the influence of some parameters is studied, and the results show that the dynamics of the tower and the gravity force have a negligible effect on the jacket deformations. The structure - soil stiffness interaction is also analysed, and it appears that considering the jacket legs as perfectly clamped in the seabed, i.e. with an infinite soil stiffness, provides similar results than with a finite soil stiffness for the considered OWT jacket. Then, four deformation modes are identified, namely the crushing of impacted tubular members, the global motion of the overall jacket, the punching of legs by compressed braces and the deformation at the base of the jacket. Material rupture of impacted cylindrical members is also investigated and is shown to have few effect on the deformation modes even if it may influence the total ship penetration.

In the thesis, it is assumed that the striking ship is perfectly rigid, i.e. the whole initial kinetic energy is dissipated by deformation of the OWT jacket, and that rupture of elements is not taken into account. Those assumptions are conservative with regard to the collided OWT jacket.

Chapter 4 aims to study the crushing resistance of impacted tubular members (Fig. 9.1). At first, assumptions on the impacted tubular member deformation pattern are made, taking into account the striking ship stem geometry and the impact point. Then, analytical expressions are derived for both vertical and horizontal cylindrical members by using the upper-bound theorem associated with a plastic limit analysis. Then, the resistance of an oblique tubular member is obtained by linear interpolation between both vertical and horizontal values. A similar approach is used to assess the resistance of a tubular member impacted by a ship bulb. The validation

is performed by comparing the results with FE simulations and show a good accordance of the developed analytical model.

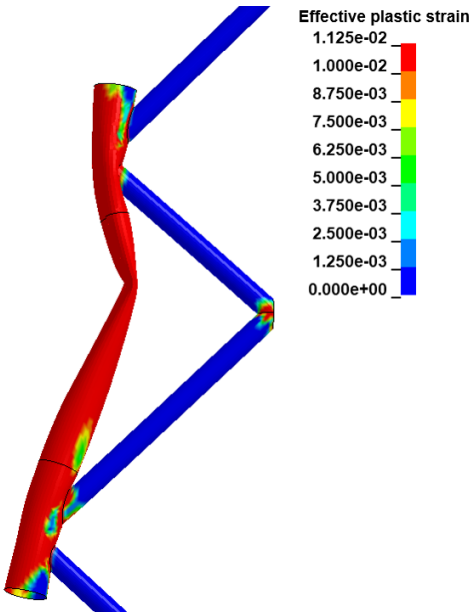

Figure 9.1: Local crushing of an impacted tubular member

The global deformation of the whole OWT jacket in investigated in **Chapter 5** using a methodology similar to FE codes in which each tubular member is modelled as one single $3D$ beam element with 6 degrees of freedom at each node. The elasto-plastic elementary stiffness matrices are computed taking into account the geometric second-order effects (using Timoshenko stability functions), semi-rigid connections at the extremities (from hinged to clamped) and potential plastic hinges at both extremities or at mid-span of the tubular member. The structure stiffness matrix is then obtained with an assembly process with all the elementary stiffness matrices. Finally, the displacements and internal efforts are computed by imposing a displacement at the impact point. Validation of the results against FE simulations demonstrate the accuracy of the developed algorithm.

Chapter 6 is dedicated to the punching deformation mode (Fig. 9.2). As a first step, the resistance of a leg punched by a brace is studied. Using a methodology similar than for the local crushing of impacted tubular members, analytical expressions are derived for tubular members crushed by a linear indenter and are affected by empirical parameters taking into account leg and brace diameters ratio. Those formulations are successfully validated with FE simulations. Then, as punching may occur at several connections of the impacted OWT jacket, a methodology is described to assess the punching behaviour on the whole height of the structure. Here again, the confrontation to FE results demonstrates the accuracy of the model.

The fourth deformation mode concerns the deformation at the base of the OWT jacket (Fig. 9.3), also called “elephant foot”, and is investigated in **Chapter 7**. The elements involved in this mechanism consist in both the impacted and rear legs and the bottom horizontal brace. Four zones are defined at the base of the jacket and analytical expressions to compute their

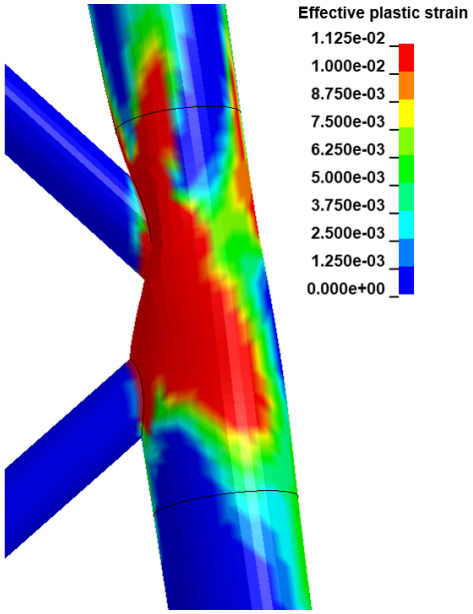

Figure 9.2: Punching of a leg by a compressed brace

resistance are developed for each of them. A comparison with numerical results is successfully performed.

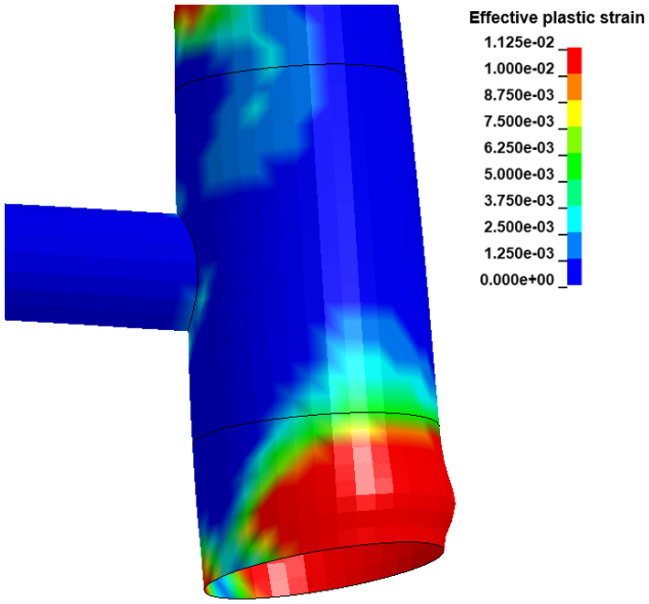

Figure 9.3: Deformation of the rear leg near the foundation level, also called “elephant foot”

In **Chapter 8**, the general algorithm to assess the total crashworthiness of the OWT jacket (Fig. 9.4), based on the so-called “continuous element method”, is detailed. Therefore, the four deformation modes detailed in the previous Chapters are combined and their interactions during the impact are discussed. After listing the required data to fully describe the impact scenario, the collision process is divided into several time steps. For each of them, the impacted elements are first identified. Then, the resistant force F_i is computed for each deformation mode i. At the considered time step, it is assumed that the total resistant force F_{tot} is the lowest

one ($F_{tot} = min(F_i)$) and that the whole deformation occurs in the corresponding deformation mode i. Based on this force, the acceleration of the striking ship is computed and its speed is updated. This procedure is followed until the ship stops.

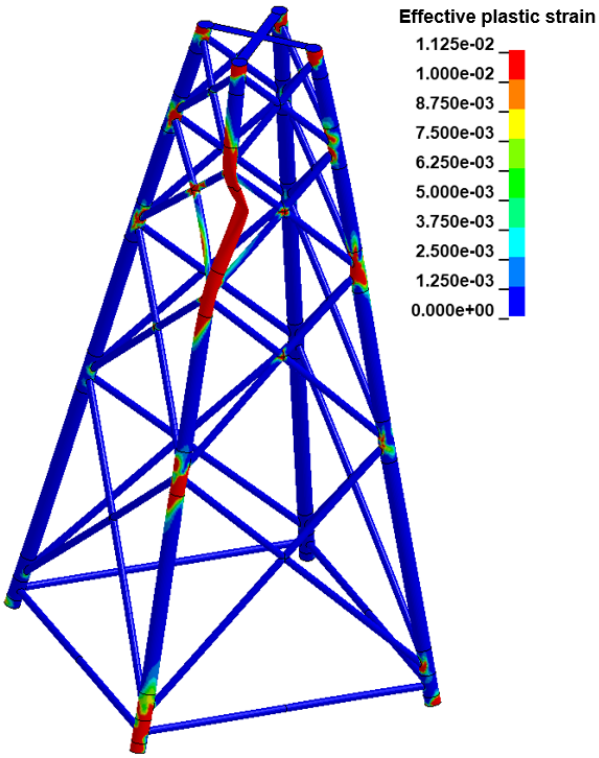

Figure 9.4: Impacted OWT jacket deformation

The validation of the general algorithm is performed for several collision scenarios and involves both non-bulbous and bulbous striking ships. For most cases, both semi-analytical and FE models are in good accordance with discrepancies lower than 10% on the dissipated energy during the whole collision and a mean discrepancy of 6% with a CoV of 8%. For some specific collision scenarios, new analytical developments are suggested to improve the model. The distribution of dissipated energy between the four deformation modes and the most critical collision scenarios are also discussed. The gain of computation time with regard to FE simulations is finally shown to be significant.

The present thesis is summarised in **Chapter 9**. All the personal scientific contributions are listed and further research topics are suggested.

9.2 Personal contributions

The purpose of this PhD thesis is to provide a simplified semi-analytical tool able to assess the resistance of an OWT jacket impacted by a ship.

The main original contributions performed during this PhD are thus related to analytical or semi-analytical developments assessing the resistance in the four deformations modes and to the general algorithm combining all of them. They are discussed in the following list.

- The local deformation of an impacted vertical tubular member is assessed considering the shape of the striking ship stem or bulb. The formulations also take into account the location of the impact point, allowing to investigate non-centred collisions on the tubular member (Fig. 4.6).
- For a given ship penetration on the vertical tubular member, it is assumed that no additional local deformation occurs and that a three-hinge mechanism is activated (Fig. 4.10); a switch between local and global mode is defined. The resistant force in this global mode takes into account the reduction of resistant plastic bending moment at the dented cross-section and the axial force in the tubular member due to large displacements.
- A similar approach is performed for impact on a horizontal tubular member both for the local cross-section deformation and the global three-hinges mechanism.
- In the case of an oblique impacted tubular member (Fig. 4.4), the displacement field is difficult to assess analytically. Therefore, the resistance is computed for equivalent vertical and horizontal tubular members and the resistant force is assumed to be computed with a linear interpolation between both extreme cases. The comparison of the obtained results and FE simulations tends to validate this approach.
- Using the semi-analytical formulations developed to compute the punching resistance at one leg - braces connections, a methodology is developed to assess the punching behaviour on the whole impacted OWT jacket (Fig. 6.6). As punching at one connection is initiated for a non-zero compressive load in the brace, this *punching* deformation mode is coupled with the *overall motion* deformation mode that provides the internal forces in all the tubular elements (Fig. 6.7).
- The investigations on the deformation at the base of the jacket (Figs. 7.2 and 7.3), also called “elephant foot”, represent an original work. For a given ship penetration, the displacement at the base of the jacket is assessed and four areas are defined near the foundation level on both the impacted and rear legs (Fig. 7.9). For each of them, assumptions on the deformation patterns are performed and analytical expressions are derived to compute the resistant force and the dissipated energy. The model is successfully validated by comparison with FE simulations.

- The general algorithm (Fig. 8.11) is based on the so-called continuous element method as it combines all the deformation modes and takes into account their interactions, amongst others:
  - Punching at one node is initiated once the compressive load in the corresponding brace (computed with the *overall motion* deformation mode) reaches value required to initiate the deformation.
  - For a connection submitted to crushing and punching, the sum of deformation due to both modes cannot exceed the leg diameter.
- Some specific conditions are implemented in the general algorithm, amongst others:
  - In the *overall motion* deformation mode, the flow stress of the impacted tubular members and at the base of the jacket is much larger than for the other elements. Indeed, the deformations in those areas is already taken into account in their respective deformation modes and should not be considered twice.
  - If impact occurs on a connection, the three-hinges mechanism described in the *local crushing* deformation mode cannot be activated.
- For a given collision scenario, several contact points may appear and are identified. The potential impacted tubular members or connections are listed and their distances with regard to the striking ship is computed (Figs. 8.2 and 8.3). For each potential contact point, the location of the impact point on both the jacket and the ship is saved, as those properties are further used to compute the resistance of the impacted element (impacted element properties, ship parabola radii, ...).
- During the collision process, the list of impacted elements is updated at each time step. The distance between the ship and the considered element corresponds to the distance before the collision added to the element displacement (computed with the nodal displacements in the *overall motion* deformation mode) minus the ship penetration (Fig. 8.10).
- Multiple contacts are taken into account in the general algorithm:
  - The force in the *local crushing* deformation mode is equal to the sum of crushing forces of all impacted tubular members or connections.
  - The displacement is imposed on several nodes, corresponding to all the impact points, in the *overall motion* deformation mode.
  - The displacement pattern for the *punching* deformation mode is modified.

9.3 Perspectives

The results of this semi-analytical model correspond to the evolution of the resistant force and the dissipated energy during the ship - jacket collision with regard to the striking ship penetration, as plotted in Section 8.5.1. It is assumed that the striking ship is rigid and rupture is not included in the model. The maximum ship penetration and the corresponding jacket deformation are also computed and allow to assess the damage for each given collision scenario.

As discussed in Chapter 1, a complete collision risk analysis has to be performed for every new offshore project, which represents hundreds or thousands of collision scenarios to investigate. FE simulations are time-demanding and are not suitable for a pre-design stage. The purpose of the developed algorithm is thus to assess quickly the crashworthiness of an OWT jacket and aims to be used in the pre-design.

For a given collision scenario, several jacket structures may be compared to identify the optimal design. On the other hand, for a given jacket, this tool may be used to identify the most critical collision scenarios. The notion of "critical" has to be defined by the user, and could be for example the maximum ship penetration, the largest number of impacted element, the cost of repair, ...).

However, the developed method is not accurate enough to perform the final design of the OWT jacket and therefore cannot replace FE methods. The most critical scenarios, previously identified with the semi-analytical model, are thus further investigated with FE simulations.

This methodology allows to drastically reduce the required computation time to perform a complete collision risk analysis, as the number of numerical computations is limited.

For most cases, it is demonstrated in Section 8.5.2 that the semi-analytical model detailed in this thesis is in good accordance with the FE simulations, which validates the method and demonstrates its applicability for design offices.

Some additional work is suggested to further extend the model:

- In the validation of the general algorithm described in Section 8.5.2, it appears that the model could be improved for collisions on a connection with a large collision angle (Figs. 8.25 and 8.28).

  It is therefore suggested to develop analytical formulations to compute the behaviour of a connection punched from two sides and crushed, as represented in Fig. 8.43. This formulation has to capture the behaviour of the connection whatever the punching forces from both sides and the crushing force, even if those forces are not proportional.

- The algorithm computes the resistant force, the dissipated energy and the deformation of the jacket during the collision, until the striking ship velocity equals zero. In addition, gravity is not included in the model as it is demonstrated that it has a negligible effect on the maximum ship penetration. However, the damage due to the collision has an influence

on the resistance and the stability of the jacket, leading to a potential collapse of the tower and the nacelle.

Based on the deformation computed with the developed algorithm, a post-collision study could be performed to assess the stability of the whole OWT, including both the jacket, the tower and the nacelle and taking into account additional loads such as gravity, wind, waves, ...

- Rupture of elements is discussed in Section 3.6 and is demonstrated to have few influence on the deformation modes but has an effect on the ship penetration. This phenomenon could be further investigated.

  Modelling properly rupture in FE models is still an arduous challenge. In the commercial code *LS-DYNA*, one single erosive failure law is implemented and is only valid for elements mainly subjected to tension.

  In a simplified model, considering rupture is even more challenging because an analytical model is not able to provide localised strains but only mean strains on the whole cross-section. The local initiation of rupture is therefore challenging to model.

- In the present thesis, the striking ship is considered as perfectly rigid. In a real collision, the ship suffers some deformations and dissipates energy. The ratio between the ship and the jacket stiffnesses governs the distribution of energy distribution between both ship and structure, as represented in Fig. 2.3.

  Simplified analytical formulations are already developed for ship stem or bulb deformation, and could be implemented in the model. This work would require some adaptations to take into account the interactions between the ship and the jacket deformations.

- In all the collision scenarios considered, the striking ship is moving only along its surge direction. Additional analytical developments could be performed to take into account motion in the sway or heave directions (Fig. 3.15).

  Considering sway displacements, additional collision scenario could be investigated, such as ships colliding 1 or 2 legs with side shells.

- In the present thesis, the formulations and algorithms are dedicated to assess the crashworthiness of OWT jackets. Similar work using analytical developments could be performed for other OWT supporting structures, such as monopiles, tripod, tripiles, gravity base or floating structures. Such research is being performed by A. Bela and S. Echeverry, whose main publications are listed in Chapter 1, for monopiles and floating structures respectively.

Appendix A

Finite element method theory in the framework of ship collisions

A.1 Introduction

Finite element method is probably the most widely used technique today when ship collisions are investigated.

Historically, the preliminary developments of the FEM were performed at the beginning of the 20th century. However, the calculations had to be solved hand-made, limiting therefore the size of the models. The development of computers in the 50's allowed for a quick increase of calculation power and the numerical tools became very efficient and suitable for larger structures. Nowadays, researches are still performed to improve the methodology [10].

Today, the constantly increasing computational power becomes available for all design offices. Large and complex models that are required to perform numerical simulation of ship collisions can be built and solved with a decreasing computation time and for a reasonable cost. In addition, commercial FE software are easily available, such as *ABAQUS* or *LS-DYNA* that are used for impact/crash simulations.

The first advantage of the FEM is the high level of details that can be considered when modelling a structure. As can be seen in Fig. A.1, the intersections between all tubular members composing the jacket can be modelled with a high geometrical fidelity. If the striking ship is considered as deformable, its internal stiffening system can be modelled also with a high accuracy, as can be seen in Fig. A.2 for the internal details of a ship bulb.

FE simulations provide a local insight of the structural response, stresses and strains, to a given loading. Designers may therefore improve finely the structure as they have localised values of stresses to perform a complete fatigue design.

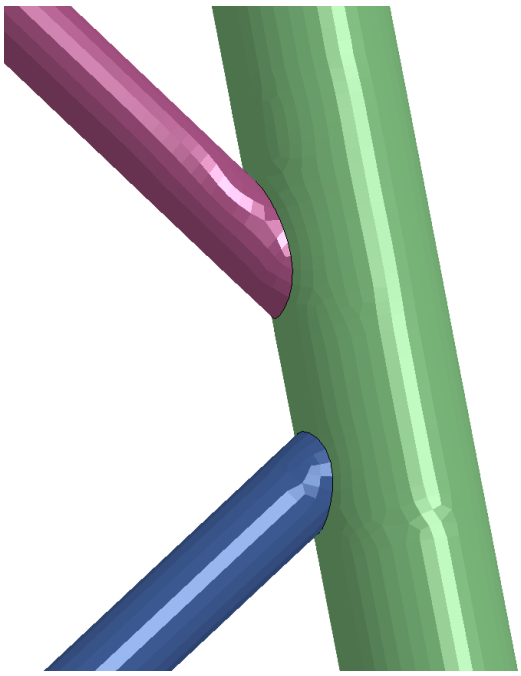

Figure A.1: Connection between a leg and braces

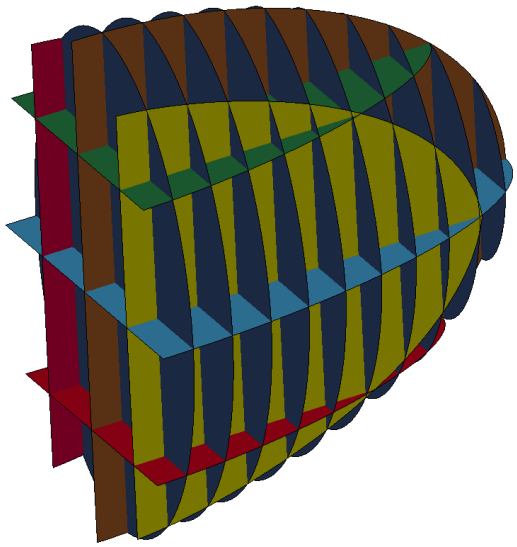

Figure A.2: Example of a bulb internal stiffening system

The results obtained from FE simulations are usually in good accordance with experiments, but this is not always the case. The most difficult phenomenon to model is probably the rupture, which is likely to occur during collision events and is one of the parameters that govern the structural response. Indeed, the strains in both the striking ship and collided structure may be large and overcome the rupture strain.

Lots of researches are performed to investigate rupture laws to be used in FE models. Amongst them, Ehlers et al. [3] investigated the effect of three different rupture laws defined in accordance to the mesh size by considering the impact response of three side ship structures. The crushing force - penetration curves computed with *LS-DYNA* were also compared with experimental results. From this study, it appeared that:

- For a given collision scenario, considering various mesh sizes with the same failure law provides different results. One can conclude that the failure law are not consistent for all the mesh sizes.
- Considering the same mesh size but different failure criteria leads to different results.
- The fact that the stress-strain curves do not dependent on the mesh size is contradictory with the failure strain defined according to the mesh size.

Additional research was performed to get realistic stress-strain curves until rupture, for example Ehlers and Varsta [4] who worked with dog-bones specimens, or Ehlers [2] who worked with circular plates. The results were shown to be in good agreement with experiments, but they cannot be extended directly to other impact scenarios.

In the framework of ship - ship or ship - submarine collisions, both vehicles may experience large overall displacements and rotations. This external dynamics of both striking and collided vessels was studied by Petersen [9] or Pedersen [8] and further developed by Le Sourne et al. [6, 7] who implemented a subroutine named *MCOL* in *LS-DYNA*.

In this last algorithm, as a first step, the collision force and resulting deformations are computed by *LS-DYNA*. This force is then transferred to *MCOL* that computes the new position, velocity and acceleration at the center of gravity of both vessels for all three directions and rotations taking into account the effects of hydrodynamic forces. Based on the results of *MCOL*, the next time step is solved by *LS-DYNA*, and so on. The interaction between *LS-DYNA* and *MCOL* is represented in Fig. A.3.

In *MCOL*, the updated position, velocities and accelerations are computed by solving the equation of motion that is described in Eq. A.1 for a body-fixed reference frame

$$\left[\underline{\underline{M}}_0 + \underline{\underline{M}}_\infty\right] \dot{\underline{y}} + \underline{\underline{G}}(\underline{y})\underline{y} = \left[\underline{F}_w + \underline{F}_h + \underline{F}_v\right](\underline{y}, \underline{x}) + \underline{F}_c \tag{A.1}$$

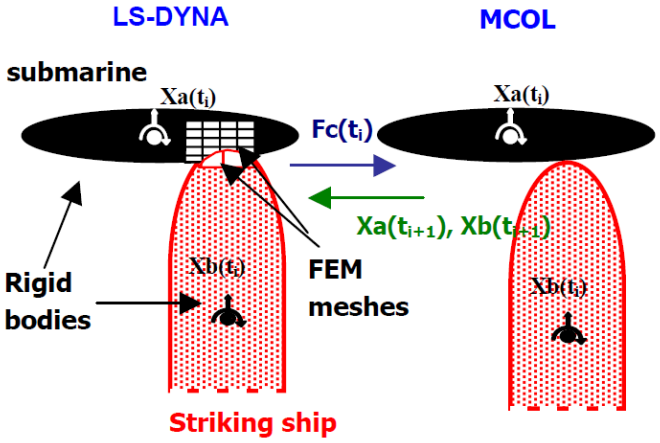

Figure A.3: Interaction between *LS-DYNA* and *MCOL* for ship-submarine collisions [7]

where

- $\underline{\underline{M}}_0$ and $\underline{\underline{M}}_\infty$ are the ship structural and added mass matrices;
- $\underline{x}$ is the position vector of the ship center of gravity in an earth-fixed reference frame;
- $\underline{y}$ is the velocity vector of the ship center of gravity in a body-fixed reference frame;
- $\underline{\underline{G}}$ is the gyroscopic matrix computed at the ship center of gravity;
- $\underline{F}_w$ is the hydrodynamic damping (wave radiation) vector at the ship center of gravity;
- $\underline{F}_h$ is the restoring forces and moments vector due to hydrostatic pressure at the ship center of gravity;
- $\underline{F}_v$ is the viscous forces and moments vector at the ship center of gravity;
- $\underline{F}_c$ is the contact forces and moments vector, as computed by *LS-DYNA*, at the ship center of gravity.

A.2 Theoretical aspects

In commercial software *LS-DYNA (LSTC)*, which is used for the FE simulations, both implicit and explicit solvers are available, but the explicit one is preferred for fast dynamics simulations due to their inherent high non linearities.

Let us consider a solid represented in Fig. A.4. It is represented in black at time n and moves to the position depicted in blue at time $n+1$. The displacement Δu of a point is given by the difference between its positions at time n and $n+1$.

The equation of motion is described by Eq. A.2 where t denotes the time.

$$\underline{\underline{M}}\ \underline{\ddot{u}}(t) + \underline{\underline{C}}\ \underline{\dot{u}}(t) + \underline{\underline{K}}\ \underline{u}(t) = \underline{F}(t) \tag{A.2}$$

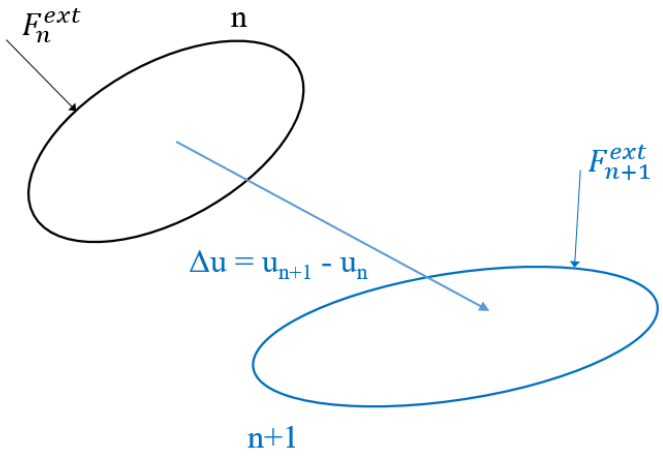

Figure A.4: Deformed solid at time n and $n+1$

where $\underline{\underline{M}}$, $\underline{\underline{C}}$ and $\underline{\underline{K}}$ are the mass, damping and stiffness matrices of the system respectively; $\underline{\ddot{u}}(t)$, $\underline{\dot{u}}(t)$ and $\underline{u}(t)$ the nodal acceleration, velocity and displacement vectors respectively; $\underline{F}(t)$ is the external force vector.

Eq. A.2 may be solved either in temporal or frequency domain. Newmark method, which is part of the temporal methods, is based on Taylor series and aims to compute the displacement, velocity and acceleration at time $n+1$ based on known solutions at time n. The system of equations to be solved at time $n+1$ is described in Eq. A.3.

$$\begin{cases} \underline{\underline{M}}\ \underline{\ddot{u}}_{n+1} + \underline{\underline{C}}\ \underline{\dot{u}}_{n+1} + \underline{\underline{K}}\ \underline{u}_{n+1} = \underline{F}_{n+1} \\ \underline{u}_{n+1} = \underline{u}_n + \Delta t \underline{\dot{u}}_n + \frac{\Delta t^2}{2}\left[(1-2\beta)\,\underline{\ddot{u}}_n + 2\beta \underline{\ddot{u}}_{n+1}\right] \\ \underline{\dot{u}}_{n+1} = \underline{\dot{u}}_n + \Delta t\left[(1-\gamma)\,\underline{\ddot{u}}_n + \gamma \underline{\ddot{u}}_{n+1}\right] \end{cases} \tag{A.3}$$

where β and γ are the constants of Newmark. In this system, the first equation corresponds to the equation of motion at time $n+1$. The second and third equations are Taylor developments at second order for the displacement and at first order for the acceleration respectively.

To solve the system described in Eq. A.3, a predictor $\underline{\tilde{u}}_{n+1}$ is used. This predictor is the solution obtained by assuming that the solution at time $n+1$ depends only on the acceleration at time n, as given in Eq. A.4.

$$\begin{cases} \underline{\tilde{u}}_{n+1} = \underline{u}_n + \Delta t \underline{\dot{u}}_n + \frac{\Delta t^2}{2}\left[1-2\beta\right]\underline{\ddot{u}}_n \\ \underline{\dot{\tilde{u}}}_{n+1} = \underline{\dot{u}}_n + (1-\gamma)\,\Delta t \underline{\ddot{u}}_n \end{cases} \tag{A.4}$$

Including Eq. A.4 into Eq. A.3 gives Eq. A.5.

$$\begin{cases} \left(\underline{\underline{M}} + \gamma \Delta t \underline{\underline{C}} + \beta \Delta t^2 \underline{\underline{K}}\right) \underline{\ddot{u}}_{n+1} = \underline{F}_{n+1} - \underline{\underline{C}}\ \underline{\dot{\tilde{u}}}_{n+1} - \underline{\underline{K}}\ \underline{\tilde{u}}_{n+1} \\ \underline{u}_{n+1} = \underline{\tilde{u}}_{n+1} + \beta \Delta t^2 \underline{\ddot{u}}_{n+1} \\ \underline{\dot{u}}_{n+1} = \underline{\dot{\tilde{u}}}_{n+1} + \gamma \Delta t \underline{\ddot{u}} \end{cases} \tag{A.5}$$

In an explicit integration scheme, it is assumed that the solution at time $n+1$ depends only on the solutions at time n, by setting $\beta = 0$. Therefore, the displacement at time $n+1$ is equal to the predictor, as described in Eq. A.6.

$$\underline{u}_{n+1} = \underline{\tilde{u}}_{n+1} = \underline{u}_n + \Delta t \underline{\dot{u}}_n + \frac{\Delta t^2}{2} \underline{\ddot{u}}_n \quad \Rightarrow \quad \Delta \underline{u} = \underline{u}_{n+1} - \underline{u}_n = \Delta t \underline{\dot{u}}_n + \frac{\Delta t^2}{2} \underline{\ddot{u}}_n \tag{A.6}$$

In *LS-DYNA*, the most used explicit integration scheme is the so-called centred differences scheme, in which $\gamma = \frac{1}{2}$. It is further assumed that damping can be neglected ($\underline{\underline{C}} = \underline{\underline{0}}$). Then, Eq. A.5 becomes Eq. A.7

$$\begin{cases} \underline{\underline{M}}\ \underline{\ddot{u}}_{n+1} = \underline{F}^{ext}_{n+1} - \underline{F}^{int}_{n+1} \\ \underline{u}_{n+1} = \underline{\tilde{u}}_{n+1} \\ \underline{\dot{u}}_{n+1} = \underline{\dot{\tilde{u}}}_n + \frac{1}{2}\Delta t \underline{\ddot{u}}_{n+1} \end{cases} \tag{A.7}$$

where

- $\underline{F}^{ext}_{n+1}$ is the vector of external forces applied on the structure at time $n+1$
- $\underline{F}^{int}_{n+1} = \int_{V_{n+1}} B^T(\underline{\underline{\sigma}}_{n+1})\ dV$ is the vectors of internal forces at time $n+1$. The operator B links displacements to deformations and is such as $\underline{\underline{\varepsilon}} = B(\underline{u})$. The matrix $\underline{\underline{\sigma}}_{n+1}$ is the Cauchy stress matrix and its derivation will be detailed later.

It is demonstrated that Newmark method is conditionally stable if $\gamma \geq \frac{1}{2}$ and $\beta \leq \frac{\gamma}{2}$, which is the case for the centred differences explicit method. In order to ensure the stability of the method, the time step Δt has to be small enough and respect the CFL (Courant-Friedrichs-Lewy) condition [1]. This condition states that the largest time step Δt_c to ensure the stability is the ratio between a characteristic length and the sound velocity, as given in Eq. A.8.

$$\Delta t_c \leq \frac{l_c}{c} \tag{A.8}$$

The time step should therefore be smaller than the time required for a shock wave to cross the smallest finite element in the model.

For shell elements, the characteristic length is defined by Eq. A.9

$$l_c \leq \frac{A}{max(l_1; l_2; l_3; l_4)} \tag{A.9}$$

where A is the area of the shell elements and $l_1; l_2; l_3; l_4$ are the lengths of its four edges. Therefore, the elements with a crushed shape, such as represented in Fig. A.5, should be avoided in the model.

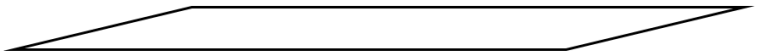

Figure A.5: Crushed shell element

For a material with a Young modulus E, a Poisson ratio ν and a density ρ, the sound velocity is given in Eq. A.10 for beam, shell and solid finite elements.

$$\begin{cases} c = \sqrt{\frac{E}{\rho}} & \text{for beam elements (1D)} \\ c = \sqrt{\frac{E}{\rho(1-\nu^2)}} & \text{for shelle elements (2D)} \\ c = \sqrt{\frac{E(1-\nu)}{\rho(1+\nu)(1-2\nu)}} & \text{for solid elements (3D)} \end{cases} \tag{A.10}$$

In order to solve Eq. A.7, the vector of internal forces at time $n+1$ has to be computed, which requires to compute the Cauchy stress matrix $\underline{\underline{\sigma}}_{n+1}$ as well. This is performed with an incremental procedure.

- The incremental Green-Lagrange strain tensor $\Delta\underline{\underline{E}}$ is computed, as given in Eq. A.11

$$\Delta\underline{\underline{E}} = \frac{1}{2}\left(\nabla_n(\Delta\underline{u}) + \nabla_n^T(\Delta\underline{u}) + \nabla_n^T(\Delta\underline{u})\nabla_n(\Delta\underline{u})\right) \tag{A.11}$$

  where ∇_n denotes the derivation with respect to the coordinate system related to the configuration at time n.

- The Piola-Kirchhoff stress matrix $\underline{\underline{\pi}}_{n+1}$ comes in Eq. A.12

$$\underline{\underline{\pi}}_{n+1} = \underline{\underline{\sigma}}_n + \underline{\underline{H}}\Delta\underline{\underline{E}} \tag{A.12}$$

  where $\underline{\underline{H}}$ is the matrix that links stress and strain (Hooke's matrix in elastic regime).

- The gradient of the deformation matrix $\underline{\underline{F}}$ is computed with Eq. A.13

$$\underline{\underline{F}} = \underline{\underline{I}} + \nabla_n(\Delta\underline{u}) \tag{A.13}$$

  where $\underline{\underline{I}}$ is the identity matrix.

- Finally, the Cauchy stress matrix $\underline{\underline{\sigma}}_{n+1}$ is given in Eq. A.14.

$$\underline{\underline{\sigma}}_{n+1} = \frac{1}{det(\underline{\underline{F}})}\left[\underline{\underline{F}}^T\underline{\underline{\pi}}_{n+1}\underline{\underline{F}}\right] \tag{A.14}$$

Then, the first equation of Eq. A.7, which is $\underline{\underline{M}}\ \underline{\ddot{u}}_{n+1} = \underline{F}^{ext}_{n+1} - \underline{F}^{int}_{n+1}$, is solved to determine $\underline{\ddot{u}}_{n+1}$. The algorithm implemented in fast dynamic solvers such as *LS-DYNA* is described in Fig. A.6.

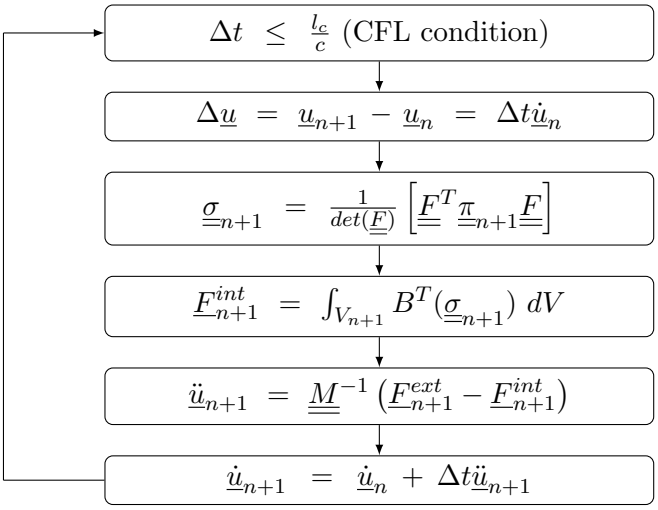

Figure A.6: Explicit integration scheme, as implemented in *LS-DYNA*

A.3 Treatment of contacts in *LS-DYNA*

As collisions are investigated, the contact between the striking ship and the collided jacket has to be modelled. In *LS-DYNA*, several algorithms are available therefore. In the framework of this thesis, contact is assessed by using the *AUTOMATIC_SURFACE_TO_SURFACE* card that is based on the penalty approach. This method consists in considering normal interface springs between the nodes of surfaces in contact [5].

First of all, a methodology is established to check if contact between both surfaces occurs. Those two surfaces are denoted respectively *master* and *slave*.

At each iteration, the distance d between the master and the slave is computed for each slave node. A line normal to the master shell element and passing through the investigated slave node is considered. d corresponds then to the distance between the slave node and the intersection between the master shell element and the normal line, as represented in Fig. A.7.

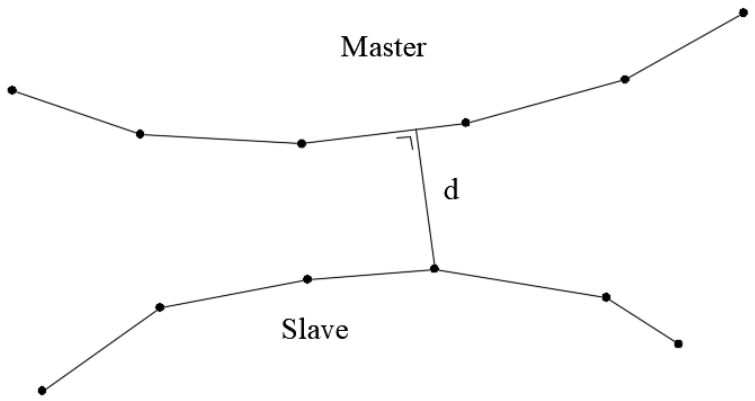

Figure A.7: Distance between the master and the slave

Let us consider the slave node n_S and assume that the normal to the master passing through n_S crosses the master surface at shell element S_1. As represented in Fig. A.8, we considered

$\underline{r}$ the position vector of the master shell element S_1 and $\underline{t}$ the position vector of node n_S. We denote the isoparametric coordinates of the master contact point as (ξ_c, η_c).

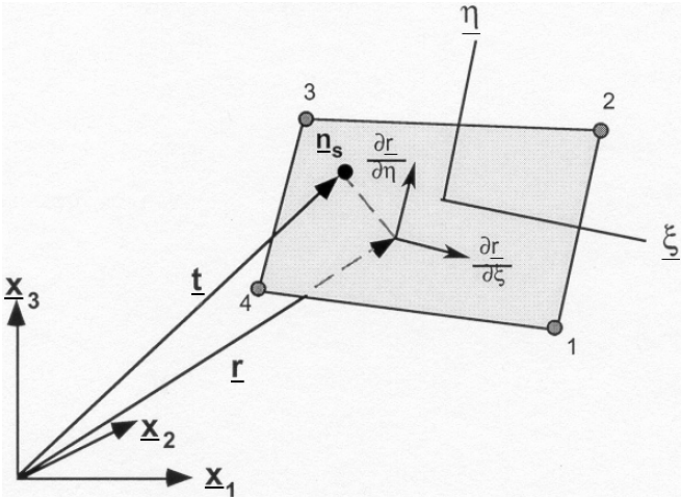

Figure A.8: Slave node, master shell element and position vectors [5]

Mathematically, penetration of node n_S through the shell element S_1 occurs if

$$l = \underline{n}_i \times [\underline{t} - \underline{r}\,(\xi_c, \eta_c)] < 0 \tag{A.15}$$

where

$$\underline{n}_i = \underline{n}_i\,(\xi_c, \eta_c) \tag{A.16}$$

is the normal of the shell element at contact point.

If penetration occurs, a contact force is computed in Eq. A.17

$$\underline{f}_S = l k_i \underline{n}_i \tag{A.17}$$

which is distributed over the four nodes ($j = 1, 2, 3, 4$) of the master shell element, as given in Eq. A.18

$$\underline{f}_j^i = \phi_j\,(\xi_c, \eta_c)\,\underline{f}_S \tag{A.18}$$

where ϕ_j corresponds to the interpolation functions of the shell element. The stiffness factor k_i computed in Eq. A.19 for the master shell element depends on both the bulk modulus K_i of the material, the face area of the element A_i and a scale factor f_{si} usually taken equal to 0.1.

$$k_i = \frac{f_{si} K_i A_i}{max(shell\ diagonal)} \tag{A.19}$$

Performing one FE simulation is often time-demanding, which makes this method perfect for final and accurate design validation but not suitable at pre-design stage during which several designs have to be investigated and thousands of collision scenarios have to be modelled.

Bibliography

[1] R Courant, K Friedrichs, and H Lewy. Uber die partiellen differenzengleichungen der mathematischen physik. *Mathematische Annalen*, (100(1)):32–74, 1928.

[2] S Ehlers. Strain and stress relation until fracture for finite element simulations of a thin circular plate. *Thin-Walled Structures*, (48):1–8, 2010.

[3] S Ehlers, J Broekhuijsen, HS Alsos, F Biehl, and K Tabri. Simulating the collision response of ship side structures: a failure criteria benchmark study. *International Shipbuilding Progress*, (55):127–144, 2008.

[4] S Ehlers and P Varsta. Strain and stress relation for non-linear finite element simulations. *Thin-Walled Structures*, (47):1203–1217, 2009.

[5] H Hallquist. *LS-DYNA theory manual*, 2006.

[6] H Le Sourne. A ship collision analysis program based on super-elements method coupled with large rotational ship movement analysis tool. In *Proceedings of the Forth International Conference on Collision and Grounding of Ships*, Hamburg, Germany, 2007.

[7] H Le Sourne, ER Donner, F Besnier, and M Ferry. External dynamics of ship-submarine collision. In *2nd International Conference on Collision and Grounding of Ships*, pages 137–144, Copenhagen, Denmark, 2001.

[8] PT Pedersen. Collision and grounding mechanics. In *Proceedings of WEMT'95*, pages 125–157, 1995.

[9] MJ Petersen. Dynamics of ship collisions. *Ocean Engineering*, (4):295–329, 1982.

[10] M Reza Eslami. *Finite Elements Methods in Mechanics*. Springer, 2014.